Recalage non-linéaire d'images TEP et CT du thorax pour la caractérisation des tumeurs : application à la radiothérapie

Antonio Moreno Ingelmo

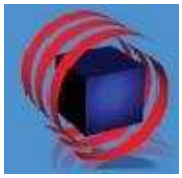

THÈSE

présentée par

Antonio MORENO INGELMO

pour l'obtention du

GRADE DE DOCTEUR

de l'Ecole Nationale Supérieure des Télécommunications

Spécialité : Signal et Images

Non-Linear Registration of Thoracic PET and CT Images for the Characterization of Tumors: Application to Radiotherapy

Recalage non-linéaire d'images TEP et CT du thorax pour la caractérisation des tumeurs : application à la radiothérapie

Soutenue le 19 septembre 2007 devant le jury composé de :

Christian BARILLOT	Président
Grégoire MALANDAIN	Rapporteur
Marinette REVENU	Rapporteur
David SARRUT	Examinateur
Sylvie JARDIN	Invitée
Isabelle BLOCH	Directeur de thèse

Abstract

The main topic of this PhD thesis is to combine the information coming from PET (Positron Emission Tomography) and CT (Computed Tomography) images to locate, with a good quality and in a robust way, the tumors placed in the thoracic regions. For this, *a priori* information about the anatomy and the spatial organization of the organs inside the body is integrated at different levels: as inputs of the algorithms (integration *a priori*), for guiding the processing (integration directly in the method) or for checking the results and correct them automatically if necessary (integration in order to detect potential errors and repair).

The first step consists in segmenting organs which are visible in both modalities by exploiting their structural relative positions and the *a priori* anatomical knowledge. We propose a robust approach which uses anatomical knowledge in order to guide the segmentation and correct it, when it is necessary, by using some consistency tests. In particular, we have developed an original method for segmenting the heart on non-contrast CT images. This method is described in detail in this work. The approach uses the spatial relation "between the lungs" in order to find a region of interest and then this relation is used in order to guide a deformable model which combines anatomical knowledge, the information of the contours in the image (GVF) and a pressure force derived from *a priori* knowledge. We propose a semi-automatic method for the detection of the pathologies (because some interaction, defined with the medical experts, is requested).

The main contribution of this thesis is the registration method with constraints that we have developed. This approach relies on landmarks, defined automatically on the surfaces of the lungs, and on rigidity constraints on the pathologies. The landmarks are detected via the computation of the curvature. The rigidity constraints on the tumors guarantee that no information provided by the PET image about their shape and their grey levels is lost. The transformation between the PET image and the CT image is computed by interpolation based on the landmarks and on the rigid structures, and it is weighted by a distance function to these structures in order to guarantee the continuity of the deformation.

Another originality of this PhD thesis is the introduction of a dynamic model of breathing in the registration method. This contribution seems extremely interesting because it makes it possible to find the trajectory that the tumor follows during the respiratory cycle and, in this way, registration could be performed with a better precision. The breathing model is used in order to find the corresponding landmarks on both images (CT and PET). This approach yields results that are physiologically more plausible than those obtained using correspondences based purely on geometry. Moreover, this original component makes it possible to predict the position of the tumor at the time of the radiotherapy, which is not done under the same conditions as the imagery exams.

The ultimate aim of this research is to define correctly the position and the movement of the tumors (preserving the qualitative information provided by PET images) in order to control very precisely (in time and in space) the doses of radiation which have to be applied

in radiotherapy for the treatment of these pathologies.

This work has been done within a CIFRE PhD thesis in collaboration with the company Segami and under the direction of Isabelle Bloch, professor at the Ecole Nationale Supérieure des Télécommunications (ENST), Signal and Images Processing department (Traitement du Signal et des Images, TSI), Paris.

Keywords: CT, PET, thorax, segmentation, elastic registration, dynamic model of breathing, radiotherapy, oncology.

Résumé

Le sujet principal de cette thèse est le recalage d'informations issues d'images TEP (Tomographie par Emission de Positons) et CT (Computed Tomography, tomodensitométrie) pour localiser, avec une bonne qualité et de façon robuste, les tumeurs situées dans les régions thoraciques. Pour cela des informations a priori sur l'anatomie et l'agencement des organes dans le corps sont intégrées à différents niveaux : comme entrées des algorithmes (intégration a priori), pour guider les traitements (intégration directement dans la méthode) ou pour vérifier les résultats et les corriger automatiquement si c'est nécessaire (intégration pour détecter les erreurs et les réparer).

Une première étape consiste à segmenter les organes visibles dans les deux modalités en exploitant pour cela leur agencement spatial structurel et les connaissances a priori sur l'anatomie. Nous proposons une approche robuste qui utilise les connaissances anatomiques pour guider la segmentation et la corriger quand c'est nécessaire grâce à des tests de cohérence. En particulier, nous avons développé une méthode originale pour segmenter le coeur sur les images CT non-contrastées. Cette méthode est décrite en détail dans ces travaux. L'approche utilise la relation spatiale "entre les poumons" pour trouver une région d'intérêt et ensuite cette relation est utilisée pour guider un modèle déformable qui combine les connaissances anatomiques, les informations des contours dans l'image (GVF) et une force de pression dérivée des connaissances a priori. Pour la détection des pathologies, nous utilisons une méthode semi-automatique (car une certaine interaction, définie avec les experts médicaux, est souhaitée).

Le noyau principal de cette thèse est la méthode de recalage avec contraintes que nous avons développée. Cette approche s'appuie sur des marqueurs, définis automatiquement sur les surfaces des poumons, et sur des contraintes de rigidité sur les pathologies. Les marqueurs sont détectés via le calcul de la courbure. Les contraintes de rigidité sur les tumeurs garantissent que l'on ne perd pas les informations sur leur forme et leurs niveaux de gris fournies par l'image TEP. La transformation entre l'image TEP et l'image CT est calculée par interpolation à partir des marqueurs et des structures rigides, et elle est pondérée par une fonction de la distance à ces structures ce qui garantit la continuité de la déformation.

Une autre des originalités de cette thèse est l'introduction d'un modèle de respiration dynamique dans la méthode de recalage. Cet apport semble extrêmement intéressant car il permettra de trouver la trajectoire que suit la tumeur pendant le cycle respiratoire et, de cette façon, le recalage pourra être fait avec une meilleure précision. Le modèle de respiration est utilisé pour trouver des marqueurs correspondants sur les deux images (CT et TEP) ce qui fournit des résultats physiologiquement plus plausibles qu'avec des correspondances uniquement fondées sur la géométrie. Cette composante originale permettra de prédire la position de la tumeur au moment de la radiothérapie, celle-ci n'étant pas faite dans les mêmes conditions que les examens d'imagerie.

Le but ultime de cette recherche est de bien définir la position et le mouvement des

tumeurs (tout en préservant les informations qualitatives fournies par les images TEP) pour ainsi contrôler très précisément (dans le temps et dans l'espace) les doses de radiation qui doivent être appliquées en radiothérapie pour le traitement de ces pathologies.

Ces travaux ont été réalisés dans le cadre d'une thèse CIFRE en collaboration avec la société Segami et sous la direction d'Isabelle Bloch, professeur à l'Ecole Nationale Supérieure des Télécommunications (ENST), département de Traitement du Signal et des Images (TSI), Paris.

Mot-Clés : Tomodensitométrie, TEP, thorax, segmentation, recalage élastique, modèle dynamique de respiration, radiothérapie, oncologie.

"Perseguir los sueños es la única forma de alcanzarlos"
Elena Vega Fernández

A Eva y Abel,
por su valor y su buen humor
por encima de todo

Remerciements

En premier lieu je souhaite remercier infiniment Isabelle Bloch de m'avoir permis de réaliser cette thèse de doctorat sous sa direction. Cela n'a pas seulement été un honneur mais aussi un plaisir. J'ai toujours pu compter sur elle pour me guider et m'orienter, et elle a toujours su me dire les mots qu'il fallait pour m'encourager et me motiver dans le travail. Merci Isabelle pour ta disponibilité, pour tes conseils, pour ton aide chaleureuse à tout moment, pour avoir toujours été là. Tous les mots que je pourrais dire seraient insuffisants pour exprimer ma gratitude. Je dirai juste une phrase de plus, qui peut sembler évidente mais qui ne l'est pas : je n'aurais jamais fini (ni commencé d'ailleurs) ma thèse sans toi, Isabelle !

Je souhaite remercier les membres de mon jury de thèse. Grand merci à Marinette Revenu d'avoir relu mon manuscrit et de m'avoir donné des conseils pour l'améliorer. Merci beaucoup à Grégoire Malandain pour avoir accepté la tâche difficile d'être rapporteur de ma thèse. Je tiens à remercier Christian Barillot d'avoir accepté d'être président de mon jury de thèse. Un merci chaleureux à David Sarrut pour avoir été examinateur de ma thèse, pour sa disponibilité et pour le grand intérêt qu'il a montré pour notre travail.

Ce travail a été réalisé en collaboration avec l'entreprise Segami Corporation dans le cadre d'une bourse CIFRE. Je tiens à remercier tous les membres de Segami et, en particulier, merci à Philippe Briandet de m'avoir permis de réaliser ma thèse avec eux. Merci également à Jean-François Stévenet et Jean-Yves Roul. Un merci spécial à Sylvie Jardin pour avoir accepté d'être dans mon jury de thèse et pour le travail que nous avons pu réaliser ensemble.

Dans le cadre de ma thèse, j'ai eu la chance de pouvoir travailler avec des personnes de différents milieux grâce à diverses collaborations. Ainsi, je souhaite remercier les hôpitaux avec lesquels nous avons travaillé et qui nous ont fourni des données (Hôpital de Louisville et C. H. R. U. Lille). Merci très spécialement, pour les images et pour les discussions constructives, à Claire Bernard du C. H. U. de Liège, à Hervé Foehrenbach et Marine Soret de l'H. I. A. Val-de-Grâce, à Yolande Petegnief de l'Hôpital de Tenon à Paris, et à Patrick Kupelian du MD Anderson Cancer Center à Orlando, Etats-Unis.

Je suis très content d'avoir pu travailler, pendant ces années de thèse, avec d'autres doctorants et docteurs, ce qui nous a permis d'être co-auteurs de plusieurs articles. Un grand merci à Oscar Camara Rey : *gracias tío por tu ayuda, pour tus mails "para meter presión" y por ser mi mentor. Gràcies també a* Gaspar Delsó : *no sé qué habría hecho sin tu ayuda para programar.* Merci beaucoup à Celina Maki Takemura pour ses discussions de travail très intéressantes, pour son aide, pour sa tendresse et son appui malgré la distance. Merci aussi à Olivier Colliot pour les discussions, les relectures. Je tiens à remercier également David Lesage et Gareth Funka-Lea, ainsi que Racha El Berbari pour l'aide qu'ils m'ont apportée pour le travail sur la segmentation du cœur.

Une bonne partie de ma thèse s'est déroulée dans le cadre d'un projet ANR : MARIO (Modélisation de l'Anatomie normale et pathologique pour le Recalage non-linéaire entre Images CT et TEP en Oncologie). Dans ce contexte j'ai pu travailler avec l'Université de

la Floride Centrale à Orlando, Etats-Unis, où j'ai réalisé un séjour d'un mois. Je tiens à remercier spécialement les personnes qui ont participé au projet MARIO. Merci à Jannick Rolland et Anand Santhanam de m'avoir accueilli dans leur laboratoire. *Thank you very much for all the work that we have done together. This has been (and still is) a very constructive experience.* Merci beaucoup à Elsa Angelini pour les relectures, les discussions et tous les conseils. Un grand merci à Roberta Brocardo, qui a partagé notre chemin dans MARIO pendant quelques mois. Grâce à toi le projet a remarquablement avancé ! Merci de ton aide, de ton travail rigoureux et efficace, et merci pour ta disponibilité, ton sourire et ta gentillesse. Je tiens à remercier très spécialement Sylvie Chambon. Elle a été l'âme du projet MARIO pendant ces derniers mois. Elle m'a montré le grand plaisir de travailler avec des amis. Je ne pourrais jamais te remercier assez pour ta patience, ta disponibilité à toute heure, les discussions scientifiques passionnées, les délires (aussi scientifiques) et un long et cetera. Merci aussi pour les discussions moins scientifiques et pour tous les moments passés ensemble, pour ton immense gentillesse et ton amitié.

Pendant mon doctorat à l'ENST j'ai aussi eu le plaisir d'encadrer des stagiaires et des étudiants en projet. Merci beaucoup à tous. Sachez que votre travail m'a toujours aidé et m'a beaucoup encouragé.

Je remercie tout le département TSI de l'ENST de l'accueil chaleureux que j'ai reçu pendant toutes ces années. En plus de l'extraordinaire environement scientifique, merci pour l'ambiance très conviviale. Merci beaucoup à tous mes compagnons au sein de TSI. Merci à la faune de la C011 : Tony (tu étais là, tu es resté, tu es parti et tu es revenu !), Gero (le meilleur compagnon avec qui j'aurais pu faire la course pour finir la thèse), Jasmine (le tien a été mon premier mariage français !), Céline H., Pau, Florent, Eve... Merci à tous ceux qui ont partagé avec moi les repas à la cantine, les pauses café, les pots : Penélope (*¡ánimo, ánimo!*), Jérémie (*¡sí, señor!*), Vincent, Olivier N., Jeff, Geoffroy, Hassan, Ceyhun, David L., Saïd, Francis, Florence, Henri, Catherine... Et merci à ceux qui étaient là il y a quelque temps : Jamal, Bénédicte, Sveta, Daniel (merci d'être venu à ma soutenance depuis Grenoble !), Céline T., Carlos, Alejandro... Je tiens à remercier chaleureusement Catherine Giraud pour son écoute et pour nos conversations, qui m'ont beaucoup aidé. Merci beaucoup à Patricia pour sa bonne humeur et sa gentillesse infinie, et a Bahman et Sophie-Charlotte pour leur patience et leur efficacité avec mes problèmes informatiques. *I also want to thank the people in Odalab who welcomed me and made my stay in Orlando a very nice one : Cali, Florian, Supraja...*

Je tiens à remercier également mes nouveaux collègues à NeuroSpin. Merci à Stanislas Dehaene de m'avoir accueilli aussi chaleureusement. Je suis très content de faire partie de l'équipe Unicog et je vous remercie sincèrement de votre sympathie (et aussi de votre patience ces premiers mois). Merci pour la bonne ambiance qui a fait que je me sente à l'aise depuis mon arrivée. Merci à tous : Stan, Philippe, Anne-Do (ne change jamais !), Antoinette, Laurence, Marie-Hélène, Ghislaine, André, Ed, Kepa, François, Christophe, Felipe, Antoine, Mari, Guillaume, Guido, Sarah, Susannah, Evelyn, Sepideh, Catherine, Jérémie, Karla, Floris, Caroline, Andreas, Rosalie... Merci également à toutes les personnes de l'IFR49, d'Imagen, du LNAO et des autres équipes avec qui je travaille (ou pas) : Dominique, Isabelle, Yann, Denis, Alexis, Jean-Baptiste, Jeff, Cyril, Fabrice, Yannick, Nicole, Maryline, etc.

Ce qui est très clair pour moi c'est que je n'aurais jamais pu commencer, m'accrocher et finir ma thèse de doctorat si j'avais été tout seul. Je n'aurais jamais pu le faire sans les gens qui ont été autour de moi pendant les heures que je ne dédiais pas au travail. Certains l'ont vécu de plus près, d'autres de plus loin (physiquement), mais mes amis ont toujours

été là. Quelques mots ne suffiront pas, mais je tiens à remercier de tout mon cœur : Fatima (gros BAC pour toujours !), Guillaume et Katka (pour les invitations, les cartes postales...), Cédric (parce qu'on n'a pas pu se voir souvent), Natalia (*en París, en Bruselas, en Londres*), Fernando *y* Damien (*por seguir invitándonos a pesar de todo*), Marta *y* Karim (*¡lo celebramos en Barcelona pronto!*), Sylvain (pour être venu à ma soutenance, pour les photos, les vidéos). *Muchas gracias a mis amigos que desde España no han dejado de apoyarme*: Alicia (*sí, Aliki, mola*), Angélica *y* Natalia (*y familia*), Antonio Luis *y* Paz, Eva *y* Abel (*a quienes dedico esta tesis*). *Quiero dar las gracias aquí a unos amigos especiales, puesto que son amigos de mi familia desde hace años y siempre han estado ahí. Considero que sin ellos, muy probablemente, yo no estaría donde estoy: muchas gracias a* Ludi, Paco *y familia*.

El último párrafo podría ser infinito y se quedaría corto...

Sin quienes nunca habría podido llegar aquí es sin mis padres. Nunca podré agradecerles todo lo que siempre han hecho por mí. Gracias mamá por habernos educado como lo has hecho, por ser tan fuerte y por querernos tanto. Gracias por estar siempre ahí y por tu apoyo en todo. Gracias papá. ¡Qué pena que ya no estés aquí! Muchas gracias Cris, *"imooto", por estar también siempre ahí, por todas nuestras conversaciones a altas horas de la noche (o no tanto), por tu confianza, por tu decisión, por tu carisma, por ser la mejor hermana que uno pudiera desear y por ser como eres, un ejemplo a seguir. Y gracias a ti también* Kike, *¡¡¡cuñao!!! Y aquí quiero dar las gracias a* Elena *y* Antonio, *relectores también de mi tesis.* Elena, *los dos sabemos que sin ti yo no estaría donde estoy. El resto ya lo sabes, porque te lo he dicho y porque entre nosotros sobran las palabras... Y para terminar, un GRACIAS en mayúsculas a* Anton, *que me ha aguantado día a día durante la tesis y eso no ha sido nada, nada fácil. Blagodarya ti, che si s mene, m. k. m.!*

Table of Contents

List of Figures

List of Tables

Résumé long en français

Introduction

Le sujet principal de cette thèse est le recalage d'informations issues d'images TEP (Tomographie par Emission de Positons) et CT (Computed Tomography) pour localiser, avec une bonne qualité et de façon robuste, les tumeurs situées dans les régions thoraciques.

Contexte d'application

De nos jours, le cancer est une des causes de mortalité les plus importantes chez les humains. En particulier, le cancer du poumon est un des types les plus fréquents. Un des traitements possibles pour cette pathologie est la radiothérapie. Cependant, le principal inconvénient de la radiothérapie est que les tissus sains peuvent être affectés par le traitement. Il est donc très important de connaître avec précision la position et l'extension de la pathologie pour réduire les doses de radiation dans les tissus sains.

Une méthode qui peut s'avérer utile pour réduire la zone irradiée est le recalage. Avec le recalage, les images issues de différents appareils d'imagerie et apportant des informations complémentaires sur l'anatomie et le métabolisme du corps humain peuvent être mises en correspondance pour ainsi mieux détecter l'état et l'extension de la tumeur.

La figure 3 illustre les différences entre une acquisition CT et une acquisition TEP pour un même patient avec une tumeur dans le poumon droit. Les images CT ou TDM (tomodensitométrie) fournissent des informations précises sur l'anatomie. Il s'agit d'une acquisition rapide (quelques secondes) qui peut être réalisée en apnée ou en respiration normale. De leur côté, les images TEP ou PET (Positron Emission Tomography) apportent des informations sur le métabolisme. Dans ce cas, l'acquisition est plus lente (autour de 30 minutes) et l'image acquise est donc une image moyennée, floue. La combinaison de ces deux modalités d'imagerie qui fournissent des informations complémentaires est très utile, en particulier en oncologie, pour planifier le traitement et faire face aux difficultés particulières dans le cas de tumeurs.

Objectifs de ces travaux

Dans ce contexte, un des objectifs de ces travaux est la localisation et la segmentation des organes et des pathologies pour aider le traitement par radiothérapie. En particulier il est très utile de savoir comment ils sont placés les uns par rapport aux autres. Cela est spécialement vrai pour le cœur qui est un organe très sensible à ce type de traitement. Un autre objectif important est de développer des outils pour le recalage CT/TEP dans le cas des tumeurs en tenant compte des contraintes pour la radiothérapie. Il faut donc prendre en compte l'effet de la respiration.

Notre objectif est de fournir des outils pour le traitement d'images. Notre travail s'arrête, cependant, avant le traitement par radiothérapie.

La figure 1 illustre le schéma général de la méthode que nous proposons dans ce travail et montre les différents types de connaissances anatomiques utilisées et comment elles sont intégrées dans les différentes étapes. Ces informations a priori sur l'anatomie et l'agencement des organes dans le corps sont intégrées à différents niveaux : comme entrées des algorithmes (intégration a priori), pour guider les traitements (intégration directement dans la méthode) ou pour vérifier les résultats et les corriger automatiquement si c'est nécessaire (intégration pour détecter les erreurs et les réparer).

Segmentation des structures anatomiques et pathologiques

La première étape de notre méthode consiste à segmenter les organes visibles dans les deux modalités en exploitant pour cela leur agencement spatial structurel et les connaissances a priori sur l'anatomie. Nous proposons une approche robuste qui utilise les connaissances anatomiques pour guider la segmentation et la corriger quand c'est nécessaire grâce à des tests de cohérence. Il s'agit d'une approche hiérarchique qui commence par les structures les plus faciles à segmenter et ensuite s'occupe des structures plus difficiles en utilisant pour cela la position par rapport aux structures préalablement segmentées (voir figures 3.1 et 3.2).

Segmentation des poumons

La première étape consiste à segmenter le contour du corps dans les deux modalités. Cela est réalisé avec des opérations de morphologie mathématique et des seuillages. Ensuite, on restreint la région de travail à l'intérieur du corps pour segmenter les différents organes.

Pour la segmentation des poumons nous avons utilisé également des opérations morphologiques, la méthode des k-moyennes et des seuillages. De plus, nous avons ajouté des tests de cohérence pour que la segmentation soit plus robuste. Ces tests de cohérence utilisent des connaissances anatomiques pour garantir que le résultat est cohérent avec ces connaissances. La figure 3.7 montre le schéma de la segmentation des poumons en CT. Les boîtes rouges indiquent que l'intégration des connaissances anatomiques est réalisée pour détecter et corriger les erreurs.

La segmentation en TEP reste pourtant spécialement difficile. La figure 3.10 illustre le schéma de la segmentation des poumons en TEP en utilisant directement les images TEP originales. Ici aussi, les boîtes rouges indiquent que l'intégration des connaissances anatomiques est réalisée pour détecter et corriger les erreurs et les boîtes bleues indiquent une intégration directement dans la méthode. Cependant, même avec les tests de cohérence, il y a des cas pour lequels la segmentation n'est pas satisfaisante. Pour résoudre ce problème nous avons amélioré la segmentation en utilisant soit l'image TEP de transmission (si elle est disponible) soit l'image CT quand les images ont été acquises avec une machine combinée CT/TEP. Les algorithmes utilisés pour ces deux cas sont représentés dans les figures 3.12(a), quand on utilise l'image TEP de transmission (quand elle est disponible), et 3.12(b), pour le cas où l'on utilise les poumons segmentés en CT (quand les images proviennent d'une machine combinée CT/TEP).

Une fois que les poumons sont segmentés, on peut segmenter avec des méthodes similaires le squelette (seulement en CT), les reins et le foie. Les schémas utilisés pour segmenter ces organes sont illustrés dans l'annexe A.

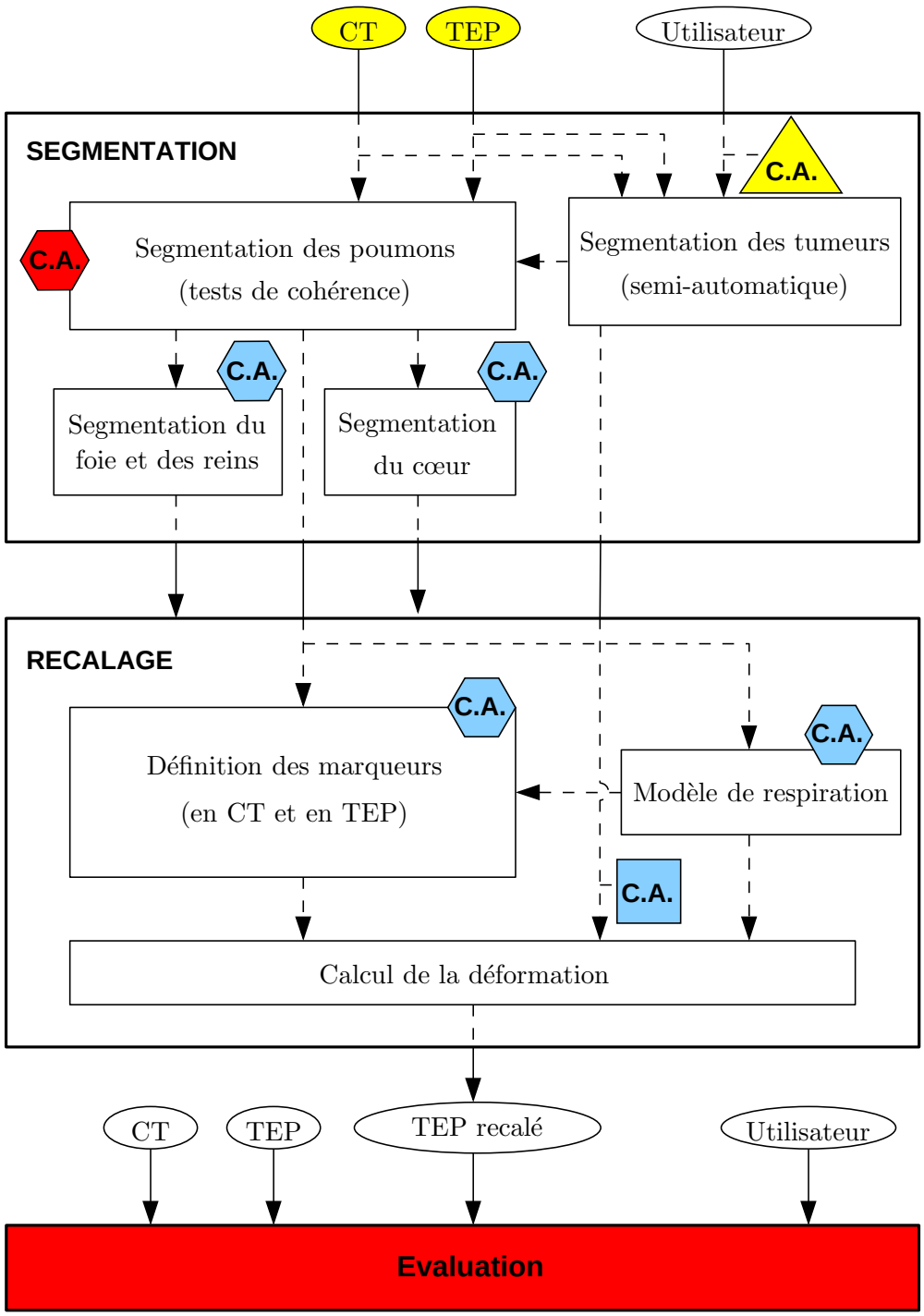

Figure 1: Schéma de notre méthode générale de recalage d'images CT et TEP en utilisant des connaissances anatomiques (C.A.). Les connaissances *générales* sont représentées par des hexagones, les connaissances *individuelles* par des triangles et les connaissances *adaptées* par des carrés. Les différents types d'intégration sont indiqués avec des couleurs : jaune veut dire intégration *a priori*; bleu clair, intégration *directement dans la méthode*; et rouge, intégration *pour détecter et réparer les erreurs*.

En conclusion de cette partie, nous avons proposé une méthode qui fournit des résultats corrects pour la segmentation de différentes structures du corps humain. Nos algorithmes pour segmenter le contour du corps, les poumons et le squelette sont exactement les mêmes indépendamment de l'origine des images. Cependant les chaînes de traitement pour les reins et le foie devraient être adaptées pour fournir des algorithmes automatiques et robustes. En général, la segmentation en CT ne présente pas d'obstacles particuliers. La tâche la plus difficile est la segmentation des poumons en TEP quand l'image TEP de transmission n'est pas disponible et que l'examen n'a pas été acquis avec une machine combinée CT/TEP. L'ajout de connaissances anatomiques et les tests de cohérence améliorent la robustesse de l'algorithme pour des images provenant de différents patients et différents centres médicaux. Les seuils utilisés dans les tests de cohérence ont été calculés empiriquement pour l'ensemble des cas disponibles. Cependant, la grande variabilité entre différentes anatomies rend nécessaire une évaluation plus poussée pour valider la méthode.

Segmentation du cœur

Une des contributions principales de ces travaux est le développement d'une méthode originale pour segmenter le cœur sur les images CT non-contrastées. Cela est très important pour beaucoup d'applications médicales comme le recalage d'images, l'estimation de la dose en radiothérapie, etc. Pour ces applications, les images CT sont les plus couramment utilisées, mais il faut cependant surmonter la principale difficulté : les structures autour du cœur (foie, aorte, tumeurs) ont des niveaux de gris très similaires à ceux du cœur, comme cela peut être observé sur la figure 3.17.

La plupart des méthodes qui existent segmentent les structures internes du cœur (par exemple, le ventricule gauche) et parmi les méthodes qui segmentent le cœur comme un tout, la plupart d'entre eux le font en 2D [Gregson, 1994] ou sur d'autres modalités comme l'IRM [Noble et al., 2002 ; Lynch et al., 2006 ; Lelieveldt et al., 1999]. Quelques approches proposent la segmentation du cœur sur des images CT [Jolly, 2006 ; Funka-Lea et al., 2006 ; Ecabert et al., 2005; 2007] mais il s'agit toujours d'images CT de haute résolution et contrastées, très utilisées en cardiologie. La méthode que nous proposons fonctionne en 3D sur des images CT de basse résolution non contrastées, courantes en routine clinique car le patient est soumis à moins de radiation.

Relation "entre" – Les descriptions anatomiques habituelles incluent l'énoncé "le cœur est entre les poumons". Pour cette raison, notre approche s'appuie sur la segmentation des poumons (robuste en CT comme on l'a décrit plus haut) et utilise la relation spatiale "entre les poumons" pour, d'abord, trouver une région d'intérêt et, ensuite, guider un modèle déformable pour segmenter le cœur.

Une enveloppe convexe (définition binaire d'"entre") n'est pas adaptée à notre cas puisque certaines parties du cœur ne sont pas incluses dans cette région. Cela est illustré sur la figure 3.18. Il est souhaitable donc d'utiliser une définition plus sophistiquée qui peut prendre en compte une région d'intérêt plus large que l'enveloppe convexe. Ainsi, parmi les définitions de "entre" détaillées dans [Bloch et al., 2006], nous avons choisi celle des dilatations directionnelles floues :

$$\begin{aligned}\beta_{btw}(A_1, A_2) = \quad & D_{\nu_2}(A_1) \cap D_{\nu_1}(A_2) \cap A_1^C \cap A_2^C \\ & \cap [D_{\nu_1}(A_1) \cap D_{\nu_1}(A_2)]^C \cap [D_{\nu_2}(A_1) \cap D_{\nu_2}(A_2)]^C\end{aligned}$$

La figure 3.20 illustre les différentes étapes pour le calcul de la relation "entre" $\beta_{btw}(A_1, A_2)$:

(a) les poumons segmentés A_1 (en rouge) et A_2 (en bleu), (b) l'histogramme d'angle normalisé $H_{(A_1,A_2)}$ par rapport à l'axe horizontal, (c) les éléments structurants ν_1 (en haut) et ν_2 (en bas), (d) dilatation floue du poumon droit (A_1) avec l'élément structurant flou ν_2, $D_{\nu_2}(A_1)$, (e) région floue β_{btw} entre les poumons, superposée sur les poumons segmentés. Les valeurs de la relation d'appartenance β_{btw} varient de 0 (blanc) à 1 (noir). L'avantage d'utiliser une définition floue est que la région "entre" s'étend graduellement en dehors de l'enveloppe convexe de la réunion des deux objets (les poumons).

Définition de la région d'intérêt – En 2D, [Gregson, 1994] avait utilisé le maximum de la distance aux poumons comme le centre d'un disque qui contiendrait le cœur. Néanmoins, cela n'est pas suffisant en 3D. Pour cette raison nous proposons de combiner la relation "entre les poumons" β_{btw} avec les connaissances anatomiques :

- β_{ffl} : "le centre du cœur est entre les poumons, loin d'eux mais plus proche du poumon gauche" (la fonction distance aux poumons normalisée est interprétée comme un ensemble flou qui répresente la région "loin des poumons"),
- β_{BB} : "le cœur est placé dans la région antérieure et inférieure de la boîte englobante des poumons".

Ensuite, ces trois connaissances sont combinées avec une fusion conjonctive (la t-norme "produit") de la façon suivante :

$$\beta_R(x) = \beta_{btw}(A_1, A_2)(x) \cdot \beta_{ffl}(x) \cdot \beta_{BB}(x).$$

Les différentes connaissances et leur fusion sont illustrés sur un exemple sur la figure 3.21.

Enfin, le maximum de β_R sera le centre d'une sphère-région d'intérêt qui contient le cœur.

Cette méthode fournit, d'une manière robuste, une région d'intérêt pour le cœur qui n'inclut pas trop d'autres structures. Les résultats obtenus pour 5 cas différents sont montrés sur la figure 3.22.

Evolution d'un modèle déformable – Un modèle déformable consiste en l'évolution d'une surface initiale (en 3D) sous l'effet de forces vers un état final (l'objet à segmenter, le cœur dans notre cas) :

$$\gamma \frac{\partial \mathbf{X}}{\partial t} = \mathbf{F}_{int}(\mathbf{X}) + \mathbf{F}_{ext}(\mathbf{X})$$

Nous définisons la surface initiale comme une petite sphère centrée dans la région d'intérêt (cf. figure 3.23). Cette surface initiale va évoluer selon l'influence des forces internes $\mathbf{F}_{int}$ et des forces externes $\mathbf{F}_{ext}$ tout en restant dans la région d'intérêt. Dans notre approche les forces externes combinent des informations des contours dans l'image, des connaissances anatomiques et une force de pression dérivée des connaissances a priori :

$$\mathbf{F}_{ext} = \lambda\, \mathbf{F}_{gvf} + (1 - \lambda)\, \mathbf{F}_R + \mathbf{F}_p$$

où

- $\mathbf{F}_{gvf}$ est la force du GVF (Gradient Vector Flow), qui définit un champ de vecteurs vers les contours de l'image (cf. figure 3.24) ;

- $\mathbf{F}_R$ est la force dérivée des connaissances anatomiques (β_R). Cette force contraint le modèle pour qu'il évolue vers les régions plus proches des poumons et "moins entre" eux que le centre (valeurs grandes de $\beta'_R = 1 - \beta_R$). Quand la relation β'_R est complètement satisfaite (non entre et dans les poumons), le modèle doit être seulement guidé par l'information sur les contours ;

- $\mathbf{F}_p$ est une force de pression normale à la surface et de module proportionnel à β_R ce qui améliore la convergence du modèle.

Un des avantages des relations spatiales floues est que l'on peut définir un champ de vecteurs vers les régions où les relations sont mieux satisfaites.

Résultats – Nous avons appliqué notre méthode sur 10 examens CT provenant de différents patients et de différents centres médicaux.

La figure 3.26 montre l'influence des différentes forces dans le modèle déformable. En 3.26(a) la segmentation du cœur a été calculée en utilisant seulement les forces $\mathbf{F}_{gvf}$ et $\mathbf{F}_R$ ce qui n'a pas permis une segmentation complète du cœur. Dans 3.26(b) une force de pression constante a été ajoutée, ce qui a fait que quelques parties de l'aorte sont incluses dans la segmentation du cœur. Finalement, dans 3.26(c) les trois forces $\mathbf{F}_{gvf}$, $\mathbf{F}_R$ et $\mathbf{F}_p$ ont été utilisées, ce qui a permis une bonne segmentation du cœur sans l'inclusion d'autres structures.

D'autres résultats des segmentations du cœur sont illustrés sur la figure 3.28, où ils sont comparés à des segmentations manuelles.

Notre approche utilise deux types différents de paramètres : ceux qui sont invariables pour les différents patients (montrés sur le tableau 3.3) et ceux qui doivent être adaptés pour les différents cas (tableau 3.4).

Discussion – Le tableau 3.6 contient les résultats quantitatifs pour tous les cas traités. Nous pouvons observer que l'indice de similarité est supérieur à 0,7 pour presque tous les 10 cas, ce qui indique que les résultats sont satisfaisants. Cela est également confirmé par les valeurs élévées de la sensitivité et la spécificité. La résolution des voxels en Z varie entre 4,5 et 7,5 mm : des distances moyennes entre 3,9 et 9,3 mm sont donc parfaitement acceptables. Ces résultats sont aussi satisfaisants si l'on les compare avec les 5,5 mm d'erreur moyenne obtenus par [Funka-Lea et al., 2006] sur des images CT contrastées avec des résolutions sous-millimétriques.

Notre algorithme a été utilisé sur des images acquises dans différents centres médicaux et sur différents patients. Ainsi, il y a des différences de contraste dans les images et des différences dans l'anatomie. A cause des différents contrastes, certaines séparations entre organes peuvent être visibles sur quelques études et pas sur d'autres. Notre méthode automatique prend en compte ces différences. Cependant, dans certains cas, les variations anatomiques inter-patients sont très importantes et quelques paramètres de la méthode doivent être ajustés. Cela est particulièrement vrai sur des examens réalisés sur des enfants ou sur des patients qui ont subi des opérations des poumons, par exemple. Une normalisation des distances calculées par rapport à la taille des poumons pourrait contourner en partie ce problème afin de pouvoir utiliser les mêmes paramètres pour tous les patients.

Conclusion – Nous avons proposé une approche originale pour la segmentation du cœur avec l'introduction de connaissances anatomiques. Notre méthode utilise des relations spa-

tiales pour définir la région d'intérêt du cœur et une nouvelle force externe d'un modèle déformable. Les premiers résultats quantitatifs confirment l'intérêt de la méthode proposée et nous pouvons souligner que notre méthode est robuste et qu'elle offre une amélioration par rapport aux approches classiques qui utilisent uniquement une force de pression et le GVF. De plus, les structures autour du cœur ne sont pas incluses dans la segmentation finale.

Le travail de cette partie a donné lieu à plusieurs publications [Moreno et al., 2006b; 2008b;a].

Perspectives – Plusieurs perspectives sont envisageables sur la segmentation du cœur. Par exemple, il est nécessaire de valider la méthode sur des bases de données plus grandes en collaboration avec des experts médicaux. Une autre application possible est d'utiliser la méthode sur d'autres modalités d'imagerie comme la TEP. Une amélioration possible consisterait à déterminer automatiquement les paramètres optimaux pour chaque cas. Enfin, on pourra appliquer la segmentation du cœur à des algorithmes de recalage qui s'appuient sur les structures et elle pourra être utilisée pour la planification de la radiothérapie.

Segmentation semi-interactive des tumeurs

La segmentation des tumeurs est très importante afin de quantifier des pathologies pour le diagnostic et la planification de la radiothérapie en particulier. Dans ces travaux, la segmentation des tumeurs est un pré-traitement pour l'algorithme de recalage.

Pour la détection des pathologies, nous utilisons une méthode semi-automatique car une certaine interaction, définie avec les experts médicaux, est souhaitée. L'algorithme comporte trois étapes :

1. sélection d'un point "germe" dans la tumeur (ce qui est fait par l'utilisateur) ;
2. segmentation grossière de la tumeur avec un algorithme de croissance de régions ;
3. raffinement de la segmentation avec la ligne de partage des eaux (cela est illustré sur la figure 3.33).

Enfin, la segmentation des tumeurs permet de raffiner la segmentation des poumons avec les tumeurs segmentées.

Conclusion

Les algorithmes de segmentation des différentes structures et des pathologies intègrent des *connaissances anatomiques* afin de les rendre plus robustes et de guider la segmentation. Par exemple, les connaissances anatomiques sur les *positions relatives* des organes sont introduites pour guider leur segmentation. Les *tests de cohérence* incluent également des connaissances anatomiques afin de détecter les erreurs potentielles et les réparer. Les algorithmes de segmentation du contour du corps, des poumons et du squelette sont robustes et fournissent des résultats satisfaisants pour des images provenant de différents patients et différents centres médicaux. Cependant, la tâche la plus complexe reste la segmentation des poumons en TEP quand l'image de transmission n'est pas disponible et que l'examen n'a pas été acquis avec une machine combinée CT/TEP. La segmentation des reins et du foie n'a pas été généralisée pour garantir des résultats robustes pour n'importe quel patient. Cela pourra être mis en place en utilisant des tests de cohérence comme pour les autres structures.

Nous avons également décrit une approche originale pour segmenter, d'une façon robuste, le cœur dans des images CT non-contrastées. Cette méthode utilise des *connaissances structurelles floues* exprimées comme des *relations spatiales* pour définir la région d'intérêt du cœur et, ensuite, pour définir de nouvelles forces externes introduites dans le schéma d'évolution d'un modèle déformable. Les résultats ont été évalués en les comparant avec des segmentations manuelles réalisées par un expert, ce qui montre la précision atteinte avec notre méthode. Les résultats quantitatifs préliminaires confirment le potentiel de la méthode proposée.

La méthode semi-interactive proposée pour la segmentation des tumeurs fournit des résultats corrects en CT et en TEP. Le fait d'ajouter une étape semi-interactive n'est pas un inconvénient puisque les médecins préfèrent contrôler cette initialisation fondamentale. De plus, avec un geste très simple, l'algorithme bénéficie des connaissances médicales d'un expert. Une validation sur une base de données plus grande reste pourtant nécessaire afin de vérifier la robustesse de notre approche, en particulier quand les tumeurs sont en contact avec les parois des poumons. La segmentation des tumeurs est nécessaire dans notre approche pour introduire des contraintes qui garantissent des déformations réalistes et qui améliorent le recalage non-linéaire entre les images anatomiques et fonctionnelles, décrit dans la section suivante.

Recalage avec contraintes de rigidité

Le noyau principal de cette thèse est la méthode de recalage avec contraintes que nous avons développée. Cette approche s'appuie sur des marqueurs, définis automatiquement sur les surfaces des poumons, et sur des contraintes de rigidité sur les pathologies.

Nous travaillons sur des images du thorax qui contiennent des objets qui subissent différentes déformations, en particulier, les poumons et les tumeurs. Nous partons de l'hypothèse que les tumeurs sont des structures rigides et qu'elles se déplacent juste en translation pendant la respiration. Cette hypothèse est en accord avec l'avis d'experts médicaux.

Pour cette raison, le recalage non-linéaire semble la meilleure option pour combiner les informations complémentaires apportées par les images CT et TEP, et cela même dans le cas d'acquisitions réalisées avec des machines combinées CT/TEP pour le même état de la tumeur. Le but est donc d'obtenir un recalage correct des structures principales en préservant l'information sur la tumeur. Cela veut dire que nous devons introduire des contraintes pour éviter que la tumeur suive les déformations des organes pendant la respiration. S'il n'y a pas de contraintes sur la tumeur, les résultats obtenus ne sont pas du tout réalistes, comme l'illustre la figure 1.1. Sans contraintes la tumeur subit des déformations irréalistes et l'information sur la pathologie est perdue.

Travaux existants

Il existe des nombreux travaux sur le recalage non-linéaire. Cependant, ils ne sont pas tous adaptés à notre problèmatique. Afin de sélectionner la méthode la mieux adaptée, nous avons défini les quatre critères suivants :

- *C1* – Les tumeurs doivent être prises en compte, ce qui implique qu'un algorithme de recalage non-linéaire sans contraintes n'est pas suffisant.
- *C2* – Le volume et la forme des tumeurs doivent être préservés afin de ne pas perdre l'information sur la pathologie, c'est-à-dire, l'intensité dans l'image TEP ; ainsi, les

objets rigides doivent rester complètement rigides ce qui implique qu'ils ne doivent pas être déformés, même légèrement.

- *C3* – La région rigide doit correspondre exactement à l'objet rigide. Elle ne doit pas être ni plus grande ni plus petite. Si l'on définit une région rigide trop petite, l'information réelle sur la pathologie peut être perdue. Si la région est trop grande, des structures déformables peuvent être forcées à rester rigides ce qui n'est pas réaliste.

- *C4* – Le champ de déformation doit être continu et lisse pour garantir des déformations physiologiquement plausibles

Le tableau 1.1 montre les différents types de méthodes de recalage avec contraintes et les critères qu'elles vérifient. Les méthodes fondées sur des Déformations de Forme Libre (Free-Form Deformations ou FFD) ne garantissent pas que la région rigide correspond *exactement* à l'objet rigide. Les méthodes variationnelles et probabilistes n'assurent pas que le volume et la forme des tumeurs seront toujours préservés. Enfin, parmi les méthodes qui incluent des déformations localement rigides, ce sont les méthodes de [Little et al., 1997] et [Huesman et al., 2003] qui vérifient les quatre critères que nous avons définis. Pour cette raison, nous proposons une extension de ce type d'approche pour la rendre automatique et robuste avec l'introduction de connaissances anatomiques. Ainsi, nous avons ajouté une définition automatique des marqueurs qui est adaptée à la forme des structures puis nous avons introduit un modèle de respiration pour trouver des correspondances entre les marqueurs ce qui produit des déformations plus réalistes.

Méthode proposée

La méthode que nous proposons comporte les étapes suivantes :

1. Définition de paires de points homologues (marqueurs) sur les deux images en s'appuyant sur les structures déjà segmentées (poumons).

2. Calcul de la déformation sur toute l'image par interpolation du déplacement en prenant en compte les marqueurs et la déformation de chaque marqueur selon la structure à laquelle il appartient.

3. Ajout de contraintes sur les structures rigides.

Définition des marqueurs et mise en correspondance – Les marqueurs sont détectés via le calcul de la courbure. Dans notre application, nous sélectionnons des marqueurs sur la surface des poumons en CT en utilisant les points de courbure maximale en valeur absolue (courbures gaussienne et moyenne). Ensuite, d'autres points sont rajoutés afin d'avoir une distribution pseudo-uniforme des marqueurs. Nous avons comparé les différentes méthodes pour la sélection des marqueurs avec la courbure. Cela est illustré sur la figure 4.4 et a donné lieu à une publication [Chambon et al., 2007].

Ensuite, nous utilisons la méthode ICP (Iterative Closest Point) [Besl and McKay, 1992] pour calculer de façon automatique les points correspondants sur l'image TEP.

Interpolation du déplacement – Avec les paires de marqueurs, maintenant nous pouvons calculer la déformation en chaque point $\boldsymbol{t}$ de la manière suivante :

$$\boldsymbol{f}(\boldsymbol{t}) = \mathcal{L}(\boldsymbol{t}) + \sum_{j=1}^{n} \boldsymbol{b}_j \, \sigma(\boldsymbol{t}, \boldsymbol{t}_j)$$

- Le premier terme représente la transformation linéaire, qui est une somme pondérée des transformations linéaires L_i de chaque objet rigide :

$$\mathcal{L}(\boldsymbol{t}) = \sum_{i=1}^{n_0} w_i(\boldsymbol{t}) \, L_i \quad \text{pour les } n_0 \text{ objets rigides } O_1, O_2, \ldots, O_{n_0}$$

  Les poids $w_i(\boldsymbol{t})$ dépendent de la distance entre le point $\boldsymbol{t}$ et l'objet rigide O_i, $d(\boldsymbol{t}, O_i)$. Ainsi, quand $\boldsymbol{t}$ est proche de l'objet O_i, sa transformation linéaire est proche de L_i.

- Le deuxième terme représente la transformation non-linéaire. $\boldsymbol{t}_i$ et $\boldsymbol{u}_i$ sont les marqueurs sur les images source et cible, respectivement. La matrice B peut être donc calculée pour satisfaire les contraintes de ces marqueurs :

$$\forall i, \quad \boldsymbol{u}_i = \boldsymbol{t}_i + \boldsymbol{f}(\boldsymbol{t}_i)$$

Introduction des structures rigides – Afin d'introduir l'influence des structures rigides, la fonction $\sigma(\boldsymbol{t}, \boldsymbol{t}_j)$ dans le terme non-linéaire est définie de la manière suivante :

$$\sigma(\boldsymbol{t}, \boldsymbol{t}_j) = d(\boldsymbol{t}, O_0) \, d(\boldsymbol{t}_j, O_0) \, |\boldsymbol{t} - \boldsymbol{t}_j|$$

où d est une fonction distance continue de $\boldsymbol{t}$ à O_0, avec $O_0 = O_1 \cup O_2 \cup \ldots \cup O_{n_0}$:

$$d(\boldsymbol{t}, O_0) \begin{cases} = 0 & \text{si } \boldsymbol{t} \in O_0 \\ \to 0 & \text{si } \boldsymbol{t} \to O_0 \end{cases}$$

La figure 4.3 illustre l'influence de la distance aux objets rigides dans la déformation non-linéaire. Ainsi, la valeur de la fonction σ sera proche de zéro :

- si le point $\boldsymbol{t}$ est proche d'un des objets rigides,
- si le marqueur $\boldsymbol{t}_j$ est proche d'un des objets rigides,
- si la distance entre le point $\boldsymbol{t}$ et le marqueur $\boldsymbol{t}_j$ est proche de zéro.

Ces contraintes de rigidité sur les tumeurs garantissent que l'on ne perd pas les informations sur leur forme et leurs niveaux de gris fournies par l'image TEP. La transformation entre l'image TEP et l'image CT est donc calculée par interpolation à partir des marqueurs et des structures rigides, et elle est pondérée par une fonction de la distance à ces structures ce qui garantit la continuité de la déformation.

Ce travail a donné lieu à deux publications [Moreno et al., 2005; 2006a].

Résultats et conclusion – Nous montrons dans le chapitre sur la méthode de recalage quelques résultats obtenus sur des images synthétiques, sur des images segmentées et sur des images réelles.

Les résultats sur des images synthétiques nous ont permis de vérifier que les structures rigides sont transformées de façon rigide (translation), que les marqueurs sont correctement déplacés et que la transformation est cohérente et régulière. Cela est illustré sur la figure 4.5 qui montre comment les résultats sont améliorés par rapport à une méthode de recalage sans contraintes de rigidité (figure 4.6).

Les résultats calculés sur des images segmentées nous permettent d'apprécier plus clairement l'effet de la transformation, d'analyser la déformation et de définir plus facilement les marqueurs sur les surfaces des poumons. La figure 4.9 montre quelques résultats avec différents nombres et différentes distributions des marqueurs.

Finalement, les résultats sur la figure 4.11 avec des images réelles nous confirment aussi que la qualité du résultat augmente avec le nombre de marqueurs et que la distribution des marqueurs joue un rôle important. Cependant, le nombre minimal de marqueurs peut rester petit (dans l'exemple seulement 16 sur une coupe axiale) s'ils sont sélectionnés correctement, c'est-à-dire, en utilisant des points de forte courbure.

En conclusion, notre méthode de recalage non-linéaire fonctionne en 3D et utilise des connaissances anatomiques ainsi que des marqueurs définis automatiquement sur l'image CT et sur l'image TEP. Il s'agit d'une méthode cohérente et robuste, même si la segmentation des tumeurs n'est pas parfaite, et elle préserve la géométrie de la tumeur et son intensité. L'information de l'image TEP est ainsi préservée ce qui est important pour le diagnostic et la radiothérapie.

Pour compléter ce travail une phase d'évaluation en collaboration avec des médecins reste nécessaire. Il faudrait également réaliser une étude physiologique détaillée des propriétés de rigidité des tissus autour de la pathologie pour savoir si cette rigidité varie de façon linéaire avec la distance à la pathologie. Si ce n'est pas le cas, le remplacement de la fonction distance par une autre fonction serait directe avec notre formulation.

Recalage en utilisant un modèle de respiration

Une autre des originalités de cette thèse est l'introduction d'un modèle de respiration dynamique dans la méthode de recalage. Cet apport semble très intéressant car il permettra de trouver la trajectoire que suit la tumeur pendant le cycle respiratoire et, de cette façon, le recalage pourra être fait avec une meilleure précision. Le modèle de respiration est utilisé pour trouver des marqueurs se correspondant sur les deux images (CT et TEP) ce qui fournit des résultats physiologiquement plus plausibles qu'avec des correspondances uniquement fondées sur la géométrie. Cette composante originale permettra de prédire la position de la tumeur au moment de la radiothérapie, celle-ci n'étant pas faite dans les mêmes conditions que les examens d'imagerie.

Le but ultime de cette recherche est de bien définir la position et le mouvement des tumeurs (tout en préservant les informations qualitatives fournies par les images TEP) pour ainsi contrôler très précisément (dans le temps et dans l'espace) les doses de radiation qui doivent être appliquées en radiothérapie pour le traitement de ces pathologies.

Pour illustrer cette problématique, la figure 5.1 montre deux images CT à des instants différents du cycle respiratoire et l'image TEP du même patient. Il peut être observé que l'anatomie des poumons est très différente selon l'instant du cycle respiratoire. Pour cette rai-

son, il est très important de prendre en compte la respiration pour garantir des déformations physiologiquement plausibles. L'objectif ici est donc d'améliorer le recalage non-linéaire et pour cela nous voulons "faire respirer le CT".

Nous avons combiné notre méthode de recalage avec un modèle de respiration comme le montre le schéma suivant :

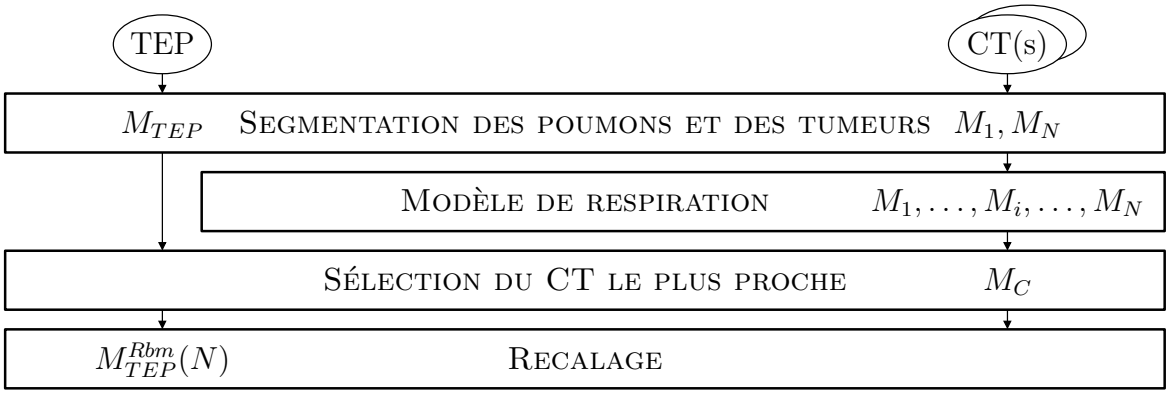

Modèles existants et choix du modèle – Le tableau 5.1 montre une classification des différents types de modèles de respiration existants. Pour le résumer, nous pouvons dire que le mouvement respiratoire peut être pris en compte :

- pendant la reconstruction du volume 3D [Crawford et al., 1996 ; Rit et al., 2005; 2006 ; Reyes-Aguirre et al., 2004 ; Sarrut et al., 2006] ;
- pendant le traitement par radiothérapie avec :
  - des techniques actives [Zhang et al., 2003],
  - des techniques passives [Sarrut et al., 2005 ; Schweikard et al., 2000 ; McClelland et al., 2006],
  - des techniques qui s'appuient sur des modèles :
    - géométriques [Segars et al., 2001; 2002a;b ; Reyes-Aguirre et al., 2005b],
    - physiques [Promayon et al., 1997 ; Zordan et al., 2006 ; Santhanam et al., 2006b].

Parmi tous les modèles, peu d'entre eux sont utilisés pour le recalage [Rohlfing and Maurer, 2001 ; Sundaram and Gee, 2005 ; Guerrero et al., 2005 ; Sarrut et al., 2005; 2006].

Dans le cadre d'une collaboration avec l'University of Central Florida, nous avons choisi le modèle de Santhanam et al. parce qu'il s'agit d'un modèle physique qui est dont mieux adapté à la simulation de la dynamique des poumons pour générer des instants intermédiaires, il est facilement adaptable à différents patients sans besoin d'adaptations externes et parce que la fonction de transfert du modèle permet l'adaptation à des cas pathologiques, qui est le but final de ces travaux. Ce modèle utilise la relation PV (Pression-Volume) pour calculer les différents instants entre l'expiration maximale et l'inspiration maximale (cf. figure 5.2).

Algorithme – L'algorithme que nous avons développé comporte les étapes suivantes :

1. Génération du modèle de respiration adapté au patient : les poumons sont préalablement segmentés en CT et en TEP et, à partir des maillages obtenus des segmentations en CT, tous les instants le long du cycle respiratoire peuvent être calculés.

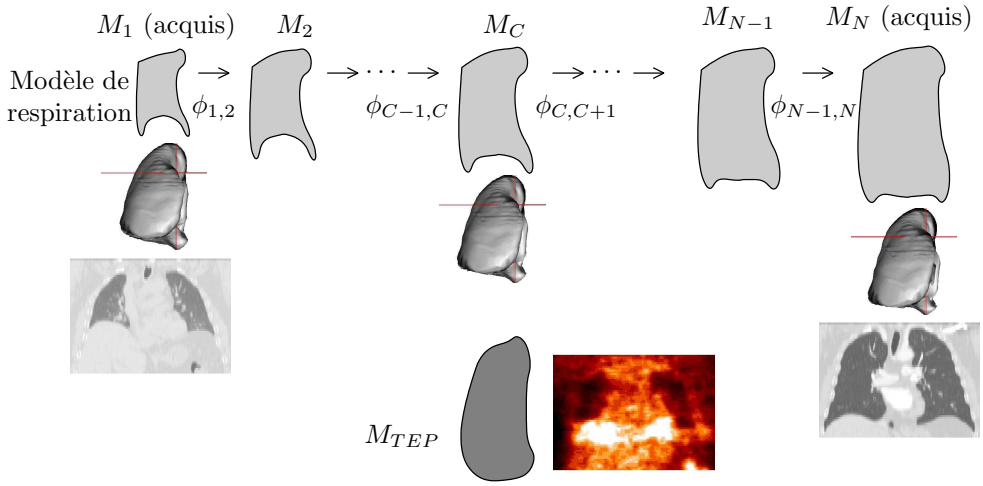

2. Sélection des marqueurs sur le maillage CT le plus proche du TEP (M_C) : le maillage CT le plus proche du maillage TEP est calculé en utilisant différentes mesures de similarité et les marqueurs sont sélectionnés avec la méthode décrite plus haut.

3. Estimation des points correspondants sur le maillage TEP, M_{TEP}, en utilisant l'algorithme ICP.

4. Suivi des marqueurs du maillage M_C au maillage CT M_N : les correspondances sont directement données par le modèle de respiration.

5. Déformation dense de toute l'image : c'est-à-dire, recalage du TEP et du CT original avec notre méthode de recalage.

La figure suivante (équivalente à la figure 5.4) illustre le schéma de l'algorithme de recalage en utilisant le modèle de respiration (ligne continue) et la méthode de recalage directe (ligne discontinue) :

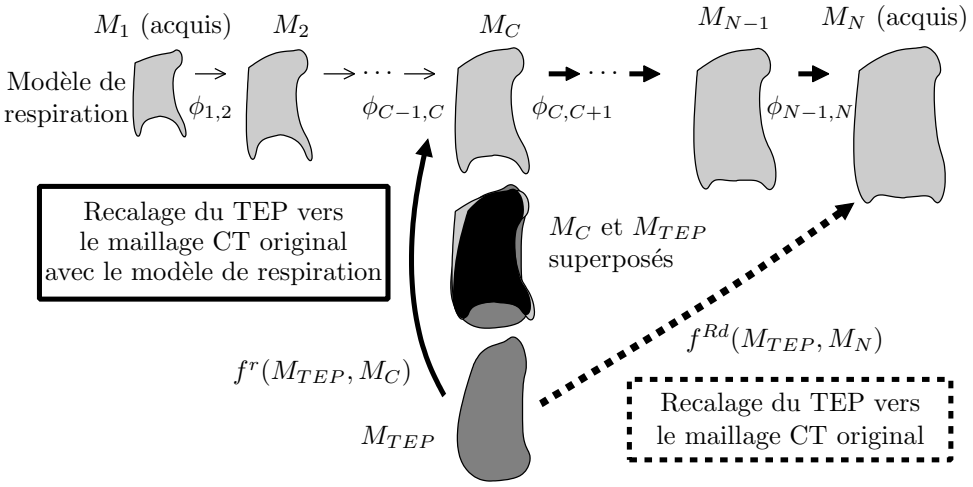

Premiers résultats – Les premiers résultats obtenus avec la combinaison du modèle de respiration et notre méthode de recalage sont illustrés sur les figures 5.6 et 5.7 pour un cas normal et sur les figures 5.8 et 5.9 pour un cas pathologique. Il peut être observé que les correspondances entre les marqueurs en CT et en TEP sont plus réalistes quand on utilise le modèle de respiration. La méthode qui utilise le modèle de respiration produit un meilleur recalage des surfaces des poumons et évite des déformations irréalistes. Cela est visible sur la figure 5.9 dans la région entre les poumons ou sur la figure 5.7 dans la région du poumon droit proche du foie. Dans cette région le contour du poumon sur le TEP recalé est plus proche du contour du poumon en CT quand le modèle de respiration est utilisé. Dans le cas pathologique (figure 5.8) la tumeur est correctement recalée et elle n'est pas déformée.

En conclusion, les résultats obtenus avec l'algorithme proposé sont fondés sur la physiologie et ils sont plus réalistes que les résultats obtenus en recalant le TEP directement avec l'image CT originale. Ces premiers résultats ont été calculés en utilisant des marqueurs déterminés par la combinaison des courbures moyenne et gaussienne avec l'ajout des marqueurs distribués de façon pseudo-uniforme. Néanmoins, une validation poussée reste nécessaire et est détaillée dans la section suivante.

Ce travail a donné lieu à deux publications [Moreno et al., 2007 ; Chambon et al., 2008].

Evaluation et comparaison des deux méthodes de recalage

Bien qu'il existe différentes méthodes pour valider le recalage CT-TEP, elles sont assez complexes et coûteuses en temps de calcul. Pour ces raisons, nous proposons dans ce travail une évaluation composée de deux approches différentes :

- une interface web conçue dans [Camara-Rey, 2003] en collaboration avec les médecins de l'hôpital du Val-de-Grâce à Paris, qui définit un protocole d'évaluation semi-quantitative visuelle (voir figure 6.1) ;

- une évaluation quantitative qui utilise différentes métriques pour comparer les volumes et les surfaces des poumons avant et après le recalage.

Les tableaux 6.1 et 6.2 montrent les résultats de comparaisons des volumes et des surfaces des poumons segmentés pour le recalage sans modèle de respiration et avec modèle de respiration respectivement.

Au vu des résultats, nous pouvons conclure que l'algorithme de recalage fournit des résultats corrects et qu'ils sont améliorés avec l'utilisation du modèle de respiration. Cependant, nous proposons plusieurs pistes pour améliorer l'étape d'évaluation :

- Comme l'évaluation des résultats du recalage n'est pas facile, et cela même avec les métriques que nous avons définies, il peut être intéressant de combiner les différents critères afin de décider quantitativement quel résultat est le meilleur. L'approche proposée par [Chambon, 2005] pourrait être utilisée pour ce faire.

- L'étape d'évaluation doit être améliorée avec plus de données et plus de tests afin de comparer en détail les différentes étapes de la méthode. Par exemple, l'influence du nombre de marqueurs et les différentes distributions possibles devraient être étudiées en profondeur.

- Le protocole d'évaluation n'a pas été conçu pour prendre en compte des cas pathologiques. L'interface web peut ainsi être améliorée en collaboration avec des radiologues pour mieux cerner leurs besoins et leur expertise pour évaluer le recalage des tumeurs en particulier.

- De plus, l'évaluation devrait être réalisée par un groupe d'experts médicaux et de radiologues afin de valider l'approche proposée.

Conclusions et perspectives

Nous avons développé une méthode de recalage CT/TEP d'images thoraciques avec des tumeurs dans les poumons. La contribution générale de cette thèse est l'introduction de connaissances anatomiques dans les différentes parties de notre approche.

Nous proposons des algorithmes de segmentation automatiques pour différentes structures du thorax et nous les appliquons à des images CT et TEP provenant de différents patients et différents centres médicaux. En particulier, les algorithmes de segmentation des poumons sont robustes grâce à l'utilisation de tests de cohérence qui garantissent des résultats physiologiquement réalistes. La segmentation des poumons en TEP reste néanmoins une tâche très difficile quand l'image TEP de transmission n'est pas disponible ou les images n'ont pas été acquises avec une machine combinée CT/TEP. Les procédures de segmentation des reins et du foie devraient être adaptées afin de fournir des méthodes automatiques et robustes comme pour les autres structures.

Pour la segmentation du cœur sur des images CT non-contrastées, la relation spatiale "entre les poumons" est utilisée. D'abord, elle permet d'obtenir une région d'intérêt et, ensuite, elle définit une force externe qui est introduite dans le schéma d'évolution d'un modèle déformable. L'étape la plus sensible est l'initialisation du modèle déformable, qui pourrait être adaptée pour permettre une certaine interaction avec l'utilisateur. Dans tous les cas, les résultats obtenus montrent l'intérêt de cette méthode.

Enfin, pour la segmentation des tumeurs nous proposons une approche semi-automatique qui bénéficie des connaissances des experts directement.

Le noyau principal de ces travaux est la méthode de recalage avec contraintes de rigidité, qui s'appuie sur les tumeurs. Cette méthode est automatique et elle est adaptée aux formes anatomiques et aux pathologies. Notre méthode présente deux avantages importants : le recalage reste cohérent et robuste même si la segmentation de la tumeur n'est pas parfaite et il préserve les différences locales.

Nous avons montré que l'introduction d'un modèle de respiration améliore les résultats du recalage en garantissant des déformations physiologiquement plausibles. Cela est une autre des originalités de ce travail.

Perspectives

Afin de valider nos différentes méthodes (segmentation, recalage), une évaluation poussée reste nécessaire et devra être réalisée en collaboration avec des experts médicaux sur un nombre plus important de données. Pour évaluer correctement les résultats du recalage, il faudra adapter l'interface d'évaluation pour prendre en compte les cas pathologiques.

Une des perspectives à court terme serait de segmenter le cœur en TEP puis de l'inclure dans la méthode de recalage. En effet, dans certains cas il y a des problèmes de recalage sur le cœur, comme le montre la figure suivante :

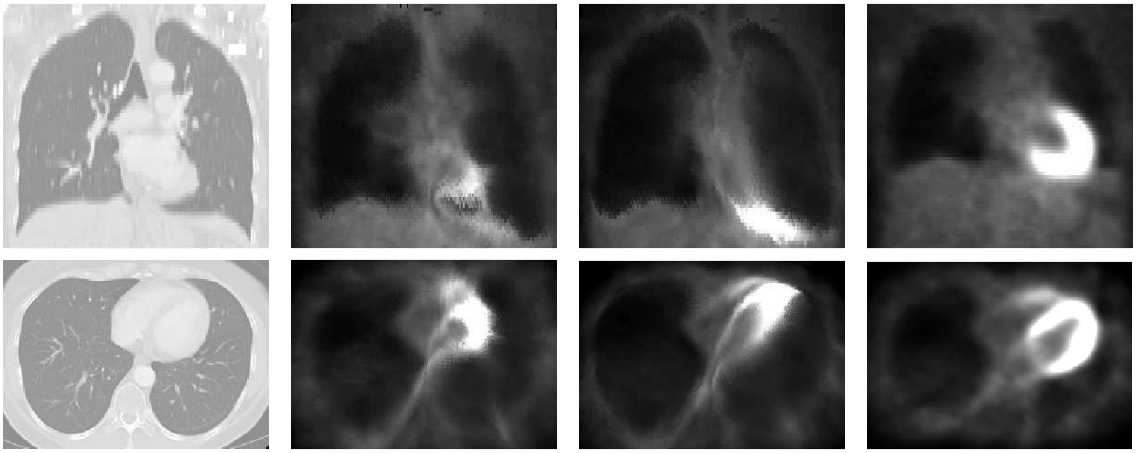

CT original | Résultat sans modèle de respiration | Résultat avec modèle de respiration | TEP original

Pour éviter ce genre de problème où le cœur est déformé d'une manière irréaliste, la segmentation du cœur peut être utilisée pour ajouter des contraintes de rigidité sur cet organe, puisqu'on peut considérer qu'il subit juste une translation entre l'image TEP et l'image CT. L'ajout de ces contraintes évite la déformation du cœur et fournit des résultats satisfaisants, comme il peut être observé sur un premier cas illustré ici :

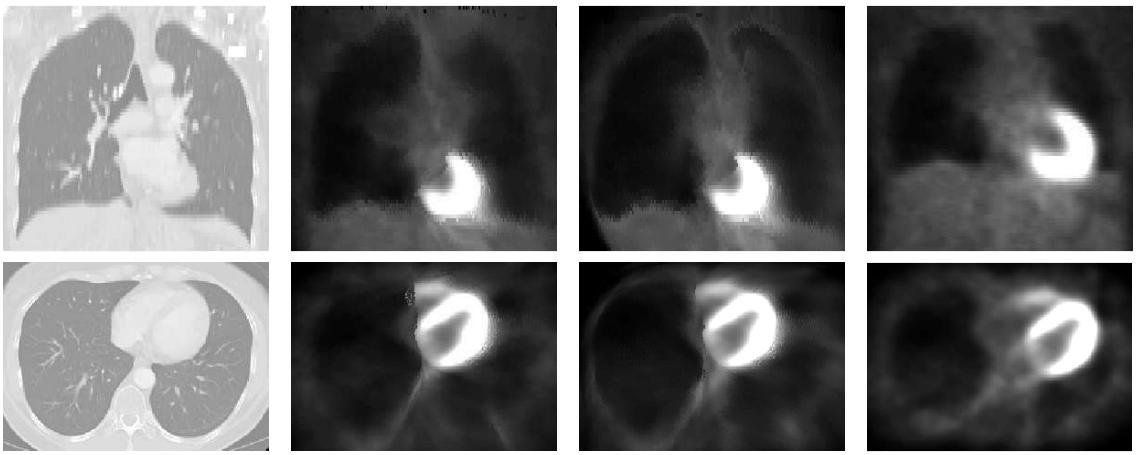

CT original | Résultat sans modèle de respiration | Résultat avec modèle de respiration | TEP original

Dans ce travail et comme première approche, le modèle de respiration utilisé est fondé sur des données de référence de sujets sains. Pour des travaux futurs, il faudrait adapter le modèle de respiration à des cas pathologiques en tenant compte du mouvement de la tumeur et son influence sur la respiration.

Notre méthode peut être comparée, voire combinée, avec d'autres méthodes, comme celles de [Camara et al., 2007] ou [Sarrut et al., 2006], ce qui fournirait des conclusions sur les limites de chaque méthode et leur domaine d'application.

Il serait également nécessaire de réaliser une étude sur la rigidité de la tumeur et des tissus environnants, pour pouvoir adapter notre méthode si nécessaire.

Enfin, notre approche peut être intégrée dans un outil clinique, pour le suivi des tumeurs pendant le cycle respiratoire et pour la planification du traitement en radiothérapie, ce qui aidera à réduire les marges de sécurité ainsi que les doses de radiation.

Introduction

Context – Nowadays, *cancer* is one of the most important causes of mortality in humans. Each year over 10 million new cases of cancer appear and more than 6 million people die in the world. Fortunately, medical imaging techniques are being developed and improved in order to fight against one of the most important plagues of this time. In particular, lung cancer is one of the most frequent types of this pathology. *Oncology* is the branch of medicine that studies cancer disease and *radiotherapy* one of the most popular methods for cancer treatment. This technique is based on a precise localization of the pathology and applies radiations (X-rays in general) with the appropriate dose to destroy the tumor. Conventional, or fractionated, radiotherapy is a form of external beam radiation that delivers a fraction of the complete radiation dose over many sessions to shrink or destroy tumors [Precision Radiotherapy, 2007]. It is often used for treating non-small cell lung cancer (NSCLC) in the lungs [Giraud, 2000]. Some studies have indicated a relationship between dose-response and survival and local control in early stage NSCLC patients. Higher doses of radiotherapy seem to provide improved local control. Therefore, studies of dose escalation are accepted until toxicity due to the dose is observed [Sibley et al., 1998 ; Martel et al., 1999]. Indeed, the major obstacle to the delivery of tumorcidal doses of radiation therapy is the resultant normal tissue toxicity. Radiation pneumonitis is felt to be one of the major dose limiting toxicities in the treatment of lung cancer [Kwa et al., 1998 ; Graham et al., 1999]. An important constraint relies on the knowledge of the exact position and spatial extension of the target region. This information is defined during the planning phase of the radiation protocol and remains very delicate. Its automation raises difficult problems which are not solved yet, involving data fusion and image interpretation, in order to achieve a precise, reliable and reproducible irradiation. Improving the therapeutic ratio of lung cancer treatment is based on one major premise: reducing the effective volume of lung irradiated.

In order to reduce the irradiated margins around the tumors, in particular in conformal radiotherapy[1], it is useful to use morphing techniques in cancer treatment [Atoui et al., 2004]. These techniques are also called *registration* methods. Registration is very useful in medical imaging for different applications. In particular in multi-modality, it is an appropriate tool in order to combine complementary information coming from different acquisitions. In the present work, we deal with the registration of positron emission tomography (PET) images and computed tomography (CT) images. PET is one of the most used modalities in medical imaging for oncological applications. This technique provides a good sensitivity in initial cancer detection and relapses. However, it does not always provide a precise location of the pathology. On the other hand, CT images provide precise information on the size and shape of lesions, as well as on normal anatomical structures. However they provide reduced

[1] Conformal radiotherapy uses computer technology to see the tumor in three dimensions (3D). The computer programs then design radiation beams that "conform" more closely to the shape of the tumor and avoid healthy tissue as far as possible.

information about malignancy. These two imaging modalities differ by numerous aspects: patient positioning, spatial resolution, breathing conditions, contrast agents in CT, PET tracers, signal to noise ratio. Therefore, the combination of information issued from both modalities is very useful in order to improve diagnosis, therapy and therapy planning. New systems combining PET and CT are now available. They provide an elegant but high-cost solution for the fusion of these data. Acquisitions with both modalities are not strictly simultaneous, which makes the development of precise registration methods still a requirement for such systems, in order to correct for shifts and deformations induced by different breathing conditions during PET and CT acquisitions and by physiological movements of the patient (over breathing and cardiac cycles).

Objectives and summary of this work – In this context, the aim of this work is to develop tools for fusion of PET and CT data in pulmonary oncology. For radiotherapy, it is necessary to quantify in real-time the position and deformation of lung tumors. This tracking is most crucial when tumors are close to the parenchyma and is important as well to distinguish between anatomical and functional pathologies. Radiotherapy also requires the knowledge of tumor position with respect to neighboring organs that can be affected by the radiations.

The registration procedure also requires an accurate description of the structures extracted from images. This description has to include the localization of the pathology and its segmentation if well delineated (for infiltrating and diffuse pathologies, only an approximate segmentation is reasonable). Image interpretation also requires segmentation and description of neighboring structures and their spatial relations with respect to the pathology, as well as their deformations and possible infiltrations. This information is important to understand the relations between pathology and normal structures and its effects on them.

Our approach relies on the segmentation of organs visible in both modalities and on their spatial arrangement, to guide the non-linear registration process. In [Camara-Rey, 2003], the segmented structures included body contours, lungs, liver and kidneys. Physiological movements and radiotherapy requirements impose that the heart has to be segmented as well. The heart is represented as a structure of known approximate localization (in particular its laterality) located "between" the lungs (see Figure 2). These spatial relations are used in our method to guide the search towards a reduced region of interest matching these characteristics. The spatial relations are modeled within the fuzzy set theory in order to cope with their intrinsic imprecision.

Segmentation of tumors is more difficult and cannot be directly solved in a similar way, since structural information, in particular spatial relations with respect to other structures, are not known a priori and can exhibit a large inter-patient variability. A specific semi-automatic method has been developed, rather than a completely automatic one, since some interaction is desirable (defined with the medical experts). An example CT and PET images including tumors is shown in Figure 3.

The combination of information acquired under different conditions and in highly deformable areas such as the thorax requires the development of non-linear registration methods. A non-linear registration approach is necessary to compensate locally large deformations mainly due to breathing, as illustrated in Figure 4. In order to guarantee a physiological plausibility of the computed deformations, we propose to take into account normal structures to assure their good match during the registration, as well as possible pathologies such as pulmonary tumors. Such tumors undergo specific movements, which are usually different

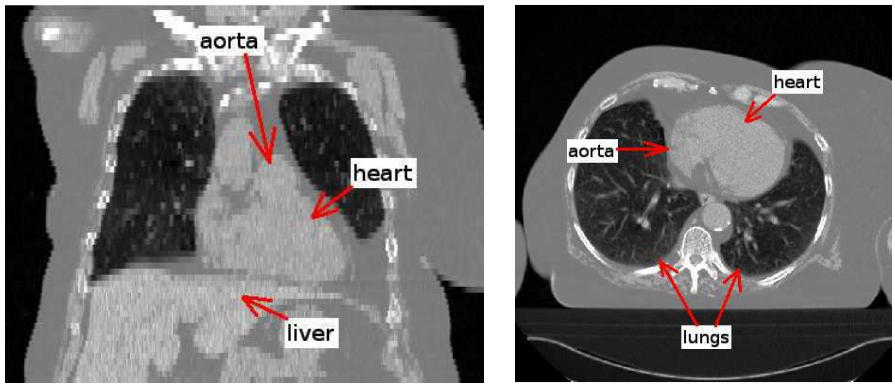

(a) (b)

Figure 2: Heart identification on a coronal (a) and an axial (b) views of a CT image.

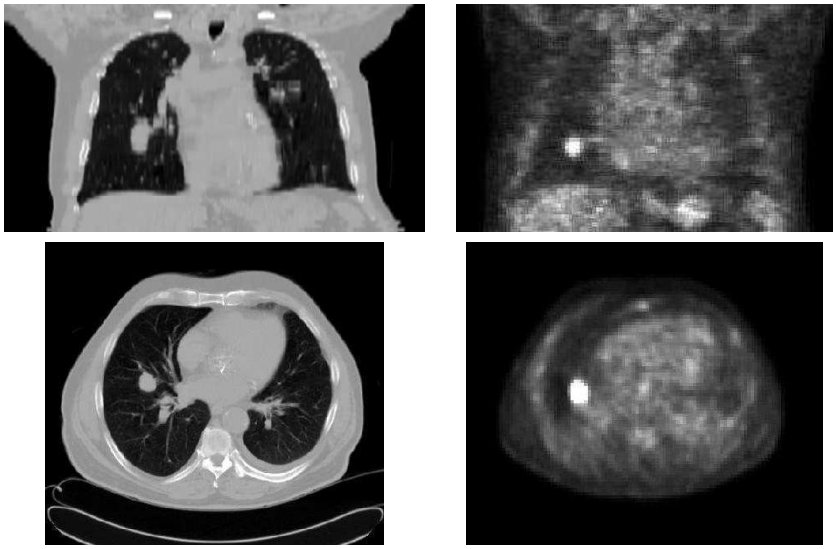

(a) (b)

Figure 3: Coronal (top) and axial (bottom) views of an original CT image (a) and the corresponding PET (b). The images include a tumor in the right lung.

from the one of lungs. As an original feature of this work, we propose to combine different individual movements while guaranteeing the continuity at the interfaces. The proposed scheme includes:

1. a first rigid registration of the tumor, obtained from segmentation results;

2. a constraint on the tumor which is not deformed further;

3. a non-linear registration applied to the other structures with continuity constraints.

In order to guarantee the continuity of the deformation, and avoid tearing or folding, the deformation at each point will be weighted by its distance to the tumor. Regions which are close to the tumor will move very little, while regions further away will follow the deformations imposed by the matching between normal structures. The originality of this approach

(a) (b) (c)

Figure 4: CT images (a,b) corresponding to two different instants of the breathing cycle and PET image (c) of the same patient (coronal views).

is that it combines constraints on normal structures and constraints specific to pathologies (i.e. the tumors).

Another original contribution of this work is the development and introduction of a dynamical breathing model. This is extremely interesting since it allows tracking the tumor during the breathing cycle and leading to a more precise registration. This has been done within a collaboration with the University of Central Florida (Jannick P. Rolland, Anand P. Santhanam) in the project ANR MARIO. A physiological breathing model has been integrated in the registration methodology in order to improve the results by introducing information about the physiology of the deformations during breathing.

The general algorithm that summarizes the work developed in this PhD thesis is shown in Figure 5.

The ultimate goal of this research is to provide a good definition of the position and motion of the tumors, while preserving PET information, in order to precisely control the radiation dose which should be applied in radiotherapy. The segmentation and registration methods developed in this thesis contribute to this aim.

Clinical collaborations – This PhD thesis has been carried out in collaboration with several clinical partners, in particular the Val-de-Grâce Hospital in Paris (Dr Hervé Foehrenbach, Dr Marine Soret), the University Hospital in Liège in Belgium (Dr Claire Bernard, Dr Hustinx, Dr Nicole Barthélémy-Brichant, Françoise Malchair), Tenon Hospital in Paris (Dr Yolande Petegnief) and the Anderson Cancer Center in Orlando, USA (Dr Patrick Kupelian, Dr Sandford Meeks, Dr Katja Langen). This work has benefited from these collaborations, as well as other contacts at Lille and Monaco Hospitals.

This thesis has been developed in collaboration with Segami Corporation (convention CIFRE).

Structure of the document – The objectives described above lead us to propose an approach structured along the following lines:

- identification of limitations of existing methods (Chapter 1);
- development of a structural description of anatomical and pathological structures (Chapter 2);

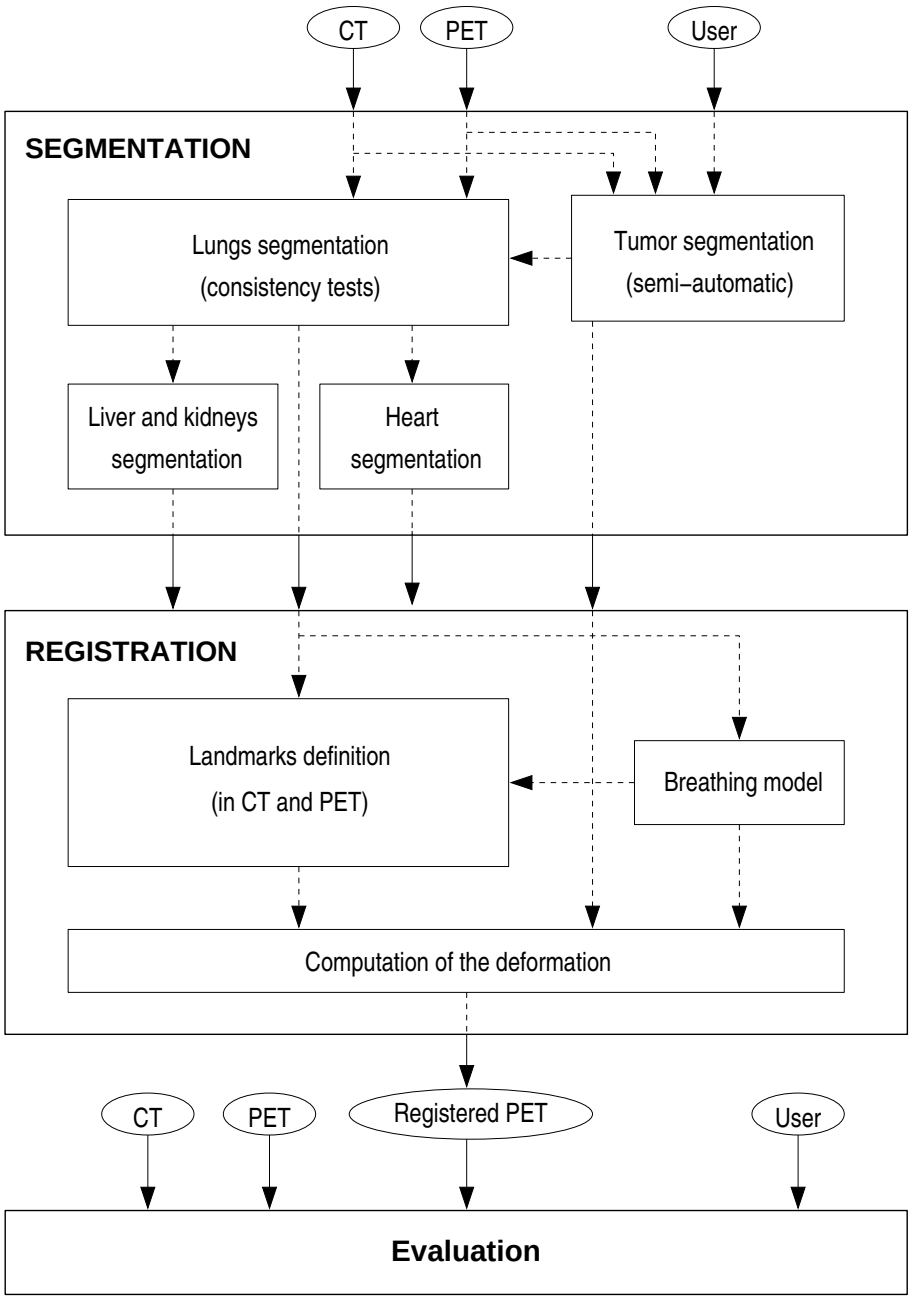

Figure 5: Diagram of our general algorithm for registration of CT and PET images.

- development of segmentation methods for these structures, in order to specify the description for the individual case, and to impose constraints on non-linear registration methods (Chapter 3);
- introduction of constraints on the tumor and its deformations during multi-modal registration (Chapter 4);
- integration of a breathing model in the procedure (Chapter 5);
- evaluation and comparison of the results (Chapter 6).

CHAPTER 1

Registration with constraints

As explained in the introduction, registration between several images of the same scene is a widely addressed topic and is important in many different domains. In general, the images include objects undergoing different types of deformation that have to be compensated during the registration procedure. Thus, the behavior of the registration close to the interfaces between such objects has to be carefully controlled in order to avoid discontinuities or other unrealistic phenomena.

The main aim of this work is to address this problem. First, in Section 1.1, we describe the particular context and the interest of CT/PET non-rigid registration. In Section 1.2, we explain why it is necessary to add constraints to registration with pathological cases, and we describe which type of constraints are most appropriate. Next, in Section 1.3, we present the state of the art in non-linear registration for medical applications, in particular with rigidity constraints. Then, in Section 1.4, we provide an overview of the proposed approach in which our rigidity constraints are defined by our particular application: thoracic images in pathological cases, where an issue is to cope with tumors and local deformations.

1.1 Interest of CT/PET non-rigid registration

We consider Computed Tomography (CT) and Positron Emission Tomography (PET) in thoracic regions, which furnish complementary information about the anatomy and the metabolism of human body. Registration of these two modalities is a challenging application, in particular with separate devices, due to the poor quality of the PET image and the large deformations involved in these regions. Nevertheless, their combination has a significant impact on improving medical decisions for diagnosis and therapy [Wagner Jr., 2003; 2004 ; Lavely et al., 2004 ; Rizzo et al., 2005 ; Vogel et al., 2006]. Although they still have some pitfalls [Truong et al., 2006], combined PET/CT scanners, which furnish rigidly registered images, have significantly reduced the problems of registering these two modalities [Townsend et al., 2004]. However, even with combined scanners, non-linear registration remains necessary to compensate patient respiration and heart beating [Shekhar et al., 2005]. This conclusion is also supported by the study of registration results in combined PET/CT devices realized by [Goerres et al., 2002]. They observed that the lesions mismatch varies significantly depending on the lung region where they are located. If a lesion is located adjacent to the pleura (the liver or a rib), the mismatch of image coregistration can cause problems, which is a well-known problem in radiation therapy planning using CT.

As illustrative examples of CT/PET non-linear registration of thoracic images, [Delso,

2003] and [Camara-Rey, 2003 ; Camara et al., 2007] have applied an approach based on Free-Form Deformations (FFD), which deals with local deformations. This kind of methods has as a limitation that regions placed inside or near the main structures will be deformed more or less according to the registration computed for the latter, depending on how local is the deformation. The addition of more degrees of freedom to cope with more local deformations is not a solution because of prohibitive computational costs and the lack of robustness with respect to noise, artefacts and local minima. A critical example of this situation occurs when a tumor is located inside the lungs and there is a large volume difference between CT and PET images due to the breathing. In this case, if the tumor is registered according to the transformation computed for the lungs, it may take unrealistic shapes, such as shown in Figure 1.1. This example is obtained with a structure-based registration approach. However an intensity-based refinement step [Camara et al., 2007] does not correct the important deformations of the tumor in the registered PET image.

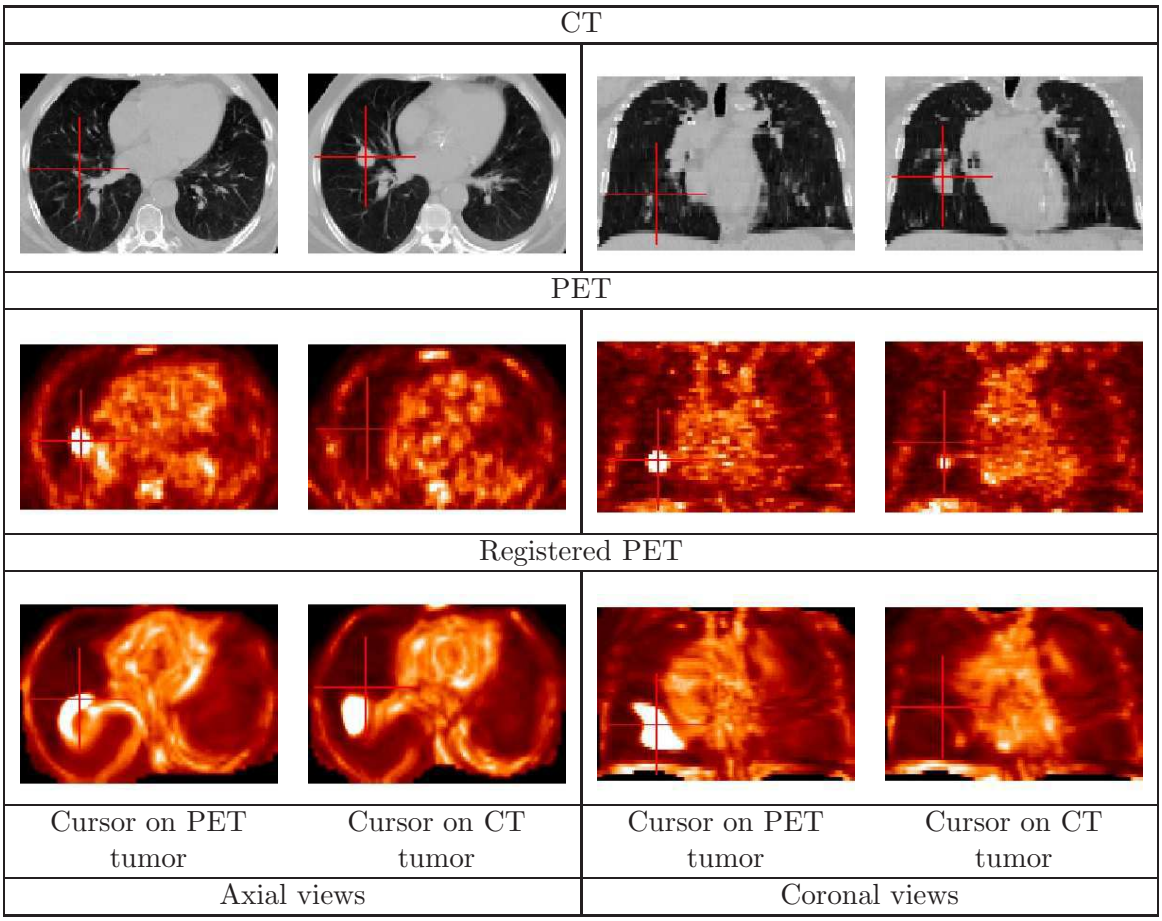

Figure 1.1: Result of the non-linear registration without tumor-based constraints. The absence of these constraints leads to undesired and irrelevant deformations of the pathology. On the images of the first and third columns, the cursor is positioned on the tumor localization in PET data, while in the second and fourth columns, it is positioned on the tumor localization in CT data. This example shows an erroneous positioning of the tumor and illustrates the importance of tumor segmentation and the use of tumor-specific constraints during the registration.

1.2 Necessity of constraints on the tumors

In the context of thoracic images including pathologies in the lungs, two very different deformations exist:

- the non-linear deformations of the lungs due to the breathing and
- the linear displacement of the tumor during the breathing cycle.

Indeed, tumors can be considered as rigid objects which move linearly during the respiration. This is supported by the work by [Paszek et al., 2005] who conclude that "tumors are stiffer than normal tissue" and, in particular compared to pulmonary parenchyma, they can be considered as rigid structures. A more detailed explanation about tumor rigidity can be found in [Huang and Ingber, 2005] where it is stated that tumors are more rigid because they have a stiffer extracellular matrix. For this reason, in our work, *tumors are considered as rigid structures*, which is the assumption we have made for our registration algorithm.

There exist some studies about the movement of the tumors inside the lungs during breathing, specially for radiotherapy applications. These works have been realized on different modalities as CT [Shih et al., 2004; 2002 ; McClelland et al., 2006] or MRI [Plathow et al., 2004] and for different applications as, for example, tumor-tracking [Sharp et al., 2004]. All these approaches assume that the tumor is a rigid body and that it undergoes a linear transformation during breathing. Thus, the objective of [Shimizu et al., 2001 ; Seppenwoolde et al., 2002] for tumor-tracking is to find the amplitude and the curvature of the trajectory of the tumor. [McClelland et al., 2006] have developed a method for constructing patient-specific computational motion models that describe the motion and the deformation which occur to a lung tumor and surrounding anatomy over an average respiratory cycle. The study by [Smyczynski et al., 2001] shows that the magnitude and direction of the motion of structures within the lung vary based on the specific anatomic region of the lung. However, they assume that the change in location of the tumor with respiration can be modeled as a linear motion between the two extreme locations. In addition to this, [Noyola-Martinez et al., 2005] concluded that "rigid body registration of sub-image regions surrounding the tumor is a feasible method to map tumor regions across CT images that represent various phases of the respiratory cycle". In this work, and as a first approximation, it is assumed that the *linear transformation of the tumor is simply a translation* during the breathing cycle. Further work should include a possible rotation of the pathology.

The aim of this work is to avoid undesired tumor misregistrations by adding some rigidity constraints on the tumors. Another goal is to preserve tumor geometry and, specially, intensity since it is critical for clinical applications. The preservation of intensity in PET images is a major requirement for clinical studies based on SUV (Standardized Uptake Value) [Feuardent et al., 2003] and for diagnosis and radiotherapy planning.

For all these reasons, we have defined some criteria in order to design a registration method adapted to our specific problem:

- *C1* – Tumors must be taken into account; thus, a non-linear registration algorithm without constraints is not sufficient.
- *C2* – Volume and shape of the object must be preserved in order not to lose valuable information about the pathology, i.e. intensity in the PET image, as stated above; thus, rigid objects must remain completely rigid, which means that they must not be deformed, even slightly.

- *C3* – The rigid region must correspond exactly to the rigid object and not to a smaller or a larger region. If a too small rigid region is defined, the real pathological information can be lost, and if a too large region is defined as rigid, some deformable structures can be forced to remain rigid which is not realistic.

- *C4* – Deformation fields must be continuous, even at the interfaces between objects, and smooth in order to guarantee physically plausible deformations.

1.3 Related work

A complete survey on image registration [Zitovà and Flusser, 2003] is out of the scope of this manuscript. The interested reader is referred to [Maintz and Viergever, 1998] and [Pluim and Fitzpatrick, 2003] for some reviews of registration methods for medical images. Among the most successful registration approaches we can cite:

- Elastic registration [Bajcsy and Kovačič, 1989 ; Kybic and Unser, 2003]: based on physical models of the behavior of elastic materials under the influence of external forces.

- Fluid registration [Christensen et al., 1996 ; Bro-Nielsen and Gramkow, 1996 ; D'Agostino et al., 2003 ; Mellor and Brady, 2005]: based on physical laws that provide an unconstrained model which allows free deformations similar to the behavior of viscous fluids.

- Optical flow [Horn and Schunck, 1981 ; Hellier, 2000]: based on an intensity conservation hypothesis in order to compute the displacement field between the images to register.

- Demons algorithm [Thirion, 1996; 1998 ; Roche, 2001 ; Guimond et al., 2001]: based on the search of attraction or repulsion forces between points belonging to the contour of the structures to register.

We focus in this state of the art on methods which can be applied to pathological data, i.e. in the presence of tumors, and which can provide local deformations.

1.3.1 Registration of pathological data

Different efforts have been done in order to preserve important information about the pathologies and to take into account the local nature of the deformations. [Blaffert and Wiemker, 2004] apply some of the most well-known existing methods on pathological data. Their goal was to detect and classify lung nodules in a CT follow up study. They investigated the accuracy and computation times of a rigid body, an affine, and a spline based elastic registration approach, and concluded that a good compromise was the affine registration on a previously segmented lung volume. However, this approach does not take into account the local nature of the deformations.

A typical approach to deal with local deformations is based on Free-Form Deformations (FFD). [Rueckert et al., 1999] apply this type of method to breast MR images. There are many works on the FFD approach and its possible improvements. For instance, [Castro-Pareja and Shekhar, 2004] propose a new solution to prevent mesh folding artifacts, common in FFD-based nonrigid registration, by controlling the deformation based on a priori knowledge of the magnitude of possible local deformations (local maximum voxel displacement).

Recently, [Rueckert et al., 2006] have also proposed an improvement of their approach by using diffeomorphic transformations in order to prevent folding.

1.3.2 Addition of rigidity constraints

We restrict our review of the literature to methods dealing with different types of deformations, in particular including rigidity constraints, and we comment them according to criteria *C1* to *C4*. We propose the following classification of these methods.

Non-rigid registration based on B-spline Free-Form Deformations (FFD)

Some of the most popular non-linear registration methods are based on B-spline FFDs. As mentioned above, [Rueckert et al., 2006] have proposed two registration methods for generating diffeomorphic FFDs by adding soft and hard constraints[1], which prevent folding. However, this approach does not account for preservation of volume or shape of the structures (criterion *C2* is not satisfied).

[Rohlfing and Maurer, 2001 ; Rohlfing et al., 2003] use grid refinement and added incompressibility constraints to the FFD approach using the properties of the Jacobian in order to guarantee the preservation of the volume of the structures. However, for this method, the shape of the structures is not preserved (*C2* is not satisfied).

[Tanner et al., 2000] have developed a method where control points in the B-spline based approach are coupled to enforce rigidity of the transformation locally. Their algorithm guarantees volume and shape preservation in the rigid regions defined by the lesions. Nevertheless, the region of the coupled control points has to be defined larger than the lesions (*C3* is not satisfied) in order to guarantee that the pathology remains completely rigid.

[Loeckx et al., 2004], [Staring et al., 2006] and [Ruan et al., 2006], inspired by the work of Rohlfing, add a local rigidity constraint in order to guarantee shape preservation. Here the rigidity is enforced by penalizing deviation of the Jacobian from being orthonormal. The rigidity penalty term indeed penalizes nonrigid deformations, but complete rigidity is sometimes not achieved (*C2* is not satisfied). This is due to the fact that the rigidity penalty term is not a hard constraint: it is merely a tradeoff between similarity and penalty.

The main disadvantage of these methods in our particular application is that, as cubic B-splines are used, the control points outside the defined rigid region influence the deformation inside this region. Therefore, criteria *C2* and *C3* cannot be fulfilled simultaneously.

Variational and probabilistic approaches

In this kind of approach, the transformation of the registration process is computed to optimize the segmentation simultaneously, thus, to a certain extent, it is constrained, even if segmentation and registration can be viewed as a same process. For instance, [Atif et al., 2004] and [Ripoche et al., 2004] use a variational approach for registration and segmentation respectively.

Another novel scheme for this kind of approach is described by [Xiaohua et al., 2004]. Their method is developed within a Bayesian framework, based on a maximum a posteriori (MAP) model. They introduce a hidden Markov random vector field into the model in order to enable interactions between segmentation and registration. It is used in the segmentation

[1]The soft constraints consist in adding a penalty function using the Jacobian and the hard constraints in bounding the maximum displacement of the control points

step to label each pixel with the highest probability to belong to a certain tissue type and in the registration step to act as a key element in the similarity measure. This approach is improved in [Xiaohua et al., 2005], where they incorporate a pharmacokinetic model in order to improve the performance of their algorithm. This pharmacokinetic model, used for curve fitting, can provide a mathematical measure to calculate the attribute vector for each pixel. With this approach, the segmentation and registration are smooth and random noise effect is also greatly reduced.

[Haber and Modersitzki, 2005] propose a variational approach that preserves the volume of the structures. This method improves their "Traditional Tikhonov regularization approach" [Haber and Modersitzki, 2004] by using a new scale space algorithm. There are two main advantages to this approach: every iteration of the scale space method is significantly simpler compared to the Tikhonov regularization approach and there is no need of searching the regularization parameter, i.e. a rough choice is sufficient.

[Zhang et al., 2006] propose a novel variational approach for multi-modal image registration based on consistent non-rigid transforms ensuring that the forward and backward transforms are close approximate inverses of each other. This is done by adding a consistency energy and solving the Euler-Lagrange equation implicitly using a numerically stable method. However, with this approach it is not possible to integrate rigid structures which impose abrupt deformation fields at some points.

[Ashburner and Friston, 2005] explain how tissue classification, bias correction and image registration can be integrated within the same generative model. They present a probabilistic framework where the model is based on a mixture of Gaussians and is extended to incorporate a smooth intensity variation and non-linear registration with tissue probability maps.

[Hachama et al., 2006b;a;c] propose a Bayesian framework in order to characterize the pathologies as outliers of a probabilistic distribution. The key idea is to assume that pixels can be divided into two classes: normal tissue and abnormalities. The registration constraints are defined as a mixture of two distributions which describe statistically image grey-level variations for both pixel classes. An implicit assumption is that grey levels in both images are similar, thus making the method appropriate for mono-modality images. This assumption should be relaxed to extend the method to multimodality images, which could be done by using mutual information as similarity criterion, instead of differences in grey-levels.

All these approaches do not include hard constraints in order to guarantee the rigidity of the lesion (*C2* is not satisfied).

Methods using landmarks

There is a huge amount of works in the literature which use corresponding points in order to impose deformations that exactly match these landmarks. [Joshi and Miller, 2000]

[Edwards et al., 1998] propose a three-component deformation model with respect to physical properties of the different tissues: rigid, deformable and fluid regions. The image is split into a grid of nodes which are connected by springs. Each node of the grid is labeled according to its physical properties and the stiffness of each spring is a function of the nodes at either end of it. Some selected landmarks are used as constraints of the model.

The combination of intensity- and feature-based approaches have been largely used for non-rigid registration [Collins et al., 1998a ; Vaillant and Davatzikos, 1999 ; Cachier et al., 2001 ; Johnson and Christensen, 2002 ; Hartkens et al., 2002a ; Hellier and Barillot, 2003 ; Rohr et al., 2004 ; Shen et al., 2005] and it has been proved that it improves the registration accuracy with respect to intensity-based or feature-based methods separately. Some of these

approaches use FFDs [Kim et al., 2003 ; Papademetris et al., 2004]. In most cases [West et al., 2005 ; Azar et al., 2006] landmarks (sometimes also called "features") are manually identified which is an important limitation. In addition to this, it is not easy to find a tradeoff between the landmark and intensity influence. In general, this parameter is tuned empirically, but some of the existing works [Hartkens et al., 2002a ; Azar et al., 2006] compute it automatically.

One limitation of all these methods is that they do not take into account explicitly the rigid structures (*C1* is not satisfied).

A description of the methods to select the appropriate landmarks or features on the images is detailed in Chapter 4.

Methods including locally rigid deformations

Other methods focus on the local nature of the deformations and the combination of different transformations which are associated to different regions or structures of the images. In the algorithms proposed by [Little et al., 1997] and [Huesman et al., 2003], the rigid structures are incorporated in a Thin-Plate Spline (TPS) [Bookstein, 1989] based nonrigid registration algorithm. These methods are based on the use of point interpolation techniques, together with a weighting of the deformation according to a distance function (as detailed in Chapter 4).

[Castellanos et al., 2004] present a slightly different methodology, in which the composition of local non-rigid warpings (*C2* is not satisfied) guarantees continuity, differentiability and a one-to-one transformation. This is computed throughout several levels of resolution, from coarse to fine. The composition of local warpings is constrained to a region of interest (ROI) by localizing a seed point automatically or manually and defining a resolution domain were the deformation is carried out.

[Duay et al., 2004] simulate the rigid motions by adaptively adjusting TPS radial basis functions according to local stiffness. The objective of this work is to automatically segment cerebral structures by registering a predefined atlas. This algorithm does not require any previous segmentation and it automatically adjusts the stiffness of the transformation because the stiffness map is defined once for all in the atlas. However, continuity is not guaranteed (*C4* is not satisfied).

[Arsigny et al., 2005] propose an approach using polyrigid and polyaffine transformations, i.e. transformations with several rigid or affine components. A given number of fuzzy regions are defined, on which the global transformation is mostly rigid or affine. However, this approach does not guarantee that a region defined as rigid is not slightly deformed (*C2* is not satisfied).

[Wang et al., 2005] model local rigidity of pre-identified rigid structures as well as global non-rigidity in the transformation field using triangular B-splines. Landmarks are selected interactively and brought into correspondence between source and target images as point-based constraints. This method is adaptable to 3D and to multimodality registration by using alternative metrics measuring image similarities as mutual information or normalized correlation. They state that the methods by [Tanner et al., 2000], [Loeckx et al., 2004] and [Duay et al., 2004] cannot precisely describe C^0 continuity in the displacement field (*C4* is not satisfied). However, the method by [Little et al., 1997] can.

Methods using breathing or anatomical models

Another family of methods use anatomical models of the thorax for the computation of the registration. They take into account the movements of the different structures during the breathing cycle in order to guide the registration procedure. Thus, some of them introduce physiologically plausible deformations which are closer to reality than geometry- or intensity-based approaches. All this is detailed and discussed in Chapter 5.

1.4 Overview of the proposed method

Among the aforementioned approaches, some of them have important disadvantages with respect to the criteria defined for our particular application. Methods based on B-spline FFD cannot fulfill simultaneously *C2* and *C3*, i.e. complete rigidity of the tumor and the fact that the rigid region must be equal to the lesion, respectively. Variational and probabilistic approaches do not include hard constraints in order to guarantee the rigidity of the lesion (*C2* is not satisfied). Methods using landmarks do not fulfill *C1* because they do not take into account explicitly the rigid structures except if the landmarks are located on the rigid objects. However, in that case, the rigidity of these structures is not guaranteed (*C2* is not satisfied). The advantages of some of the approaches that include locally rigid deformations is that they take into account rigid structures (*C1* is satisfied), they preserve "exactly" their shape (*C2* and *C3* are satisfied) and the deformations applied to the image are continuous and smooth (*C4* is satisfied). For these reasons we consider them to better match the physiological reality of the human body. Table 1.1 summarizes the different families of registration methods with constraints, with the list of criteria they fulfill.

The method we propose is inspired by these ones and adapted to develop a registration algorithm for the thoracic region in the presence of pathologies. We deal with medical data consisting of 3D CT and PET images of pathological cases, exhibiting tumors in the lungs. We assume that the tumor is rigid and thus a linear transformation is sufficient to cope with its movements between CT and PET images, as explained in Section 1.2. This hypothesis is relevant and in accordance with the clinicians' point of view, since tumors are often a compact mass of pathological tissue. One of the originalities of our approach compared to the aforementioned methods is that the positions of the landmarks are adapted to the shapes of the structures in the images. In addition to this, with our algorithm, the landmarks are defined automatically in both images. In the CT, they are selected by taking into account the regions of maximum curvature. Then, the corresponding points in the PET can be found using the ICP (Iterative Closest Point) algorithm. A first attempt to introduce a breathing model in the registration is detailed in Chapter 5. We aim at including physiological information coming from the model in our registration procedure. This guarantees that the deformations are more realistic compared to a geometrical approach.

We propose a method that benefits from anatomical knowledge in order to improve the robustness and accuracy of the different steps of the algorithm. The use of this anatomical knowledge is different for each stage and for the different structures (as detailed in Chapter 2).

The first step of our algorithm consists of an automatic segmentation of structures clearly identifiable in CT and PET: lungs, liver, kidneys, heart and tumor (cf. Chapter 3). Then we define automatically two groups of landmarks in both images, which correspond to homologous points. These landmarks guide the deformation of the PET image towards the CT image. The positions of the landmarks are adapted to anatomical shapes which is an important feature and one of the originalities of our method. The selection of the landmarks,

TYPES OF METHODS	REFERENCES	RESPECTED CRITERIA
Based on B-spline FFD	[Rohlfing and Maurer, 2001 ; Rohlfing et al., 2003 ; Rueckert et al., 2006]	*C1,C4*
	[Tanner et al., 2000 ; Loeckx et al., 2004 ; Staring et al., 2006 ; Ruan et al., 2006]	*C1,C2*
Variational and probabilistic	[Atif et al., 2004 ; Ripoche et al., 2004 ; Xiaohua et al., 2004; 2005 ; Haber and Modersitzki, 2005 ; Ashburner and Friston, 2005 ; Zhang et al., 2006 ; Hachama et al., 2006b;a;c]	*C1*
Using landmarks	[Edwards et al., 1998 ; Collins et al., 1998a ; Vaillant and Davatzikos, 1999 ; Cachier et al., 2001 ; Johnson and Christensen, 2002 ; Hartkens et al., 2002a ; Hellier and Barillot, 2003 ; Kim et al., 2003 ; Rohr et al., 2004 ; Papademetris et al., 2004 ; Shen et al., 2005 ; West et al., 2005 ; Azar et al., 2006]	-
Including locally rigid deformations	[Little et al., 1997 ; Huesman et al., 2003]	*C1,C2,C3,C4*
	[Castellanos et al., 2004]	*C4*
	[Duay et al., 2004]	*C1*
	[Arsigny et al., 2005]	*C1,C4*

Table 1.1: Summary of the different types of methods for registration with constraints and the criteria they fulfill.

the computation of the deformation as well as a study of the results of the registration with respect to the quality of landmark selection are detailed in Chapter 4.

In summary, our method has the following features: the rigid structures (tumors) are easily taken into account (*C1*); the rigid objects remain completely rigid which means that their volume and shape are preserved (*C2*), which corresponds to functional information of the PET image; the rigid transformation is not larger nor smaller than the lesion (*C3*); and the continuity of the transformation is guaranteed (*C4*). Again, the originality of the proposed approach is to strongly rely on anatomical structures to guide a feature-based registration algorithm, to integrate constraints specific to these structures on the one hand, and to the pathologies on the other hand. In order to improve the registration by introducing physiologically plausible deformations, we have also introduced a breathing model which is described in Chapter 5. The comparison and the evaluation of the different results can be found in Chapter 6.

CHAPTER 2

Use of anatomical knowledge for segmentation and registration

In this chapter we present a transversal view of our methodology, based on a common feature. This common link is the use of anatomical knowledge in order to guide the different processes or algorithms. But why is anatomical knowledge important? Is it useful for segmentation and registration of medical images? And, if it is useful, how can we use it? The goal of this chapter is to answer these questions.

2.1 Introduction

In the last centuries, the knowledge about human anatomy has largely increased and the representation of this knowledge has also been improved. As an example, compare the two images in Figure 2.1, one from the XVIth century and the other a contemporary one. These representations come from general anatomical knowledge acquired by experienced people. These experts usually describe their knowledge by saying or writing what they know. Then, other kinds of experts (as Leonardo[1] or a computer graphic engineer, in our examples) "translate" this knowledge into images, which are easier to understand for most people. One of the major aims in medical image processing in the last years is to "translate" this knowledge in order to make it understandable by computers and as automatic as possible.

In the following sections, we show the importance of anatomical knowledge in our context, we classify the different pieces of knowledge depending on how general they are and we explain how we integrate them in our general algorithm. Finally, we briefly describe how we introduce them in our methodology. The detailed description of each stage is developed in the corresponding chapter.

2.2 Importance of anatomical knowledge

Image interpretation has to face the difficult problem of matching the perceptual level and the semantic level. This matching consists in "translating" the anatomical knowledge from one level to the other. On one side, the perceptual level is composed of features, mainly pixels (voxels in 3D), or groups of pixels (or voxels), which can be extracted from the image.

[1] In the case of Leonardo, he was probably expert in both human anatomy and graphical representations, but this is not very common.

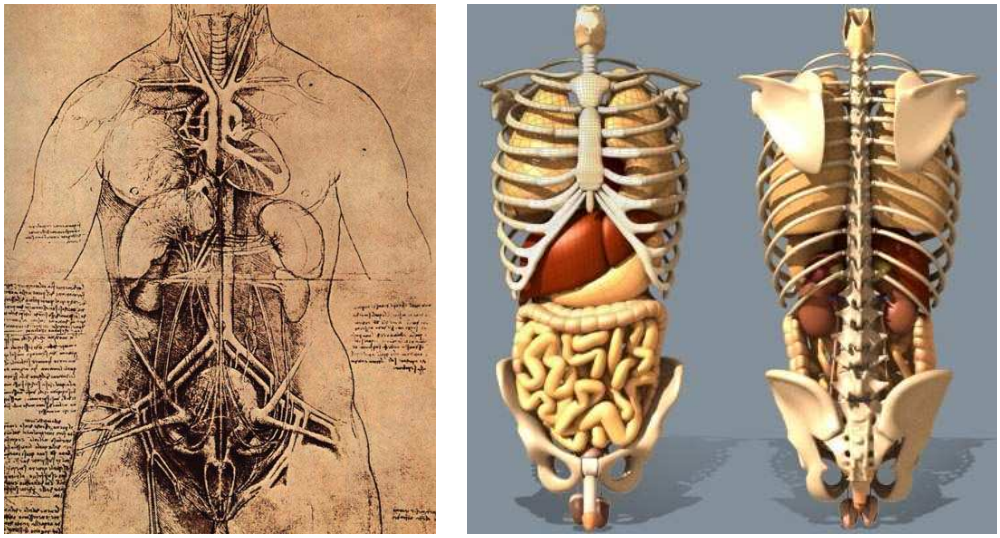

(a) (b)

Figure 2.1: Leonardo's [Web Gallery, 2006] and 3D modern [Exchange3D, 2006] representations of the anatomy of the human torso.

On the other side, the image semantics cannot be considered as being included explicitly in the image itself. It rather depends on prior knowledge on the domain and the context of the image.

For medical image interpretation, in particular, anatomical knowledge provides different pieces of information such as the position of the organs, their size or their shape. Hence, image interpretation can highly benefit from this additional knowledge in order to reach higher level interpretation. As one of our goals is to conceive an automatic method for segmentation and registration of medical images, the integration of this knowledge in our algorithms can be very helpful, for example:

- *to select the region of interest (ROI) where an organ is included*: by simplifying our algorithm and reducing the computing time because the region to process is smaller than the whole image,
- *to guide the segmentation*: by introducing constraints about the shape or the position of the contours of an organ,
- *to control the registration*: by adding constraints on the corresponding regions in both images and on the type of deformation that each organ can undergo,
- *to improve robustness*: by correcting the result if it does not match prior knowledge on the concerned organ and its variability.

Without this anatomical knowledge the segmentation and the registration could remain possible, but they would be more difficult. For this reason, one of the objectives of this work is to understand the different kinds of anatomical knowledge and the different manners of using them in order to assist image processing, in particular, for medical imaging. This has been also discussed by [Clarysse et al., 2004]. The result is that the combination of the perceptual level and the semantic level allows to succeed a semantic segmentation, simplifies the algo-

rithms, improves the effectiveness by reducing computing time, increases the automaticity, makes them more robust and closer to reality, i.e. physiologically plausible.

2.3 Formalization of anatomical knowledge

The formalization of the anatomical knowledge is one of the necessary steps in order to link the perceptual level and the semantic level There exist very useful tools for the combination of these two levels, such as the web applications of the Digital Anatomist Interactive Atlases [Brinkley et al., 1997 ; DAIA, 2004] or e-Anatomy [eAnatomy, 2006]. Some examples obtained with these interactive atlases are illustrated in Figure 2.2.

The interest for this domain has increased during the last years as is shown by [Dameron, 2003] who has done a detailed work on modeling and representing anatomical knowledge on brain cortex. Recent developments in the ontology community have shown that ontologies can efficiently encode generic and shared knowledge of a domain. For instance, the Foundational Model of Anatomy (FMA) [Rosse and Mejino, 2003 ; Smith et al., 2005 ; FMA, 2005] provides an ontology of the canonical anatomy of the human body. It proposes a complete conceptual model of the anatomy in order to help the biomedical information management. Another example, based on a similar approach, is Galen [Rogers and Rector, 2000 ; OpenGALEN, 2005]. As an illustrative example, Figure 2.3 shows a part of the Foundational Model for the heart.

2.4 Classification of anatomical knowledge

When looking for anatomical descriptions of the human torso, we can find statements that express different types of knowledge. We classify this anatomical knowledge, depending on how general it is, in: *general* knowledge, *individual* knowledge and *adapted* knowledge. Figure 2.4 illustrates the anatomy of the torso, to which the following examples refer to.

1. *General* knowledge represents some information that is common to all human beings. This includes information about:

   - The organs themselves: the (typical) volume, the shape.

     Some examples of this kind of knowledge are illustrated by the following statements:

     > "The heart is a hollow muscular organ of a somewhat conical form" [Gray's Anatomy, 2005].
     > "The kidney is a bean-shaped organ, about 12 cm long" [Tamir, 2002].
     > "The liver has an overall wedge shape, which is in part determined by the form of the upper abdominal cavity into which it grows" [Gray's Anatomy, 2005].
     > "Each lung is conical in shape, and presents for examination an apex, a base, three borders, and two surfaces" [Gray's Anatomy, 2005].

   - The relative positions between organs, as illustrated by the following sentences:

     > "The heart and lungs are situated in the thorax, the walls of which afford them protection. The heart lies between the two lungs" [Gray's Anatomy, 2005].

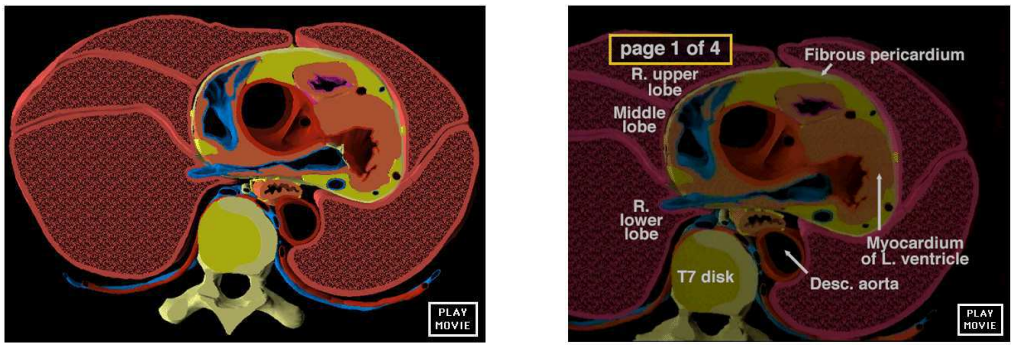

(a) (b)

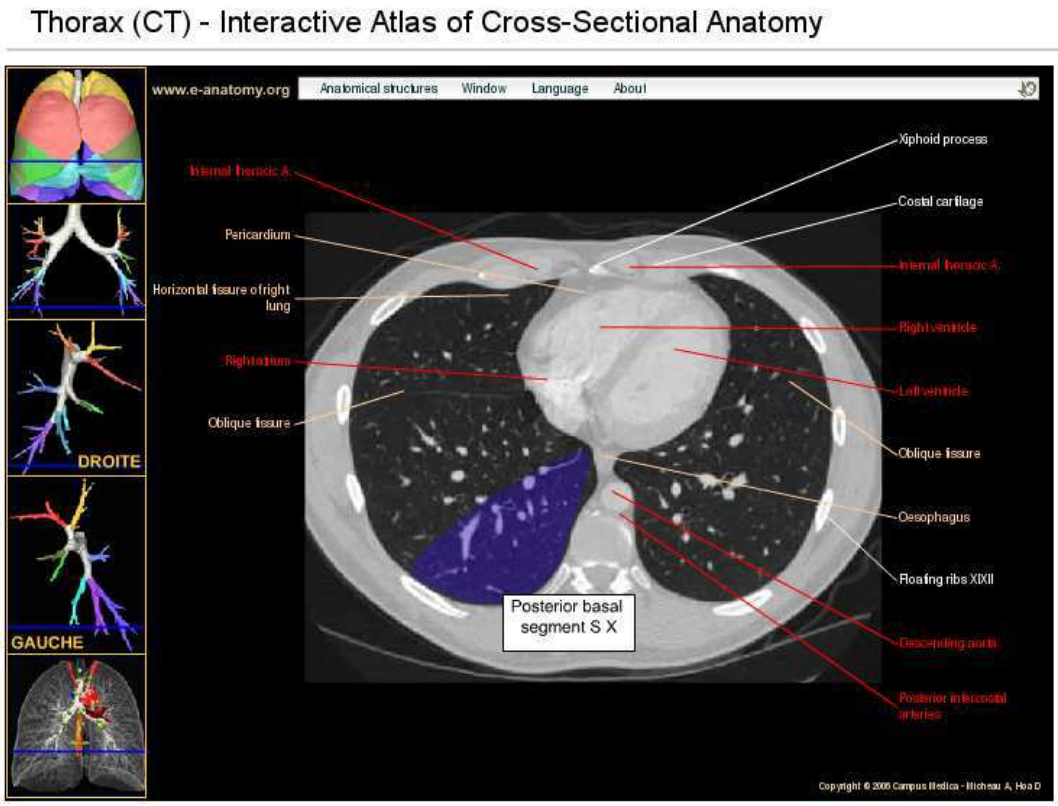

(c)

Figure 2.2: Examples of interactive atlases in the thoracic region: outlined (a) and labeled (b) structures of the Digital Anatomist Interactive Atlas [DAIA, 2004] and labeled structures on a CT slice with e-Anatomy [eAnatomy, 2006].

> "Beneath the lungs is the diaphragm, a dome-shaped muscle that works with your lungs to allow you to inhale (breathe in) and exhale (breathe out) air" [KidsHealth, 2006].
> "The liver lies in the upper right part of the abdominal cavity" [Gray's Anatomy, 2005].

- The deformations in the body, in particular for breathing. Thus, we can also establish what is an incorrect deformation:

  > "The muscles of respiration and the diaphragm act together to increase

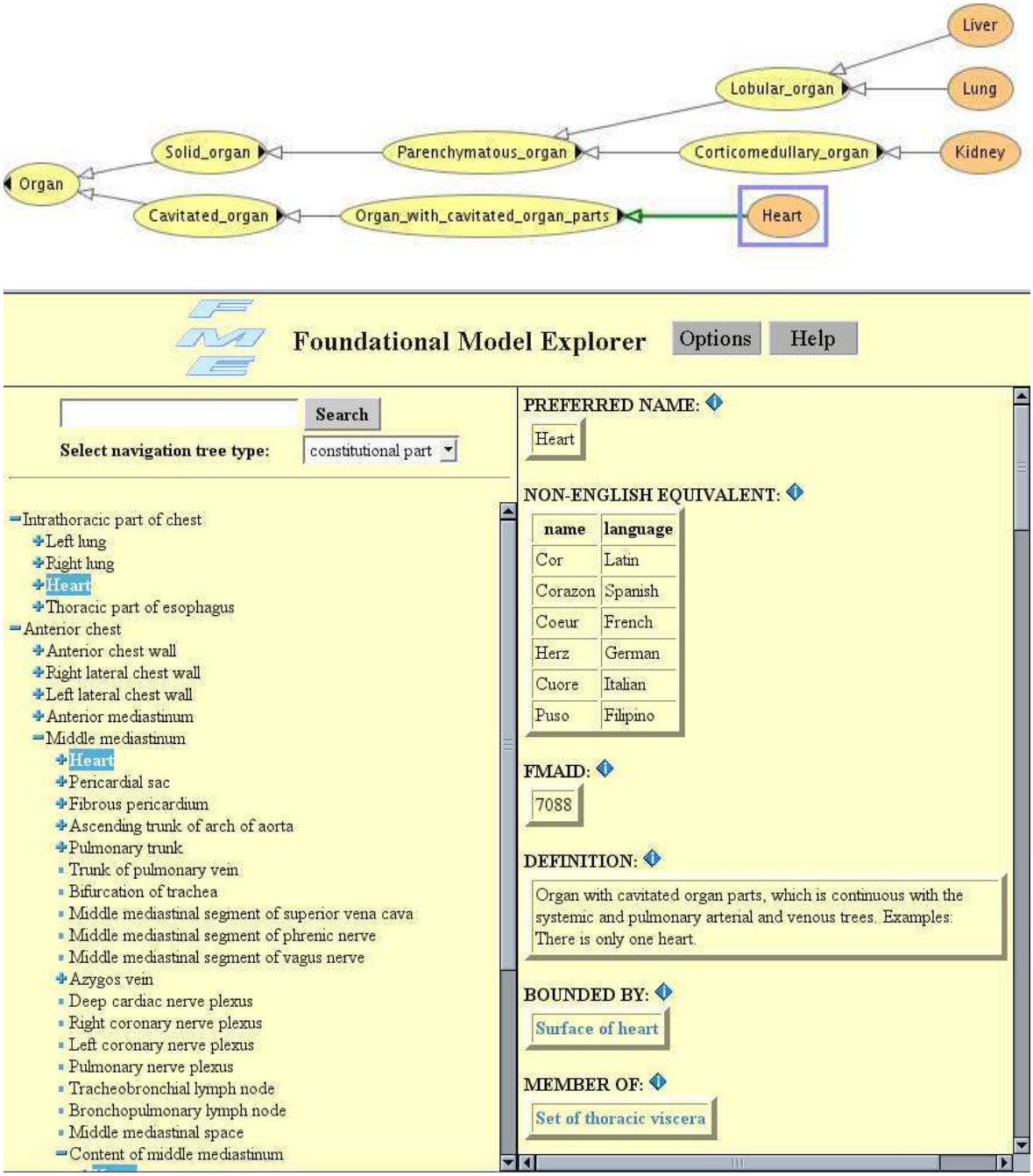

Figure 2.3: Anatomy modeling for some organs of the thorax and the abdomen in the Foundational Model of Anatomy [FMA, 2005] (top) and its Foundational Model Explorer [FME, 2005] (bottom).

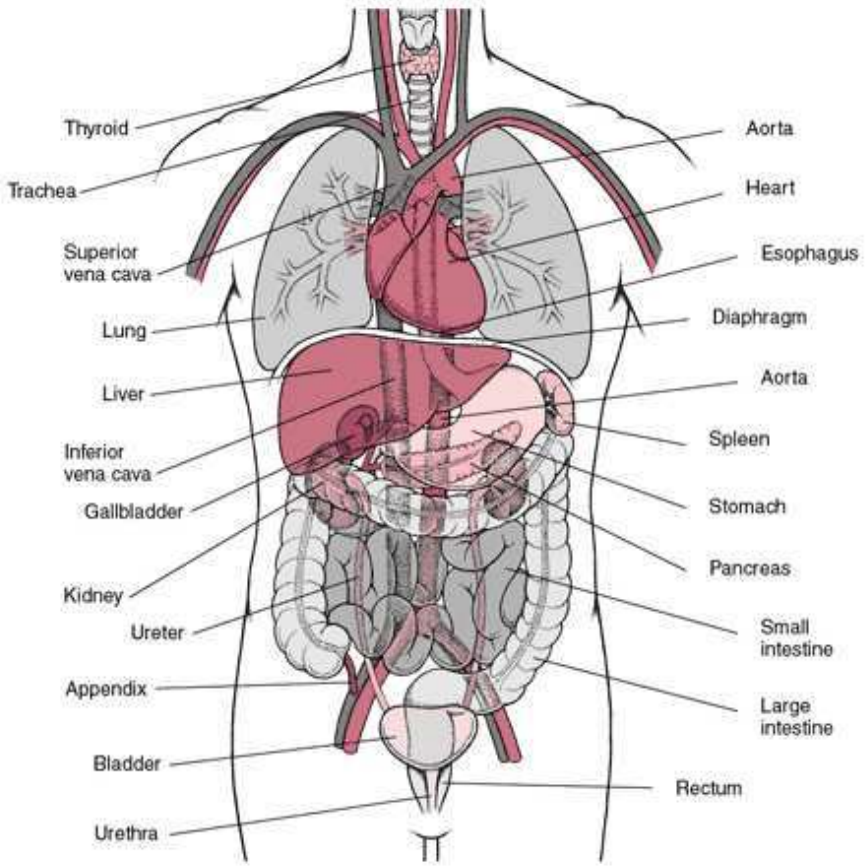

Figure 2.4: Anatomy of the human torso [Merck Manuals, 2003].

the intrathoracic volume: this creates a negative pressure within the pleural space surrounding the lung and causes expansion of the lung. The resultant reduction in the intra-alveolar pressure prompts the conduction of air through the upper respiratory tract into the trachea and airways and thence into the alveoli where gas exchange occurs" [Gray's Anatomy, 2005].

2. *Individual* knowledge can be introduced when we have some *a priori* knowledge which is different for each patient. For instance, in a pathological case, the position of the tumors (either approximate or with the exact coordinates) can be furnished by experts after a visual analysis of the images. These data provide very useful information for the processing of the images. Here are some examples of descriptions of pathologies:

   "Isolated hyperfixation by the apical nodule of the right superior lobe".
   "Presence of an intense hyperfixation on the lesion of the left top region indicating its malignant nature".
   "Hyperfixation of malignant tumoral level close to the left hilum".

3. *Adapted* knowledge is in fact general knowledge that depends on some parameters that change from one patient to another. Thus, it has to be adapted to each case. For

example, we know that the tissue elasticity varies with the distance to the tumors. Nevertheless, for each patient, tumors will be located in a different position and, thus, the regions influenced by the pathologies will be different:

> "Tumor-bearing lung regions showed a significantly lower mobility than the corresponding noninvolved regions" [Plathow et al., 2004].
>
> "Solid tumors have a distinct structure that comprises two distinct but interdependent compartments: the *parenchyma* (neoplastic cells) and the *stroma* that the neoplastic cells induce and in which they are dispersed. [...] Stroma is interposed between malignant cells and normal host tissues. [...] It comprises nonmalignant supporting tissue and includes connective tissue, blood vessels, and, very often, inflammatory cells" [Connolly et al., 2000].

All these types of knowledge can be used in very different ways. In the next section, we describe how these pieces of anatomical knowledge are used and integrated in our general methodology.

2.5 Integration of anatomical knowledge

In our work, we translate the different pieces of anatomical knowledge in order to integrate them in our algorithms for segmentation and registration of CT and PET images. The translation and integration can be done differently depending on the particular piece of knowledge. Figure 2.5 illustrates a diagram of our general method on which the different kinds of anatomical knowledge and the different manners of integrating them are marked. The latter are detailed in the following paragraphs.

2.5.1 Integration *a priori*

This type of integration corresponds to knowledge that comes directly from clinical experts:

- Before the acquisition of the images, experts choose the modality or modalities to be used depending on whether there is a pathology or not, and on the organs they want to observe. This is typically decided by clinicians depending on the symptoms of the patient.
- Some information is directly visible on the images. For example, the position of the tumors can be visually assessed by the user, provided as a point or a rough location, and introduced in the method for their segmentation. This is described in Chapter 3 (Section 3.4).

2.5.2 Integration *directly in the method*

This kind of integration takes into account anatomical knowledge during the segmentation or registration process. For example:

- The relative positions between organs can be used to define regions of interest. Then, the segmentation algorithms work inside these regions. These relative positions can also guide the segmentation algorithms. For instance, we can consider the relative positions of the heart, the liver and the kidneys with respect to the lungs for the segmentation of the former organs. This is detailed in Chapter 3.

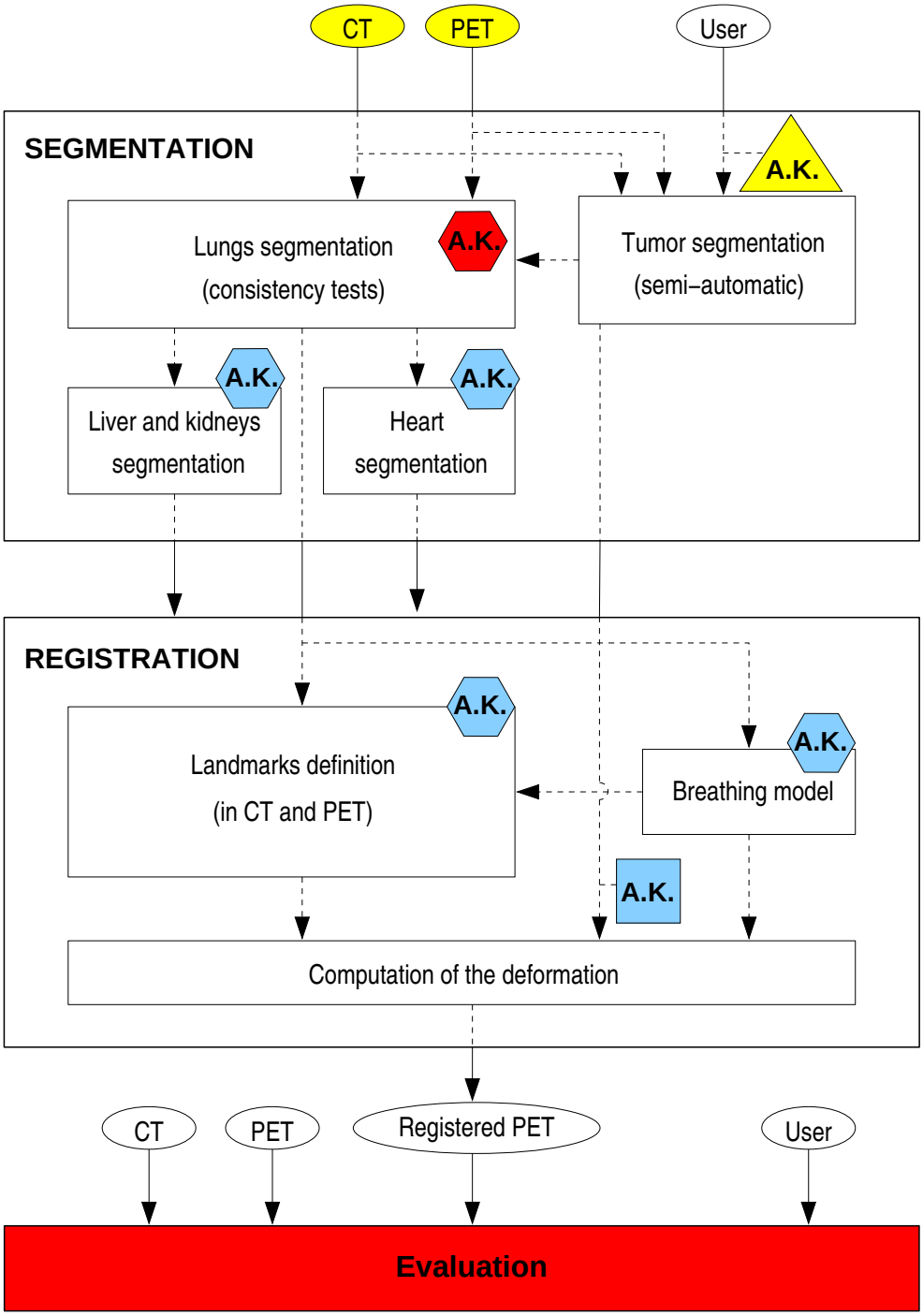

Figure 2.5: Diagram of our general algorithm for registration of CT and PET images using anatomical knowledge (A.K.). *General* knowledge is represented by hexagons, *individual* knowledge by triangles and *adapted* knowledge by squares. The different types of integration are marked with colors: yellow means integration *a priori*; light blue, integration *directly in the method*; and red, integration *in order to detect potential errors and repair*.

- After the segmentation of the tumors, the distance function to them can be computed. This distance is used in order to weight the non-rigidity of the deformation in the registration process. This is described in Chapter 4.

- The computation of the curvature of the surface of some organs furnishes regions with high curvature that are more or less invariant during the breathing cycle. In our method, we use these regions in order to define appropriate landmarks, which are used in our registration method (Chapter 4).

- The knowledge about the movement of the lungs (represented by a breathing model) provides information about the deformations suffered by the lungs during the respiration. This is used in order to correctly register our data by controlling the deformations so that they are physiologically plausible. We detail this in Chapter 5.

2.5.3 Integration *in order to detect potential errors and repair*

Anatomical knowledge can also be integrated *a posteriori* by analyzing the results and, then, adapting the algorithm to our data when possible. Thus, for instance, we can detect whether there has been an error in the segmentation and, if this proves to be the case, we try to correct it by changing some of the parameters of the method. This can be applied during an automatic segmentation algorithm and at the end of the general algorithm:

- As our data come from different medical centers and from different patients, it is very difficult to apply one segmentation algorithm to all the data and obtain correct results. For this reason, we introduce some knowledge to analyze the result with a simple "consistency test" and, if it is not correct, we adapt the algorithm to our particular case. For example, some information about the organs (as the volume of the lungs) is used for these "consistency tests". The advantage of this approach is that the algorithm becomes automatically adaptable even for very different data and thus, we improve the robustness of the segmentation. This is detailed in Chapter 3 (Section 3.2).

- In the final step of evaluation of the results (Chapter 6), different pieces of knowledge are employed by the user in order to perform the visual assessment: knowledge about the shape and positions of the organs, knowledge of what is a wrong deformation and what we expect as a good result, etc.

2.6 Conclusion

In this chapter we have presented a transversal view of our methodology, based on a common link: the use of anatomical knowledge in order to guide the segmentation and registration of CT and PET images. We have shown the importance of anatomical knowledge for medical image interpretation which can highly benefit from this additional knowledge. The combination of the perceptual level and the semantic level simplifies the algorithms, improves the effectiveness, increases the automaticity, makes them more robust and closer to reality. We have classified the different kinds of anatomical knowledge depending on how general they are and explained how they are integrated in our general algorithm.

CHAPTER 3

Segmentation of anatomical and pathological structures

In this chapter, we describe the segmentation of the different structures of the body. First, the method used for segmenting the lungs, the kidneys and the liver in CT and PET is briefly described in Section 3.2. Then, we describe our original approach to segment the heart in non-contrast CT images. This is the main contribution in this chapter and is detailed in Section 3.3. The segmentation of tumors is described in Section 3.4 and the refinement of lung segmentation using the segmented tumors in Section 3.5.

All the segmentation algorithms integrate anatomical knowledge in order to improve the robustness and/or to guide the segmentation itself as mentioned in Chapter 2. This is detailed in each section.

3.1 Introduction

The general schemes for the segmentation of the different structures in CT and PET are illustrated in Figures 3.1 and 3.2, respectively.

For the processing of the grey-level images different methods have been used, as for example: *mathematical morphology*, *classification using k-means algorithm*, *thresholding*, *deformable models*, etc. We use a *hierarchical method* where the structures which are easier to detect in the images are segmented first. Then, the structures with increasing difficulty are segmented progressively. This has been inspired by the work by [Delso, 2003 ; Camara-Rey, 2003 ; Camara et al., 2004 ; Colliot et al., 2006]. Here, we do not describe again the details of this methodology, but we invite the reader to refer to [Camara-Rey, 2003]. In this work, this hierarchical approach has been improved by integrating anatomical knowledge. This leads to a more robust and automatic method for the segmentation of the different structures of the body in CT and in PET. In addition to this, one of the main contributions of this work is the development of a new and original method for the segmentation of the heart.

In CT images, we start segmenting the contours of the body and then the lungs. Next we create a mask using the previously segmented structures. This mask determines the region where the other organs to segment are included. The skeleton and the kidneys are then segmented, a new mask excluding all these organs is created and finally the segmentation of the liver and the heart is computed.

The approach used for PET images is very similar. One difference is that, when available,

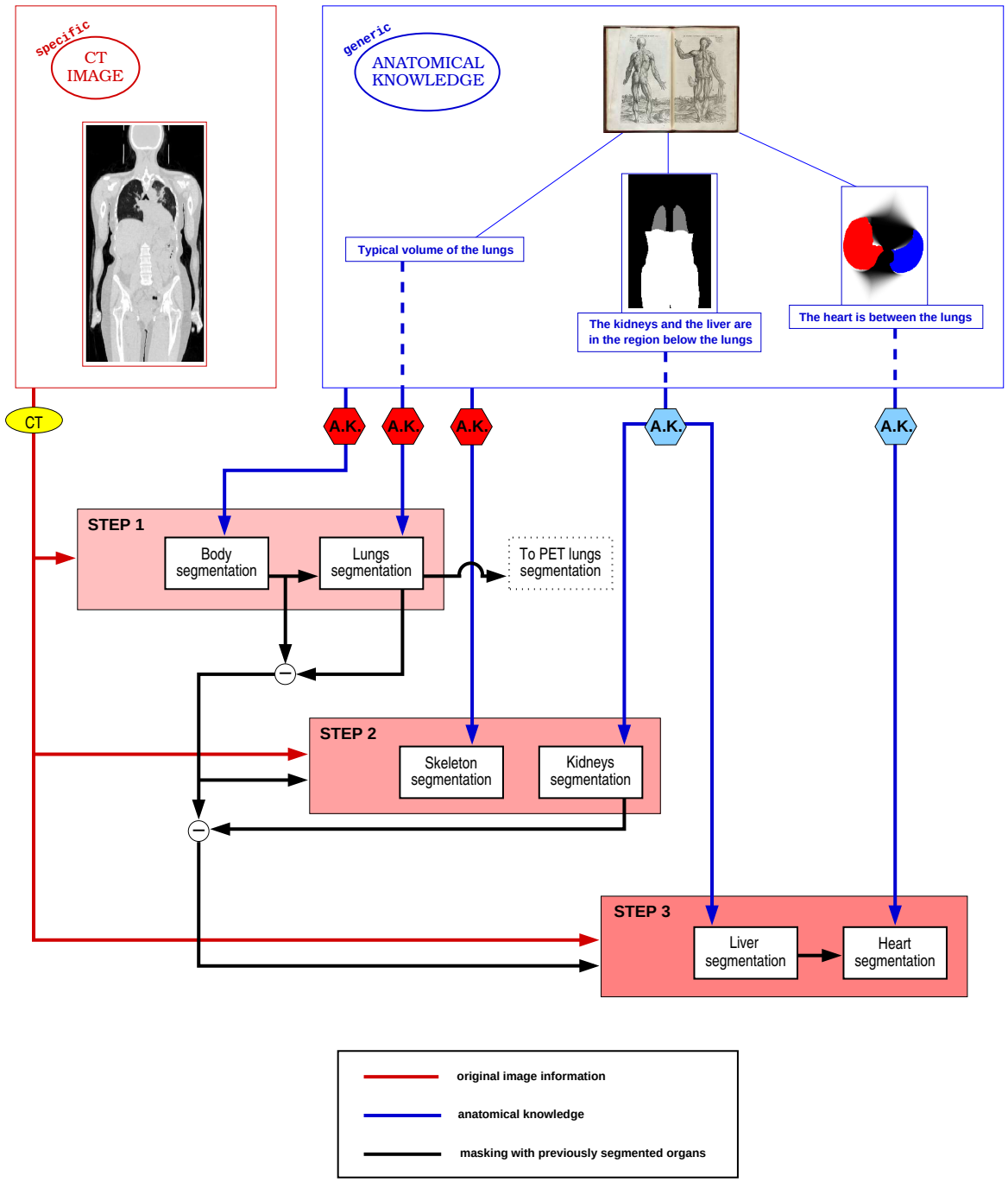

Figure 3.1: General diagram for segmentation of CT images. *General* anatomical knowledge (A.K.) is integrated *a priori* (ellipses in yellow), *directly in the method* (hexagons in light blue) and *in order to detect potential errors and repair* (hexagons in red) as explained in Chapter 2, Figure 2.5.

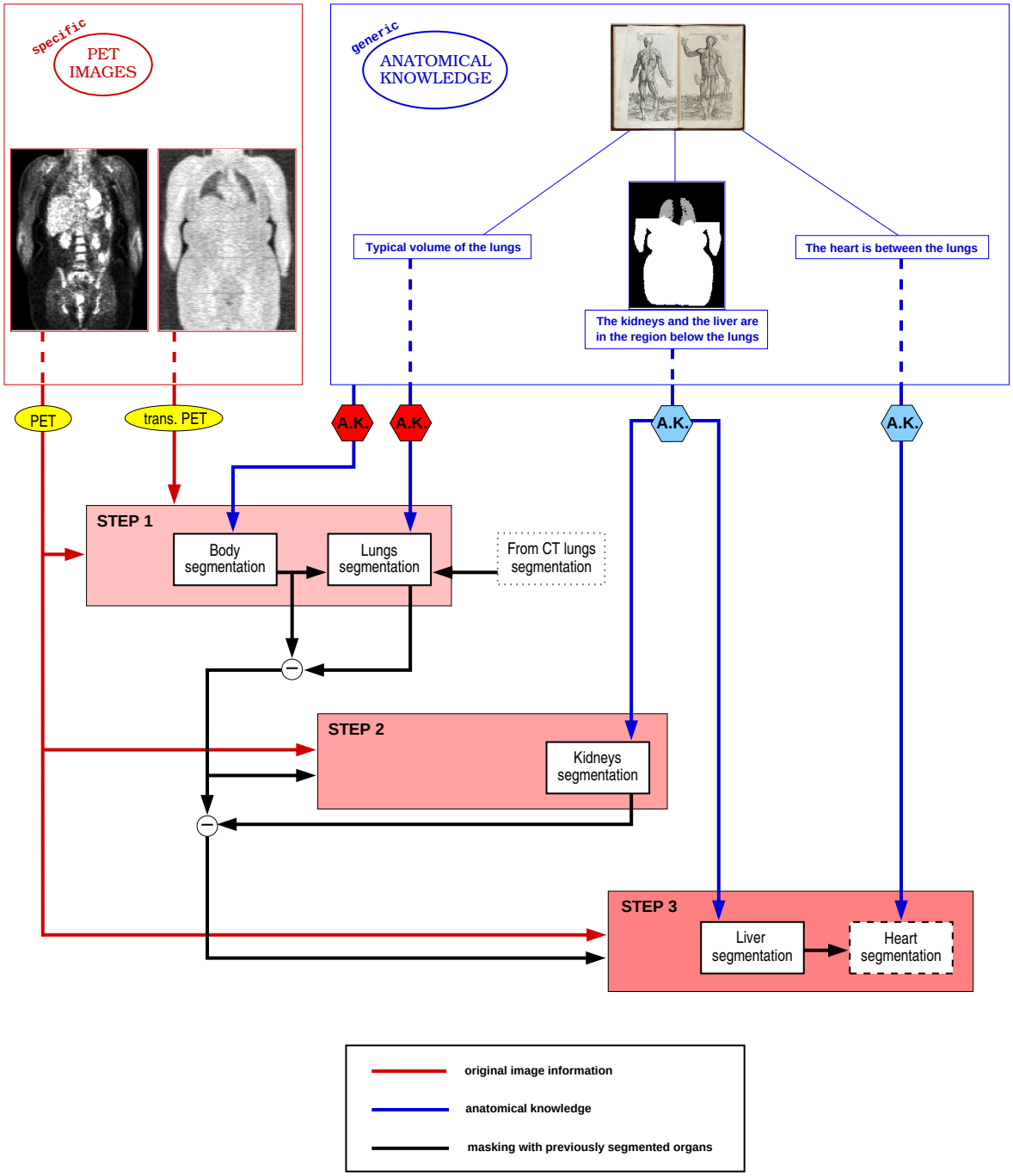

Figure 3.2: General diagram for segmentation of PET images. *General* anatomical knowledge (A.K.) is integrated *a priori* (ellipses in yellow), *directly in the method* (hexagons in light blue) and *in order to detect potential errors and repair* (hexagons in red) as explained in Chapter 2, Figure 2.5.

the transmission PET image is used for the segmentation of the contour of the body and the lungs. In this type of image the lungs and the contour of the body are better contrasted and are easier to detect. The rest of the scheme is equivalent to that of CT images, except that the skeleton cannot be segmented in PET because it is not visible in this modality. According to our clinical partners, this may also happen for the heart, i.e. it may not appear in PET images and, therefore, it could not be segmented.

As it is explained later, the segmentation of the lungs in PET is very challenging. For this reason, when possible, we use the segmentation of the lungs in the transmission PET or in CT in order to help the segmentation of the lungs in PET. The improvements of the algorithm with this approach are illustrated in Section 3.2.

The different pieces of anatomical knowledge used in the segmentation process are described in the following sections. In Figures 3.1 and 3.2 this is marked with "A.K". For the segmentation of the body contours, the lungs and the skeleton, we have introduced some "consistency tests" in the segmentation process in order to verify that the obtained results are realistic. If it is not the case, some parameters of the processing chain are changed in order to obtain correct results. This is referred as integration *in order to detect potential errors and repair* in Chapter 2. For the segmentation of the kidneys, the liver and the heart, the anatomical knowledge is integrated *directly in the method* by using information about the relative positions of the organs with respect to the previously segmented structures.

As a final step, the segmentations of the lungs, the kidneys and the liver are refined by using a *deformable model* in order to correct small errors of the previous processing and to smooth the surfaces of the segmented objects. The principle of deformable models is described in Section 3.3.5.

In the following sections we describe the algorithms used for the segmentation of the different structures. We do not detail all the steps of the segmentation of the lungs, but the main stages. In practice, the integration of anatomical knowledge which is used *in order to detect potential errors and repair* is translated into "consistency tests". The goal of these tests (in red boxes in the figures) is to increase the robustness of the segmentation algorithms so that they furnish good results for any CT and PET images. This objective is very challenging because the images come from different medical centers, from different patients and are acquired in different conditions (position of the patient, contrast). Thus the characteristics of the different exams may vary considerably. Despite these difficulties, our method improves the robustness of the algorithm as illustrated in Section 3.2.3.

3.2 Segmentation of the lungs

In this section, the segmentation of the lungs and other structures of the human trunk is described. First, the contours of the body are detected in order to limit the processing of the images to the interior of the body. Next, the lungs are segmented and then the segmentation of the other structures is guided by the previously segmented ones.

Our algorithm has been applied on 23 datasets of different patients, coming from different medical centers. Each dataset is composed of one CT image, one emission PET image and, in 4 cases, of one transmission PET image. The sizes of the CT images are typically of $512 \times 512 \times Z$ voxels with Z varying from 63 to 370 and their resolutions are $dx \times dy \times dz$ mm^3 for the three directions of the space, with dx and dy varying from 1 to 2 mm and dz from 2.5 to 7.5 mm. The sizes of the emission and transmission PET images are of $X \times Y \times Z$ voxels with X and Y varying from 128 to 256 and Z from 120 to 287 voxels. Their resolutions are

$dx \times dy \times dz$ mm^3 for the three directions of the space, with dx and dy varying from 2 to 5 mm and dz from 3 to 5 mm.

3.2.1 Body contour segmentation

The simplified algorithms used for the segmentation of the body contours in CT and in PET are illustrated in Figures 3.3 and 3.5 respectively.

Here we mention some of the difficulties our algorithm has to deal with, for the segmentation of the body in CT:

- In some exams, the useful data of the image are contained in a grey cylinder (see Figure 3.4(a)). Our algorithm detects this and adapts the processing accordingly. Without the consistency test the cylinder is segmented as the body.
- In other exams, the bed where the patient is laying appears in the image connected to the body. With our algorithm, it can be removed as illustrated in Figures 3.4(c) and (d).

A final consistency test is introduced to verify that the volume of the segmented body is not to low and it can be considered as correct.

In general, one of the main difficulties is that, in the classification step, the number of classes to be used varies for different cases. In particular, in CT images, this depends on the presence of the grey cylinder. In PET it is more difficult to find the appropriate number of classes and it has to be adapted for each case. The consistency tests in Figure 3.5 help to do this by verifying that the obtained result is not unrealistic (too small or too extended). Figure 3.6 illustrates some steps of the segmentation of the body in a PET image. The computed thresholds are empirical values which produce correct results for all the cases in our database.

Emission PET images[1] present important variations in contrast from one patient to another and between different acquisition devices. For this reason, and in order to design a more robust segmentation method, the segmentation of the body in PET is performed on the transmission PET image when it is available (see Figure 3.5(a)).

3.2.2 Robust segmentation of the lungs

The segmentation of the lungs in CT is a widely discussed problem [Reinhardt et al., 2000 ; Hu et al., 2001 ; Armato III and Sensakovic, 2004 ; Hoffman et al., 2004 ; Sluimer et al., 2006] even for pathological cases [Sluimer et al., 2005]. However, a detailed state of the art on lung segmentation is out of the scope of this work. We rely on the method proposed by [Camara-Rey, 2003] which has been modified and improved in order to furnish robust results independently of the origin of the images. Figure 3.7 illustrates the method we propose. First, a classification using the k-means algorithm is used in order to detect the lungs (see Figure 3.8(b)). Then, a consistency test is applied in order to verify that the volume of the segmented lungs has a plausible value. If it is the case, the result is refined by using some mathematical morphology operations (a hole filling and a closing) and a deformable model in which the GVF (Gradient Vector Flow) [Xu and Prince, 1997] is used as a term of fidelity to the data. Otherwise, the process is repeated with another class in the k-means algorithm. The effect of the refinement is illustrated in Figure 3.9. Anatomical knowledge is integrated

[1] For the sake of fluidity in the reading, we call PET images the emission PET images.

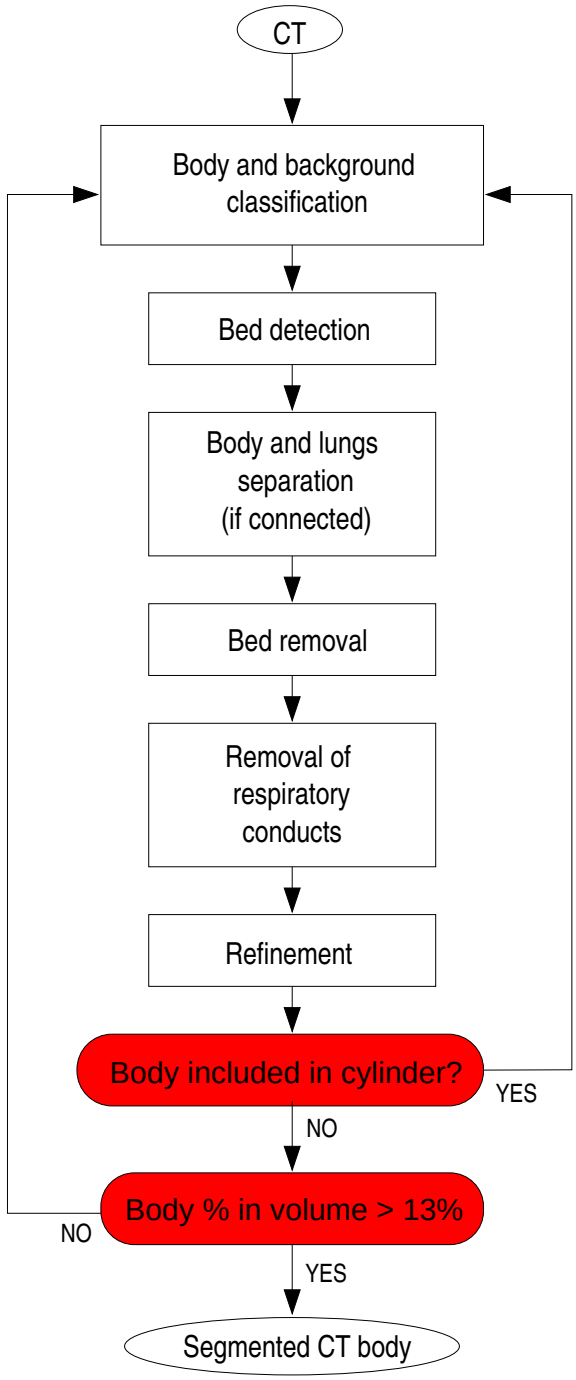

Figure 3.3: Diagram of the segmentation of the body in CT images. Red boxes indicate integration of anatomical knowledge *in order to detect potential errors and repair.*

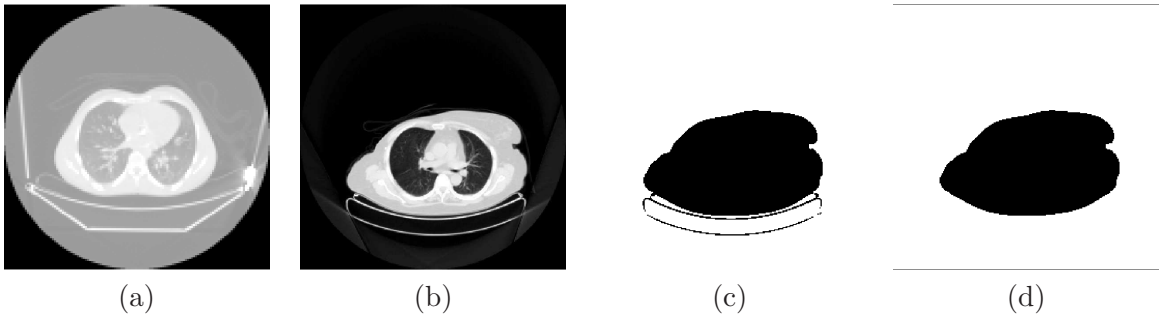

(a) (b) (c) (d)

Figure 3.4: Axial views of (a) a CT image where the body is included in a grey cylinder, (b) other CT image where the cylinder is not present, (c) the intermediate result where the bed is included in the segmentation of the body and (d) the final result.

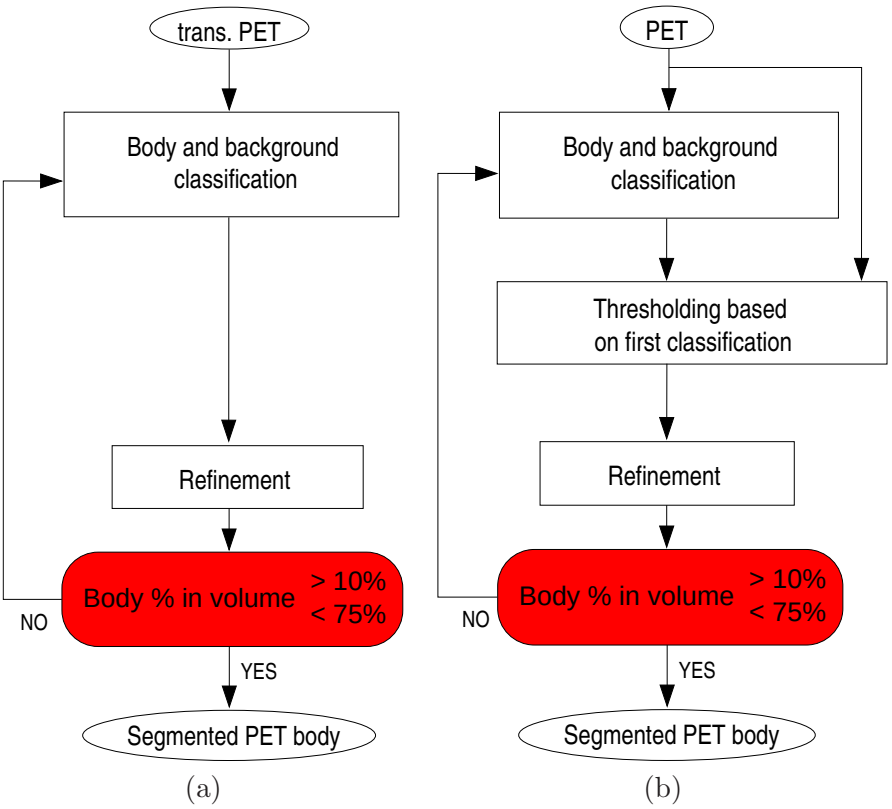

Figure 3.5: Diagrams of the segmentation of the body in PET images (a) using the transmission PET image (when available) and (b) using directly the original PET image. Red boxes indicate integration of anatomical knowledge *in order to detect potential errors and repair*.

in order to guarantee correct results for images coming from different devices and clinical centers. In this case, this knowledge is translated as a percentage of the volume of the images that the lungs must occupy. This has been calculated empirically and has to be improved as we discuss later.

To the best of our knowledge, the problem of segmenting the lungs in PET has not been addressed in the literature. This is explained by the fact that the segmentation of the lungs in PET is very challenging. In order to perform a *direct segmentation* of the lungs in the PET image, the integration of anatomical knowledge and consistency tests are necessary

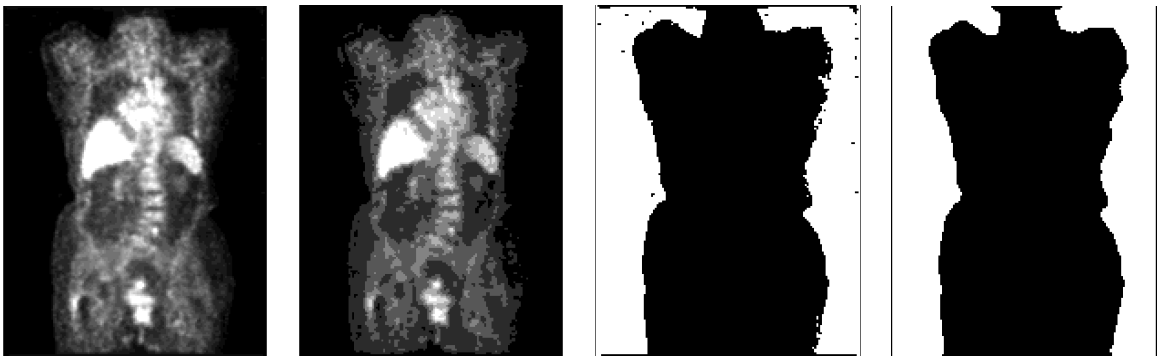

(a) (b) (c) (d)

Figure 3.6: Coronal views of (a) a PET image, (b) the result of the classification using k-means algorithm, (c) after the selection of the appropriate class, and (d) the final result.

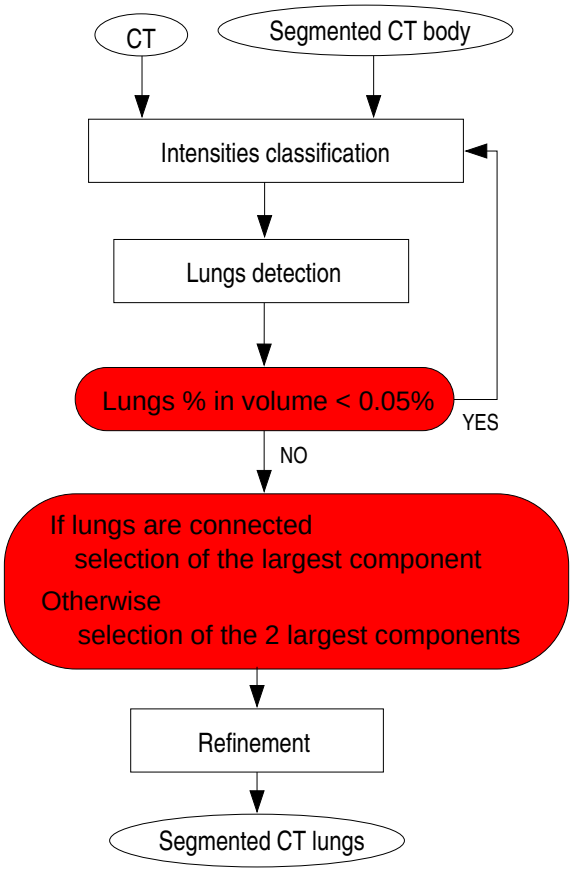

Figure 3.7: Diagram of the segmentation of the lungs in CT images. Red boxes indicate integration of anatomical knowledge *in order to detect potential errors and repair.*

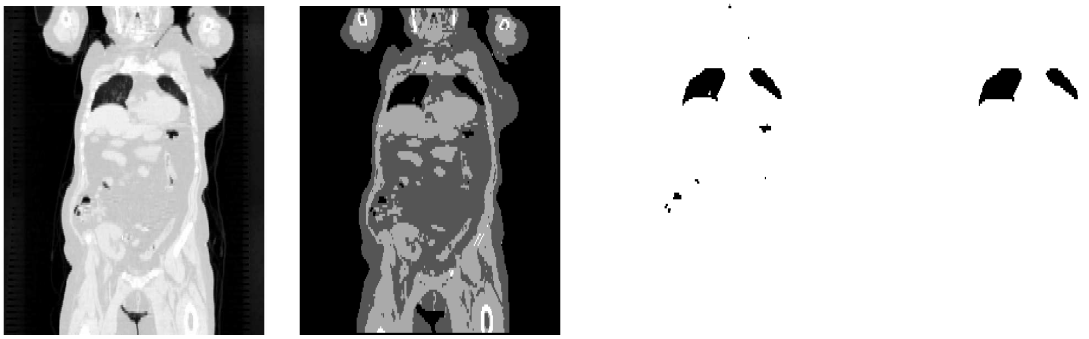

(a) (b) (c) (d)

Figure 3.8: Coronal views of (a) a CT image, (b) the result of the classification using k-means algorithm, (c) after the detection of the lungs, and (d) the final result.

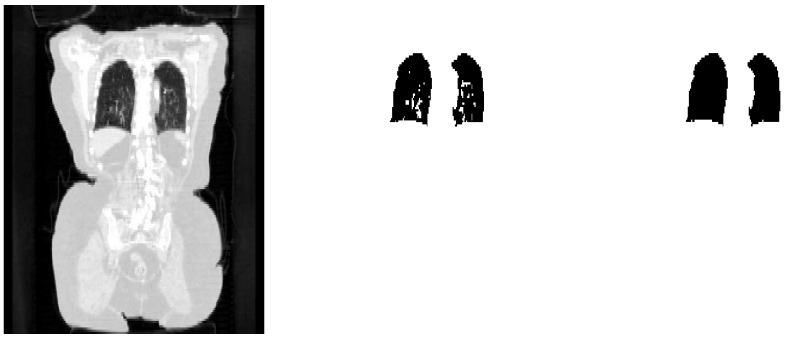

(a) (b) (c)

Figure 3.9: Coronal views of (a) a CT image, (b) the detected lungs, and (c) the segmented lungs after the refinement step.

in order to provide a robust algorithm. The pieces of anatomical knowledge used in the algorithm in Figure 3.10 are the position of the lungs in the thorax (in the region below the shoulders) and the fact that they are two approximately symmetric organs. One of the more sensitive steps is the classification. With the addition of a consistency test, the thresholding is adapted in order not to obtain unrealistic results. This threshold is defined as a percentage of the volume of the image and it has been fixed empirically. There is a stage for selecting the region of interest where the lungs are included, which is defined as the region below the shoulders, illustrated in Figure 3.11. Another consistency test determines the number of iterations of a filtering with successive morphological openings. However, even with the consistency tests, incorrect results can be obtained for some cases due to the very different characteristics between the images coming from different medical centers. This is illustrated in Figures 3.13(b-d).

Therefore, in order to improve the robustness of the segmentation of the lungs in PET, when it is available, we use the transmission PET in order to compute a first mask of the lungs. This mask defines the region of interest where the algorithm searches for the lungs in the emission PET. If the transmission PET is not available, and if the PET image comes from a combined CT/PET machine, then the segmentation of the lungs in CT is used to constrain the algorithm to this region (see Figures 3.13(e-g)). These two possibilities are included in the *improved method* and they are implemented according to the schemes in

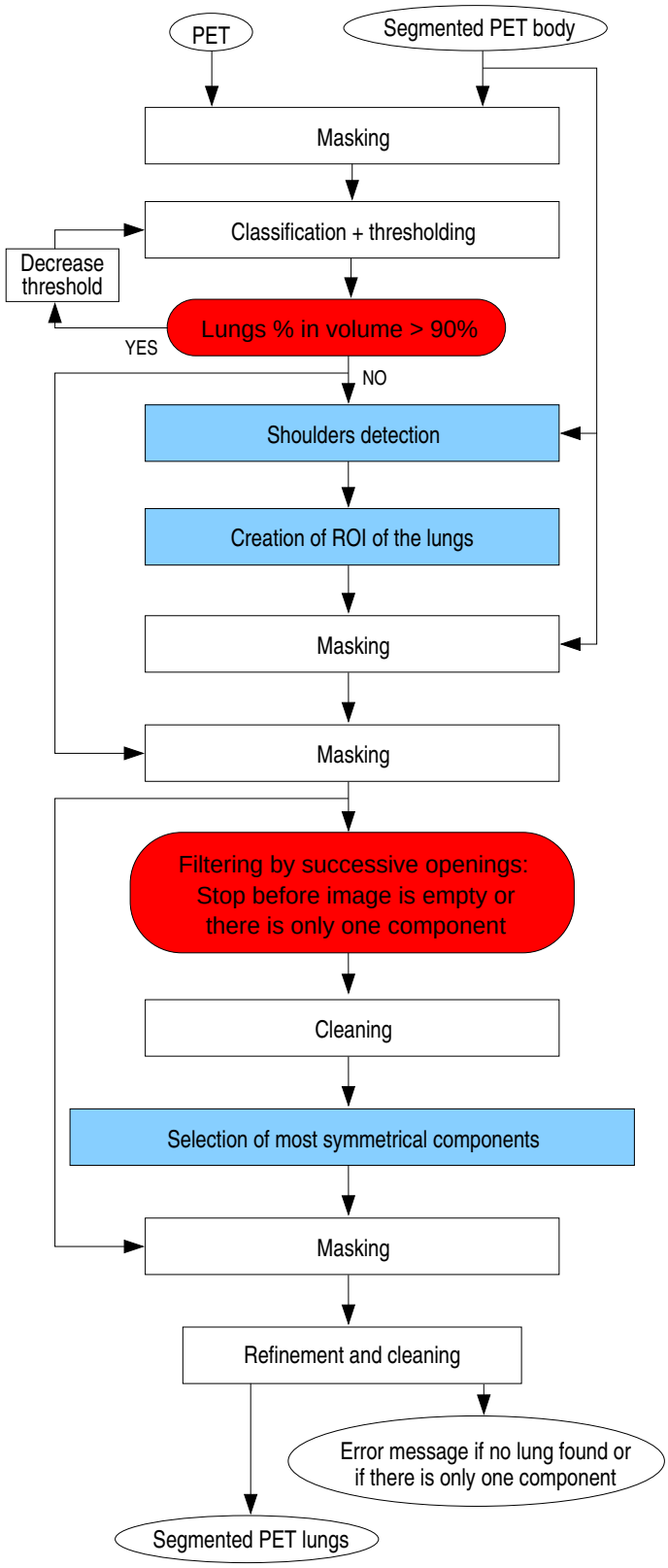

Figure 3.10: Diagram of the segmentation of the lungs in PET images using directly the original PET image. Red boxes indicate integration of anatomical knowledge *in order to detect potential errors and repair* and blue boxes indicate integration *directly in the method*.

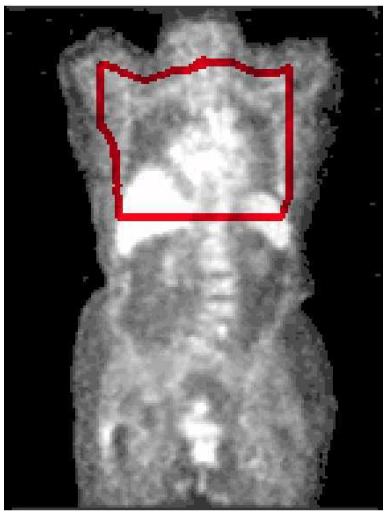

Figure 3.11: Coronal view of a PET image where the contour of the region of the lungs (below the shoulders) is superimposed.

Figure 3.12. In both cases, the algorithm is robust and does not need any consistency test.

The improvements of the segmentation with the consecutive approaches are detailed in the following.

3.2.3 Illustration of the improvements

Our approach has been applied on the database of 23 cases, with one CT and one PET image for each case. In 4 cases the transmission PET image was available. The segmentation of the lungs in CT is correct in all cases. Nevertheless, due to the difficulties of PET images, the segmentation of the lungs in this modality does not always furnish optimal results. Here we discuss the improvements on PET lungs segmentation.

The percentages of correct, incomplete or incorrect results furnished with the *direct segmentation* and with the *improved method* are shown in Table 3.1. Incorrect results are those where the results of the segmentation are completely outside the lungs or are too small to be considered as acceptable. We call "incomplete" results those which are inside the lungs, but where some regions of the organs are not included.

	Direct segmentation	Improved method
	Figures 3.10 and 3.12(a)	Figures 3.10, 3.12(a) and 3.12(b)
Correct results	65%	75%
Incomplete results	5%	25%
Incorrect results	30%	0%

Table 3.1: Quantification of the improvement of the results of lung segmentation.

With the *direct approach* illustrated in Figure 3.10, even with the consistency tests, the correct results are of 65% and, most important, we obtained 30% of incorrect results. An example of an incorrect result is illustrated in Figure 3.14(a).

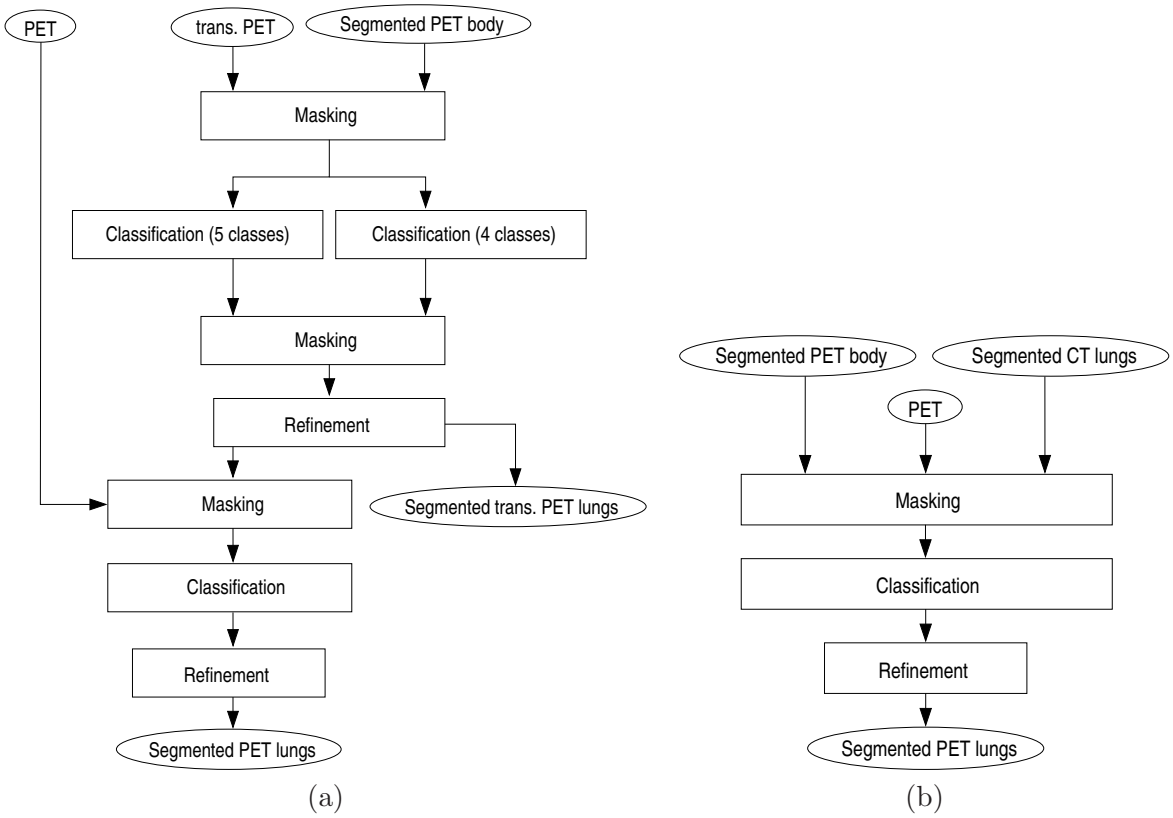

Figure 3.12: Diagrams of the segmentation of the lungs in PET images (a) using the transmission PET image (when available) and (b) using the segmented lungs in CT (when images come from a CT/PET combined device).

An important improvement is obtained when the segmented CT lungs are used to initialize the segmentation of the PET lungs (*improved method*). This is very simple to do in the cases where the CT and PET images are acquired with a combined CT/PET machine[2] because the CT and PET images are directly rigidly registered. In this case, the percentage of correct results increases to 75% and there is 0% of incorrect results. As illustration of the improvement, Figure 3.14(b) shows the new segmentation of the case in Figure 3.14(a). Some other correct segmentations of the lungs in PET are illustrated in Figure 3.15.

3.2.4 Skeleton, kidneys and liver segmentation

A similar approach as for the body and the lungs has been used in order to segment the skeleton in CT images. The general scheme is shown in Figure 3.16. Here a percentage of the image has been used as a threshold to decide if the segmentation is correct or not. The skeleton cannot be segmented in PET images, because it is not visible in this modality.

For the segmentation of the kidneys and the liver in CT and PET, a similar approach including thresholding and mathematical morphology has been used. Some pieces of anatomical knowledge are integrated in the processing in order to define the region of interest where the kidneys and the liver are included (below the lungs) and to take into account some properties of the organs (the symmetry of the kidneys), for example. The schemes of the different

[2] which are becoming more and more common.

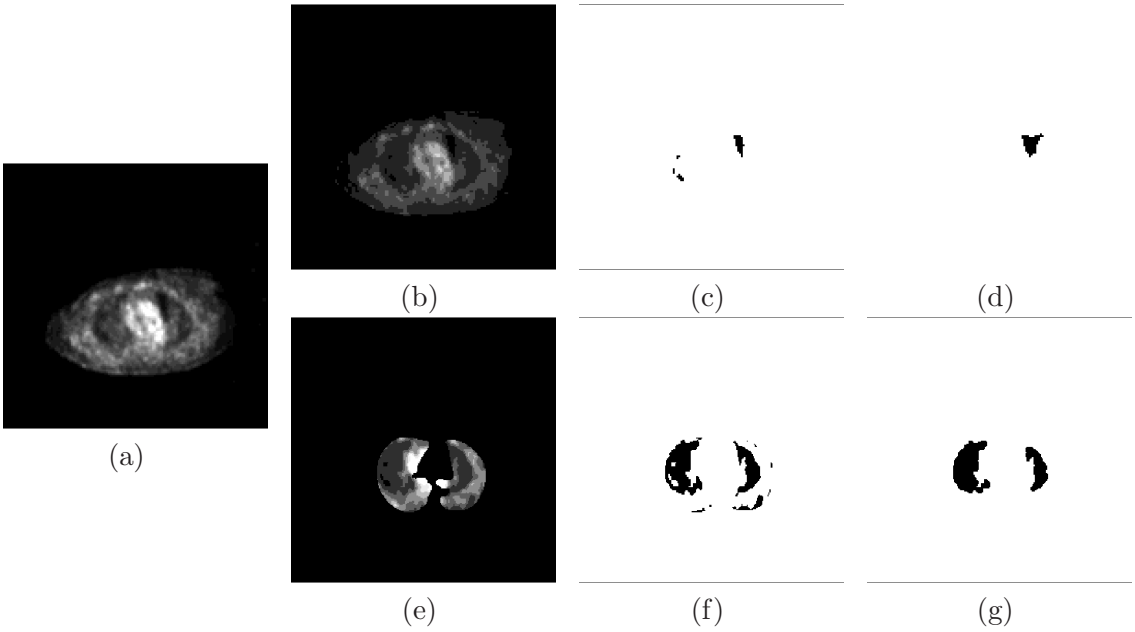

Figure 3.13: Axials views of a PET image (a) and some intermediate results of the segmentation of the lungs with the direct method (a-d) (cf. Figure 3.10) and using the CT lungs (e-g) (cf. Figure 3.12(b)). (b) shows the results after k-means classification, (c) the result after masking with the ROI of the lungs and (d) the final results with the direct method. (e) shows the result of the classification of the region masked with the CT lungs, (f) the selected class and (g) the final result.

algorithms are shown in Appendix A. These scheme can be improved, as it has been done for the lungs, by integrating anatomical knowledge *in order to detect potential errors and repair* them.

3.2.5 Discussion

The developed algorithms provide correct results for the segmentation of the different structures of the human trunk in CT and in PET images. The contours of the body, the lungs, the skeleton (only in CT), the kidneys and the liver can be computed. The segmentation algorithms for the body, the lungs and the skeleton are exactly the same for any patient. However, the processing chains for the kidneys and the liver still have to be adapted in order to furnish an automatic and robust algorithm. In general, the computation of the segmentation in CT does not present obstacles that are impossible to circumvent. The most challenging task is the segmentation of the lungs in PET when the transmission PET image is not available and the exam has not been acquired with a combined CT/PET device.

The addition of anatomical knowledge and consistency tests improve the robustness of the algorithm for images coming from different patients and different medical centers. However, it is undeniable that such an approach does not allow to obtain very precise results for all the cases. This point is not discussed here, but a further evaluation of the segmentation results is necessary in order to validate our method.

The thresholds used in the consistency tests of our algorithms have been computed empirically. They can be refined and optimized by calculating the typical volume of the organs instead of comparing volume percentages with respect to the total volume of the images. Nevertheless, this will not guarantee accurate results for all the cases because of the large

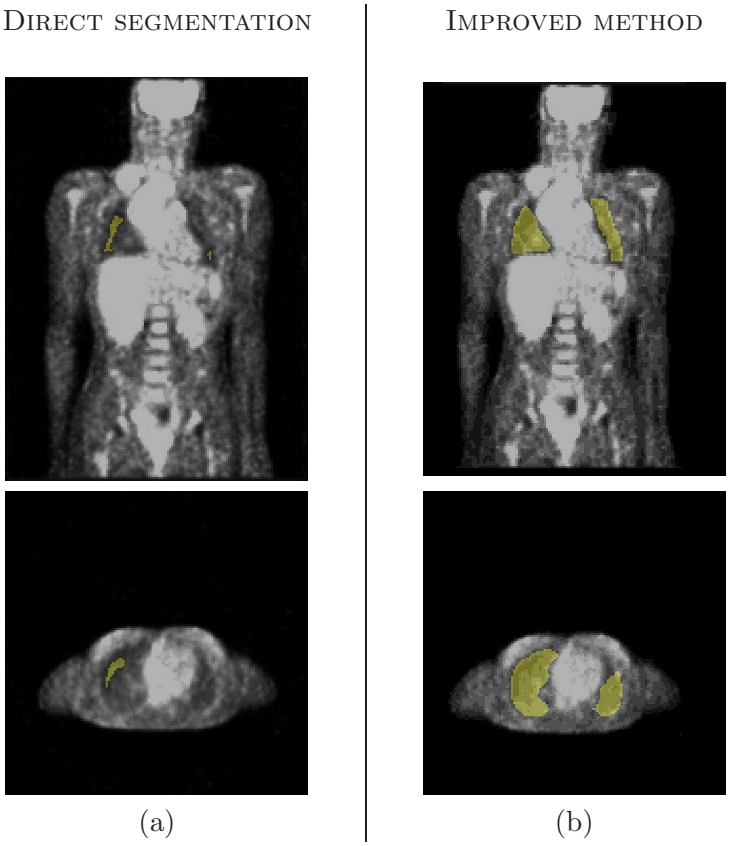

Figure 3.14: Coronal (top row) and axial (bottom row) views of (a) an incorrect result of lung segmentation of a PET image using the *direct approach* and (b) the result obtained for the same image with the *improved algorithm* using the segmented lungs in the corresponding CT.

variability between anatomies.

The segmentation of the kidneys and the liver has not been generalized to guarantee robust results for any patient. This can be implemented by adding consistency tests as for the other structures.

3.3 Segmentation of the heart

Segmenting the heart in medical images is a challenging and important task for many applications. In particular, segmenting the heart in non-contrast computed tomography (CT) images is difficult because of their low contrast and the similar grey-level values of the surrounding structures.

Many clinical applications could benefit from a reliable heart segmentation procedure, such as the study of cancer in the thoracic region or other cardiac and vascular diseases. The delineation of the heart is important in oncological applications such as dose estimation in radiotherapy. The segmentation of the heart may be used in treatment planning in order to define a security margin around this organ to prevent it from being irradiated: usually radiotherapists delineate a relatively wide margin around sensitive organs which must not be affected by radiation. This margin may be of several centimeters (particularly in the lungs due to the breathing). Heart segmentation can also be useful as a preliminary step for

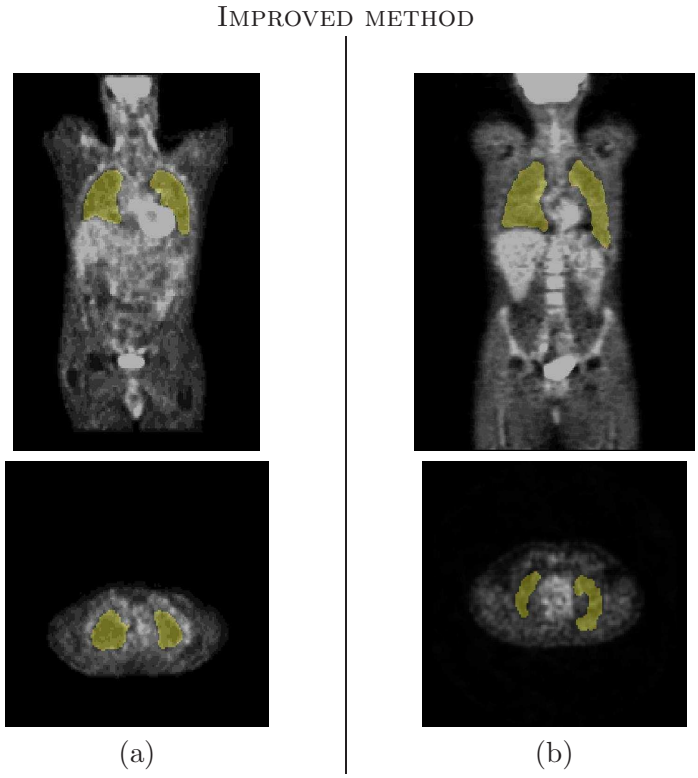

Figure 3.15: Coronal (top row) and axial (bottom row) views of the results of lung segmentation in PET for two other cases using the *improved method*.

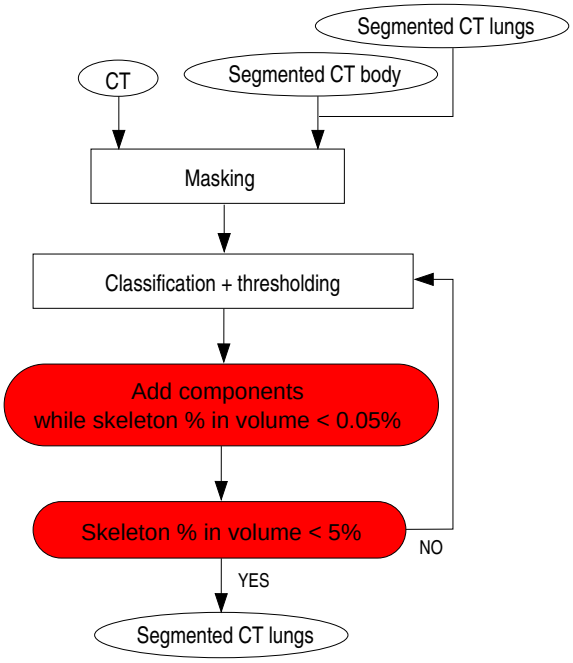

Figure 3.16: Diagram of the segmentation of the skeleton in CT images. Red boxes indicate integration of anatomical knowledge *in order to detect potential errors and repair*.

registration of multimodality images, such as CT, positron emission tomography (PET), single photon emission computed tomography (SPECT) or magnetic resonance imaging (MRI), and in particular for those obtained with new combined PET/CT or SPECT/CT devices. For instance, the segmented heart can be integrated in the registration algorithm described in [Camara et al., 2007] (in Appendix D) or in the method we propose in Chapter 4.

Although the majority of methods in the literature are designed for ventricle segmentation, there is a real interest in segmenting the heart as a whole in CT. In this section, we address this problem and propose an automatic and robust method, based on anatomical knowledge about the heart, in particular its position with respect to the lungs. This knowledge is represented in a fuzzy formalism and it is used both to define a region of interest and to drive the evolution of a deformable model in order to segment the heart inside this region. The proposed method has been applied on non-contrast CT images and the obtained results have been compared to manual segmentations of the heart, showing the good accuracy and high robustness of our approach. This work is also described in [Moreno et al., 2008a].

3.3.1 Related work

Most heart segmentation methods proposed in the literature deal with the segmentation of internal structures (in particular the left ventricle) as in [McInerney and Terzopoulos, 1995 ; Suri, 2000 ; Assen et al., 2006 ; Zhukov et al., 2002 ; Noble et al., 2002 ; Tauber et al., 2006 ; Lynch et al., 2006] for instance. However, there is also a need to segment the heart as a whole in order to distinguish its limits and the separations with surrounding structures such as the liver or the aorta. The existing methods for segmenting the heart have been focused on MRI modality [Noble et al., 2002 ; Lynch et al., 2006 ; Gregson, 1994 ; Lelieveldt et al., 1999 ; Kaus et al., 2003 ; Pluempitiwiriyawej et al., 2005] or ultrasound [Tauber et al., 2006 ; Pfeifer et al., 2005] but rarely on CT [Funka-Lea et al., 2006 ; Jolly, 2006 ; Ecabert et al., 2005; 2007]. However, CT is one of the most common anatomical imaging modalities used for the study of cancer (or other cardiac and vascular diseases) in the thoracic region, for the delineation of the heart in oncological applications such as dose estimation in radiotherapy and for registration of multimodality images, in particular for those obtained with new combined PET/CT or SPECT/CT devices.

Numerous cardiac segmentation methods have been developed to estimate the myocardial boundaries in MR images. A registration-based model is used in [Noble et al., 2002] and a clustering technique in [Lynch et al., 2006]. Some methods [Kaus et al., 2003 ; Pluempitiwiriyawej et al., 2005] use prior knowledge learned from images models. Deformable models have also been widely used in segmenting cardiac images [Pluempitiwiriyawej et al., 2005]. However, all these approaches rely on models obtained from MR images, on the modality acquisition (intensity values) or on the structures visible in this modality, in particular, the left ventricle. Therefore, they are not adapted to our problem on CT images.

Among the existing methods for segmenting the heart as a whole, Gregson [Gregson, 1994] works on MR images where he manually selects a 2D slice containing the heart and then uses a hierarchical algorithm to segment other structures in this slice (torso, lungs, background). Once the heart is recognized in the selected slice, the segmentation is propagated to adjacent slices. Lelieveldt et al. [Lelieveldt et al., 1999] proposed another method to segment the heart as a whole in MR images. They base their segmentation on a fuzzy atlas of thoracic structures. Their method is applied on MR data and the fuzzy model must be built beforehand, which is a strong limitation, in particular for the segmentation of pathological images that may have a different structural configuration than the ones used for the atlas

construction.

The segmentation method proposed by [Jolly, 2006] was first developed to segment the left ventricle in 2D MR slices, and it has been extended to CT with minimal adjustments. Her method proceeds in two steps. First, a global localization step roughly localizes the left ventricle and then a local deformation step combines EM-based (Expectation-Maximization) region segmentation and Dijkstra active contours. One of the main difficulties she has found is that the epicardium is difficult to recover because there are no image edges between the myocardium and the liver. This method furnishes very satisfactory results for high-resolution contrast CT images. However, it is not directly applicable to non-contrast and low resolution 3D CT images and major adaptations and extensions would be needed.

The work by [Funka-Lea et al., 2006] deals with the segmentation of the heart as a whole in CT. Their goal is to isolate the outer surface of the entire heart in order to easily visualize the coronary vessels. They make use of graph-cuts for the segmentation [Boykov and Funka-Lea, 2006 ; Juan and Boykov, 2006]. Their method is fast and robust for contrast CT studies with sub-millimeter resolution where the brightest regions are bone and blood. However, as the initialization of the graph-cut algorithm depends on the characteristics of a contrast study, it is not adapted to non-contrast CT images, which are common in radiotherapy applications. The goal and the type of images are therefore different from the ones in the present application.

The work by [Ecabert et al., 2005; 2007] describes a multi-compartment mesh of both atria, both ventricles, the myocardium around the left ventricle and the trunks of the great vessels and it is adapted to an image volume. The adaptation is performed in a coarse-to-fine manner by progressively relaxing constraints on the degrees of freedom of the allowed deformations. Their method is largely validated on high resolution contrast CT and it furnishes very satisfactory results.

However, these methods are not directly applicable to non-contrast and low resolution 3D CT images and major adaptations and extensions would be needed. The segmentation of the heart in non-contrast CT images presents specific difficulties due to their low contrast and the similar grey-level values of the surrounding structures (liver, tumors). This is illustrated in Figure 3.17 where it can be observed that the limits between the heart and the aorta or the liver are difficult to distinguish visually (even for experts). The low resolution (compared to existing submillimetric CT data) and the anisotropy of these CT exams are additional difficulties for the segmentation of the heart. Due to these difficulties, non-contrast CT is not generally used in cardiology. Other non irradiant techniques such as ultrasounds, which are less invasive, or MRI, which can provide a better resolution and contrast, are usually preferred in this field. However, ultrasounds do not furnish enough quality for many applications and MRI is not yet a routine technique in many medical centers. In the case of using CT for cardiac applications, contrast CT exams are acquired. For these reasons, to the best of our knowledge, there exists no method for the segmentation of the heart for non-contrast CT images and the existing methods for other modalities cannot deal with this type of images. Even the methods applied on CT images cannot be used on non-contrast studies without previous adaptation. Non-contrast CT is widely used in clinical routine and additionally provides better quality for the study of hard tissues such as bones, which can serve as a rigid references for several applications such as registration, surgery or radiotherapy planning. For oncology and radiotherapy, heart segmentation is very useful and the processing of this modality would avoid the necessity of other supplementary imaging acquisitions.

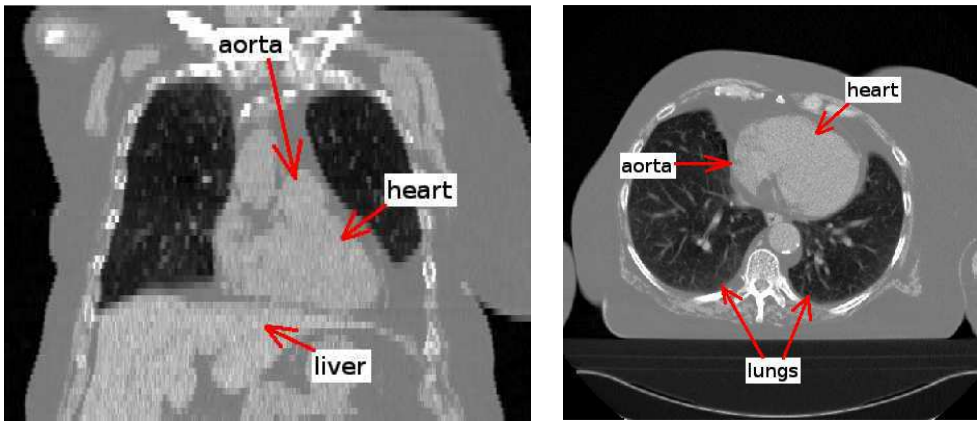

Figure 3.17: Coronal (left) and axial (right) views of a CT image.

3.3.2 Overview of the proposed method

In spite of the aforementioned drawbacks of the CT images used in radiotherapy, they have some particular characteristics, as the homogeneity of morphologic structures signal and the high contrast of the lungs compared to their surrounding structures. Therefore, we propose an original method that relies on these particular features of the images. The proposed algorithm includes constraints and anatomical knowledge in order to perform a robust segmentation of the heart by guiding a deformable model and thus, overcome the limits of the image acquisition.

Our approach relies on the segmentation of neighboring structures, which provide a strong constraint on the relative position and shape of the targeted structure. The idea is to deal first with the easiest structures to segment and then continue with those of increasing difficulty, using prior knowledge about the position of a structure with respect to the previously segmented ones. As shown in [Atif et al., 2007 ; Khotanlou et al., 2007], spatial relations improve the robustness of the segmentation of the structures even in the presence of pathologies. Another class of methods segment multiple objects simultaneously. For example, a level set approach based on a maximum a posteriori (MAP) framework using a neighbor prior constraint is used in [Yang et al., 2004].

In this work, we propose an automatic method to segment the heart as a whole based on the modeling of spatial relations between the heart and the lungs. Since the segmentation of the lungs is generally simple in CT scans due to their high contrast with respect to surrounding tissues, they are segmented first (see Section 3.2) in order to define a region of interest (ROI) of the heart. This region is used to define the initialization of a deformable model. Then the anatomical knowledge is included in the deformable model to segment the heart. A preliminary version of our method can be found in [Moreno et al., 2006b], where the use of the spatial relation "between" is explored in order to segment the heart. This study has shown encouraging results. Here a deeper study is developed, new pieces of anatomical knowledge are taken into account to improve the robustness and the automaticity of our approach, and the method is applied on a larger database.

In Section 3.3.3, our approach based on anatomical knowledge representation is introduced. In Section 3.3.4, we describe the first step of our method which defines the region of interest of the heart. Then in Section 3.3.5 the segmentation of the heart using deformable models constrained by anatomical knowledge is described. Next, in Section 3.3.6 some results

are shown and compared with manual segmentations.

3.3.3 Expression of anatomical knowledge

Although the delineation of the heart is a difficult task in CT, experts are able to segment this organ manually because they rely on their expertise and their knowledge of the anatomy. This a priori knowledge is usually represented by anatomical descriptions using qualitative and imprecise statements as discussed in Chapter 2. Translating this type of knowledge in a computationally efficient form, suitable for image processing, requires to model mathematically vague statements and imprecision. Therefore, a fuzzy representation of this kind of knowledge fulfills our requirements.

The anatomical descriptions of the heart usually include the statement "the heart is between the lungs". Our method relies on modeling this statement (denoted by K1) as well as the position of the heart (K2 and K3) inside this region:

- K1: "the heart is between the lungs".
- K2: the center of the heart is "between the lungs and far from them (i.e. the center of the heart is in the middle of the lungs in the region which is the furthest from both lungs) but closer to the left lung than to the right lung".
- K3: the heart is placed "in the anterior (closer to the chest than to the back) and inferior (near the diaphragm) region of the bounding box of the lungs".

The preliminary step consists in segmenting the lungs as described in Section 3.2.

3.3.3.1 Modeling K1

A complete study of the spatial relation "between" has been made in [Bloch et al., 2006], in which different definitions of this spatial relation are proposed, compared and discussed according to different types of situations.

A simple (crisp) definition of "between" consists in using the convex hull of the union of the two involved objects. However, the use of a convex hull to find the heart is not suitable because some parts of the organ are outside the resulting region as illustrated in Figure 3.18. This is a strong argument in favor of more sophisticated definitions which should take into account a larger region than the convex hull corresponding to a somewhat looser meaning of the "between" area.

This idea is achieved by means of fuzzy dilation of each object in the direction of the other. Thus, among the definitions detailed in [Bloch et al., 2006], we have chosen the fuzzy directional dilation definition of the relation "between". The different definitions are compared in Appendix B and in [Moreno et al., 2008b]. The interest of this definition is that the "between" region extends smoothly outside the convex hull of the union of both objects which is a required feature for our application. The region between A_1 and A_2 is defined as a fuzzy set in the image domain, as:

$$\begin{aligned}\beta_{btw}(A_1, A_2) = D_{\nu_2}(A_1) \cap D_{\nu_1}(A_2) \cap A_1^C \cap A_2^C \\ \cap [D_{\nu_1}(A_1) \cap D_{\nu_1}(A_2)]^C \cap [D_{\nu_2}(A_1) \cap D_{\nu_2}(A_2)]^C\end{aligned} \tag{3.1}$$

where A_1 and A_2 represent the objects (the lungs in our case), A^C represents the (fuzzy) complementation of A and $D_{\nu_i}(A_j)$, $i, j \in \{1, 2\}$, is the fuzzy dilation of A_j with the fuzzy

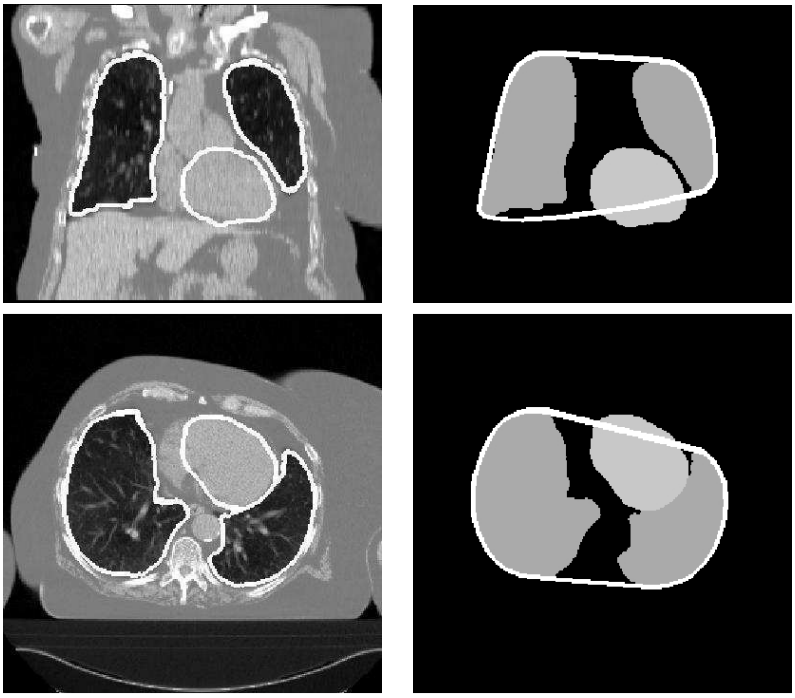

(a) (b)

Figure 3.18: Coronal (top row) and axial (bottom row) views of an example of the segmentation of the lungs and the heart: (a) the contours of these organs are superimposed on the original image and (b) the convex hull of the lungs is superimposed on the segmented lungs and heart (some parts of the heart are not contained in this region).

structuring element ν_i as defined in [Bloch and Maître, 1995]:

$$D_\nu(\mu)(x) = \sup_y t[\mu(y), \nu(x-y)]. \tag{3.2}$$

Thus, fuzzy dilation corresponds to a degree of intersection between the fuzzy set to be dilated μ and the fuzzy structuring element ν translated at point x. t denotes a t-norm and x and y points of space [Bloch and Maître, 1995]. An example of fuzzy dilation is shown in Figure 3.20(d). The conjunctions ($\cap$) in Equation 3.1 are performed using the t-norm "minimum". The membership degree $\beta_{btw}(A_1, A_2)(x)$ represents the degree to which x is between A_1 and A_2.

The structuring elements are derived from the angle histogram between both objects [Miyajima and Ralescu, 1994]. In 3D (using spherical coordinates) the direction is represented by two angles, that are denoted by α_1 and α_2 (with $\alpha_1 \in [0, 2\pi[$ and $\alpha_2 \in [-\pi/2, \pi/2]$, the 2D case corresponding to $\alpha_2 = 0$) [Bloch and Ralescu, 2003]. Given an axis of reference, say the x axis denoted by $\vec{u}_x$, for each pair of points (p_1, p_2) with $p_1 \in A_1$ and $p_2 \in A_2$, the angles between the axis and the segment joining these two points, $\overrightarrow{p_1p_2}$, are computed: α_2 is the angle between $\overrightarrow{p_1p_2}$ and its projection on the x-y plane and α_1 is the angle between this projection and $\vec{u}_x$ (see Figure 3.19).

The histogram of the obtained angles $h_{(A_1,A_2)}(\alpha_1, \alpha_2)$ for all possible pairs of points is then defined as:

$$h_{(A_1,A_2)}(\alpha_1, \alpha_2) = |\{(p_1, p_2), p_1 \in A_1, p_2 \in A_2, \angle(\overrightarrow{p_1p_2}, \vec{u}_x) = (\alpha_1, \alpha_2)\}|. \tag{3.3}$$

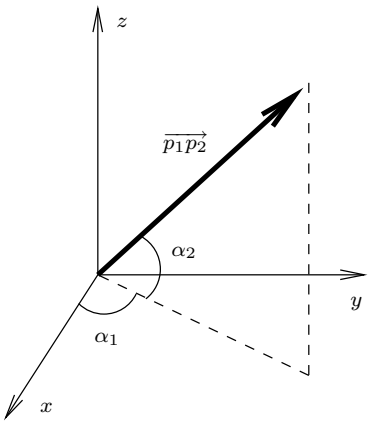

Figure 3.19: Definition of a direction in 3D by two angles.

It can be normalized as:

$$H_{(A_1,A_2)}(\alpha_1,\alpha_2) = \frac{h_{(A_1,A_2)}(\alpha_1,\alpha_2)}{\max_{(\alpha'_1,\alpha'_2)} h_{(A_1,A_2)}(\alpha'_1,\alpha'_2)} \tag{3.4}$$

in order to be interpreted as a fuzzy set.

The structuring elements are derived as:

$$\nu_2(r,\alpha_1,\alpha_2) = H_{(A_1,A_2)}(\alpha_1,\alpha_2), \tag{3.5}$$

$$\begin{aligned}\nu_1(r,\alpha_1,\alpha_2) &= H_{(A_1,A_2)}((\alpha_1+\pi)(\mathrm{mod}\,2\pi),-\alpha_2)\\ &= \nu_2(r,(\alpha_1+\pi)(\mathrm{mod}\,2\pi),-\alpha_2),\end{aligned} \tag{3.6}$$

where r is the radius in spherical coordinates. The structuring elements represent the relation between the two objects and they define the direction to be used for the fuzzy dilation [Bloch, 1999]. ν_1 represents the direction from object A_2 to object A_1 and ν_2 the opposite direction.

An illustrative example in 2D is shown in Figure 3.20 where A_1 (the right lung) is on the left in the figure and A_2 (the left lung) is on the right. For instance, if object A_2 is mainly to the right of object A_1 (see Figure 3.20(d)), then ν_1 represents "to the left of" and ν_2 "to the right of". Equation 3.1 defines the region which is both to the right of A_1 ($D_{\nu_2}(A_1)$) and to the left of A_2 ($D_{\nu_1}(A_2)$) excluding A_1 and A_2 ($A_1^C \cap A_2^C$), but which is not to the left of both A_1 and A_2 ($[D_{\nu_1}(A_1) \cap D_{\nu_1}(A_2)]^C$) nor to the right of both ($[D_{\nu_2}(A_1) \cap D_{\nu_2}(A_2)]^C$). Figure 3.20(e) shows the region between the lungs obtained with this definition.

3.3.3.2 Modeling K2

K2 represents the following anatomical knowledge: the center of the heart is "between the lungs and far from them (i.e. close to the middle of the lungs) but closer to the left lung than to the right lung". The computation of a distance function to the lungs combined with K1 allows the modeling of the first part of this statement. In order to account for the second part, a dilated right lung has been used to calculate the distance function. Thus, the maximum of the distance function between the lungs is closer to the left lung. In order to find how much the center of the heart is closer to the left lung than to the right lung, some measures have been performed by an expert on images from different patients. In addition

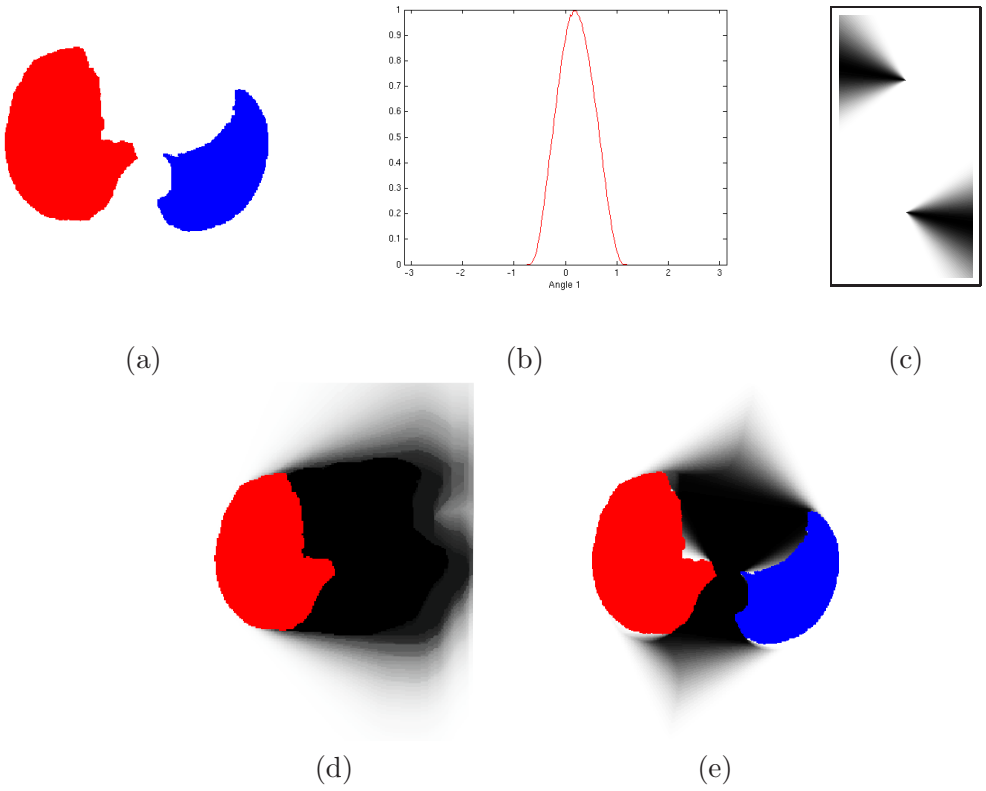

Figure 3.20: Some of the steps for computing $\beta_{btw}(A_1, A_2)$: (a) The segmented lungs A_1 (in red) and A_2 (in blue), (b) the normalized angle histogram $H_{(A_1,A_2)}$ with respect to the horizontal axis, (c) the structuring elements ν_1 (top) and ν_2 (bottom), (d) fuzzy dilation of the right lung (A_1) with the fuzzy structuring element ν_2, $D_{\nu_2}(A_1)$, (e) fuzzy region β_{btw} between the lungs, superimposed on the segmented lungs. The membership values to β_{btw} vary from 0 (white) to 1 (black). The illustration is provided in 2D for the sake of readability.

to this, the distances of the centroid of the heart (the center of its bounding box) have been computed for the 10 cases of our database where the heart has been manually segmented. The results in Table 3.2 confirm that the centroid of the heart is 2-3 cm closer to the left lung than to the right lung. For this reason, a morphological dilation of 3 cm for the right lung has been used to find correctly the approximate center of the heart. The distance function d is computed using a chamfer algorithm [Borgefors, 1986]. The normalized distance function can be interpreted as a fuzzy set which represents the region "far from the lungs but closer to the left lung". Therefore, its membership function β_{ffl}, illustrated in Figure 3.21(b), is defined at a point x as:

$$\beta_{ffl}(x) = \frac{d(x, D_3(A_1) \cup A_2)}{\max_y d(y, D_3(A_1) \cup A_2)}. \tag{3.7}$$

where $D_3(A_1)$ denotes the morphological dilation of 3 cm of the right lung and A_2 the left lung.

Distance of the heart centroid to the right lung (mm)	69.98 ± 7.96
Distance of the heart centroid to the left lung (mm)	47.35 ± 6.12
% of bounding box of lungs in y	31.7 ± 7.18
% of bounding box of lungs in z	32.1 ± 7.98

Table 3.2: Mean and standard deviation of the distances of the centroid of the heart to both lungs (for K2) and mean and standard deviation of the percentage of the bounding box of the lungs where the centroid of the heart is located (for K3).

3.3.3.3 Modeling K3

The heart is placed in the anterior (closer to the chest than to the back) and inferior (near the diaphragm) region of the bounding box of the lungs. Here it is assumed that the patients are always in a similar position and that the orientation does not change from one patient to another (there is almost no difference in rotation), and therefore the bounding boxes of the lungs are comparable. This region is defined as the inverted (normalized) distance β_{BB} to a horizontal line L which is at 1/3 (33 %) of the height of the bounding box from its inferior limit and at 1/3 (33 %) of its width in the anterior-posterior direction from its anterior limit:

$$\beta_{BB}(x) = 1 - \frac{d(x, L)}{\max_y d(y, L)} \tag{3.8}$$

As for K2, the position of the horizontal line L was estimated by an expert on images from different patients and it has been confirmed by the results illustrated in Table 3.2 which shows the mean and standard deviation of the position of the centroid of the heart with respect to the bounding box of the lungs. The fuzzy set β_{BB} is illustrated in Figure 3.21(c) where it can be observed that the value of β_{BB} decreases linearly when the distance to L increases.

3.3.3.4 Using K1, K2 and K3

Although K2 and K3 are not as critical as K1, they have proved to be useful in order to get a robust and automatic initialization in all cases. If K1 is not included, anything but the heart can be segmented (typically, something in the abdomen if it is included in the image) because the processing is not centered in the region between the lungs. If K2 is not used, the aorta can be segmented instead of the heart, since it is between the lungs but not in the widest part between them. If K3 is not used, then some parts of the heart are not segmented but the aorta is included in the result of the segmentation since it is located in the superior region of the lungs bounding box. Without K2 and K3, the algorithm furnishes an incomplete result or a result that includes too many structures. Thus the use of K2 and K3 improves the results by refining anatomical knowledge.

The exploitation of all this anatomical knowledge is performed at two levels:

1. first a region of interest (ROI) is selected by combining the different pieces of anatomical knowledge (Section 3.3.4);

2. then the anatomical knowledge is introduced in the evolution scheme of a deformable model to find the boundaries of the heart inside the ROI (Section 3.3.5).

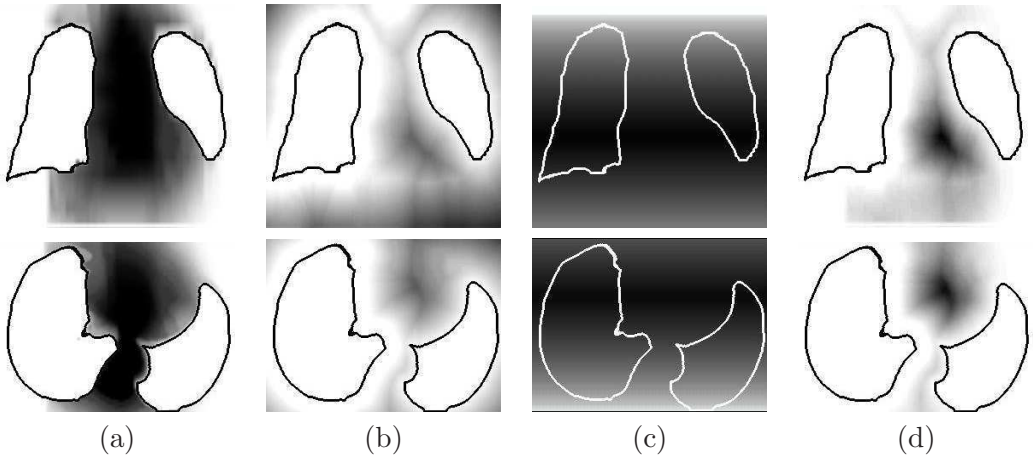

(a) (b) (c) (d)

Figure 3.21: (a) K1, the spatial relation "between", β_{btw}, (b) K2, the distance map to the lungs, β_{ffl}, (c) K3, the distance map to the horizontal line, β_{BB}, and (d) conjunctive fusion of K1, K2 and K3, β_R. The membership values vary from 0 (white) to 1 (black). Coronal views are in the top row and axial views in the bottom one. The contours of the lungs are superimposed in black (a,b,d) and in white (c) for better visualization.

3.3.4 Definition of the region of interest

The goal of the step described in this section is to find a ROI containing the heart which is defined as a sphere centered in a point obtained in a robust way using the anatomical knowledge modeled as stated in the previous section. In 2D, as explained by Gregson [Gregson, 1994], the maximum of the distance function to the lungs (on a previously selected slice containing the heart) is a good candidate to be the center of a disk containing this organ. This uses only a part of K2 in 2D, which leads to a poor robustness in general. We propose to extend this idea to 3D and to improve the localization by using K1, K2 and K3. Thus, the algorithm to find the center of the ROI has the following steps:

1. Conjunctive fusion of β_{btw}, β_{ffl} and β_{BB}:

$$\beta_R(x) = \beta_{btw}(A_1, A_2)(x) \cdot \beta_{ffl}(x) \cdot \beta_{BB}(x).$$

   This conjunctive combination of K1, K2 and K3, performed with the t-norm "product", means that the points with higher values will fulfill all the spatial constraints. The result of this combination is illustrated in Figure 3.21(d).

2. Calculation of the sphere-ROI. The center of the sphere is defined as the point having the maximum value in the fusion result. The radius is defined as the value of the minimum distance to the right lung at this point plus 10% of this distance (so that the relation is large enough to include the heart in all cases).

This stage provides a restricted ROI for the heart (not too many surrounding structures included) and it has proven to be robust enough since it uses some stable characteristics of the center of the heart and relies on general anatomical knowledge. This is illustrated in Figure 3.22, where the resulting ROIs for 5 cases are superimposed on the original CT images.

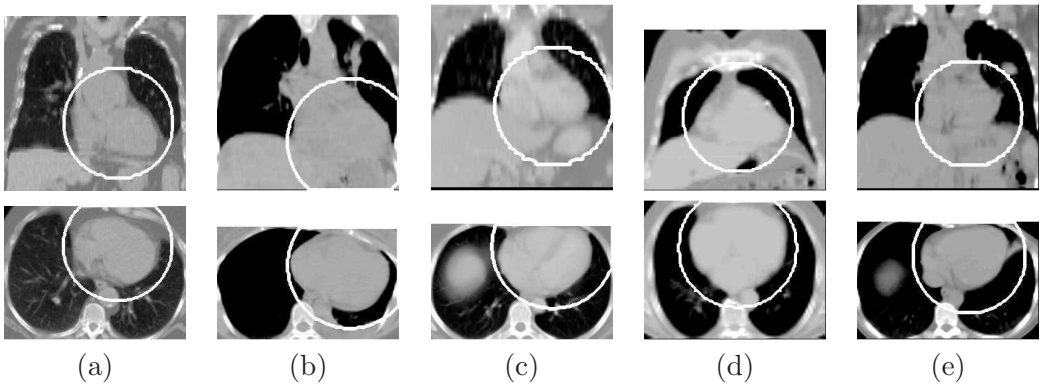

(a) (b) (c) (d) (e)

Figure 3.22: Superimposition of the obtained ROIs (circles) and the original images for 5 cases. Coronal views are in the top row and axial views in the bottom one.

3.3.5 Deformable model with anatomical constraints

Once the region of interest is selected, a deformable model is used to segment the heart inside this region.

Deformable models were introduced by Kass et al. [Kass et al., 1987] and are often used for segmentation in image processing [McInerney and Terzopoulos, 1996 ; Xu and Prince, 2000 ; Montagnat et al., 2000 ; Meier et al., 2005 ; Liang et al., 2006]. They consist in defining an initial m-D object in n-D, with $n \geq m$ (a 3D surface in 3D in the present case) that evolves under the effect of some forces towards a final state. In an optimal case, this final state corresponds to the object to be segmented.

The evolution of the deformable surface of negligible mass $\mathbf{X}$ can be described using a dynamic force formulation and written as follows:

$$\gamma \frac{\partial \mathbf{X}}{\partial t} = \mathbf{F}_{int}(\mathbf{X}) + \mathbf{F}_{ext}(\mathbf{X})$$

where $\mathbf{F}_{int}$ is the internal force related to the physical properties or constraints of the model that specifies the regularity of the surface, and $\mathbf{F}_{ext}$ is the external force that drives the surface towards the desired features in the image (in general image edges) and sometimes includes forces interactively introduced by the user. The solution is the steady state of the previous equation.

The internal force is defined as [Kass et al., 1987]:

$$\mathbf{F}_{int} = \alpha \nabla^2 \mathbf{X} - \beta \nabla^2 (\nabla^2 \mathbf{X}) \tag{3.9}$$

where α and β respectively control the surface tension (which prevents it from stretching) and rigidity (which prevents it from bending) and ∇^2 is the Laplacian operator.

The external force can be defined with the Gradient Vector Flow (GVF) [Xu and Prince, 1997] as also used in [Camara et al., 2004 ; Colliot et al., 2004b; 2006]. The GVF defines a vector field towards the previously calculated contours of the image (the edge map). As proposed in [Colliot et al., 2004a; 2006] the external force can also include spatial relations in order to constraint the segmented object to stay in a region where given spatial relations are satisfied.

The anatomical knowledge described in Section 3.3.3 is introduced in the external force $\mathbf{F}_{ext}$ combined with a weighted pressure force. Thus, the external force describes both edge information (GVF) and structural constraints:

$$\mathbf{F}_{ext} = \lambda\, \mathbf{F}_{gvf} + (1 - \lambda)\, \mathbf{F}_R + \mathbf{F}_p \tag{3.10}$$

where $\mathbf{F}_{gvf}$ is a classical data term that drives the model towards the edges [Xu and Prince, 1997], $\mathbf{F}_R$ is a force associated to the spatial relations, $\lambda \in [0, 1]$ is a weighting parameter and $\mathbf{F}_p$ represents a pressure force [Cohen, 1991], normal to the surface.

3.3.5.1 Initialization of the deformable model

The initial surface is a sphere included in the ROI (same center) chosen small enough so that it can be assumed that it has to expand to segment correctly the heart. In this work, the size of the small sphere has been fixed to 10 mm, but it could also be defined as a percentage of the radius of the ROI. A small sphere has been chosen as initialization (instead of directly the sphere-ROI) in order to ease the evolution of the deformable model. If the sphere-ROI is used as initialization and deformed by enforcing contraction, the deformable model stops at the high contrast contours outside the heart and an erroneous segmentation would be obtained. However, inside the heart, there exist much less contrasted contours and thus the deformable model evolves towards the external limits of this organ. The initial small sphere is illustrated in Figure 3.23. During its evolution, the deformable model is constrained to remain inside the sphere-ROI. This can be seen as a restriction. However, the sphere-ROI is large enough to ensure that the heart is contained in it in all tested cases. If the center of the ROI has been computed correctly (i.e. it is in the center of the heart), the heart will be contained in the ROI.

Figure 3.23: Coronal and axial views of the obtained ROI of the heart and the initial contour of the deformable model superimposed on the CT image.

3.3.5.2 Spatial relations force

The force $\mathbf{F}_R$ must constraint the model to evolve towards the regions with high values of $\beta'_R = 1 - \beta_R$. This means that the force $\mathbf{F}_R$ drives the deformable model towards regions closer to the lungs and "less between" them than the center, which is the complementary of K1, K2 and K3 defined in Section 3.3.3. When the relation β'_R is completely satisfied (inside the lungs and in the regions not between them), the model should only be driven by edge information ($\mathbf{F}_{gvf}$) and $\mathbf{F}_R$ should be 0 if $\beta'_R = 1$. These vector fields are shown in Figure 3.24. This illustrates an important advantage of using fuzzy spatial relations to guide the model, as a vector field can be defined towards the regions where the relations are more satisfied.

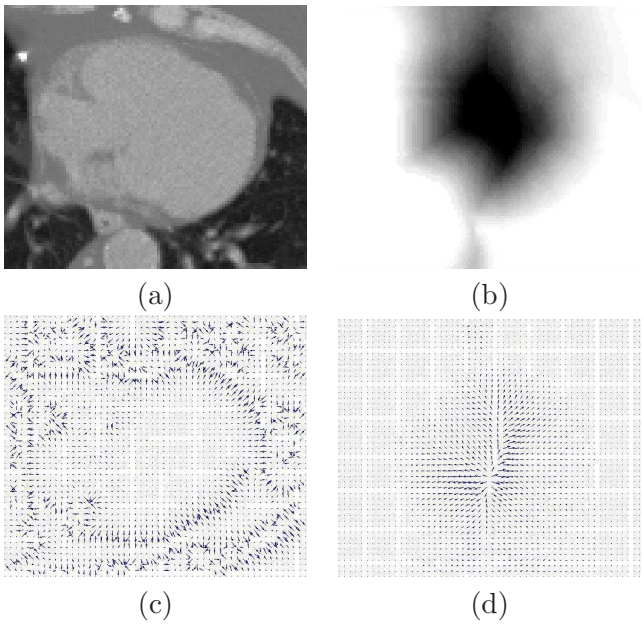

Figure 3.24: Detail of the original CT image (a) and vector field $\mathbf{F}_{gvf}$ corresponding to the GVF (c). Detail of β_R (b) and vector field $\mathbf{F}_R$ associated (d).

Several methods for external forces that fulfill these properties are described in [Colliot et al., 2004a]. A gradient diffusion technique has been chosen due to the smoothness and the wide attraction range of the resulting vector field. Thus, the GVF is calculated by replacing the edge map of the original formulation with our fuzzy set β'_R:

$$\begin{cases} \frac{\partial \mathbf{u}}{\partial t} = c\nabla^2\mathbf{u} - ||\nabla\beta'_R||^2(\mathbf{u} - \nabla\beta'_R) \\ \mathbf{u}(x,0) = \nabla\beta'_R(x) \end{cases} \tag{3.11}$$

where t is the time parameter, x a point of space and c defines the trade-off between the two terms (here it is equal to 0.15 as suggested in [Xu and Prince, 1998]). The first equation is a combination of a diffusion term that will produce a smooth vector field and a data term that encourages $\mathbf{u}$ to stay close to $\nabla\beta'_R$, i.e. we want it to be stronger when the variations of β'_R are more important so that the deformable surface evolves from regions completely between the lungs towards regions not between the lungs. In regions where $||\nabla\beta'_R||$ is low, the diffusion term will prevail. The less the relation β'_R is satisfied the higher the modulus

of the force should be, thus it has to be proportional to β_R. The following normalization is used: $\mathbf{F}_R = \beta_R \frac{\mathbf{u}}{||\mathbf{u}||}$ where $\mathbf{u}$ is the GVF defined by Equation 3.11.

3.3.5.3 Pressure force proportional to spatial relations

The term $\mathbf{F}_p$ in Equation 3.10 represents a pressure force [Cohen, 1991], normal to the surface and which amplitude is $w_p(x) = k_1\,\beta_R + k_2$ where k_2 represents the modulus of a constant pressure in all points of space and k_1 weights a pressure term proportional to β_R. Their effect is explained in Section 3.3.6. This pressure force reinforces the effect of spatial relations and improves convergence as it is stronger at the points between the lungs which are the farthest from them (where β_R takes higher values), and it decreases when getting closer to them (where β_R takes lower values because the chosen spatial relations are less fulfilled). Indeed, this pressure force is needed to avoid the following effect: if the weight of $\mathbf{F}_R$ is increased only with respect to $\mathbf{F}_{gvf}$, the influence of the edge map is reduced and the accuracy of the segmentation near the contours of the image worsens.

3.3.6 Results

Our algorithm has been applied on 10 different cases of CT images. These exams come from different medical centers and have different characteristics (size, resolution, contrast). Their sizes are $512 \times 512 \times Z$ voxels with Z varying from 63 to 122 and their resolutions are typically around $2 \times 2 \times dz$ mm^3 for the three directions of the space (x, y and z respectively), with dz varying from 4.5 to 7.5 mm.

3.3.6.1 Parameter tuning

In our experiments, the following parameters have been used:

- The radius of the initial sphere for the deformable model is small enough (10 mm) to ensure that the starting surface is completely contained inside the contours of the heart. An example of the initial contour is shown in Figure 3.23.

- The value of λ is adapted for each particular case (see Table 3.4). In general, it gives a more important weight to the GVF force ($\mathbf{F}_{gvf}$) because it guides the deformable model towards the contours, whereas $\mathbf{F}_R$ represents a more general evolution. However, the spatial relation force remains necessary for the evolution of the deformable model as illustrated in Figure 3.25(a).

- The values of the constants k_1 and k_2 for the pressure force weight are shown in Tables 3.3 and 3.4. The parameter k_1 balances the pressure force in order to prevent the deformable model from inflating too much or too little and k_2 pushes softly the model in order to reach the contours of the heart far from the initial small sphere.

- The internal force coefficients in Equation 3.9 are $\alpha = 0.2$ and $\beta = 0.1$ which provide a good trade-off between tension and rigidity.

- The value of c in Equation 3.11 has been chosen equal to 0.15 because it is the classical value, as suggested in [Xu and Prince, 1998]. However, similar results are obtained for values of c between 0.05 and 0.3.

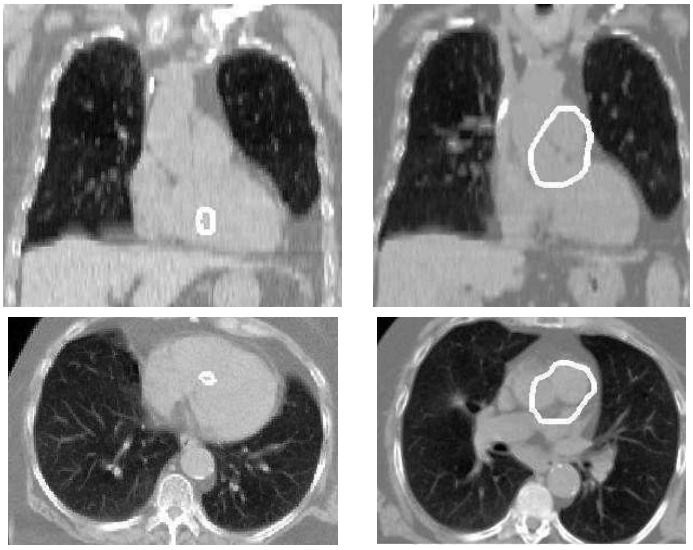

(a) (b)

Figure 3.25: Coronal (top row) and axial (bottom row) views of some results of heart segmentation. The contours, superimposed on the CT image, have been calculated: (a) using only the GVF force, which is not sufficient at all; and (b) using the GVF and a pressure force weighted with the membership function of the spatial relations ($\mathbf{F}_p$), without the force derived directly from spatial relations ($\mathbf{F}_R$). The result in (b) shows that the segmentation is not satisfactory without $\mathbf{F}_R$ and, therefore, this force is fundamental for the segmentation of the heart. These images correspond to the patient illustrated in Figure 3.22(a).

Radius of the initial sphere	Number of iterations	α	β	k_2	c
10 mm	10000	0.2	0.1	0.2	0.15 (0.05-0.3)

Table 3.3: Invariable parameters for all the cases in the database.

Patient	Dilation of right lung used for K2	% of bounding box of lungs used for K3	λ	k_1
1	3 cm	40 %	0.6	1
2	3 cm	33 %	0.7	1
3	3 cm	33 %	0.7	1
4	3 cm	25 %	0.6	0.1
5	3 cm	33 %	0.8	0.1
6	8 cm	33 %	0.7	2
7	3 cm	33 %	0.8	2
8	3 cm	25 %	0.7	2
9	3 cm	33 %	0.8	1
10	4 cm	33 %	0.5	2

Table 3.4: Parameters used for the patients in the database.

These parameters have been chosen empirically. Table 3.3 shows the values of the parameters that remain stable for all cases. Table 3.4 shows the values of the parameters to be adapted for different cases in order to obtain satisfactory results. λ may vary between 0.5 and 0.8 and k_1 has to be adapted depending on the case. The size of the dilation of the right lung (for K2) and the percentage of the bounding box of the lungs (used for K3) do not have to be changed in general, except for some particular cases (outliers of the distributions illustrated in Table 3.2).

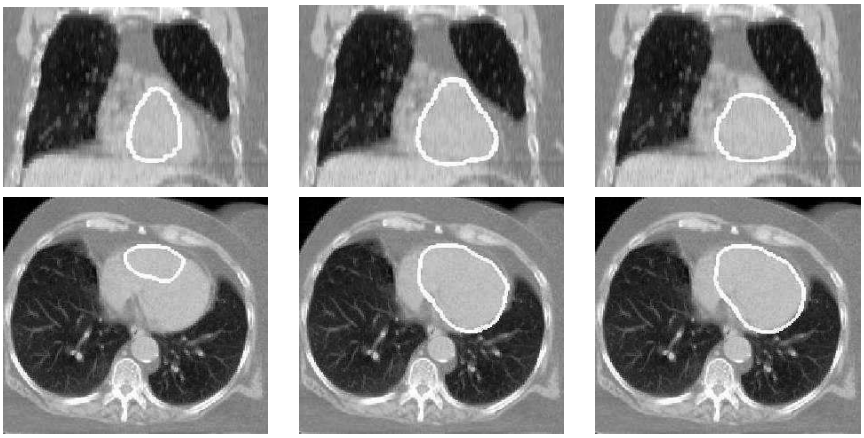

(a) (b) (c)

Figure 3.26: Coronal and axial views of some results of heart segmentation. The contours, superimposed on the CT image, have been obtained: (a) using $\mathbf{F}_{gvf}$ and $\mathbf{F}_R$: the heart is not completely segmented; (b) adding a constant pressure force for the evolution of the deformable model: some parts of the aorta are included in the heart segmentation; (c) using $\mathbf{F}_{gvf}$, $\mathbf{F}_R$ and $\mathbf{F}_p$: this combination avoids the inclusion of other structures in the heart segmentation. These images correspond to the patient illustrated in Figure 3.22(a).

How to tune the parameters – The first parameters to fix are the distances for K2 and K3. This can be done by computing the sphere-ROI and the initial small sphere. If it is centered in the heart, it is a good initialization. Otherwise, the morphological dilation of the right lung should probably be increased. This stage could be realized by using a user interface in order to ease interaction. Then λ and k_1 have to be tuned. $\lambda = 0.7$ and $k_1 = 1$ are good initial parameters. Once the first result is computed, there exist several possibilities:

- If the resulting contour is too small compared with the heart or some parts of the organ (typically the apex) are not included in the segmentation, then k_1 (the pressure force) has to be increased.
- If the resulting segmentation is too large, then λ has to be increased in order to give more importance to the influence of the contours (the GVF) with respect to the spatial relations force.
- If the heart is correctly delineated but the segmentation includes some parts of the aorta or the liver, either λ has to be slightly increased or k_1 should be decreased a little.

These guidelines may be useful in cases the results are not completely satisfactory with the standard values of the parameters. However, in most cases, these standard values lead to results that are accurate enough for radiotherapy purposes (since an additional security margin is added anyway).

Figures 3.25 and 3.26 show some results of the segmentation of the heart using different combinations of the forces:

- In Figure 3.26(a) the heart has been segmented using the GVF and a force derived from spatial relations. The GVF guides the model towards the contours of the images and $\mathbf{F}_R$ represents a more general evolution towards the regions not between the lungs as explained in Section 3.3.5. However, this combination is not sufficient to segment completely the heart since the deformable model does not reach the contours of the heart. For this reason, $\mathbf{F}_R$ must be reinforced with a pressure force if an under-segmentation of the heart is not desired.

- The addition of a constant pressure force for the evolution of the deformable model improves the result. Nevertheless, the model inflates with the same strength in all directions, including parts of the surrounding structures (the aorta, the mediastinum and the liver) in the heart segmentation (Figure 3.26(b)).

- The use of a pressure force weighted with the spatial relations avoids this undesired effect. This is illustrated in Figure 3.26(c) where a satisfactory result is obtained. In this case, we have used the GVF, a force derived from spatial relations and a pressure force weighted with the membership function of the spatial relations as in Equation 3.10. The addition of the spatial relations significantly improves the results. This is particularly visible near the left lung.

- If this weighted pressure force is used without the force directly derived from spatial relations, the results are not satisfactory at all, as it can be observed in Figure 3.25(b). In this case, the deformable model expands but, as the force of spatial relations is not present, the GVF guides the surface towards the strongest contours of the image and not towards the appropriate regions.

3.3.6.2 Computation time and complexity

The computation of the membership function "between the lungs" (K1) is the most expensive step with respect to computation time. The algorithm to compute the region "between" has a complexity in $O(n^2)$ where n is the number of voxels of the input image. However, the computation time is not a limitation (even in 3D) because the images can be under-sampled to obtain the region between the lungs, as a very precise result is not necessary at this stage. Thus, the image of the segmented lungs (with original sizes $512 \times 512 \times Z$ voxels with Z varying from 63 to 122) is under-sampled to a much lower size ($15 \times 15 \times 15$ voxels), the region between them is computed using Equation 3.1 and finally the resulting image is resampled to the original size (using a linear interpolation). In these conditions, the total computation time is less than 4 minutes and the computation of the region between the lungs takes about 65% of the total time. However, without under-sampling the computation time is much higher as shown in Table 3.5. The manual segmentation of the heart can take about one hour for an expert. Therefore, the interest of the proposed method is to provide a fast result in a few minutes. Even if some interaction or even some correction of the result is necessary, our approach can ease the segmentation of the heart.

Operation	Computer performances	Time
Total computation time under-sampling the images to $15 \times 15 \times 15$	Sun Sparc Ultra-4, 2 GB RAM	< 4 min
Total computation time without under-sampling the images: $512 \times 512 \times 63$	Sun Sparc Ultra-4, 2 GB RAM	~ 17 h

Table 3.5: Computation times for the membership function "between" the lungs without and with resampling of the images.

Noticeably, the important under-sampling of the images does not prevent obtaining a correct result. However, some parameters may have to be adapted. Figure 3.27 shows the results obtained without and with under-sampling and the optimal parameters for each case.

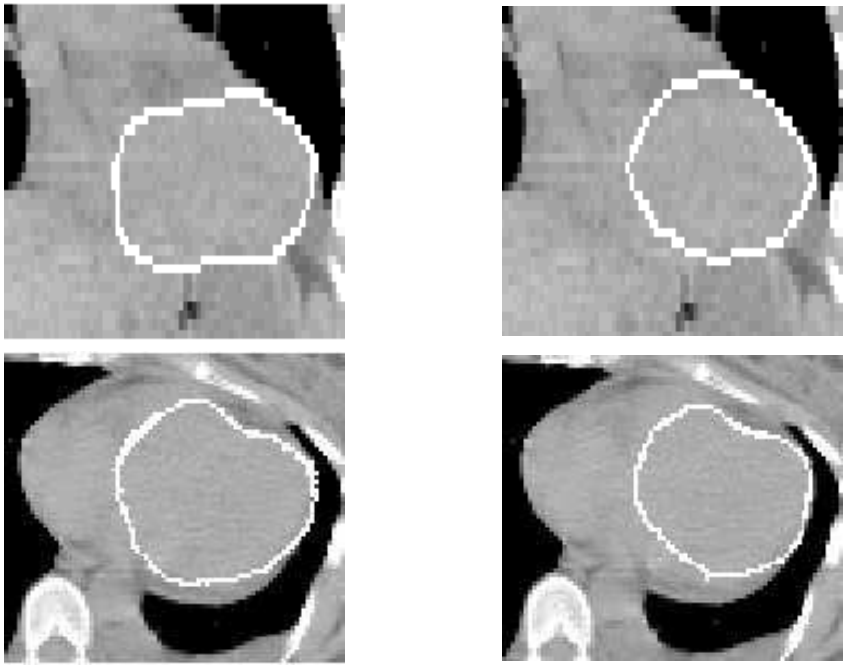

Resampling: $15 \times 15 \times 15$
$\lambda = 0.6$; $k_1 = 0.1$

No resampling: $512 \times 512 \times 63$
$\lambda = 0.5$; $k_1 = 2$

Figure 3.27: Detail of the results of the segmentation of the heart for patient 4 with and without resampling and the adapted parameters.

The number of iterations for the evolution of the deformable model is set to 10000, which has been empirically proven to be sufficient for convergence of the model, as the same results are obtained with a higher number of iterations. This takes less than 1 minute with a 3.2 GHz (Pentium 4) Intel CPU, 1 GB RAM.

3.3.6.3 Evaluation

In Figure 3.28 the results of our automatic heart segmentation method (in white) are compared with the manual segmentations (in black) for patients in Figures 3.22(b-e). It can be observed that even for an expert the delineation of the limits of the heart in these regions remains very challenging due to the low contrast of the images. The further application of our segmentation algorithm is radiotherapy planning, where a large margin is outlined around the pathologies to irradiate. Therefore, the results illustrated here are considered as satisfactory.

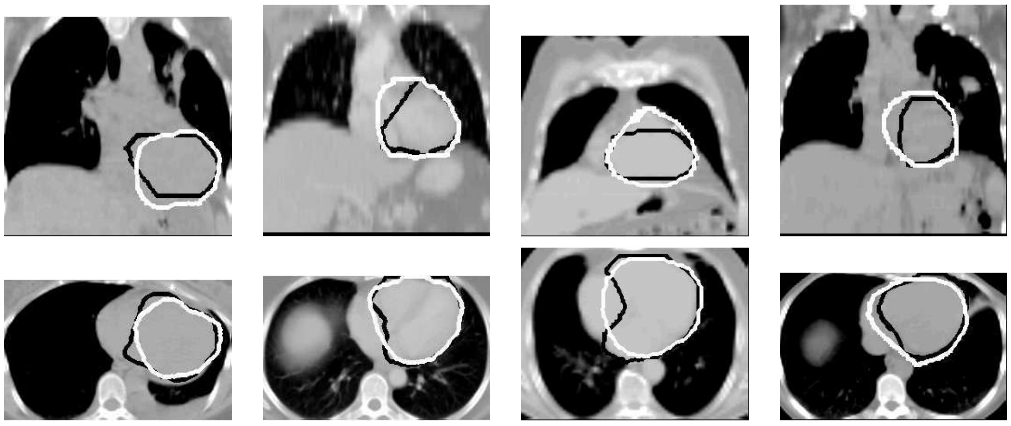

(a) (b) (c) (d)

Figure 3.28: Manual (black) and automatic (white) segmentations of the heart using our method for patients illustrated in Figures 3.22(b-e).

In order to evaluate quantitatively our results, the 10 automatic segmentations obtained with our algorithm (A) have been compared with the 10 corresponding manual segmentations furnished by an expert (M). In the following $|A|$ is the cardinality of the set of voxels A. Results are quantitatively assessed using different criteria:

- the similarity index $S = \frac{2|M \cap A|}{|M|+|A|}$ [Zijdenbos et al., 1994],
- the sensitivity $SENS(M, A) = \frac{|M \cap A|}{|M|}$,
- the specificity $SPEC(M, A) = \frac{|M \cap A|}{|A|}$ between both volumes,
- the mean distance $D_m(M, A) = \frac{1}{2}[d_m(M, A) + d_m(A, M)]$
  with $d_m(M, A) = \frac{1}{|M|} \sum_{p \in M} \min_{q \in A} d(p, q)$,
  where d is the Euclidean distance, between the surfaces.

As explained in [Zijdenbos et al., 1994] the similarity index S is sensitive to variations in shape, size and position and a value of $S > 0.7$ indicates a strong agreement. The value of S is equal to 1 when A and M totally overlap. The sensitivity ($SENS$) and specificity ($SPEC$) measures give us additional information about how the overlap of both structures is achieved. For instance, if the comparison of A and M yields a low sensitivity value but a high specificity one, it means that the automatic segmentation is too small. Both criteria

Patient	Similarity index	Sensitivity	Specificity	Mean distance
1	0.77	0.96	0.64	6.4
2	0.70	0.90	0.58	9.3
3	0.74	0.92	0.62	7.4
4	0.84	0.83	0.84	3.9
5	0.80	0.91	0.71	4.9
6 (3 cm)	0.57	0.46	0.40	11.2
6 (8 cm)	0.75	0.78	0.72	6.1
7	0.71	0.88	0.60	6.6
8	0.67	0.71	0.62	7.1
9	0.77	0.81	0.73	4.5
10	0.64	0.60	0.70	7.8

Table 3.6: Results of comparing the manual segmentations of the heart with the results obtained with our automatic method for different patient images. Distance are in millimeters (mm).

are also equal to 1 if total overlap is achieved. More details about comparative measures can be found in Appendix C.

3.3.6.4 Discussion

Table 3.6 shows the obtained results. It can be observed that results are satisfactory as S is higher than 0.7 for almost all 10 cases. This is also confirmed by the high values of sensitivity and specificity. As stated above, the voxel resolutions in Z of these CT exams varies from 4.5 to 7.5 mm. Therefore, mean distances from 3.9 to 9.3 mm are perfectly acceptable. These results are also satisfactory if they are compared with the 5.5 mm of average error obtained by [Funka-Lea et al., 2006] on contrast CT exams with sub-millimeter resolutions.

It can be observed that the values of the specificity are in general lower than those of the sensitivity. This means that our method furnishes segmentations of the heart larger than the manual delineations, which is consistent with the fact that, in radiotherapy applications, larger results are preferred to under-segmentations (see examples in Figures 3.28(b), (c) and (d) corresponding to patients 5, 2 and 1 respectively).

The best results are obtained for patient 4, illustrated in Figure 3.28(a). Indeed, the result of the automatic segmentation is visually close to the manual one. This is confirmed by the high value of S (0.84) and the low mean distance (3.9 mm). Sensitivity and specificity have high values (0.83 and 0.84 respectively) in this case.

The highest mean distance is the one of patient 2. In this case, the segmentation includes a part of the aorta (see Figure 3.28(c)). This is due to the fact that there is no edge information to separate it from the heart. This is one of the most challenging difficulties of our approach. Another difficulty is the separation of the heart and the liver. However, our method furnishes correct results for all cases. Only for patient 4 (Figure 3.28(a)) a small part of the liver has been included in the heart segmentation.

Two different results are shown for patient 6 in Table 3.6. For one of them a morphological dilation of 3 cm was performed for K2, and for the other one the dilation was of 8 cm. The low values of the similarity index, sensitivity and specificity, and the high mean distance, show that the segmentation was not correct with 3 cm. The used parameters furnished a

wrong initialization (the small sphere was not centered in the heart). Therefore, based on visual inspection of the images, this was corrected by using a dilation of 8 cm and results have been notably improved.

Our algorithm has been used on images coming from different centers and from different patients. Thus, there are differences in the contrast of the images and in the anatomy of the patients. Due to the differences in contrast, some limits between organs (or inside them) are visible in some of the studies and not in others. For example, a quite clear contour can be seen inside the heart in Figure 3.28(b), which is not present in the other cases. Our automatic segmentation approach deals with these differences. However, as illustrated with patient 6, the variations in anatomy from one patient to another are sometimes important and thus some parameters have to be adjusted for different images. In particular, in exams performed on children or in the case of lung resection, the parameters (and specially those based on distances) will probably need to be tuned. This may happen with different CT acquisition protocols, i.e. images acquired during normal breathing or in maximal inspiration (in this work the CT images are acquired in maximal inspiration). All the distances could be normalized with respect to the size of the lungs or to the size of the body, in order to find the parameters that could fit in all cases.

3.3.7 Conclusion

We propose an approach that uses fuzzy structural knowledge coming from spatial relations in order to segment the heart in CT images in a robust way. First, spatial relations are used to define the region of interest of the heart and then, from the fuzzy sets representing the spatial relations, a new external force is derived and it is introduced in the evolution scheme of a deformable model.

As illustrated by our results, the modeling of the spatial relations and their incorporation into the deformable model evolution significantly improve the segmentation of the heart compared with the classical approaches that are guided by a pressure force and GVF, by excluding non-desirable structures such as the aorta or the liver. The results have been evaluated by comparing them with segmentations of the heart carried out manually by an expert, which shows the accuracy attained with our approach. These preliminary quantitative results show a strong agreement between the manual segmentations and the ones obtained by our approach, and confirm the potential of the proposed method. Nevertheless, the segmentation of the heart in CT images remains a difficult task as, even for experts, it is complicated to define the limits of this organ in this modality. For this reason, our method should be applied to larger databases, with manual segmentations obtained from a common agreement of a group of experts to go further in the evaluation.

One of the foreseen applications of our method is radiotherapy planning. Usually radiotherapists delineate a relatively wide margin around sensitive organs which must not be affected by radiation. This margin, which may be of several centimeters (particularly in the lungs due to the breathing) is much larger than the mean distances shown in Table 3.6. Thus, the obtained results show that our segmentation method provides accurate enough results for the segmentation of the heart. Figure 3.29 shows some results of heart segmentation with a tumor in the lungs. This illustrates the usefulness of the segmentation of the heart in radiotherapy planning as, once the segmentations of the heart and the tumor are computed, the delineation of the security margins are much easier and could even be automated. In addition to this, our method can also be used for diagnosis of other cardiovascular diseases. In particular, the new combined devices PET/CT and SPECT/CT, widely used in cardiology

and oncology, often furnish non-contrast and low-resolution CT images. Our approach, as opposed to the one by [Funka-Lea et al., 2006] for example, is adapted to this type of data.

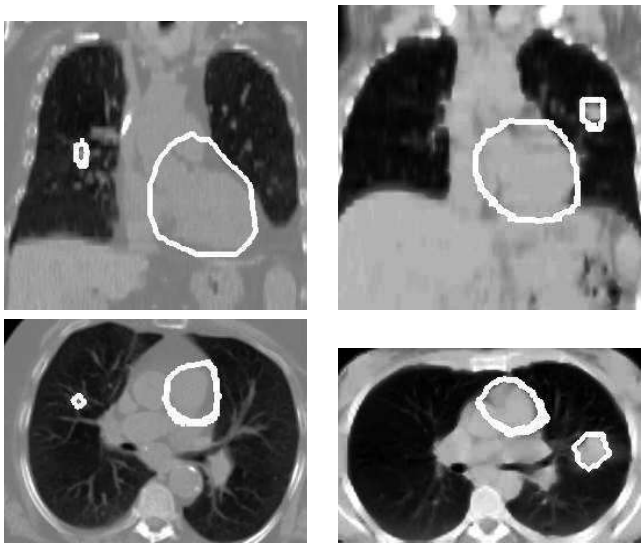

(a) (b)

Figure 3.29: Results of automatic heart segmentation for two cases where a tumor is present in the right (a) and in the left lung (b). Images in (a) correspond to the patient illustrated in Figure 3.22(a) and images in (b) to the patient in Figure 3.22(e).

Future work aims at applying our algorithm to other imaging modalities such as positron emission tomography (PET) images. In general, in this modality, the heart presents higher intensity values than the surrounding structures. In this case, the segmentation of the heart could be relatively straightforward. However, in some cases (even for the same patient), the heart does not appear clearly in PET images. According to consulted clinicians, the reasons of this effect are unknown for the moment. This can be a limitation for multimodality registration and other heart-based studies.

In addition to this, the research of the best parameter combination could be automated in order to take into account potential variations in anatomy. The most sensitive step of our method is the initialization of the deformable model. If the small sphere is not centered inside the heart, the results of the segmentation may be unsatisfactory. This step can be improved by adding an interactive interface at this stage in order to let the user correct the initialization if necessary. This kind of interaction is easily accepted and even often desired by clinicians.

Further applications include the use of the segmentation of the heart in registration algorithms based on structures [Camara et al., 2007] (see Appendix D) or based on features/landmarks (see Chapter 4), necessary even in PET/CT and SPECT/CT combined devices, and subsequently, in radiotherapy planning procedures.

3.4 Semi-interactive tumor segmentation

In this section, we describe the semi-interactive method we have developed to segment tumors both in CT and in PET. Tumor segmentation is very important for the quantification of

pathologies for diagnosis and, in particular, for radiotherapy planning. In our work, the segmentation of tumors is a preprocessing for our registration algorithm. As detailed in Chapter 4, tumor segmentation is necessary in our approach in order to introduce constraints that guarantee relevant deformations and improve non-linear registration between anatomical and functional images.

3.4.1 Motivation and choice of the approach

Most of the existing registration methods have as a limitation that regions placed inside or near the main structures will be deformed according to the registration computed for the latter. A critical example of this situation occurs when a tumor is located inside the lungs and there is a large volume difference between CT and PET images (due to the breathing) as illustrated in Figure 1.1 in Chapter 1. In this case, the tumor undergoes unrealistic deformations.

Thus, the aim of our work is to avoid the undesired tumor misregistrations by adding some rigidity constraints on the tumors, hence the need for the tumor segmentation.

Tumor segmentation in PET is not as difficult as in CT, because the intensity of the tumor is quite different from the intensity of surrounding structures especially when the pathology is located inside the lungs. The work by [Lee et al., 2005] deals with tumor segmentation in PET for the small animal and uses a region growing algorithm based on gradient magnitude. In our case, the resolution and variations of intensities are good enough to apply directly a region growing algorithm.

The automatic segmentation of tumors is a difficult task, specially in CT images, because of the similar grey-levels of the structures that can be in contact with the pathologies. We deal with tumors that are relatively big (15 mm or more of diameter) and located inside the lungs. Their positions and their extensions can be very different from one patient to another, and they may be isolated from or attached to other structures such as blood vessels, bronchi or the pleura.

Existing methods for tumor segmentation work mainly in CT, because it is considered to be the most accurate imaging modality available for early detection and diagnosis of lung cancer. Some recent works on nodule segmentation provide an interesting state of the art on this subject, such as [Okada et al., 2005 ; Zhao et al., 2003].

Among the methods for segmentation and classification of lung nodules in CT, the work by [Zhao et al., 2003] presents an algorithm for automated identification of small lung nodules (2-7 mm) on multislice CT images. Their method has three steps. First, they separate the lungs from the other anatomical structures by finding a threshold in the density histogram of CT chest images. Next they detect some nodule candidates in the extracted lungs (automatic search for higher density structures). Finally they reduce the false-positives among the detected nodule candidates applying a priori knowledge such as the size and the shape of the nodules to be detected. A similar approach for segmentation and classification of nodules has been used by [Bahlmann et al., 2006] in the context of computer aided detection (CAD) of lung nodules. They describe a novel method for the classification of nodules, attached nodules, vessels and junctions in thoracic CT scans. Their method transforms the complex problem of classifying various 3D topological structures into a much simpler 2D data clustering problem which can be solved using many well-known solutions. They propose an EM-based clustering solution by fitting a Gaussian mixture model to samples drawn from the bounding manifold image. Their classification relies on a post-processing filter within a lung CAD system that provides an effective means for removing false positives

caused by vessels and junctions. Another method for segmenting small nodules in the lungs is proposed by [Fetita and Prêteux, 2004 ; Raffy et al., 2004]. They use a strong morphological filter, the connection cost [Prêteux, 1993], to segment pulmonary nodules in 3D CT images. This method is fully automatic and it is applied to clinical data concerning patients with pulmonary carcinoma. It detects isolated, juxtavascular and peripheral nodules with sizes ranging from 2 to 20 mm of diameter. [Okada et al., 2005] use a semi-automatic segmentation solution consisting in a one-click nodule segmentation algorithm. Their work focuses on geometrical and volumetric characterization of pulmonary nodules in CT images, given a marker indicating a rough location of a target. One of the main strengths of their solution is its robustness against the attachment of the nodule to vessels and pleural surfaces and against marker location variability. Another advantage is the computing time (quasi-real-time in 3D). The robustness, flexibility, and efficiency of this approach facilitate its application to pulmonary nodule segmentation in CT but also to other different imaging domains (as PET scans). This approach provides good results and has interesting properties.

In our case, tumors can have sizes out of the margins of the aforementioned methods (usually more than 15 mm of diameter). In addition to this, we prefer a simpler algorithm in a semi-interactive approach based on only one click of the user, which is a seed point for the segmentation.

The algorithm we propose has three different steps:

1. selection of a "seed point" inside the tumor (by the user);
2. rough segmentation of the tumor by a region growing method;
3. refinement of the segmentation using the watershed algorithm.

The two first steps are applied in the two modalities.

3.4.2 Selection of the "seed point"

The interaction consists for the user (the physician) in defining a "seed point" in the tumor of interest (in both CT and PET images). This is simply done by "clicking" with the mouse on the selected point. This very reduced interaction is well accepted by the users, and even required.

The choice of this point is quite flexible. It only has to be inside the tumor, but it does not have to be centered in it or in the point of maximum intensity. The selected view for the visualization and selection of the seed point does not change the result either. Therefore there is no particular constraint for the user and the following steps are robust with respect to the location of the seed point.

3.4.3 Rough segmentation using a region growing algorithm

Next, the selected point is used as the input to a relaxation region growing algorithm [Adams and Bischof, 1994 ; Chang and Li, 1994] to segment the tumors. It is applied separately in CT and in PET.

The criteria for region growing are homogeneity (similar grey-levels) and adjacency. In the relaxation region growing approach, we include in the resulting region the neighboring (adjacent) voxels that do not have very different local histograms. Let s be the seed point and h_s its local histogram in a window of size $3 \times 3 \times 3$ voxels, considered as a vector. The similarity between the local histogram of s and the one of a neighbor p is defined by

$S(h_p, h_s) = \frac{h_p \cdot h_s}{||h_p|| \cdot ||h_s||}$ and is a value between 0 and 1. Thus we can define a region Z_s with a threshold T_0 (quite low) for the similarity, $Z_s = \{p,\ S(h_p, h_s) > T_0\}$. We define inside this region another connected region where the similarity between voxels and the seed point is higher ($T_1 > T_0$): $Z_{ref} = \{p,\ S(h_p, h_s) > T_1\}$. This is the reference region and the histogram of this region is the reference histogram, h_{ref}. Finally, in order to obtain the final region, we compute the similarity between the reference histogram and the histogram of the voxels inside Z_s with a new threshold T_2 ($T_1 > T_2 > T_0$): $Z_{final} = \{p,\ S(h_p, h_{ref}) > T_2\}$. This region is a connected region around the seed point s and it contains the reference region Z_{ref} and the points whose histograms are the closest to the reference histogram h_{ref}. This is illustrated in Figure 3.30.

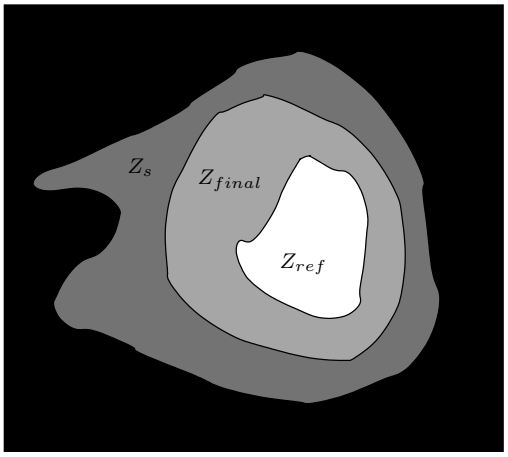

Figure 3.30: Scheme of the computed regions with the region growing algorithm.

The homogeneity properties are defined by the type of imaging modality and we have defined them empirically as follows:

- in CT: $T_0 = 0.2$, $T_1 = 0.7$, $T_2 = 0.5$;
- in PET: $T_0 = 0.2$, $T_1 = 0.9$, $T_2 = 0.7$.

In the case of isolated tumors, the region growing algorithm provides very satisfactory results. However, when the tumor is close to the walls of the lungs or other structures such as bronchi, the diaphragm or the liver which have similar grey levels in CT, or the heart in PET, the region growing algorithm includes all these regions in the segmentation as illustrated in Figures 3.31 and 3.32.

3.4.4 Correction of the segmentation using watershed

In order to improve the robustness of the region growing algorithm, we separate the tumor from spurious external parts using watershed algorithm [Vincent and Soille, 1991].

The assumption is that the tumor is connected to the other structures by a narrower path. This assumption is valid in most of the images we have. This refinement is illustrated in Figure 3.33 and it has the following steps:

- We calculate the distance function to the complementary of the region growing result and we invert the resulting distance function. The narrow path now contains local maxima of this distance function.

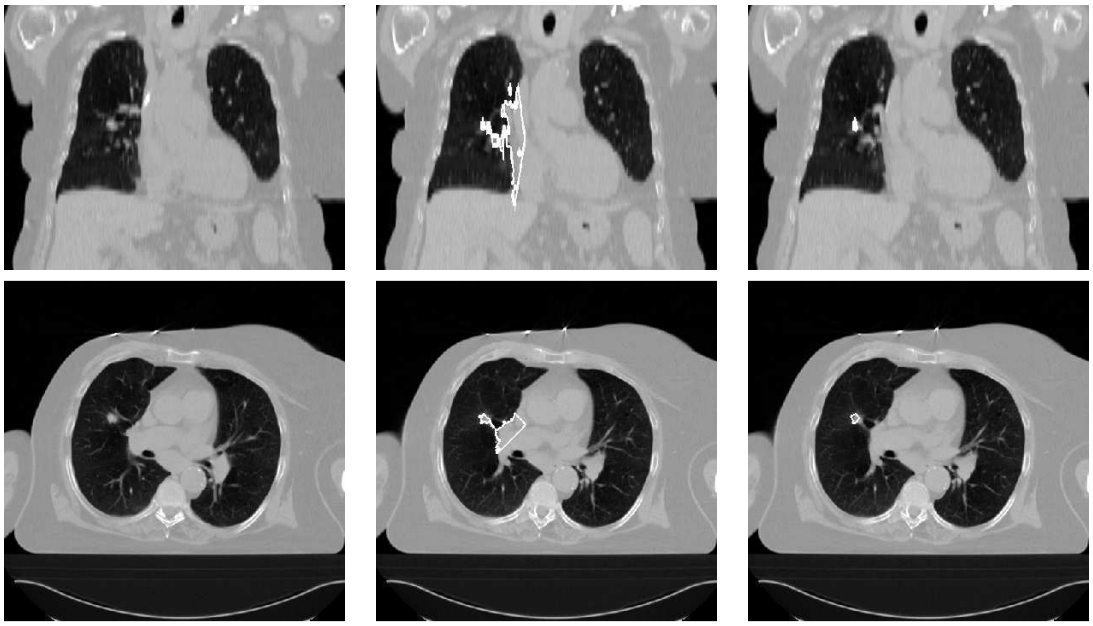

(a) (b) (c)

Figure 3.31: Coronal and axial views of an original CT image (a), the superimposition of the original CT with the contours of the segmented tumor after the region growing algorithm (b) and after the post-processing with the watershed (c). Without the post-processing some bronchi and parts of the mediastinum are included in the segmentation.

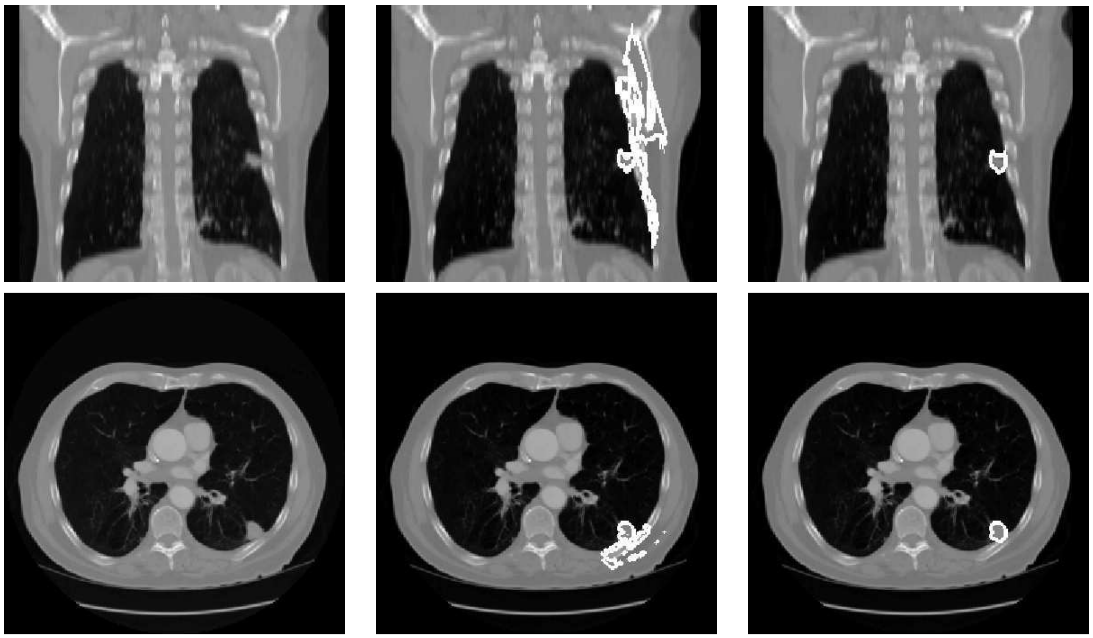

(a) (b) (c)

Figure 3.32: Coronal and axial views of an original CT image (a), the superimposition of the original CT with the contours of the segmented tumor after the region growing algorithm (b) and after the post-processing with the watershed (c). Without the post-processing the region growing algorithm includes in the tumor segmentation some parts of the wall of the lung and other structures.

- We apply the watershed algorithm to this inverted distance function. A separation through the narrow path is obtained.
- We choose the component that contains the initial seed point.

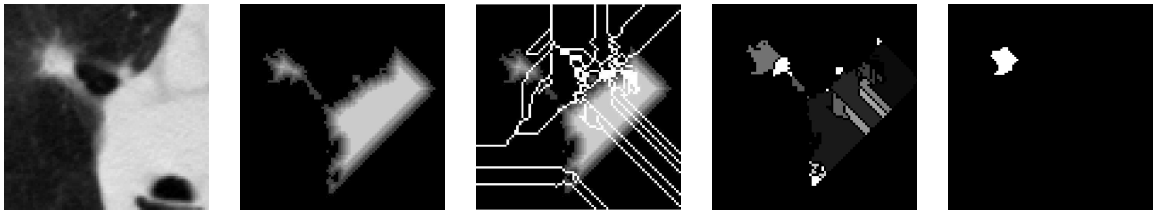

(a) (b) (c) (d) (e)

Figure 3.33: Illustration of the refinement algorithm: (a) detail of the original CT image, (b) distance function to the complementary of the rough segmentation, (c) result of the watershed on the inverted distance function (superimposed on the distance function), (d) components separated by the watershed and included in the rough segmentation, (e) final segmentation (selected component).

3.4.5 Results

We have applied our algorithm for tumor segmentation on 17 tumors from 16 different cases of CT and PET images. The sizes of the CT images are $512 \times 512 \times Z$ voxels with Z varying from 62 to 122 and the resolution is typically around $1 \times 1 \times dz$ mm^3 for the three directions of the space, with dz varying from 4 to 6.5 mm. The sizes of the PET images are $X \times Y \times Z$ voxels with X and Y equal to 128 or 144, and Z varying from 66 to 197 and the resolution is typically around $4 \times 4 \times 4$ mm^3 for the three directions.

Figures 3.34 and 3.35 show the segmentation of the tumor in PET corresponding to the patients in Figures 3.31 and 3.32 respectively. These results have been computed without the refinement step, which is often not necessary in PET.

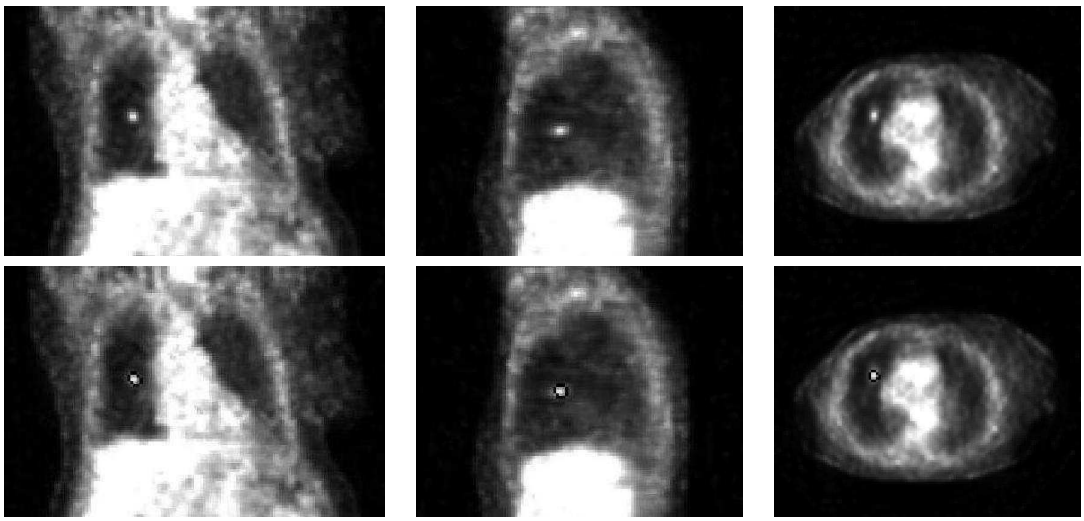

Figure 3.34: Coronal (left), sagittal (middle) and axial views (right) of an original PET image including a tumor in the right lung (top) and superimposition of the original PET with the contours of the segmented tumor in black (bottom). The corresponding CT image is shown in Figure 3.31.

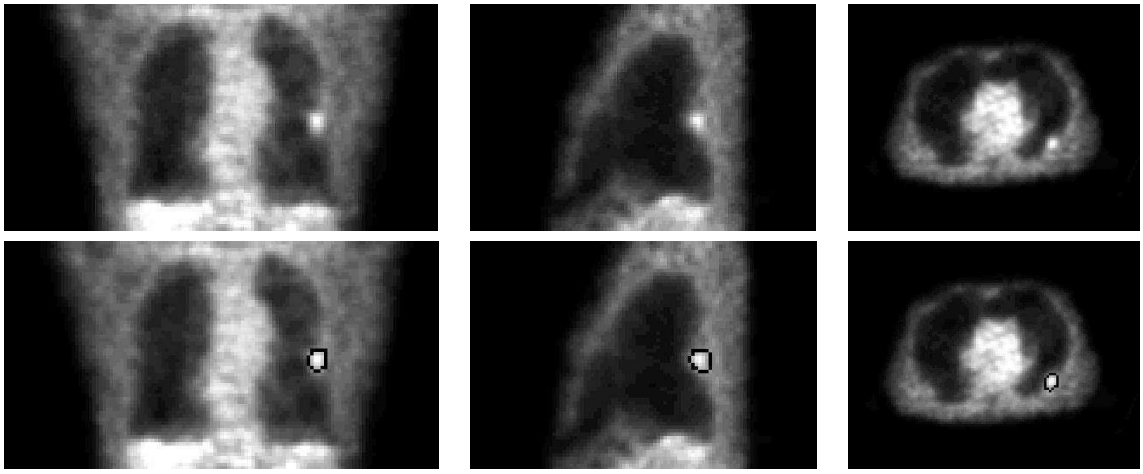

Figure 3.35: Coronal (left), sagittal (middle) and axial views (right) of an original PET image including a tumor in the left lung near the wall of the lung (top) and superimposition of the original PET with the contours of the segmented tumor in black (bottom). The corresponding CT image is shown in Figure 3.32.

Figures 3.36, 3.37 and 3.38 illustrate some other results of the final tumor segmentation in CT and PET for different patients. Table 3.7 summarizes the results obtained for the 17 processed tumors. The incomplete or incorrect results correspond to tumors with a very important size and/or with a necrosis, as the example illustrated in Figure 3.39.

	CT	PET
Correct results	59 %	53 %
Incomplete results	17.5 %	47 %
Incorrect results	23.5 %	0 %

Table 3.7: Percentage of correct and incomplete results for the segmented tumors.

3.4.6 Conclusions and future work

The proposed method segments correctly tumors in CT and in PET images. The fact of adding a semi-interactive stage is not a disadvantage because physicians prefer to control this crucial step. Moreover, with a simple gesture, the algorithm benefits from medical and expert knowledge. The proposed algorithm has been tested on 16 pairs of CT and PET images with good results for most cases even when the tumor is in contact with other structures of similar intensity (cf. Figures 3.35 and 3.36).

A validation on a larger data base in necessary in order to verify the robustness of our approach, in particular when the tumors are in contact with the walls of the lungs, when they are of an important size or contain a necrosis. For these cases the proposed algorithm is not accurate enough in some cases. The "rolling ball" algorithm proposed by [Armato III and Sensakovic, 2004] for lung segmentation refinement, could be used to improve juxtapleural tumor segmentation. Although the problem of big tumors will probably remain. The validation of the results can be performed via a comparison with manual segmentations (as in Section 3.3). However, as our registration method is robust to small errors in tumor

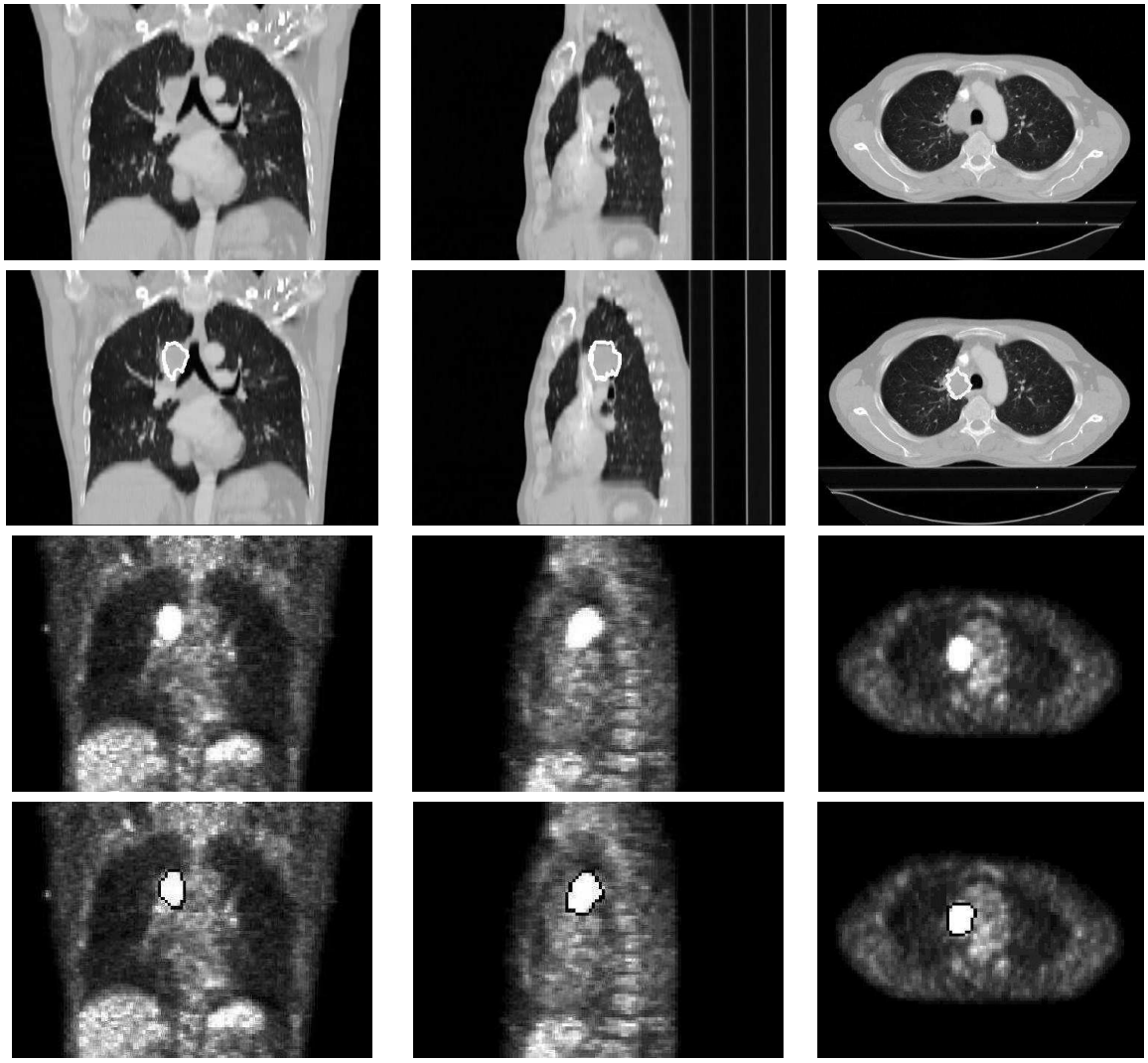

Figure 3.36: Original CT image including a tumor near the oesophagus (top row) and the corresponding PET image (third row). The results of the tumor segmentation are shown in second and bottom rows. This example shows that our algorithm for segmenting tumors is robust even in difficult cases.

segmentation (see Chapter 4), the method described here is sufficient in most cases for our specific case.

Future work could aim at reducing the two seed points (one in CT and one in PET) to only one. The selected point in one of the modalities could be used to initialize the region growing algorithm for both CT and PET images if they are appropriately registered. However, even if PET/CT combined machines furnish linearly registered exams, one point selected inside the tumor in PET is not guaranteed to be inside the tumor in CT, due to the effect of breathing. Anyway, a larger region could be defined to look for a maximum of intensity and thus find an adapted seed point. The breathing model described in Chapter 5 could also help to find this second seed point using the trajectories of the points inside the lungs but at the price of higher computation cost. Moreover, as the segmentation of a tumor in PET is relatively easy, we could conceive a fully-automatic method that segments automatically the tumor in PET and then uses it to segment the tumor in CT.

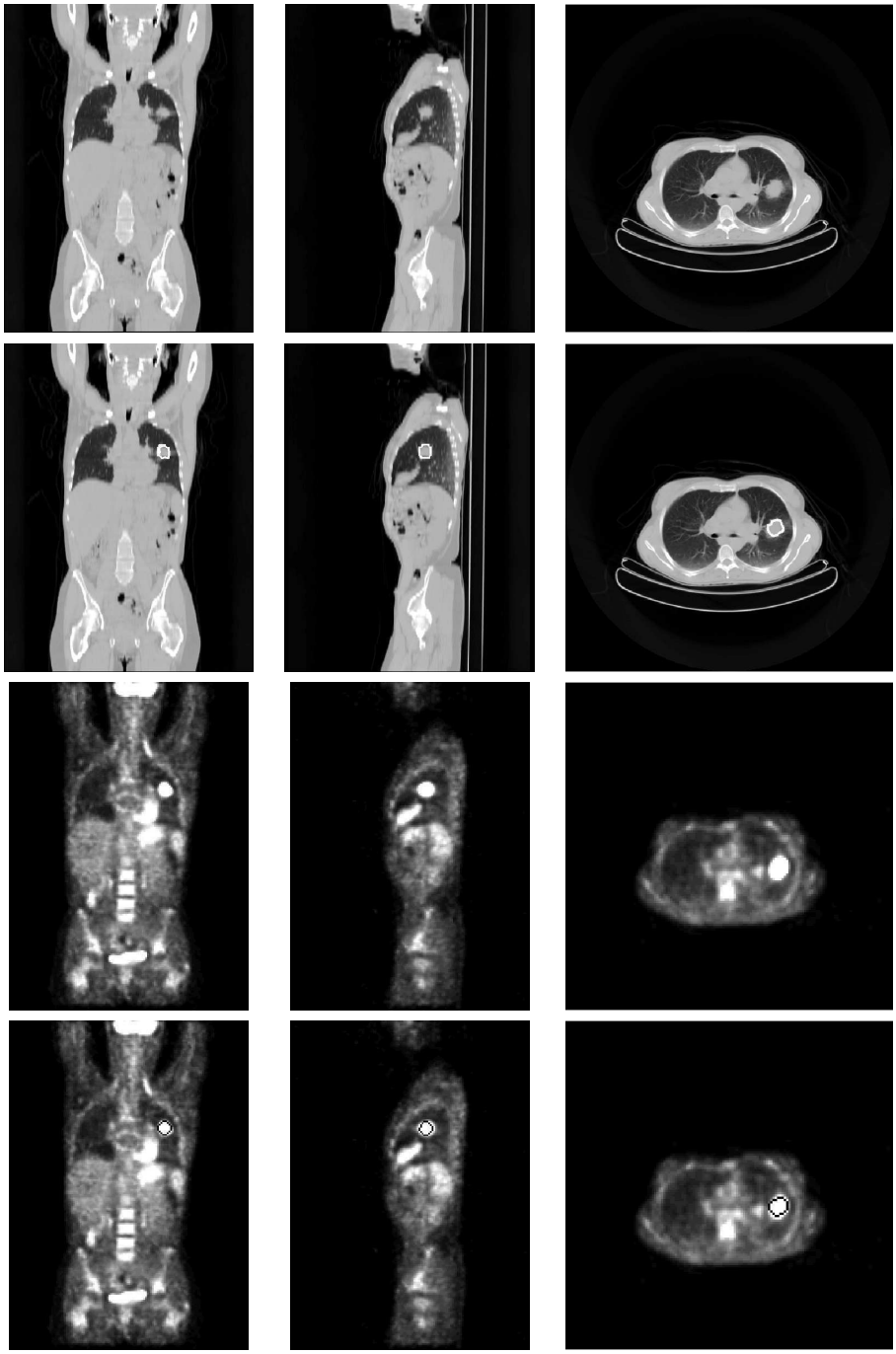

Figure 3.37: Original CT image including a tumor in the left lung (top row) and the corresponding PET image (third row). The results of the tumor segmentation are shown in second and bottom rows.

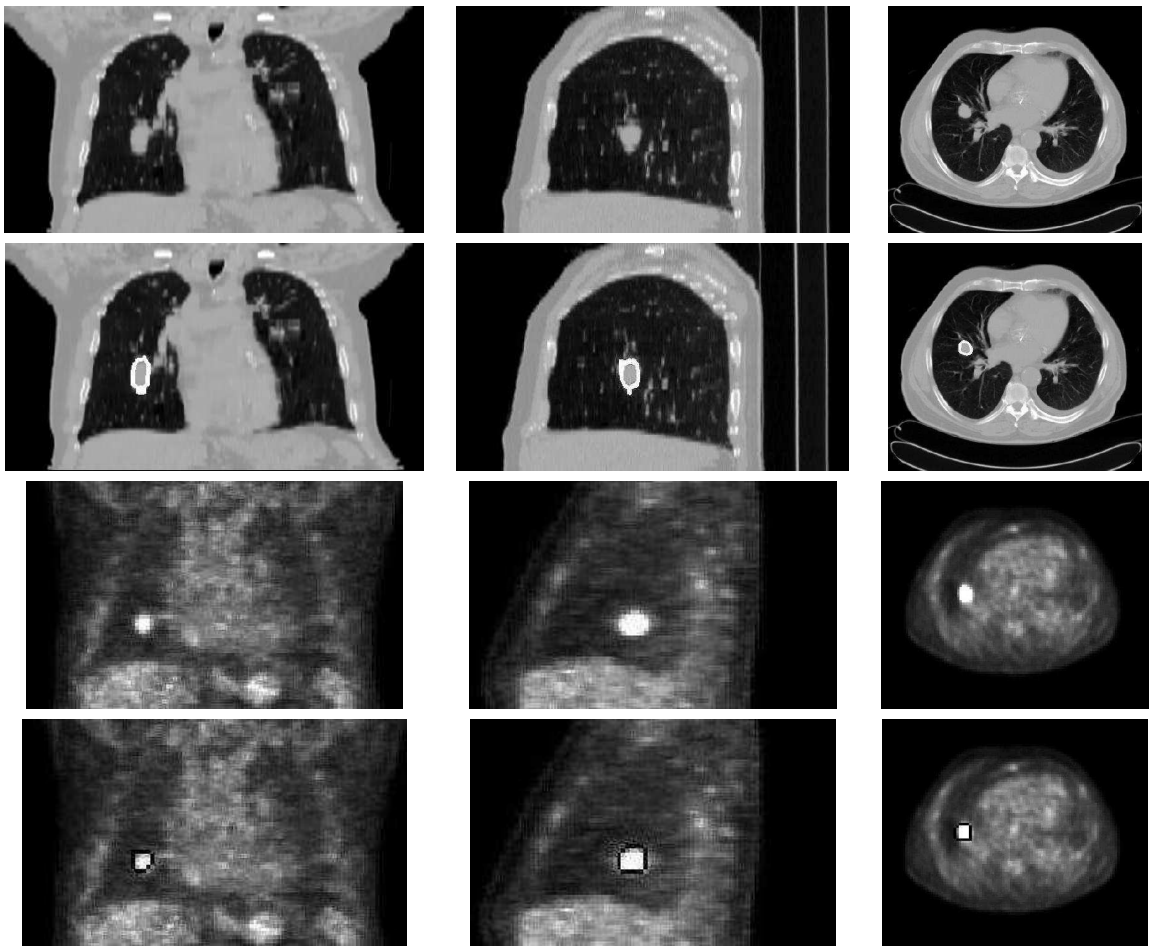

Figure 3.38: Original CT image including a tumor in the right lung (top row) and the corresponding PET image (third row). The results of the tumor segmentation are shown in second and bottom rows.

Finally, the lung segmentation computed using the procedure introduced in Section 3.2 is refined by the results of tumor segmentation as explained in next section.

3.5 Refinement of lung segmentation using segmented tumors

The segmentation of the lungs in CT and PET images is achieved using the procedure introduced in Section 3.2. In images where the tumors are located close to the walls of the lungs, the result of lung segmentation does not include these tumors as parts of the lungs. They are erroneously considered as external tissues. For this reason, we have used the tumor segmentation results in order to refine the segmentation of the lungs.

The processing consists in computing the union of lungs and tumor followed by a hole filling in 3D (in order to close small holes between the tumor and the segmented lung). An example of partial and final results of this processing on a CT image is illustrated in Figure 3.40 on the patient previously shown in Figure 3.32.

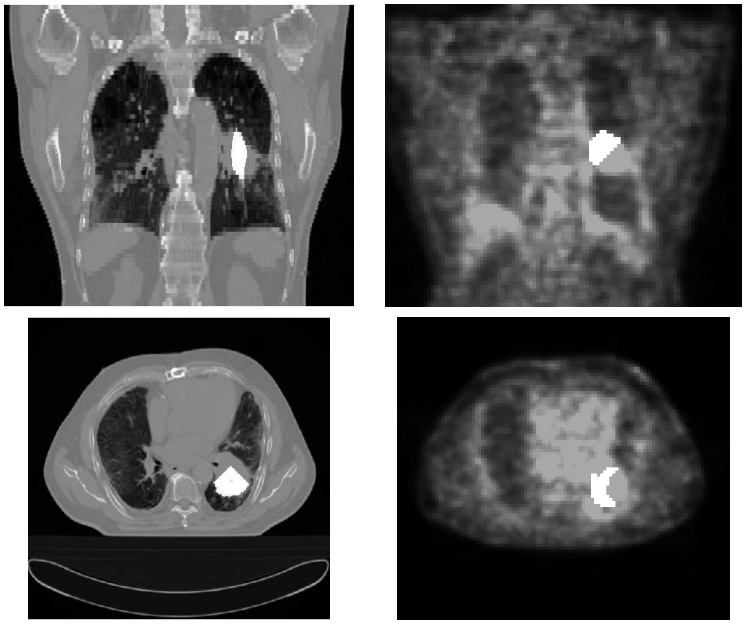

Figure 3.39: Coronal (top row) and axial (bottom row) of the superimposition of one CT and one PET image with the result of the segmentation of a tumor (in white). In this case the tumor has a very important size and it has not been completely segmented.

(a) (b) (c)

Figure 3.40: Axial views of an example of the refinement of lung segmentation with tumor segmentation. The contours of different segmentation results are superimposed on the original CT image: (a) the initial segmentation of the lungs, (b) the segmentation of the tumor close to the wall of the lungs and (c) the final refined segmentation.

3.6 Conclusion

In this chapter, we have described the segmentation of different structures of the body.

First, the methods used for segmenting the contour of the body, the lungs, the skeleton, the kidneys and the liver in CT and PET have been summarized. All the segmentation algorithms integrate *anatomical knowledge* in order to improve the robustness and/or to guide the segmentation itself. For instance, anatomical knowledge about the *relative positions* of the organs is introduced in order to guide the segmentation. The *consistency tests* also include anatomical knowledge in order to detect potential errors and repair them. The

segmentation algorithms for the body, the lungs and the skeleton are robust and they furnish satisfactory results for images coming from different patients and different medical centers. However, the most challenging task is the segmentation of the lungs in PET when the transmission PET image is not available and the exam has not been acquired with a combined CT/PET device. The segmentation of the kidneys and the liver has not been generalized to guarantee robust results for any patient. This can be implemented by adding consistency tests as for the other structures.

We have also explained our original approach to segment the heart in non-contrast CT images in a robust manner. This method uses *fuzzy structural knowledge* expressed as *spatial relations* to define the region of interest of the heart and then to define a new external force that is introduced in the evolution scheme of a deformable model. The results have been evaluated by comparing them with segmentations of the heart carried out manually by an expert, which shows the accuracy attained with our approach. The preliminary quantitative results show a strong agreement between the manual segmentations and the ones obtained by our approach, and confirm the potential of the proposed method.

The proposed semi-interactive method for tumor segmentation furnishes correct results in CT and in PET images. The fact of adding a semi-interactive stage is not a disadvantage because physicians prefer to control this crucial step. Moreover, with a simple gesture, the algorithm benefits from *medical and expert knowledge*. A validation on a larger data base in necessary in order to verify the robustness of our approach, in particular when the tumors are in contact with the walls of the lungs. Tumor segmentation is necessary in our approach in order to introduce constraints that guarantee relevant deformations and improve non-linear registration between anatomical and functional images. This is detailed in Chapter 4.

Finally, we have described and illustrated the refinement of lung segmentation using the segmented tumors. This step furnishes the final results for the segmentation of the lungs.

CHAPTER 4

Deformations with rigidity constraints

As introduced in Chapter 1, registration of CT and PET thoracic images has to cope with deformations of the lungs during breathing. One way to take into account respiration movements is to employ a landmark-based transformation where landmarks correspond to anatomical points of interest. Moreover, our aim is to better account for the influence of the tumor on the transformation. Potential tumors in the lungs usually do not follow the same deformations as the other structures, since they can be considered as almost rigid. We show in this chapter how to introduce rigidity constraints into a non-linear registration method. The proposed approach is based on registration of landmarks defined on the surface of previously segmented objects and on continuity constraints. Tumors are segmented by means of a semi-automatic procedure, as detailed in Chapter 3, and they are used to guarantee relevant deformations near the pathology. At the end of this chapter, we present some first results on synthetic and real data which demonstrate a significant improvement of the combination of anatomical and functional images for diagnosis and oncology applications. A further validation and more results are discussed in Chapter 6.

4.1 Introduction

As explained in Chapter 1, most of the existing methods have as a limitation that regions placed inside or near the main structures will be deformed more or less according to the registration computed for the latter, depending on how local is the deformation. A critical example of this situation occurs when a tumor is located inside the lungs and there is a large volume difference between CT and PET images due to the breathing. In this case, if the tumor is registered according to the transformation computed for the lungs, it may take unrealistic shapes, such as shown in Figure 1.1. In this case, two very different deformations exist: the non-linear deformations of the lungs due to the breathing and the linear displacement of the tumor during the breathing cycle. The aim of this work is to avoid undesired tumor misregistrations by adding some rigidity constraints on the tumors as illustrated in Figure 4.1. Thus, we have to account for different deformations in normal structures and in tumors, while ensuring continuity of the deformation field. Another goal is to preserve tumor geometry and, specially, intensity since it is critical for clinical applications.

The proposed registration algorithm relies on segmented structures (lungs and tumors) in order to guarantee a good registration of both normal and pathological structures. For this reason, the first step consists of a segmentation of all structures which are visible in CT and in PET. In Chapter 3, we have described the segmentation of the targeted structures,

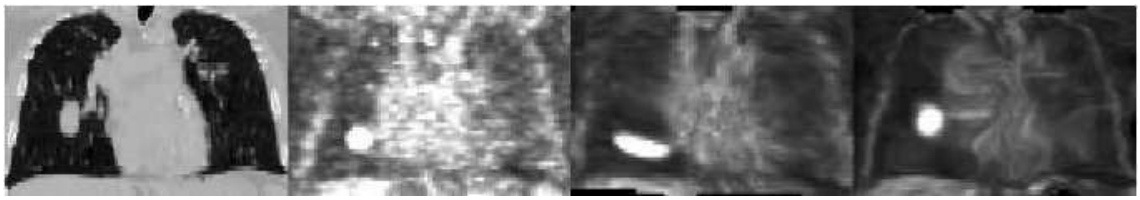

Figure 4.1: Improvement of the registration in the tumor area. From left to right: CT and PET original images; PET image registered without tumor constraints; PET image registered with tumor constraints.

i.e., the body, the lungs and the tumors. Figure 4.2 shows some results of the body contour, lungs and tumor segmentations. We introduce tumor-based constraints into the registration

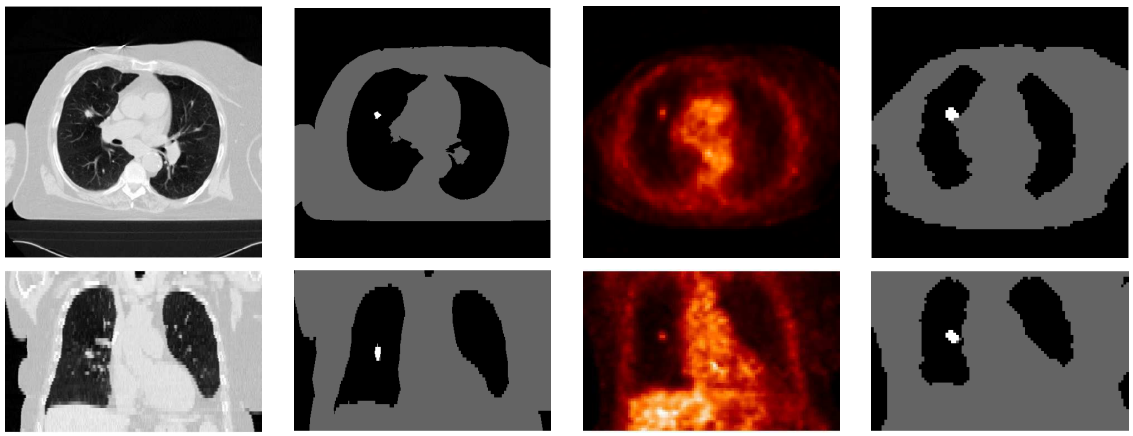

Figure 4.2: Example of some segmentation results. First and third columns: original CT and PET images (axial and coronal views). Second and fourth columns: results of the segmentation of the body contour, the lungs and the tumor in both modalities.

algorithm which is detailed in Section 4.2. Two groups of landmarks in both images, which correspond to homologous points, are defined to guide the deformation of the PET image towards the CT image. The positions of the landmarks are therefore adapted to anatomical shapes which is an important feature and one of the originalities of our method. This is detailed in Section 4.3, where we also present a brief state of the art of methods of landmark detection. The deformation at each point is computed using an interpolation procedure based on the landmarks, on the specific type of deformation of each landmark depending on the structure it belongs to, and weighted by a distance function, which guarantees that the transformation will be continuous [Moreno et al., 2005; 2006a]. In Section 4.4 we discuss the first results obtained on synthetic and real data. Finally, conclusions and future works are discussed in Section 4.5.

4.2 Combining rigid and non-linear deformations using a continuous distance function

Based on a segmentation of the objects visible in both images, pairs of homologous points are defined. They constitute landmarks guiding the registration. We assume that globally a non-linear transformation has to be found, while for some objects $O_1, \ldots, O_{n_0}$ (tumors in

our application) specific constraints have to be incorporated. In our particular case, these objects undergo only a rigid transformation between both images. The global transformation is then interpolated over the whole image. We introduce the rigid structures constraints so that the non-rigid transformation is gradually weighted down in the proximity of objects $O_1, \ldots, O_{n_0}$.

4.2.1 Point-based displacement interpolation

The first step in a point-based interpolation algorithm concerns the selection of the landmarks guiding the transformation (cf. Section 4.3). Homologous structures in both images are then registered based on landmarks defined on their surface. The resulting deformation will be exact at these landmarks and smooth elsewhere, which is achieved by interpolation.

Let us denote by $\boldsymbol{t}_i$ the n landmarks in the source image that we want to transform to new sites $\boldsymbol{u}_i$ (the homologous landmarks) in the target image.

The deformation at each point $\boldsymbol{t}$ in the image is defined as:

$$\boldsymbol{f}(\boldsymbol{t}) = \mathcal{L}(\boldsymbol{t}) + \sum_{j=1}^{n} \boldsymbol{b}_j \, \sigma(\boldsymbol{t}, \boldsymbol{t}_j) \tag{4.1}$$

under the constraints

$$\forall i, \quad \boldsymbol{u}_i = \boldsymbol{t}_i + \boldsymbol{f}(\boldsymbol{t}_i). \tag{4.2}$$

The first term, $\mathcal{L}(\boldsymbol{t})$, represents the linear transformation and the second term represents the non-linear transformation of every point $\boldsymbol{t}$ in the source image.

The linear term – When n_0 rigid objects $(O_1, O_2, \ldots, O_{n_0})$ are present, the linear term is a weighted sum of each object's linear transformation. The weights $w_i(\boldsymbol{t})$ depend on a measure of distance $d(\boldsymbol{t}, O_i)$ from the point $\boldsymbol{t}$ to the object O_i as described in [Little et al., 1997]:

$$w_i(\boldsymbol{t}) = \begin{cases} 1 \text{ if } \boldsymbol{t} \in O_i \\ 0 \text{ if } \boldsymbol{t} \in O_j, \ j = 1, \ldots, n_0, \ j \neq i \\ \frac{q_i(\boldsymbol{t})}{\sum_{j=1}^{n_0} q_j(\boldsymbol{t})} \text{ otherwise} \end{cases} \quad \text{where} \quad q_i(\boldsymbol{t}) = \frac{1}{d(\boldsymbol{t}, O_i)^{\mu}} \tag{4.3}$$

and $\mu = 1.5$ for the work illustrated here. The smoothness of the interpolation is controlled by the choice of this μ. A value of $\mu > 1$ ensures that the first derivative is continuous.

Therefore, for any point $\boldsymbol{t}$ we define our linear transformation as:

$$\mathcal{L}(\boldsymbol{t}) = \sum_{i=1}^{n_0} w_i(\boldsymbol{t}) \, L_i \tag{4.4}$$

where $L_i, \ i = 1, \ldots, n_0$ are the linear transformations of the rigid objects. The closer $\boldsymbol{t}$ is to the object O_i, the more similar its linear transformation will be to L_i.

The non-linear term – The non-linear transformation is based on a 3D[1] Thin-Plate Spline (TPS) [Bookstein, 1989]. It is, for a point $\boldsymbol{t}$, the sum of n terms, one for each

[1] In two dimensions (2D), the equivalent equation is $\sigma_{2D}(\boldsymbol{t}, \boldsymbol{t}_j) = |\boldsymbol{t} - \boldsymbol{t}_j|^2 \ln |\boldsymbol{t} - \boldsymbol{t}_j|$ which is, as in the 3D case, the fundamental solution of the biharmonic equation.

landmark. Each term is the product of the coefficients of a matrix B (that will be computed in order to satisfy the constraints on the landmarks) with a function $\sigma(\boldsymbol{t}, \boldsymbol{t}_j)$, depending on the (normalized) distance between $\boldsymbol{t}$ and $\boldsymbol{t}_j$:

$$\sigma(\boldsymbol{t}, \boldsymbol{t}_j) = |\boldsymbol{t} - \boldsymbol{t}_j|. \tag{4.5}$$

This form produces better results for image registration than other radial basis functions [Wiemker et al., 1996]. However, different functions could be used, as the one described by [Little et al., 1997].

With the constraints given by Equation 4.2, we can calculate the coefficients $\boldsymbol{b}_j$ of the non-linear term by expressing Equation 4.1 for $\boldsymbol{t} = \boldsymbol{t}_i$. The transformation can then be defined in a matricial way:

$$\Sigma B + L = U \tag{4.6}$$

where U is the matrix of the landmarks $\boldsymbol{u}_i = (u_{ix}, u_{iy}, u_{iz})$ in the target image (the constraints), $\Sigma_{ij} = \sigma(\boldsymbol{t}_i, \boldsymbol{t}_j)$ (given by Equation 4.5), B is the matrix of the coefficients of the non-linear term $\boldsymbol{b}_i = (b_{ix}, b_{iy}, b_{iz})$ and L represents the application of the linear transformations to the landmarks in the source image, $\boldsymbol{t}_i = (t_{ix}, t_{iy}, t_{iz})$:

$$\begin{pmatrix} \sigma(\boldsymbol{t}_1, \boldsymbol{t}_1) & \sigma(\boldsymbol{t}_1, \boldsymbol{t}_2) & \dots & \sigma(\boldsymbol{t}_1, \boldsymbol{t}_n) \\ \sigma(\boldsymbol{t}_2, \boldsymbol{t}_1) & \sigma(\boldsymbol{t}_2, \boldsymbol{t}_2) & \dots & \sigma(\boldsymbol{t}_2, \boldsymbol{t}_n) \\ \vdots & \vdots & \vdots & \vdots \\ \sigma(\boldsymbol{t}_n, \boldsymbol{t}_1) & \sigma(\boldsymbol{t}_n, \boldsymbol{t}_2) & \dots & \sigma(\boldsymbol{t}_n, \boldsymbol{t}_n) \end{pmatrix} \begin{pmatrix} \boldsymbol{b}_1 \\ \boldsymbol{b}_2 \\ \vdots \\ \boldsymbol{b}_n \end{pmatrix} + \begin{pmatrix} \boldsymbol{t}_1 + \mathcal{L}(\boldsymbol{t}_1) \\ \boldsymbol{t}_2 + \mathcal{L}(\boldsymbol{t}_2) \\ \vdots \\ \boldsymbol{t}_n + \mathcal{L}(\boldsymbol{t}_n) \end{pmatrix} = \begin{pmatrix} \boldsymbol{u}_1 \\ \boldsymbol{u}_2 \\ \vdots \\ \boldsymbol{u}_n \end{pmatrix} \tag{4.7}$$

From Equation 4.6, the matrix B is obtained as:

$$B = \Sigma^{-1}(U - L). \tag{4.8}$$

The inverse matrix Σ^{-1} can be computed with the Gauss-Jordan elimination algorithm for example[2]. Once the coefficients $\boldsymbol{b}_i$ of B are found, we can calculate the general interpolation solution for every point in $\mathbb{R}^3$ as shown in Equation 4.1.

4.2.2 Introducing rigid structures

In this section, we show how to introduce the constraints imposed by the rigid structures in the images.

To add the influence of the rigid structures $O_1, \dots, O_{n_0}$, we have redefined the function $\sigma(\boldsymbol{t}, \boldsymbol{t}_j)$ as $\sigma'(\boldsymbol{t}, \boldsymbol{t}_j)$ in the following way:

$$\sigma'(\boldsymbol{t}, \boldsymbol{t}_j) = d(\boldsymbol{t}, O_0)\, d(\boldsymbol{t}_j, O_0)\, \sigma(\boldsymbol{t}, \boldsymbol{t}_j) \tag{4.9}$$

where $d(\boldsymbol{t}, O_0)$ is a measure of the distance from point $\boldsymbol{t}$ to the union of rigid objects $O_0 = O_1 \cup O_2 \cup \dots \cup O_{n_0}$. It is equal to zero for $\boldsymbol{t} \in O_0$ (inside any of the rigid structures) and takes small values when $\boldsymbol{t}$ is near one of the structures. This measure of the distance is continuous over $\mathbb{R}^3$ and it weights the function $\sigma(\boldsymbol{t}, \boldsymbol{t}_j)$ (see Equation 4.5). In the digital case, this distance function d can be computed using a chamfer algorithm [Borgefors, 1986]. Thus the importance of the non-linear deformation is controlled by the distance to the rigid objects in the following manner (cf. Figure 4.3):

[2] Available in the Numerical Recipes Library [Numerical Recipes, 2007].

- $d(\boldsymbol{t}, O_0)$ makes $\sigma'(\boldsymbol{t}, \boldsymbol{t}_j)$ tend towards zero when the point for which we are calculating the transformation is close to one of the rigid objects;
- $d(\boldsymbol{t}_j, O_0)$ makes $\sigma'(\boldsymbol{t}, \boldsymbol{t}_j)$ tend towards zero when the landmark $\boldsymbol{t}_j$ is near one of the rigid objects. This means that the landmarks close to the rigid structures hardly contribute to the non-linear transformation computation;
- When both $\boldsymbol{t}$ and $\boldsymbol{t}_j$ are far from the rigid objects, then $\sigma'(\boldsymbol{t}, \boldsymbol{t}_j) \simeq \sigma(\boldsymbol{t}, \boldsymbol{t}_j) = |\boldsymbol{t} - \boldsymbol{t}_j|$.

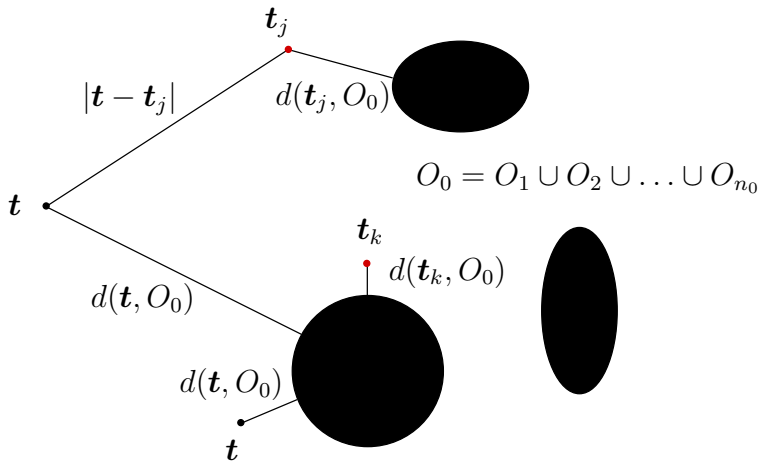

Figure 4.3: Illustration of the influence of the distance to the rigid objects in the non-linear deformation.

Note that this formalism could be more general by replacing $d(\boldsymbol{t}, O_0)$ by any function of the distance to O_0 that characterizes more accurately the behavior of the surrounding regions. Further research is necessary to define such a function in the case of lung tumors. We have used a linear (normalized) distance function as a first approach.

Finally, Equation 4.6 is rewritten by replacing Σ by Σ', leading to a new matrix B'. We can then calculate the general interpolation solution for every voxel in the images as in Equation 4.1.

4.3 Definition of landmarks and matching

"Landmarks" are points of the images with specific characteristics which make of them interesting for a particular task. In the literature these points are called *points of interest*, *dominant points*, *salient points*, *keypoints*, *features* or *landmarks*.

Landmarks can be defined according to the needs of each specific application. In particular, features selection is an important task in registration. Here, we present a brief state of the art of methods of landmark detection and then we describe the approach we have selected. This part of the work has been carried out in collaboration with Sylvie Chambon, during her post-doc at ENST.

4.3.1 Existing methods for landmark detection based on curvature

In this work, we focus on voxel selection but more complex features can be detected [Beil et al., 1997]. The selection of the landmarks or features can be *manual*, *semi-automatic* or *automatic*.

There exist lots of works that use manual selection for the selection of landmarks [Edwards et al., 1998 ; Johnson and Christensen, 2002 ; Fischer and Modersitzki, 2003 ; Kim et al., 2003 ; West et al., 2005 ; Azar et al., 2006]. However, manual selection is tedious and time-consuming.

The authors in [Hartkens et al., 2002a] suggest that semi-automatic selection is interesting because the knowledge of experts can be integrated in an automatic process. Many of these works use the cortical sulci in order to define features in the particular case of brain imaging [Collins et al., 1998a ; Vaillant and Davatzikos, 1999 ; Hellier and Barillot, 2000 ; Cachier et al., 2001 ; Hellier and Barillot, 2003 ; Papademetris et al., 2004]. Other kind of methods combine intensity and feature information in the registration procedure [Frantz et al., 1998 ; Betke et al., 2003 ; Rohr et al., 2004 ; Matsopoulos et al., 2005 ; Wörz and Rohr, 2006] in order to benefit from the advantages of both approaches. Finally, automatic selection permits reduced execution time with high accuracy. First and second derivatives are used by [Rohr et al., 1996; 2001] for the detection of landmarks by means of the curvature. They match the landmarks based on semi-automatic extraction of anatomical point landmarks, i.e. a region of interest or an approximate position of a specific landmark –or both– is given by the user. This initialization step do not has to be very precise to obtain satisfactory results. Their method is applied to brain registration with TPS. A manual selection is combined with *a priori* knowledge in the work by [Busayarat and Zrimec, 2006], which defines a semi-automatic technique for CT-CT registration. They use ray-tracing to find the correspondences between points on the two CT images. This method is difficult to adapt to CT-PET registration because the origin of the rays, in particular, can not detected with precision in PET images.

In most of the landmark-based registration methods in medical imaging, mean and Gaussian curvatures of the surfaces to register are used. For this reason, here we mention the existing works that use curvature in order to select landmarks. Six different combinations of point selection which use curvature extrema are compared by [Beil et al., 1997]. A quantitative evaluation of nine different 3D operators is realized by [Hartkens et al., 2002b]. The compared methods also exploit first and second derivatives for the computation of different definitions of the curvature. The authors conclude that the operators based on only first order partial derivatives yield the best results. [Teh and Chin, 1989] use the "relative pertinence" which relies on curvature and other criteria. [Ansari and Delp, 1991 ; Pei and Lin, 1992] compute the curvature of the contours of 2D simple images and use a Gaussian filter. All these methods work in 2D images, keeping only the points with a high curvature along a digital curve (not on a surface). A similar approach is applied by [Fatemizadeh et al., 2003] on MRI images of the brain. Although the proposed method furnishes better results than previous similar approaches, it still remains in two dimensions and it is hardly adaptable to 3D.

4.3.2 Study of landmark detection

The landmarks can be uniformly distributed over the surface of homologous objects or they can be detected based on points having specific properties (maximum of curvature, points undergoing the largest deformations, etc). In the present work (introduced in [Chambon et al., 2007]), we suppose that points with high curvature are anatomical points of interest. Thus, our landmark selection is automatic and based on Gaussian and mean curvatures, according to the following steps:

1. compute curvature for each voxel of the lung surface;
2. sort voxels in decreasing order of absolute value of curvature;
3. select voxels based on curvature and distance criteria (detailed in the following paragraph);
4. if a uniform selection is needed, then add voxels in areas with zero-curvature, i.e. where no voxels have been considered as landmarks.

This algorithm is proposed in order to select particular voxels that provide relevant information. Moreover, we intend to obtain an approximately uniform selection to take into account the entire surface of the lungs for computing the deformation. First, in step 1 we compute the mean (H) and Gaussian (K) curvatures for the voxels on the contours of the segmented lungs with the following analytical equations [Hartkens et al., 2002b]:

$$H = \frac{1}{2|\nabla g|^3}\Big[g_x^2(g_{yy}+g_{zz}) + g_y^2(g_{xx}+g_{zz}) + g_z^2(g_{xx}+g_{yy}) \\ -2(g_x g_y g_{xy} + g_x g_z g_{xz} + g_y g_z g_{yz})\Big] \tag{4.10}$$

$$K = \frac{1}{|\nabla g|^4}\Big[g_x^2(g_{yy}g_{zz} - g_{yz}^2) + 2g_y g_z(g_{xz}g_{xy} - g_{xx}g_{yz}) + g_y^2(g_{xx}g_{zz} - g_{xz}^2) \\ +2g_x g_z(g_{yz}g_{xy} - g_{yy}g_{xz}) + g_z^2(g_{xx}g_{yy} - g_{xy}^2) + 2g_x g_y(g_{xz}g_{yz} - g_{zz}g_{xy})\Big] \tag{4.11}$$

where $g(x,y,z)$ represents the 3D image in which the landmarks have to be detected. The partial derivatives (g_x, g_y, g_z, g_{xx}, g_{xy}, g_{yz}, etc.) are computed by using finite differences of the voxels of the image. In step 3, we consider $\mathcal{V} = \{\mathbf{v}_i\}_{i=0,\ldots,N_\mathcal{S}}$, the set of voxels in decreasing order of absolute value of curvature, where $N_\mathcal{S}$ is the number of voxels of the surface and $\mathcal{V}_\mathcal{L} = \{\mathbf{v}_{\mathcal{L}i}\}_{i=0,\ldots,N_\mathcal{L}}$, the set of landmarks, where $N_\mathcal{L}$ is the number of landmarks. For each voxel $\mathbf{v}_i \in \mathcal{V}$ (for $i = 0$ to $N_\mathcal{S}$) with non-zero-curvature, we add $\mathbf{v}_i$ in $\mathcal{V}_\mathcal{L}$, if $\forall\ \mathbf{v}_j \in \mathcal{V}_\mathcal{L}$, $d_g(\mathbf{v}_i, \mathbf{v}_j) > T$ where d_g is the geodesic distance on the lung surface and T is a threshold to be chosen. The geodesic distance is computed by propagation using a chamfer algorithm conditionally to the surface. This method is similar to Dijkstra algorithm which allows to find the shortest path between two points. We only take into account the voxels on the surface of the lungs and the connectivity used for propagation includes voxels in a $3 \times 3 \times 3$ neighborhood of the processed voxel [Klette and Rosenfeld, 2004, p. 129]. With this selection process, some regions (the flattest) may contain no landmark, hence the addition of step 4: for each voxel on the surface of the lung $\mathbf{v}_i \in \mathcal{V}$ with zero-curvature, if there is no voxel $\mathbf{v}_j \in \mathcal{V}_\mathcal{L}$ with $d_g(\mathbf{v}_i, \mathbf{v}_j) < T$, we add $\mathbf{v}_i$ in $\mathcal{V}_\mathcal{L}$.

Four variants are tested:

1. Mea – Mean curvature without uniform selection;
2. Gau – Gaussian curvature without uniform selection;
3. Mea-Gau – Using mean and Gaussian curvature without uniform selection;
4. Mea-Gau-Uni – Using mean and Gaussian curvature with uniform selection.

When mean and Gaussian curvatures are employed (methods Mea-Gau and Mea-Gau-Uni), the set $\mathcal{V}$ merges the set of voxels in decreasing order of mean curvature and the set of voxels in decreasing order of Gaussian curvature, by taking alternatively a value in each set. If curvature is equal to zero, the point is not selected. With this merging, neither mean nor Gaussian curvature are favored. These strategies for landmark point selection are compared in Figure 4.4. Results given by the Mea and Gau methods are different, and it is interesting to combine them (see the results obtained with the Mea-Gau method). The Mea-Gau-Uni method permits to add some points in locally flat regions (see Figure 4.4).

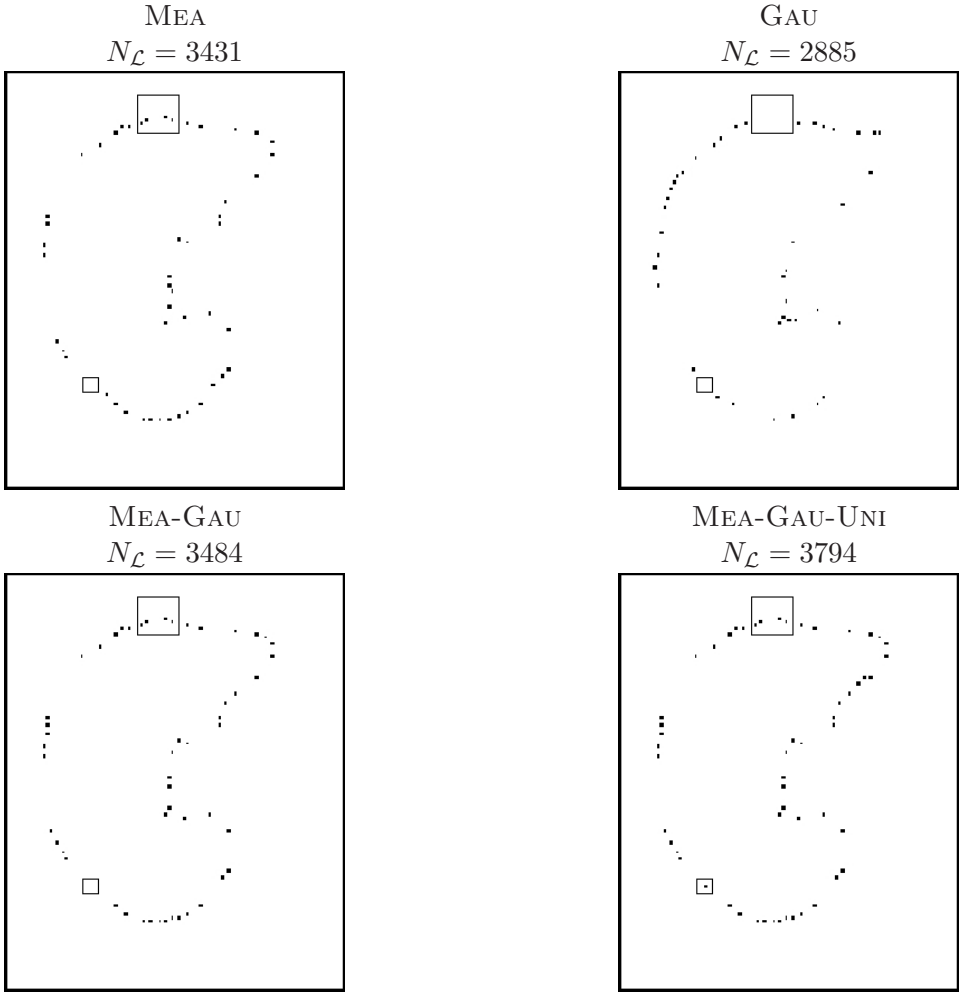

Figure 4.4: Selection of landmarks – In each image, the same regions are highlighted in small rectangles (and respectively in large rectangles). In the large rectangle, there is no landmark with Gau method whereas there are four landmarks with the Mea method. In the fusion method (Mea-Gau), these landmarks are selected. In the small rectangle, no landmark is selected with the mean and/or the Gaussian curvatures. However, a landmark is added in this area with the Mea-Gau-Uni method.

In our application, as detailed above, we first define a set of landmarks on the surface of the lungs on the CT image, because it has a much better resolution than the PET image. Then, we calculate the corresponding points on the surface of the segmented lungs in PET.

This is automatically computed by using the Iterative Closest Point (ICP) algorithm [Besl and McKay, 1992] which avoids defining by hand the landmarks on both images.

4.4 Results

We present in this section some results that we have obtained on synthetic, segmented and real images. The structures and the tumors are segmented using the methods detailed in Chapter 3 and then, based on pairs of corresponding landmarks in the CT and the PET images, the transformation is computed over the whole image. For the synthetic and segmented images, we show here the results obtained by applying the direct transformation in order to better appreciate the influence of the deformation in every region of the image and no interpolation is applied on the result. However it is clear that the final result should be based on the computation of the inverse transformation at each point of the result image in order to avoid unassigned points. For the computation of the inverse transformation, an approach similar to the one described in Section 4.2 can be adapted by exchanging the roles of $\boldsymbol{u}_i$ and $\boldsymbol{t}_i$.

As mentioned in Chapter 1, it is reasonable to assume a rigid transformation between the tumors in CT and in PET. As a first approach, we have used a translation. Each translation $L_i,\ i = 1, \ldots, n_0$ is directly obtained from the segmentation results.

4.4.1 Synthetic images

This first experiment on synthetic images aims at checking that the rigid structures are transformed rigidly, that the landmarks are correctly translated too and, finally, that the transformation elsewhere is consistent and smooth.

As we are taking the PET image as the one to be deformed (source image), we simulate an expansive transformation because the lungs in PET are usually smaller than in CT images. This is due to the fact that the CT image is often acquired in maximal inspiration of the patient. The effect of a compression is also illustrated in Figures 4.5 and 4.7. A simple translation of the "tumor" is simulated too. In order to observe the transformation all over the image, we have plotted a grid on it. It can be seen in Figure 4.5 that the results with the synthetic images are satisfactory as the shape of the rigid structure (the "tumor") is conserved and the landmarks are translated correctly. The frame, on which the landmarks are placed, is deformed in a continuous and smooth way.

If we do not apply the constraints on the rigid structure we obtain an undesired transformation as illustrated in Figure 4.6 (the tumor is expanded).

However, it must be noticed that the edges of the frame are not totally straight after the transformation. This is more clear in the results in Figure 4.7 where a lower number of landmarks has been used to compute the transformation. In general, the more landmarks we have, the better the result will be, and the positions of the landmarks are also very important. Here we have chosen to distribute them more or less uniformly over the internal and external edges of the frame.

The algorithm has also been tested on 3D synthetic images with similar results. This is illustrated with an example including three "tumors" in Figure 4.8.

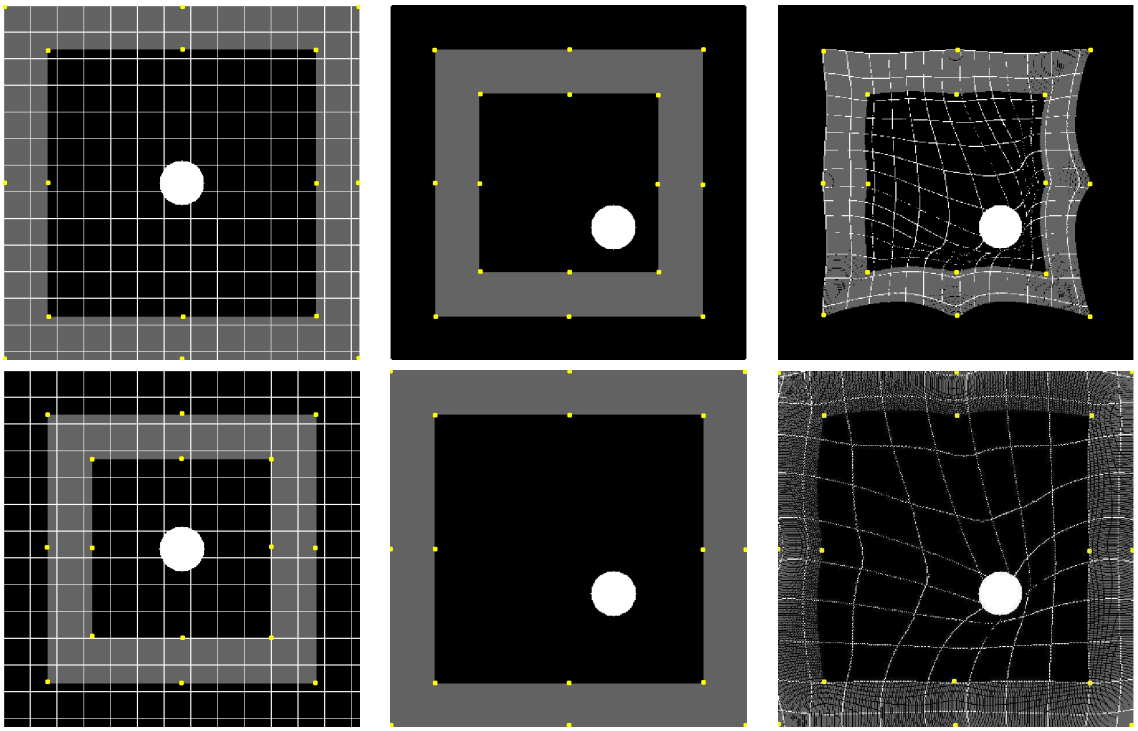

Figure 4.5: Result on synthetic images. Top row: the effect of shrinking a frame (in grey in the figure) and translating the "tumor" (in white in the figure). Bottom row: the effect of expanding a frame and translating the "tumor". The source image (with a grid) is shown on the left, the target image is in the middle and the result of the transformation on the right. The landmarks are located on the internal and external edges of the frame in grey (on the corners and in the middle of the sides –in yellow–). The total number of landmarks is 16 in both examples.

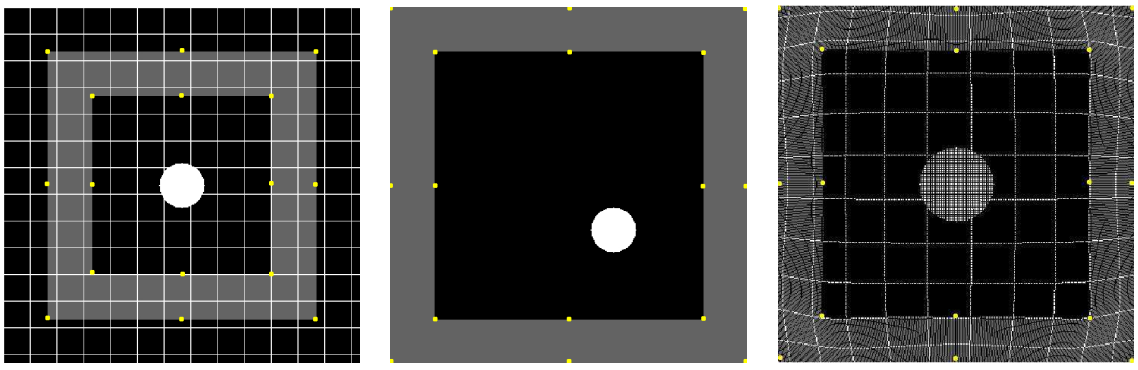

Figure 4.6: Result on a synthetic image without constraints on the rigid structure when we apply an expansion to the frame using 16 landmarks. Source image (with a grid) is shown on the left, target image is in the middle and the result of the transformation on the right.

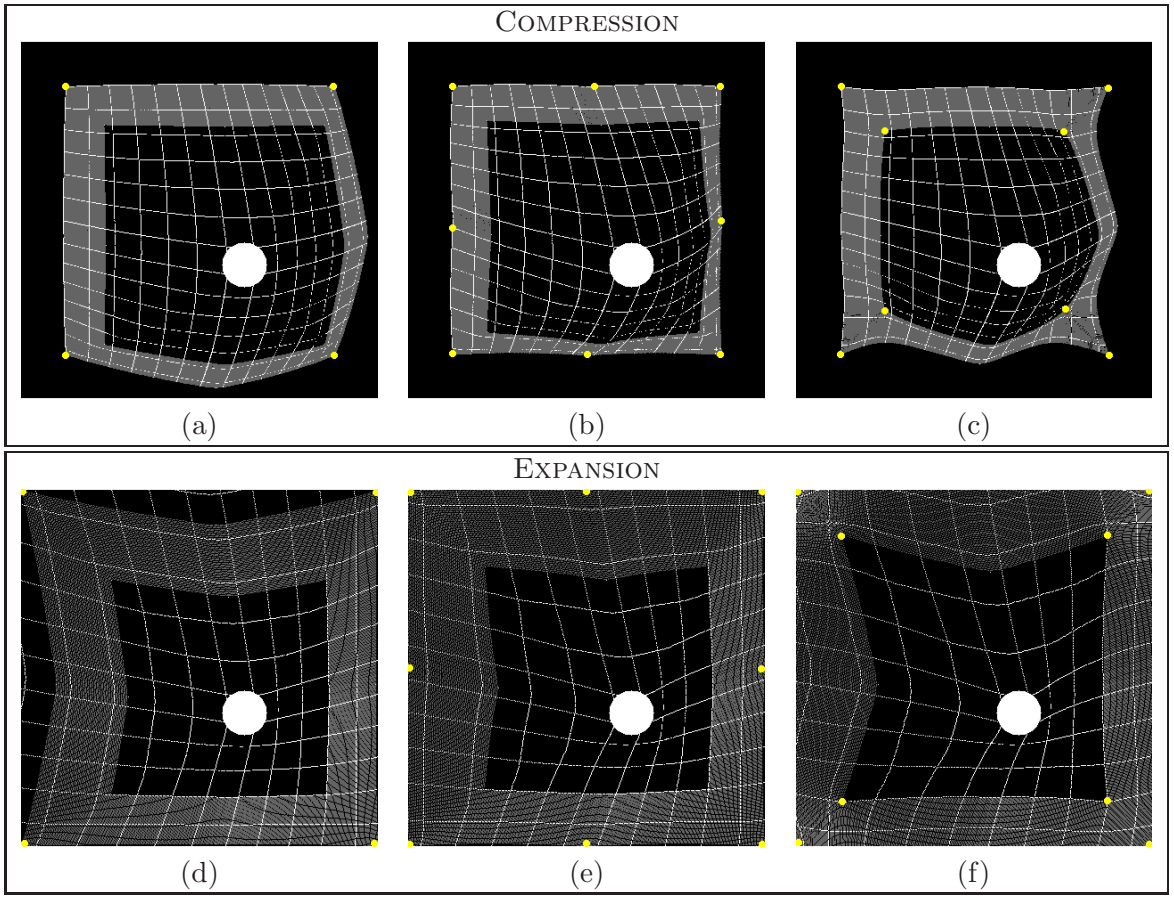

Figure 4.7: More registration results on synthetic images when shrinking (a-c) and expanding a frame (d-f). The registration is computed using 4 landmarks in (a) and (d), 8 landmarks on the external edge of the grey frame in (b) and (e), and 8 landmarks on the internal and external corners of the grey frame in (c) and (f).

4.4.2 Segmented images

In order to appreciate more clearly the effect of the transformation, we have applied the proposed approach on segmented images. They are not only useful to analyze the deformation but it is also easier to define the landmarks on them. Figure 4.9 shows some results on the segmented images. A grid is superimposed on the segmented PET image for better visualization. We have fixed the corners of the images to avoid undesired deformations (see Figure 4.10).

It can be observed that for any number of landmarks, the tumor is registered correctly with a rigid transformation. Nevertheless, the quality of the result depends on the quantity and the positions of the landmarks. If the number of landmarks is too low or their distribution on the surfaces is not appropriate, the algorithm does not have enough constraints to find the desired transformation.

4.4.3 Real images

Figure 4.11 shows the results on real images. As with the segmented images, we have to fix the corners of the images to avoid misregistrations. The tumor is registered correctly with a rigid transformation in all the cases. However, the accuracy of the registration depends on the

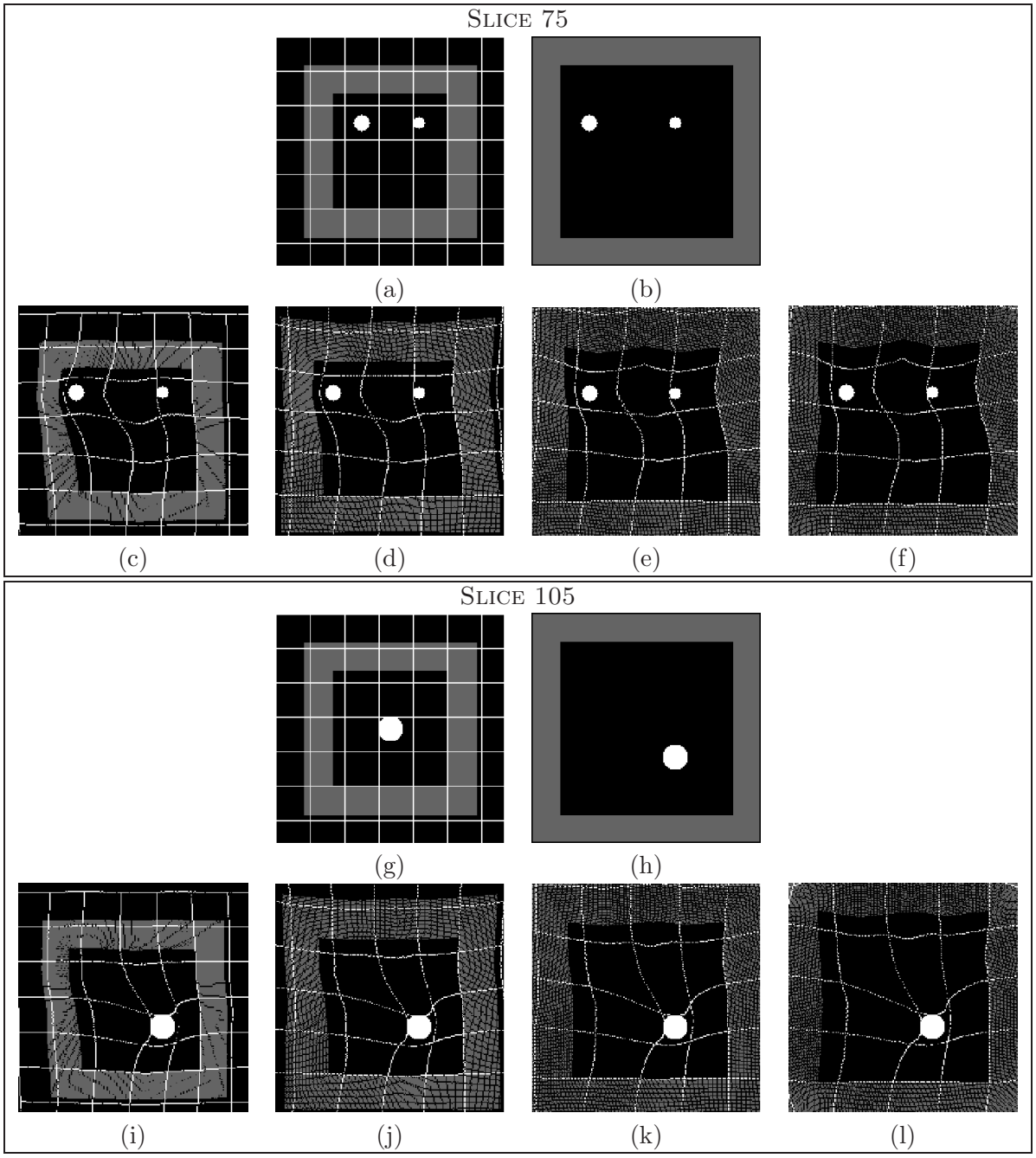

Figure 4.8: Results of registration on 3D synthetic images including three rigid structures. The results are shown on two different slices of the volumes. (a) and (g) correspond to the source image (with a grid), and (b) and (h) to the target image. (c-f) and (i-l) are the results of the transformation with 0, 8, 16 and 40 landmarks respectively. The landmarks are placed on the corners and on the middle of the edges of the grey 3D frame (not in the selected slices).

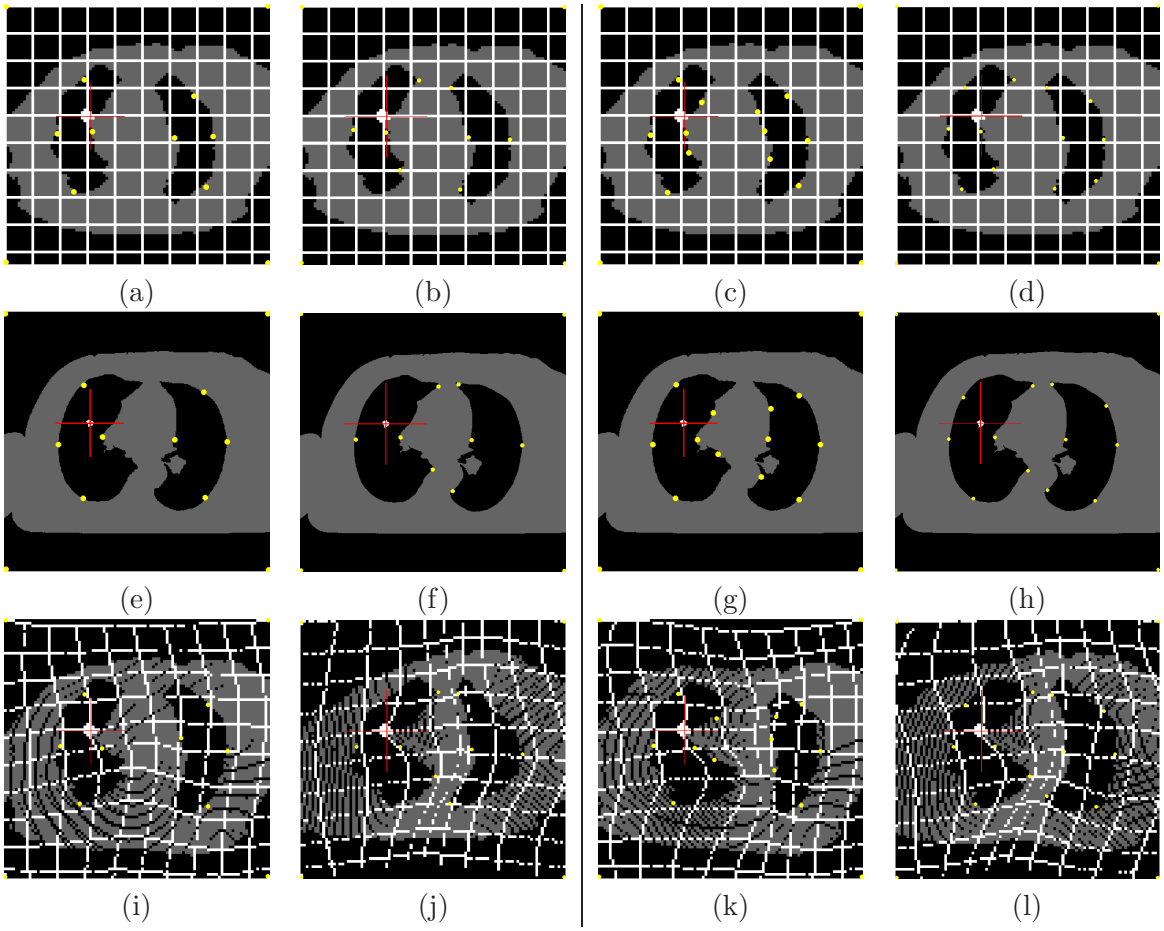

Figure 4.9: Results on segmented images. (a-d) Segmented PET images with a grid for visualization purpose (landmarks are also marked in yellow). (e-h) Segmented CT images. (i-l) Results of the registration of the segmented PET and CT images using 4 landmarks (fixed on the corners of the image) and additional landmarks on the walls of the lungs. (i) and (j): 8 landmarks are chosen on the walls of the lungs using different distributions. (k) and (l): 12 landmarks are chosen on the walls of the lungs using different distributions. In all the images the cursor is centered on the tumor in the CT image.

number and the distribution of the landmarks. If the number of landmarks is not sufficient there are errors. It can be seen that with an appropriate number of landmarks the registration is very satisfactory. The best results (Figure 4.11(d)) are obtained with 16 landmarks placed as in Figure 4.9(l). In particular, they include high curvature points. The lower part of the lungs is better registered and the walls of the lungs are perfectly superimposed. The results are considerably improved using 16 landmarks, compared to those obtained with 12 or less landmarks. This shows that the minimal number of landmarks does not need to be very large if the landmarks are correctly distributed, i.e. if they are located on the points that suffer the most important deformations. For instance, the results are better with 16 landmarks in Figure 4.11(d) than with the same number of landmarks in Figure 4.11(c). This example highlights the influence of the positions of the landmarks. We only show here the results on bi-dimensional images for the sake of simplicity. In Chapter 6 we show some results in 3D.

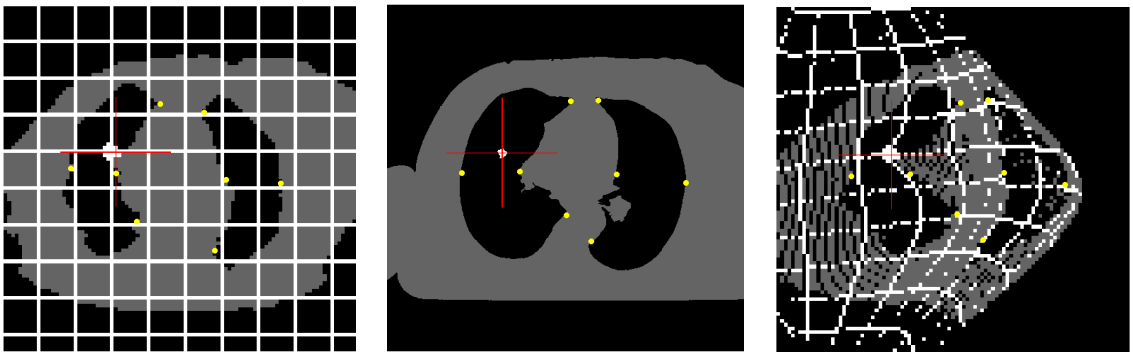

Figure 4.10: Result on the segmented images. This is the kind of result we obtain if we do not fix the corners of the image. Here we have only 8 landmarks on the walls of the lungs.

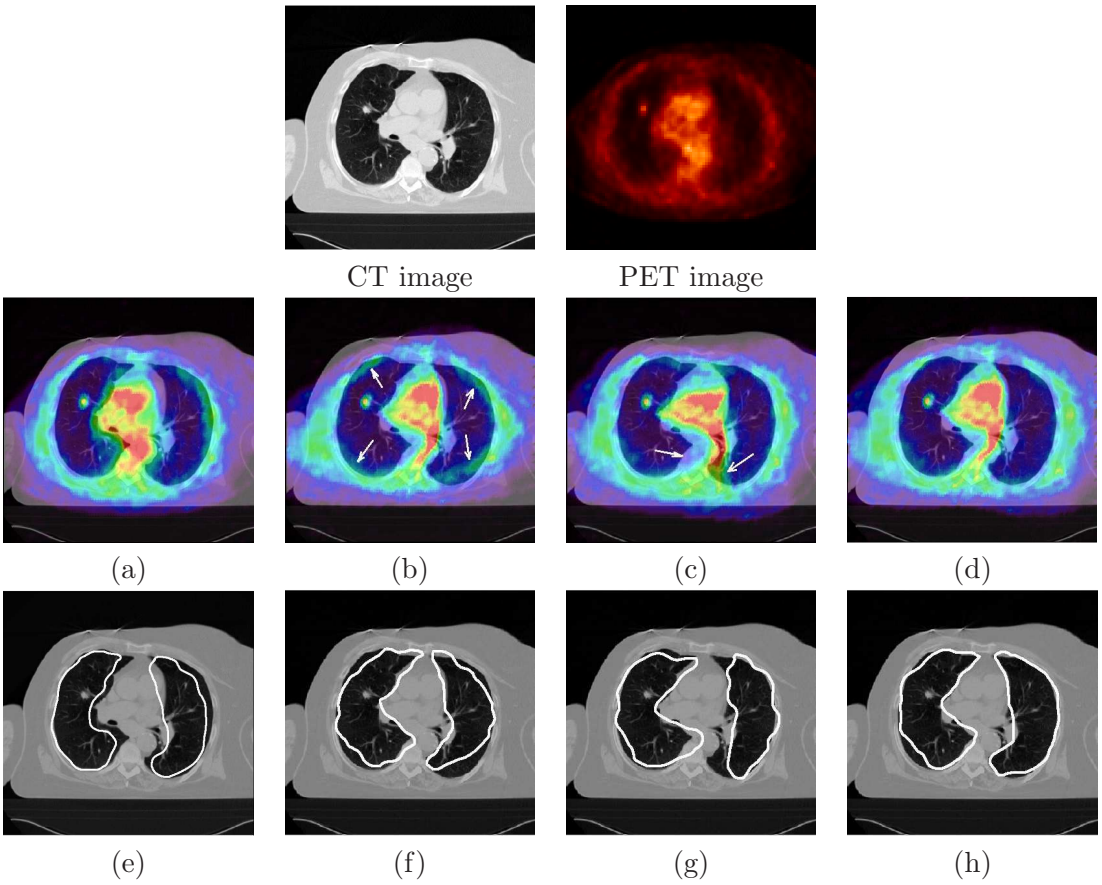

Figure 4.11: Results on real images. Superimposition of the CT image with: the original PET before registration (a), the deformed PET image using 12 (b) and 16 (c, d) landmarks. (e-h): same results as in (a-d) showing only the contours of the lungs in PET on the CT image. The locations and distribution of the landmarks in (c) are different from the ones in (d) what implies different results. Arrows show misregistrations. This illustrates the importance of the choice of the appropriate landmarks.

4.5 Conclusion and future work

We have developed a CT/PET registration method adapted to pathological cases. In pathological cases, most tissues undergo non-linear transformations due to breathing while tumors remain rigid. Our approach consists in computing a deformation of the PET image guided by a group of landmarks and with tumor-based constraints. Our algorithm avoids undesired tumor misregistrations and it preserves tumor geometry and intensity.

One of the originalities of our method, in particular compared to other approaches that include locally rigid deformations (cf. Chapter 1), is that the positions of the landmarks are adapted to anatomical shapes. In addition to this, with our algorithm, the landmarks are defined automatically in both images. In CT, we propose and study four variants, based on curvature, in order to select landmarks. The best variant to detect landmarks consists in uniformly selecting them by combining mean and Gaussian curvatures. In PET the corresponding points are found by means of the ICP algorithm. Thus, the proposed approach has two main advantages:

1. As the transformation near the tumor is reduced by the distance weight, even if the tumor segmentation is not perfect, the registration remains consistent and robust.

2. In the considered application, one important fact is that the *tumors are not the same* in the two images. For instance, the volume of the "anatomical" tumor in CT is not necessarily the same as the volume of the "functional" tumor in PET because the two modalities highlight different characteristics of the objects. The registration of these two views of the tumor must preserve these local differences, which can be very useful because we could discover a part of the anatomy that is touched by the pathology and could not be seen in the CT image. This is very important in order to know the true extension of the pathology for diagnosis and for the treatment of the tumor with radiotherapy, for example. This also advocates in favor of a rigid local registration.

Although validation is a common difficulty in registration [Schnabel et al., 2003], we have started an evaluation phase in collaboration with clinicians. We have also performed a quantitative measure of the alignment between the images, which can be used in order to find the best distribution of the landmarks that minimizes this similarity measure. This evaluation and more results are discussed in Chapter 6.

Future work will focus on performing a comparison with other methods, which will provide some conclusions on the limits of each method and their application fields. In particular, other curvature operators can be used for the selection of landmarks. For example, the multiplication with the gradient magnitude improves the results as concluded by [Hartkens et al., 2002b]. Another issue is the combination of the proposed approach with the one by [Camara et al., 2007] (detailed in Appendix D) in order to develop a hybrid algorithm which will account for features and intensity information at the same time.

It is also necessary to carry out a detailed study of the rigidity properties of the tissues surrounding a pathology (cf. Chapter 1). As a first approach, we have assumed that the rigidity of the tissues decreases with the distance to the tumor. Replacing the distance by another function would then be straightforward using our formulation.

In Chapter 5, we describe how we introduce a breathing model in order to improve the registration by introducing physiologically plausible deformations.

CHAPTER 5

Registration using a breathing model

In the context of thoracic CT-PET volume registration, we present a novel and general method to incorporate a breathing model in a non-linear registration procedure, guaranteeing physiologically plausible deformations. Then, we specify this general approach and show how to include the breathing model in our non-linear registration method dealing with pathologies and their rigid motion (detailed in Chapter 4). We present in this chapter a set of two registration experiments on a healthy and a pathological data set. Initial results demonstrate the interest of this method to significantly improve the multi-modality volume registration for diagnosis and radiotherapy applications. More results and their evaluation are detailed in Chapter 6. This part of the work has been developed within an ANR project in collaboration with Sylvie Chambon during her post-doc, Roberta Brocarto during her internship at ENST and Jannick P. Rolland and Anand P. Santhanam at the University of Central Florida.

5.1 Introduction

Many problems in thoracic imaging, in particular for radiotherapy applications, are due to respiratory movements. There exist different methods to take into account these movements in order to optimize the treatment and reduce the dose:

- *Margin adaptation.* The main difficulty of this approach is the definition of these margins: too large margins increase the irradiation to healthy tissues whereas too restricted margins might not cover all the pathological regions.
- *Patient breath-holding.* In this approach the cooperation of the patient is needed what can be an important constraint in some cases.
- *Gating.* This method requires specific synchronization systems.
- *Tracking.* An important implementation effort is necessary for this kind of methods. However, they are the most ambitious ones as they are the best ones in terms of precision because they can predict the movement and follow the tumor by using a breathing-based registration. For this reason, we have chosen to develop a method that results in the necessary information to make this approach feasible.

The interest and the necessity of non-linear registration has already been discussed in Chapters 1 and 4. Here, our registration problem is defined between two or more CT volumes and one PET volume (cf. Figure 5.1).

(a) (b) (c)

Figure 5.1: CT images (a,b) corresponding to two different instants of the breathing cycle and PET image (c) of the same patient (coronal views).

Most of the existing non-linear registration methods either find the transformation that maximizes a similarity measure between the registered image and the target image (iconic methods) or compute a transformation that matches some particular features within each image (geometrical methods) [Malandain, 2006]. All these methods are based on image information (cf. Chapter 1), but do not take into account the physiology of the human body. However, physiological information can be useful in order to ensure realistic deformations and to guide the registration process.

In this chapter, we present the existing works that use breathing models for different medical applications and we will see that few works exploit such models in a registration process. Consequently, we propose an approach in which we integrate a physiologically driven breathing model in a non-linear registration procedure. First, we detail the proposed general methodology and then we specify it in order to integrate it in our registration method based on landmarks and including rigidity constraints.

In Section 5.2, we summarize existing works, which use breathing models combined (or not) with registration algorithms and then we provide an overview of the selected model in Section 5.3. The proposed model-based non-linear registration methodology is detailed in Section 5.4. Then, the application of our registration method adapted to pathological cases combined with the breathing model is described in Section 5.5. Finally, Section 5.6 discusses some first results.

5.2 Breathing models

Different bio-mathematical formulations of the respiratory mechanics that describe the human lung have been developed since the middle of the XXth century [Mead, 1956 ; Guerrero et al., 1977 ; Cotes, 1993]. Such works led to an increased interest in obtaining objective, quantitative measures characterizing regional lung physiology and pathology. Lung deformations have been studied for different applications, in particular, for understanding pulmonary mechanics [Gee et al., 2002 ; Hoffman et al., 2004 ; Voorhees et al., 2005] or for registering Magnetic Resonance Imaging (MRI) images [Reinhardt et al., 2000 ; Sundaram et al., 2005]. A recent study highlighted the effects of breathing during a non-rigid registration process and the importance of taking it into account [Sundaram and Gee, 2005]. Currently, respiration-gated radiotherapies are being developed to improve the efficiency of radiations of lung tumors [Sarrut, 2006 ; Boldea, 2006].

There exist several surveys about registration with a breathing model. For instance,

[Goerres et al., 2002] compare CT/PET registration results in different breathing conditions, [Murphy, 2004] summarizes the existing techniques of tumor tracking for radiotherapy procedures and [Sundaram and Gee, 2005] study the breathing process and compare different breathing cycles.

We propose here a new state of the art and a classification of the methods that take into account explicitly the breathing movement. The breathing movement can be taken into account at two different levels (cf. Table 5.1):

- during the *reconstruction of the 3D volumes*;
- during the *radiotherapy treatment*.

5.2.1 During volume reconstruction

In the case of the reconstruction of the 3D volumes, the proposed methods depend on the used material.

During CT acquisition, the 2D slices are acquired at different instants of the breathing cycle. If a *breathing signal* is recorded [Wolthaus et al., 2005], then it is easy to reconstruct the 3D volume by grouping the 2D slices corresponding to the same instant. In the case of projection imaging, [Crawford et al., 1996] suppose that breathing induces variations only about the x and y axes and they applied their method to CT, Single Photon Emission Computed Tomography (SPECT), PET and MRI images.

If *no breathing signal* has been acquired, it is necessary to estimate it by using the acquired data. [Rit et al., 2005; 2006] do it by tracking points of interest and studying their trajectories. [Reyes-Aguirre et al., 2004] add a new term to a *Maximum Likelihood Expectation Maximization* (MLEM) algorithm in order to account for breathing movement. Some methods are based on the Active Breathing Coordinator (ABC) [Sarrut et al., 2006]. Their goal is to simulate CT images of the thorax between two instants of the breathing cycle. They first segment the lungs and register the two original CT images. As they use intensity information for the registration, they also modify the density of the lungs (their intensity) in order to obtain a more robust rigid registration. They compute the intermediate instants by interpolating the deformation field. They suppose that the trajectories of the points of the surface of the lungs is a straight line.

5.2.2 During radiotherapy treatment

In the case of the methods that account for respiration during the treatment, three techniques have been proposed so far [Murphy, 2004]:

1. *Active techniques* – Patient's breathing is controlled (the airflow is blocked) by means of a spirometer [Zhang et al., 2003]. Then, the treatment can be synchronized with the breathing cycle.

2. *Passive techniques* – They use external measurements in order to adapt radiation protocols to the tumor's motion ("gating").

3. *Model-based techniques* – They employ a breathing model to evaluate lungs deformations during the breathing cycle.

In the following, we only detail passive and model-based techniques.

5.2.2.1 Passive techniques

These techniques use external measurements in order to adapt radiation protocols to the tumor's motion. There exist three categories:

- methods using passive "gating", which can be based on the Active Breathing Coordinator (ABC) [Sarrut et al., 2005],
- methods using external landmark tracking, and
- methods using an empirical model.

We detail here the two las methods.

Methods using external landmark tracking – Landmarks can be tracked on the patient using a stereoscopic system in order to determine the instant of the breathing cycle and adapt the treatment [Nehmeh et al., 2004]. With the same purpose, in [Schweikard et al., 2000] infrared tracking is combined with synchronized X-ray images using a correlation method. These techniques are often invasive, they are not proposed for registration and are dedicated to specific equipments.

Methods using an empirical model – In this case, the synchronization of the treatment with the breathing cycle can be based on a first acquisition of the tumor trajectory [Xu et al., 2005]. This is called Synchronized Moving Aperture Radiation Therapy (SMART) [Neicu et al., 2003]. In [McClelland et al., 2006], a model of the respiratory movement is estimated using a temporal acquisition of CT volumes at free breathing. This is synchronized with a respiratory signal and a high-resolution CT obtained with respiratory "gating". Finally a non-linear registration between the high-resolution CT and each CT volume is computed using FFD (Free-Form Deformations). [Rohlfing and Maurer, 2001] use a kinematic model in order to estimate lung breathing movements from a 4D MRI. This is used in a multi-resolution registration approach.

5.2.2.2 Model-based techniques

We can divide model-based techniques into two categories:

- geometrical models, and
- physical models.

Geometrical models – Mathematical tools can be employed to estimate the breathing motion artefacts. Some mathematical models have been introduced in the case of CT, SPECT, PET and MRI. The work by [Krishnan et al., 2004] includes the analysis of lung morphology using image warping. The most popular technique, for medical visualization, is called NCAT (NURBS-based cardiac-torso). This model is based on Non-Uniform Rational B-Spline (NURBS) based on imaging data from CT scans of actual patients [Segars et al., 2001]. It has been proposed in order to correct respiratory artifacts of SPECT [Segars et al., 2002a] and PET images [Segars et al., 2002b]. The same method has also been used by [Smyczynski et al., 2001] in SPECT images. The authors of [Reyes-Aguirre et al., 2005b] combine NURBS with a MLEM, in order to propose PET images reconstruction

with no artifacts induced by the respiratory movement. A multi-resolution NURBS-based registration approach for 4D MRI, which uses normalized mutual information, is proposed by [Rohlfing and Maurer, 2001]. In [Guerrero et al., 2005], a 4D NCAT phantom and an original CT are used to generate 4D CT and to compute an elastic registration.

Physical models – A physical model is based on the important role of airflow inside the lungs. Based on medical image analysis, the spatial air distribution inside lungs was shown to be dependent on the gravity and thus the orientation of the subject. From the perspective of a physically-based deformation, the air distribution defines the force applied on the lung model and thus needs to be accounted for. These methods are based on the volume preservation relation [Promayon et al., 1997 ; Wagers et al., 2000 ; Takeuchi et al., 2001 ; Villard and Baudet, 2003 ; Zordan et al., 2006 ; Santhanam, 2006], which are often validated on animal imagery [Venegas et al., 1998 ; Narusawa, 2001]. A modeling of the human lung model as a linearized single-compartment model has been proposed by [Promayon et al., 1997]. Their model represents the objects by a set of contour points with a force associated to each point. This force takes into account the rigidity and the elasticity of the tissues. An FEM based model was introduced by [DeCarlo et al., 1995] for real-time medical visualization. It has been extended by [Kaye et al., 1998] in order to model pneumothorax related conditions. Here, the method has an analogy for lung deformations to an electrical circuit. A visualization-based training method has been developed for pneumothorax using a single-compartment model [Dawson, 2002]. [Villard and Baudet, 2003] acquire several CT images with an ABC. The surfaces of the lung and the tumor are modeled and a PV (Pressure Volume) relation is used. Two methods can be used: a FEM (Finite Element Method) or a mass-spring system. This method is specific to each patient. The model by [Santhanam, 2006] is detailed in Section 5.3.

All the previous physically-based approaches are single-compartment models. A multi-compartment functional FEM model, which models the tissue constituents of the lungs (i.e. parenchyma, bronchiole and alveoli), has been done by [Tawhai and Burrowes, 2003]. The run-time computational complexity of this approach is reduced by modeling solely the bronchioles and the air-flow inside the lung [Ding et al., 2005].

5.2.3 Breathing models for registration

Only few works really employ a breathing model in a registration process. The authors of [Rohlfing and Maurer, 2001 ; Sundaram and Gee, 2005] propose to register MRI in order to estimate the breathing model, and in [Guerrero et al., 2005], the NCAT phantom is used. A breathing model, which can be used in a registration, is presented by [Sarrut et al., 2005; 2006]. They adapt volumes to their algorithm by changing intensities in order to respect this assumption: intensity is conserved from one image to another, but at a different location. Then, they register two CT images by using an iconic non-linear method and, finally, they interpolate the results to generate intermediate instants of the breathing cycle. A specific equipment (ABC) is needed in this approach.

However, the usage of a high-resolution model for lung deformations and its real-time visualization are not addressed in these efforts. From a modeling and simulation point of view, physically-based deformation methods are better adapted for simulating lung dynamics as they allow precise generation of intermediate 3D lung shapes. In addition to this, these models are easier to adapt to individual patients, without the need of physical external adaptations for each treatment as in the case of empirical models. In this work, the aim is to

For the reconstruction of volumes		For adapting the radiotherapy treatment					
			Passive			**Model**	
With signal	**Without signal**	**Active**	*Respiratory "gating"*	*Tracking*	*Empirical model*	*Geometrical model*	*Physical model*
[Crawford et al., 1996 ; Wolthaus et al., 2005]	[Reyes-Aguirre et al., 2004 ; Rit et al., 2005; 2006 ; Sarrut et al., 2006]	[Zhang et al., 2003]	[Sarrut et al., 2005]	[Nehmeh et al., 2004 ; Schweikard et al., 2000]	[Rohlfing and Maurer, 2001 ; Neicu et al., 2003 ; Xu et al., 2005 ; McClelland et al., 2006]	[Rohlfing and Maurer, 2001 ; Segars et al., 2001; 2002a ; Reyes-Aguirre et al., 2005b]	[Narusawa, 2001 ; Promayon et al., 1997 ; Santhanam et al., 2004b; 2003; 2006b ; Takeuchi et al., 2001 ; Venegas et al., 1998 ; Villard and Baudet, 2003 ; Wagers et al., 2000 ; Zordan et al., 2006]

Table 5.1: Classification of the breathing models.

guarantee that physiologically plausible deformations are obtained during registration, and to predict deformations during radiotherapy. For this reason, we use the physically-based model described in Section 5.3.

5.3 Physics-based dynamic 3D surface lung model

This section is inspired by [Santhanam et al., 2006a]. The subject-specific modeling approach used in this work was previously discussed by [Santhanam et al., 2006a]. The components involved in this modeling and visualization efforts include:

1. Parameterization of PV (Pressure-Volume) data from a human subject [Santhanam et al., 2007b; 2004c] which acts as an ABC (see Figure 5.2);
2. Estimation of the deformation operator from 4D CT lung data sets [Santhanam et al., 2004a; 2006b;c; 2007c];
3. Optimization of the deformation computation on a Graphic Processing Unit (GPU) for real-time purposes [Santhanam et al., 2007a].

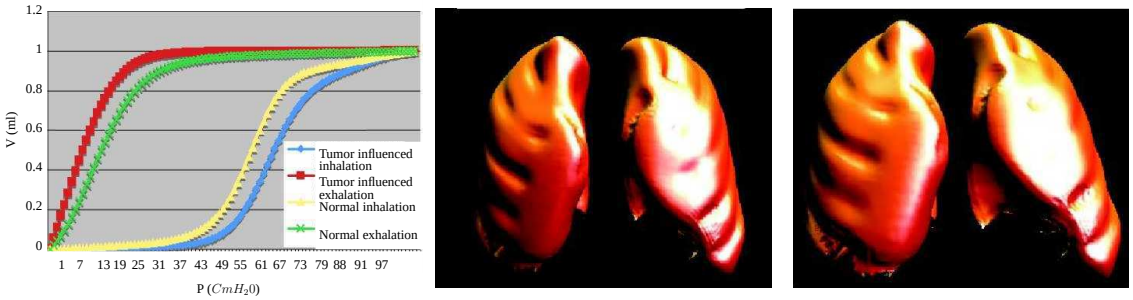

(a) (b) (c)

Figure 5.2: The breathing model by Santhanam et al. uses the PV relation (a) in order to compute the different instants between end-expiration (b) and end-inspiration (c).

It is to be noted that while item (1) and (2) of the methodology are critical for the registration of PET and CT, item (3) (done for real-time computation purposes) is only reported here for completeness but is not required for the problem in this work. In step (1) a parameterized PV curve, obtained from a normal human subject, is used as a driver for simulating the 3D lung shapes at different lung volumes. In step (2), the computation takes as inputs the nodal displacements of the 3D lung models and the estimated amount of force applied on the nodes of the meshes (which are on the surface). The direction and magnitude of the lung surface point's displacement are computed using the volume linearity constraint, i.e. the fact that the expansion of lung tissues is linearly related to the increase in lung volume [Santhanam et al., 2006b]. Displacements are obtained from 4D CT of a normal human subject. The estimated amount of applied force on each node (that represents the air-flow inside lungs) is estimated based on a PV curve and the lungs' orientation with respect to the gravity, which controls the air flow.

Given these inputs, a physics-based deformation approach based on Green's function (GF) formulation is estimated to deform the 3D lung surface models. Specifically the GF

is defined in terms of (a) a physiological factor, the regional alveolar expandability (elastic properties), and (b) a structural factor, the inter-nodal distance of the 3D surface lung model (static). The coefficients for the GF associated with these two factors are computed by making two different estimations of the GF using the method discussed in [Santhanam et al., 2006b]. An iterative approach is employed and, at each step, the force applied on a node is shared with its neighboring nodes based on a local normalization of the alveolar expandability coupled with inter-nodal distance. The process stops when this sharing of the applied force reaches equilibrium. At this point of equilibrium the force shared by a node with its neighbors forms a row of the GF's transfer function estimation. Once the deformation operator is estimated, we have the continuous breathing model. Therefore, we can accurately generate different intermediate instants ("snapshots") of the breathing cycle, and generate simulated 3D CT meshes of the lungs.

The transfer function computed in this manner is anisotropic, which provides scope for modeling the tumor-influenced 3D lung surface deformations. Validation of lung deformations using a 4D CT data set is described in [Santhanam et al., 2006b ; Santhanam, 2006 ; Santhanam et al., 2007c]. The simulated lung deformations matched the 4D CT data set with 2 mm average distance error.

5.4 Combining breathing model and image registration

We have conceived an original algorithm in order to incorporate the breathing model described above in a multimodal image registration procedure. Figure 5.3 shows the computational workflow of the complete algorithm. The input consists of one PET volume and two CT volumes of the same patient, corresponding to two different instants of the breathing cycle (end-inspiration and end-expiration, for example, collected with breath-hold maneuver). The preliminary step consists in segmenting the lung surfaces and, eventually, the tumors on the PET data and on the two CT data sets. For this stage, we use the robust mathematical-morphology-based approach described in Chapter 3. Then, the meshes corresponding to the segmented objects are extracted.

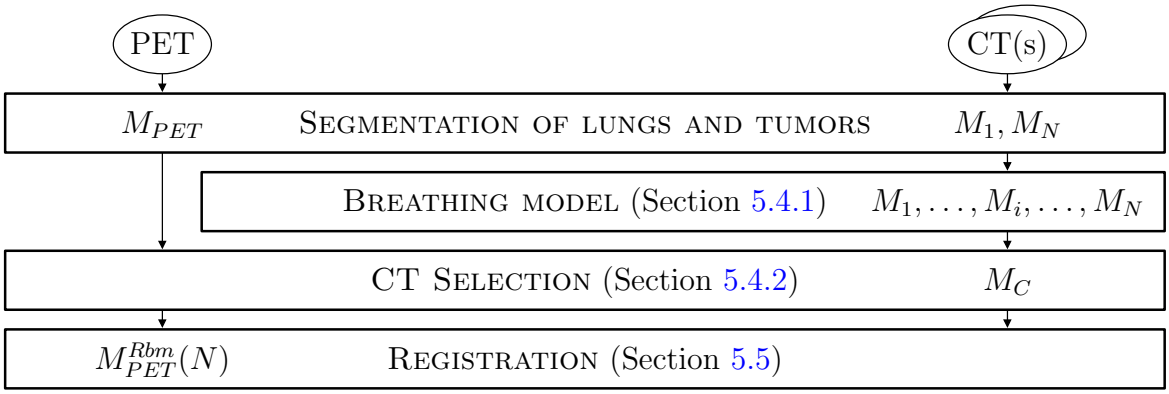

Figure 5.3: Computational workflow of the registration algorithm of CT and PET volumes using a breathing model.

5.4.1 Computation of a patient-specific breathing model

In order to compute the adapted breathing model, we intend to estimate a deformation operator from the two segmented CT lung data sets (typically end-inspiration and end-expiration). We estimate the intermediate 3D lung shapes between these two data sets. The displacements of the surface lung vertices are estimated as follows:

1. *Directions* are given by the model (computed from a 4D CT normal data set of reference).
2. *Magnitudes* are "patient-specific" and are computed from the given 3D CT lung data sets.

In other words, for known directions of displacement the magnitude of the displacement is computed from the two 3D CT lung data sets. With known estimations of applied force and "subject-specific" displacements the coefficients of the GF can be estimated (cf. Section 5.3). Then, the GF operator is used to compute the 3D lung shapes at different intermediate lung volumes. This estimation allows computing the intermediate 3D lung surface shapes in a physically and physiologically accurate manner, which can then be used for registering the PET images as further discussed in the following sections.

5.4.2 CT selection

By applying the continuous breathing model, we obtain different instants ("snapshots") of the breathing cycle, generating simulated CT meshes. By comparing each CT mesh with the PET mesh, we select the "closest" one (i. e. with the most similar anatomy). Let us denote the CT simulated meshes M_1, M_2,..., M_N with M_1 corresponding to the CT in maximum exhalation and M_N to maximum inhalation. By using the breathing model, the transformation $\phi_{i,j}$ between two instants i and j of the breathing cycle can be computed as: $M_j = \phi_{i,j}(M_i)$. We compare these CT meshes with the PET mesh (M_{PET}) based on a measure of similarity C. The mesh that minimizes C is denoted as M_C:

$$M_C = \arg\min_i C(M_i, M_{PET}). \tag{5.1}$$

The Root Mean Square (RMS) distance has been chosen as a first criterion:

$$C(M_i, M_{PET}) = D_{RMS}(M_i, M_{PET}) = \sqrt{\frac{1}{2}[d_{RMS}(M_i, M_{PET})^2 + d_{RMS}(M_{PET}, M_i)^2]}$$

where $d_{RMS}(A, B) = \sqrt{\frac{1}{|A|}\sum_{p\in A} D(p, B)^2}$ and $D(p, B) = [\min_{q\in B} d(p, q)]$ with d the Euclidean distance.

Once the closest mesh M_C is found, the selection process is refined between M_{C-1} and M_{C+1} and a new closest mesh $M_{C'}$ is computed. This iterative selection is repeated until convergence, i.e. when the difference between two consecutive "closest meshes" is lower than a threshold.

5.4.3 Deformation of the PET

Two approaches have been developed for registering the PET image on the maximum inspiration CT, as illustrated in Figure 5.4. One method computes a direct registration and the other uses the closest CT mesh calculated as explained in Section 5.4.2.

The direct registration, denoted f^{Rd}, can be computed between M_{PET} and the original CT mesh M_N (dashed line in Figure 5.4):

$$M_{PET}^{Rd}(N) = f^{Rd}(M_{PET}, M_N), \tag{5.2}$$

where $M_{PET}^{Rd}(N)$ is the result of registering the PET directly to the CT mesh M_N. The transformation f^{Rd} may be computed by any registration method adapted to the problem (note that this could be done with another instant M_i). In this *direct* approach the deformation itself is not guided by any anatomical knowledge. In addition, if the PET and the original CT are very different, it is likely that this registration procedure provides physically unrealistic results.

To avoid such potential problems, we propose an alternative approach: once the appropriate CT (M_C) is selected, we compute the registration, f^r, between the M_{PET} mesh and the M_C mesh as:

$$M_{PET}^{r}(C) = f^{r}(M_{PET}, M_C), \tag{5.3}$$

where $M_{PET}^{r}(C)$ denotes the registered mesh. Then, the transformation due to the breathing is used to register the PET to the original CT (continuous line in Figure 5.4) incorporating the known transformation between M_C and M_N:

$$\Phi_{C,N} = \phi_{N-1,N} \circ \ldots \circ \phi_{C+1,C+2} \circ \phi_{C,C+1}. \tag{5.4}$$

We apply $\Phi_{C,N}$ to $M_{PET}^{r}(C)$ in order to compute the registration with M_N:

$$M_{PET}^{Rbm}(N) = \Phi_{C,N}(M_{PET}^{r}) = \Phi_{C,N}(f^{r}(M_{PET}, M_C)), \tag{5.5}$$

where $M_{PET}^{Rbm}(N)$ denotes the PET registered mesh using the breathing model.

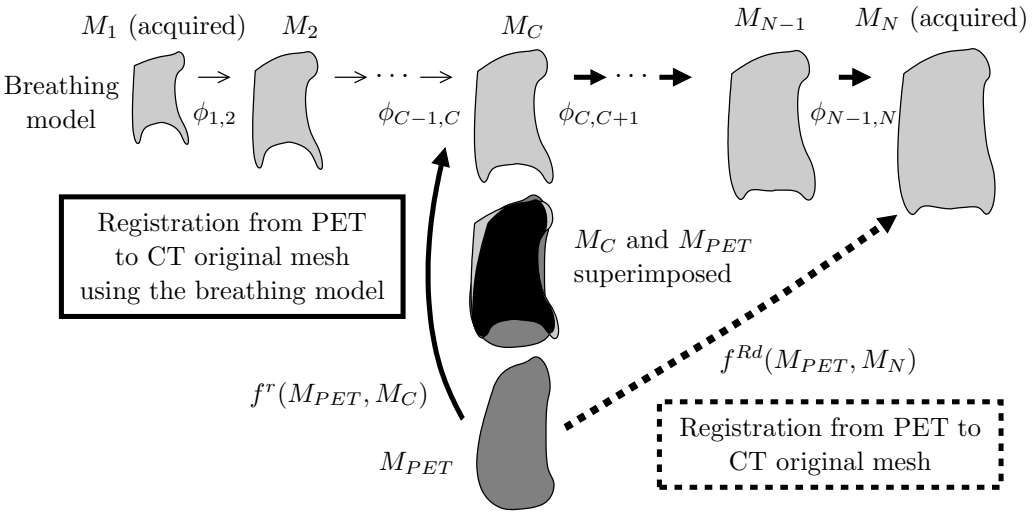

Figure 5.4: Registration framework on PET (M_{PET}) and CT mesh (M_N) – The M_C mesh is the closest to the M_{PET} mesh. We can register M_{PET} to the M_N mesh (original CT) following one of the two paths.

5.5 Breathing model-based method for registration adapted to pathologies

5.5.1 Adaptation of each component

The algorithm described in Section 5.4 can be applied with any type of registration method, i.e. f^{Rd} and f^{r} may be computed by any registration method adapted to the problem. In pathological cases, this general registration algorithm that uses the breathing model is influenced by the tumor at different levels:

- The *breathing model* has to be generated taking into account the constraints of the tissues and, thus, the tumor. This pathology hardens the lung tissue thereby changing the mechanical properties involved in the lung deformation. [Smyczynski et al., 2001] state that a standardized approach to correct for the artifacts associated with respiratory motion is not adapted to pathological cases where tumors are present inside the lungs. In the presence of tumors in the lungs, the computation of the breathing model described in Section 5.4.1 can be adapted to these pathological cases (and it can be extended in order to incorporate other pathologies, as emphysema). This adaptation consists in taking into account the tumors for the computation of the averaged transfer function (built from extracting the transfer function of each of the 3D CTs with tumors) and for establishing the direction of surface nodes deformation. This is explained in [Santhanam et al., 2006b]. For this reason, we use the breathing model described in Section 5.3 as it is adaptable to cope with the movement of the tumors during the breathing cycle.

- The *registration algorithm* must take into account the fact that the tumor undergoes a different deformation (considered as rigid in a first approximation) from the one of the lungs. The algorithm detailed in Chapter 4 is adapted to this problem.

5.5.2 Algorithm

Therefore, once the different CT meshes are computed and the closest CT mesh, M_C, is selected, we register the PET and the original CT (in our example M_N) with the following procedure:

1. Selection of landmark points on the CT mesh M_C. The four variants presented in Section 4.3 can be used.

2. Estimation of corresponding landmark points on the PET mesh M_{PET} using the Iterative Closest Point (ICP) algorithm [Besl and McKay, 1992]. Note that the ICP algorithm is based on the geometry of the sets to compare. Therefore it furnishes better results between objects with similar shapes (the PET mesh M_{PET} and the closest CT M_C) than between very different objects (M_{PET} and M_N).

3. Tracking of landmark points from M_C to the CT mesh M_N. This step does not need additional computations as the correspondences between points are directly given by the breathing model.

4. Registration of the PET and the original CT using the estimated correspondences with the method summarized in Chapter 4.

The breathing model is introduced at two levels, in order to improve the performances of the registration method:

- One of the difficulties of the registration method described in Chapter 4 is the definition of the appropriate landmarks in the CT image. High curvature points can be used as landmarks as explained in Section 4.3.
- Another difficulty is the selection of the corresponding points on the surface of the lungs in PET. As a first approach, we have used the ICP (Iterative Closest Point) by [Besl and McKay, 1992]. However, this approximation is based only on the geometrical properties of the points (distances) and not on their movement during a breathing cycle. Thus, this choice does not guarantee that the points correspond to the same anatomical reality. The use of the breathing model allows computing the trajectories of the nodes of the mesh during the respiration. The landmark points selected on M_C are tracked on the meshes estimated with the breathing model. Consequently, we can assume that the corresponding landmarks selected on the original CT are correct (and actually they represent the same anatomical point) and follow the deformations of the lungs during the respiratory cycle.

5.6 First results and discussion

We first applied our algorithm on a pathological case exhibiting one tumor and on a normal case. In both cases, we have one PET (of size $144\times144\times230$ with resolution of $4\times4\times4$ mm^3) and two CT volumes (of size $512\times512\times55$ with resolution of $0.72\times0.72\times5$ mm^3) for each case, acquired during breath-hold in maximum inspiration and in intermediate inspiration, from individual scanners. The breathing model was initialized using the lung meshes from the segmented CT. Ten meshes (corresponding to regularly distributed instants) were generated and compared with the PET[1]. Figure 5.5 shows the results of surface comparison between the PET surface (M_{PET}) and two instants from the CT data set: the closest (M_C) and the end-inspiration (M_N). In Figures 5.5 to 5.9, the images are provided in 2D for the sake of readability.

$C(M_C, M_{PET}) = 12.1$
(a)

$C(M_N, M_{PET}) = 24.2$
(b)

Figure 5.5: Superimposition of the contours of the PET (black) and the CT lungs (grey) at two instants of the breathing cycle: (a) M_C, (b) M_N (cf. Section 5.4.2).

As illustrated in Figures 5.6 to 5.9, the correspondences between landmark points on the original CT and the PET are more realistic in the results obtained with the breathing model than without model. These landmark points have been selected using curvature as

[1]Meshes have more than 40 000 nodes

detailed in Chapter 4. For example, it can be observed that the result of the registration by a direct method (Figure 5.9(b)) produces unrealistic deformations in the region between the lungs. With the proposed algorithm (Figure 5.9(c)), the result is visually more accurate. In Figure 5.7 the improvement of the results is clearly illustrated for the normal case in the region of the right lung close to the liver. Using the model, the corresponding points represent the same anatomical points and the uniqueness constraint is respected, leading to visually better looking PET registered images. In particular, in the two illustrated cases, it can be observed that the lower part of the two lungs is better registered using the breathing model: the lung contour in the registered PET is closer to the lung contour in the original CT. In the pathological case (Figure 5.8), the tumor is correctly registered and not deformed.

In summary, the results obtained with the proposed algorithm are physically-based and more realistic than results obtained by registering the PET directly with the original CT. These first results have been obtained by using landmarks determined by the combination of mean and Gaussian curvatures plus a uniform selection. This variant provided visually better results as concluded in Chapter4. However, further validation is necessary and is detailed in Chapter 6.

5.7 Conclusion and future work

In this chapter, we have described the combination of our CT/PET landmark-based registration method and a breathing model in order to guarantee physiologically plausible deformations of the lung surface. The method consists in computing deformations guided by the breathing model. The originality of the proposed approach, which combines our landmark-based registration method including rigidity constraints and a breathing model, is to strongly rely on anatomical structures, to integrate constraints specific to these structures on the one hand, and to the pathologies on the other hand, and to account for physiological plausibility. Initial experiments on two cases (one normal case and one pathological case) show promising results with significant improvement brought by the breathing model. In particular, for the pathological case, our algorithm avoids undesired tumor misregistrations and preserves tumor geometry and intensity (cf. Chapter 4). A first version of this work has been published in [Chambon et al., 2007 ; Moreno et al., 2007 ; Chambon et al., 2008].

A quantitative comparison and the evaluation on a larger database, in collaboration with clinicians, is detailed in Chapter 6.

In this work, we consider the impact of the physiology on lung surface deformation, based on reference data of normal human subjects. The methodology presented in this work will further benefit from the inclusion of patho-physiology specific data once established. The use of normal lung physiology serves to demonstrate improvements in CT and PET registration using a physics-based 3D breathing lung model. Future investigations are expected based on refining the deformation model using patho-physiological conditions and including a more precise characterization of the tumor movement and its influence on the breathing. Ultimately, validation of the breathing model in pathological cases should be task-based performance on a clinical problem.

Moreover, future work includes the use of different criteria for the selection of the appropriate CT (Section 5.4.2): the RMS distance is a global criterion which does not take into account local differences or similarities of the surfaces. For the selection of the corresponding points on the surface of the lungs in PET, an improved ICP algorithm [Almhdie et al., 2006] could be used. Another improvement would be the selection of landmarks including points

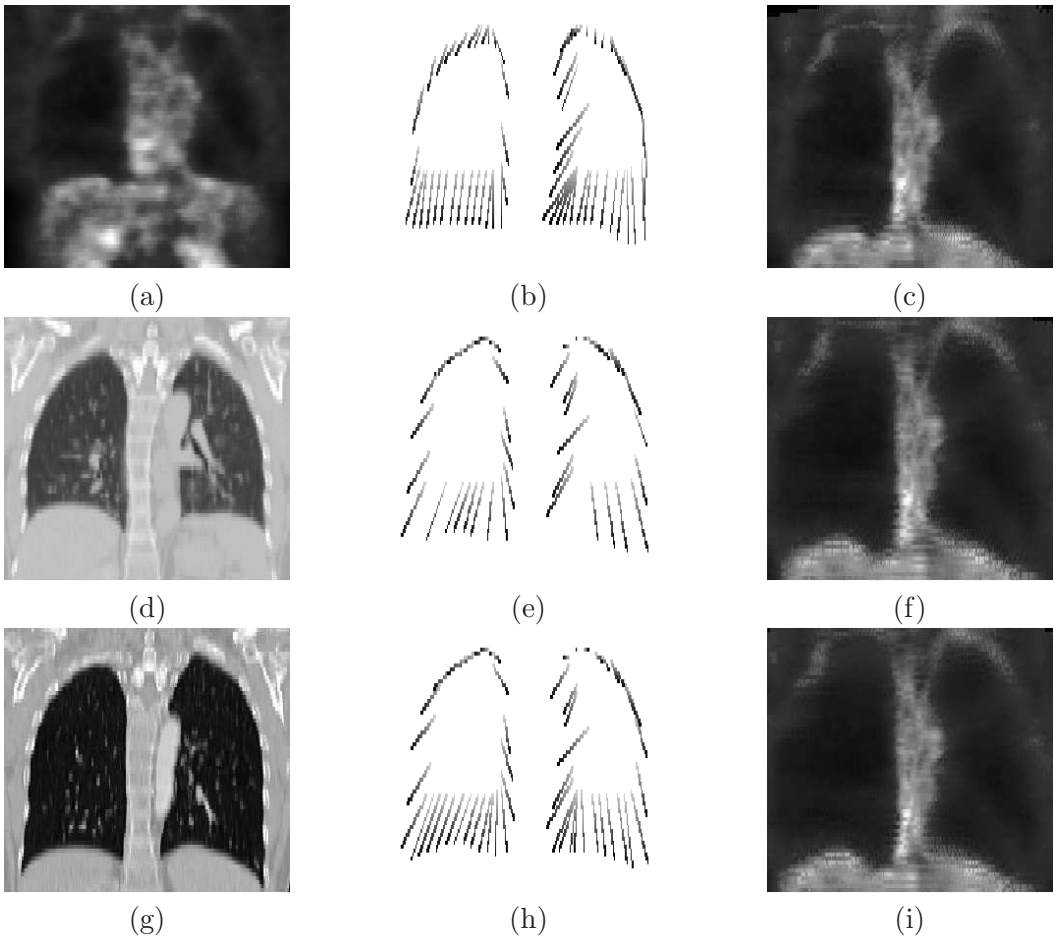

Figure 5.6: Original PET (a) and CT (d,g) images in a normal case. The correspondences between the selected points in the PET image and in the end-inspiration CT image (g) are shown in (b) for the direct method, in (e) for the method with the breathing model and a non-uniform landmarks detection and in (h) for the method with the breathing model and a uniform landmarks selection (corresponding points are linked). Registered PET is shown in (c) for the direct method, in (f) for the method with the breathing model with a non-uniform landmark distribution and in (i) for the method with the breathing model and landmarks uniformly distributed.

Figure 5.7: Details of registration on the bottom part of the right lung, in a normal case: (a) CT, (b) PET registered without breathing model, and (c) with breathing model. The white crosses correspond to the same coordinates. The method using the breathing model furnishes a better registration of the surfaces of the lungs.

undergoing important displacements during the respiration, and making these points guide the registration procedure.

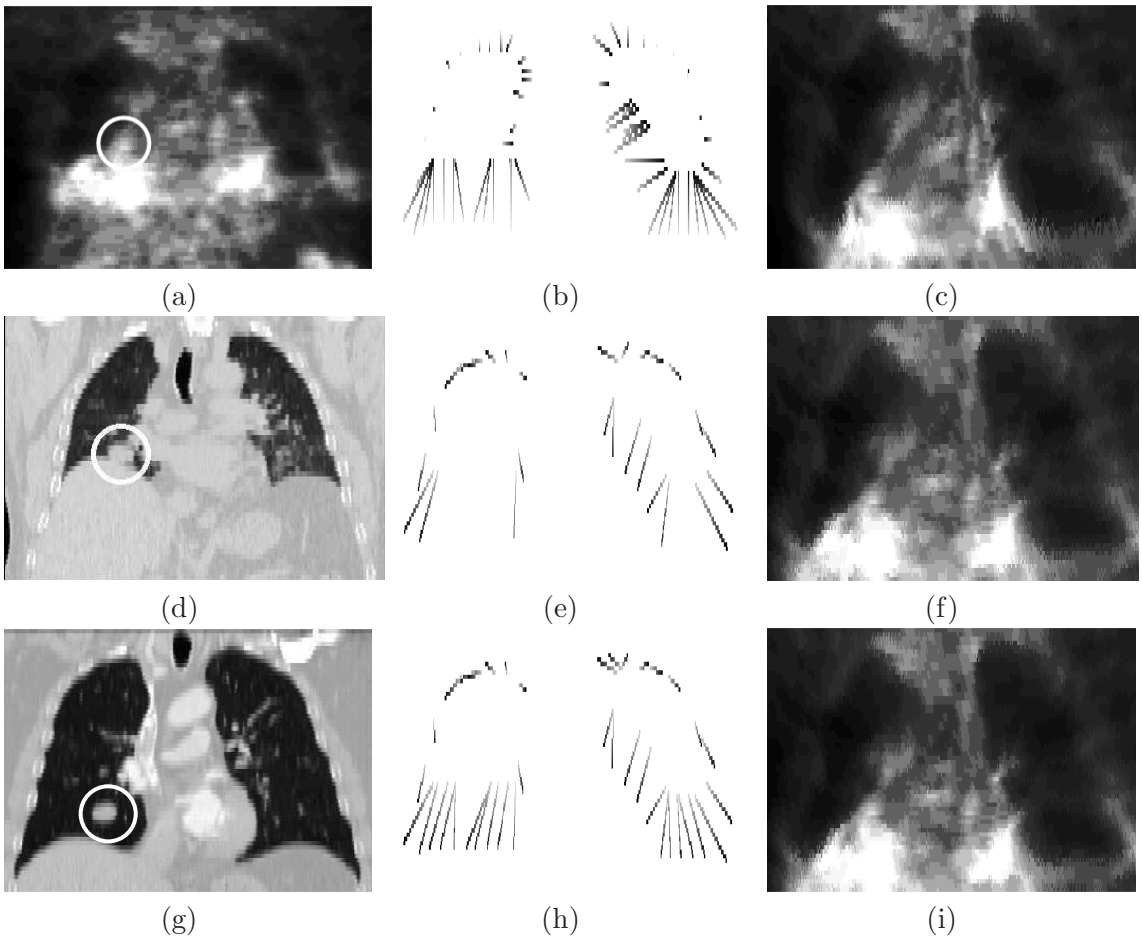

Figure 5.8: Original PET (a) and CT (d,g) images in a pathological case (the tumor is surrounded by a white circle). The correspondences between the selected points in the PET image and in the end-inspiration CT image (g) are shown in (b) for the direct method, in (e) for the method with the breathing model and a non-uniform landmarks detection and in (h) for the method with the breathing model and a uniform landmarks selection (corresponding points are linked). Registered PET is shown in (c) for the direct method, in (f) for the method with the breathing model with a non-uniform landmark distribution and in (i) for the method with the breathing model and landmarks uniformly distributed. In Figures (e) and (h), it can be observed that landmarks are better distributed with a uniform selection.

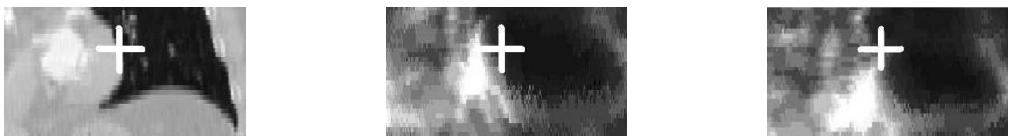

Figure 5.9: Details of registration in the region between the lungs, in a pathological case: (a) CT, (b) PET registered without breathing model, and (c) with breathing model. The white crosses correspond to the same coordinates. The method using the breathing model avoids unrealistic deformations in this region.

CHAPTER 6

Evaluation and comparison of the two registration methods

In this chapter, we briefly mention the different existing methods for evaluation of the registration and we describe the method we have used. Then, based on the proposed evaluation method, we compare the results we have obtained with our registration method applied directly between one CT and its corresponding PET image, cf. Chapter 4, and combined with a breathing model as described in Chapter 5. We show here some preliminary results and their first evaluation. Further tests and a deeper evaluation will be performed in the following months in the frame of ANR project MARIO.

6.1 Existing works on evaluation of the registration

Validation of registration methods is known to be a difficult task [Tanner et al., 2002 ; Schnabel et al., 2003] because of the absence of a *gold standard* [Vik, 2004 ; Vik et al., 2005]. However, due to the increasing interest of registration, mainly in medical applications, there exist several works which attempt to overcome this difficult problem.

In this direction, and in the context of CT/PET registration of thoracic and abdominal images, some methods are based on atlases or phantoms as the approach by [Li et al., 2003] for human lung in CT. The method by [Lavely et al., 2004] uses phantom and patient data for validation in order to demonstrate a general method for assessing the accuracy of CT/PET image registration by using externally mounted fiducial markers.

As mentioned above, developing image processing algorithms, such as registration in order to improve the information content of PET data, requires *ground truth* data to validate the algorithms. When this *ground truth* (or *gold standard*) is not available, one alternative is to simulate realistic data based on the physical and biological properties of real-life acquisition. This is especially true in the case of dynamic PET studies, in which counting statistics of the volume can vary widely over the time-course of the acquisition. Several Monte Carlo simulators have been proposed for these applications [Buvat et al., 2003]:

- SimSET has been one of the first Monte Carlo simulators [Thompson et al., 1992 ; Harrison et al., 1993]. It has been combined with Zubal's phantom [Zubal et al., 1994] or with NURBS [Segars et al., 2001; 2002b] in order to reconstruct PET images with no artifacts induced by the respiratory movement [Reyes-Aguirre et al., 2005a;b].

- GATE (Geant4 Application for Tomographic Emission) [Jan et al., 2004] is a simulation toolkit adapted to the field of nuclear medicine. It makes possible the simulation of time curves under realistic acquisition conditions using the Monte Carlo method, and the dynamic reconstruction algorithms can be tested. This kind of simulator can be combined with phantoms such as the NCAT (NURBS-based Cardiac-Torso) [Segars et al., 2001; 2002b] or the MOBY, mouse atlas by [Segars et al., 2004], in particular for validation of registration algorithms in CT/PET.

- PET-SORTEO is another very popular PET simulation protocol [Reilhac et al., 2005]. It has been used for the evaluation of the registration between cardiac MR and PET images by [Mäkelä et al., 2003 ; Pollari et al., 2004], in the context of pattern classification for automatic segmentation of PET brain images [Koivistoinen et al., 2004] and with the fully automatic deformable models by [Tohka et al., 2004]. [Lartizien et al., 2005] have adapted the PET-SORTEO to small animal PET scanners. Recently, [Schottlander et al., 2006] have used PET-SORTEO in order to generate realistic dynamic FDG-PET datasets. They have combined the PET-SORTEO Monte Carlo simulation code with the MNI digital brain phantom [Collins et al., 1998b] and pharmacokinetic data. They have used the dynamic PET data sets to evaluate the performance of intensity-based registration of brain images. [Ali et al., 2006] have extended this work to the full human torso using an annotated NCAT phantom combined with other clinically derived data for each tissue type. Again, the PET-SORTEO Monte Carlo simulator, has been used to simulate image acquisition of a whole torso over multiple bed positions. This simulated acquisition protocol mimicked the protocol for the original PET dataset. Their results suggest that PET simulation could offer a potentially useful method of obtaining realistic whole body PET data.

6.2 Our evaluation method

Although the previous methods are potentially very efficient for validation of PET-CT registration, they are also computationally expensive and complex. For these reasons and as a first approach, in this work we propose an evaluation stage composed of two different approaches: one semi-quantitative visual evaluation protocol based on a web interface and one evaluation based on quantitative criteria.

6.2.1 Visual evaluation protocol

The visual evaluation protocol, conceived for the context of CT/PET registration of thoracic images, has been developed by [Camara-Rey, 2003] in collaboration with the clinicians of the Val-de-Grâce Hospital in Paris. It consists of a visual evaluation for several reference points inside the main structures. These reference points are the intersections of the contours of the lungs with the rulers superimposed on the images (see Figures 6.1). The observers have to estimate the registration error at each reference point and classify it as "good registration" if the error is inferior to 0.5 cm, "acceptable registration" if it is less than 1.5 cm or "unacceptable registration" when the error is superior to 1.5 cm. This method provides fast semi-quantitative measures of the precision of registration results. Inter-observers variability is very low and this protocol is objective enough to be used for evaluating the results. However it was developed for diagnosis purposes. Therefore, future work should adapt the

protocol for radiotherapy applications. Moreover, some of the aforementioned methods could be used in order to improve the evaluation of the results.

6.2.2 Quantitative evaluation

As a first quantitative evaluation of the registration, we have computed different metrics in order to compare the volumes and the surfaces of the lungs segmented in the original CT and on the registered PET. The segmentation of the lungs in CT and PET images is described in Chapter 3. Here, for the segmentation of the lungs in the registered PET, we have used the same approach as for segmenting the lungs in a PET image when the corresponding CT image is available, i.e. when the images have been acquired with a CT/PET combined device. As for original PET images, the segmentation of the lungs is very challenging and, in addition to this, one could wonder if segmenting the lungs in a deformed image has any sense. We first realized an evaluation by deforming the segmented lungs in the original PET and then comparing the result of the registration with the CT lungs. The results were less realistic because the uncertainty of the segmentation in the PET (see Figure 6.2) is propagated by means of the transformation and errors are cumulated along the whole process. In order to solve this problem, a fuzzy segmentation of the PET lungs could be computed, what would improve the robustness of the evaluation method.

Even if the segmentation of the lungs in the PET images (deformed or not) remains challenging, the results illustrated here provide a first idea of the quality of the registration.

The metrics used to compare the volumes of the segmented lungs are: false positive (FP), false negative (FN), intersection-union ratio (IUR), similarity index (S), sensitivity ($SENS$) and specificity ($SPEC$). The criteria that compare the surfaces of the lungs are: mean distance (D_{mean}), RMS (root mean square) distance (D_{RMS}) and Hausdorff distance (D_H). They are defined and explained in Appendix C.

Tables 6.1 and 6.2 show the results of comparing the volumes and the surfaces of the segmented lungs. Here M_{PET}, M_N and M_C do not represent the meshes of the segmented lungs but, for the sake of simplicity, they represent both their volumes and their surfaces. For each patient, the first row, M_{PET}-M_N, compares the original CT lungs M_N (in end inspiration) with the original PET lungs M_{PET}. The last row compares the PET lungs M_{PET} with the closest CT M_C computed with the breathing model. The comparison M_{PET}-M_C furnishes some reference values because we assume that the closest CT is the one that fits the best the PET among all the instants of the breathing cycle.

In the tables, lines between M_{PET}-M_N and M_{PET}-M_C show the results of comparing the segmented lungs in the registered PET images with the original CT M_N, which is the target image. We can expect to obtain similar results as the ones obtained in the reference comparison M_{PET}-M_C.

noBM-noUni means that we evaluate the results of a registration that does not take into account the breathing model and that uses a Mea-Gau point distribution (cf. Chapter 4), which means that flat regions do not contain any landmark. The method noBM-Uni, however, use Mea-Gau-Uni for landmarks selection, in order to add some points of interest in flat regions of the surface of the lungs. In Table 6.2, BM-noUni labels the results obtained with the approach that combines our registration method and the breathing model, as described in Chapter 5. In this line, the method for selecting the landmarks is Mea-Gau. BM-Uni means that the breathing model and the method Mea-Gau-Uni are used.

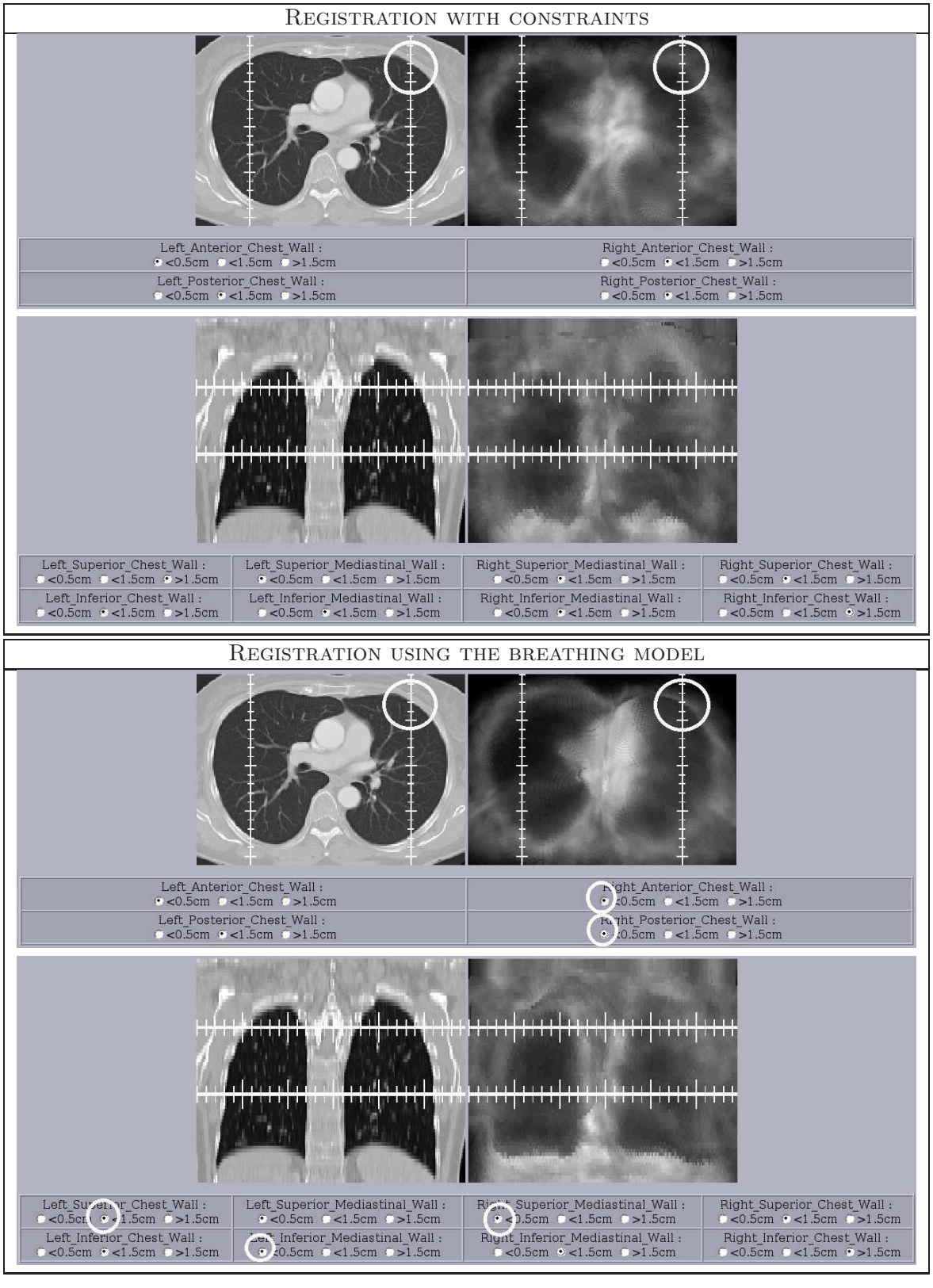

Figure 6.1: Illustration (axial and coronal views) of some results of the two registration methods ready to be evaluated with our visual evaluation protocol. The improvements are surrounded with white circles.

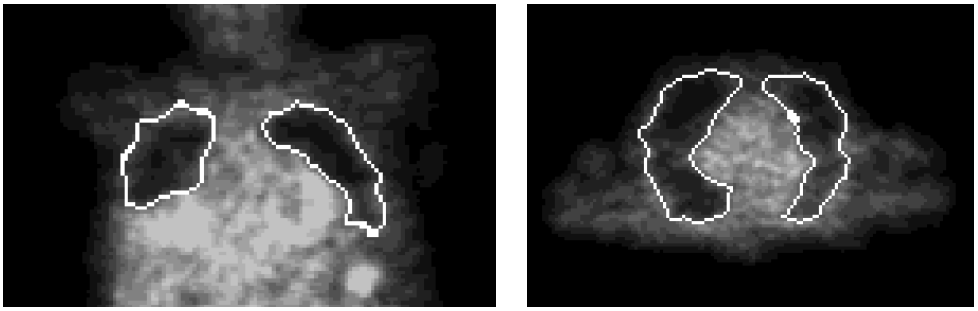

Figure 6.2: Coronal (left) and axial (right) views of a PET image with the contours of the segmented lungs superimposed. This figure illustrates the uncertainty of the segmentation in PET, as in several regions of the images it is very difficult to verify if the result is accurate or not.

6.3 Results of the registration with constraints

Our registration algorithm has been applied on 5 data sets coming from different medical centers. Each dataset is composed of one PET image and two CT images at different instants of the breathing cycle. The sizes of the CT images are typically of $512\times512\times Z$ or $256\times256\times Z$ voxels with Z varying from 52 to 137 and their resolutions are $dx \times dy \times 5$ mm^3 for the three directions of the space, with dx and dy varying from 0.7 to 1.5 mm. The sizes of the PET images are typically of $144 \times 144 \times Z$ or $168 \times 168 \times Z$ voxels with Z varying from 202 to 329 voxels. Their resolutions are typically of $4 \times 4 \times 4$ mm^3.

Figure 6.1 illustrates one example of result obtained with our registration method with constraints, when ready to be evaluated with our visual evaluation protocol. In this example, the errors estimated by the expert are good or acceptable in most cases. However, in the coronal views, the error at the left superior chest wall and at the right inferior chest wall are unacceptable.

In Table 6.1, it can be observed that with our registration method the registered PET lungs are much closer to the original CT lungs than the original PET lungs. Values of the different metrics computed for the registered images are much better than values in M_{PET}-M_N and become similar to the values in line M_{PET}-M_C. In several cases (patient 1 from Anderson Cancer Center and patient 1 from Val-de-Grâce Hospital) the results are even notably better than for M_{PET}-M_C. See, for example, the values of IUR and S, and the distances D_{mean}, D_{RMS} and D_H. For patient 12 from Val-de-Grâce Hospital, the mean and RMS distances are not much lower than for M_{PET}-M_C, but Hausdorff distance is. In most of the cases illustrated here, the landmarks selection method (noUni vs. Uni) does not influence much the final comparison.

6.4 Results of the registration using the breathing model

In this section, we show the improvement achieved by using the breathing model. A comparison of the results without and with the model is shown in Figure 6.1 and in Table 6.2.

As commented in Section 6.3, the registration method without the breathing model furnishes quite satisfactory results. Nevertheless, the results of the approach that combines the registration method with the breathing model are much better. In Figure 6.1 this is clearly visible. For example, the region inside the big white circle is visually better registered. The evaluation by the expert is better in the case where the breathing model is used. The

Comparison	FP	FN	IUR	S	$SENS$	$SPEC$	D_{mean} (mm)	D_{RMS} (mm)	D_H (mm)
Anderson Cancer Center - patient 1									
M_{PET}-M_N	0.64	0.08	0.56	0.72	0.92	0.59	11.91	14.76	54.00
noBM-noUni	0.29	0.08	**0.71**	**0.83**	0.92	0.76	**6.17**	**9.41**	**44.00**
noBM-Uni	0.30	0.08	**0.71**	**0.83**	0.92	0.75	**6.17**	**9.35**	**44.00**
M_{PET}-M_C	0.20	0.34	0.55	0.71	0.66	0.77	10.79	13.69	47.00
Val-de-Grâce Hospital - patient 1									
M_{PET}-M_N	2.86	0.04	0.25	0.40	0.96	0.25	29.46	41.20	143.00
noBM-noUni	0.33	0.15	**0.64**	**0.78**	0.85	0.72	**7.21**	**10.37**	**48.00**
noBM-Uni	0.33	0.15	**0.64**	**0.78**	0.85	0.72	**7.00**	**10.16**	**52.00**
M_{PET}-M_C	0.72	0.11	0.52	0.68	0.89	0.55	10.03	14.44	72.00
Val-de-Grâce Hospital - patient 12									
M_{PET}-M_N	1.74	0.20	0.29	0.45	0.80	0.31	29.42	43.66	141.00
noBM-noUni	0.99	0.04	0.48	0.65	0.96	0.49	11.46	14.65	**52.00**
noBM-Uni	1.03	0.04	0.48	0.64	0.96	0.48	11.82	15.12	**56.00**
M_{PET}-M_C	0.47	0.15	0.58	0.73	0.85	0.64	9.57	16.34	86.00

Table 6.1: Results of volume and surface comparisons for the segmented lungs in the CT and in the registered PET computed with the registration method with constraints.

improvements are marked with white circles in the figure. In particular, one of the reference points with unacceptable results has become acceptable and the accuracy of the registration in order regions have been notably improved.

In Table 6.2 we compare the results of our registration method without and with the breathing model. Again, it can be observed that the breathing model allows to compute more accurate results for these two patients. For instance, for patient 3 from Val-de-Grâce Hospital, which is a healthy case without a tumor in the lungs, the values of both FP and FN are reduced with the breathing model approach. The values of IUR and S are even higher than for the case M_{PET}-M_C, and the distances measures are lower. Patient 5 from Val-de-Grâce Hospital is a pathological case including one tumor in the lungs. The results in this case, in contrast with patient 3, are specially improved with a pseudo-uniform landmark selection combined with the registration method that includes the breathing model (BM-Uni). In particular, IUR, S and the mean distance D_{mean} are very close to the values obtained for M_{PET}-M_C.

6.5 Discussion and future work

In view of the results, we can conclude that the registration algorithm furnishes correct results and that they are improved by the use of the breathing model. However, several points have to be discussed regarding possible improvements of the methodology:

- Here we have shown the results of comparing the volumes and the surfaces of the lungs segmented in the original CT and the lungs segmented on the registered PET. One could wonder if segmenting the lungs in a deformed image has any sense. We first realized an evaluation by deforming the segmented lungs in the original PET and

Comparison	FP	FN	IUR	S	$SENS$	$SPEC$	D_{mean} (mm)	D_{RMS} (mm)	D_H (mm)
Val-de-Grâce Hospital - patient 3									
M_{PET}-M_N	0.99	0.12	0.44	0.62	0.88	0.47	18.61	28.32	123.00
noBM-noUni	1.45	0.01	0.40	0.57	0.99	0.40	15.73	20.73	79.00
noBM-Uni	1.45	0.01	0.40	0.57	0.99	0.40	15.65	20.63	78.00
BM-noUni	**0.82**	**0.02**	**0.54**	**0.70**	0.98	0.54	**11.36**	**16.38**	**74.00**
BM-Uni	**0.82**	**0.02**	**0.54**	**0.70**	0.98	0.55	**11.23**	**16.20**	**72.00**
M_{PET}-M_C	0.45	0.36	0.44	0.62	0.64	0.59	15.17	18.80	79.00
Val-de-Grâce Hospital - patient 5									
M_{PET}-M_N	1.37	0.07	0.39	0.56	0.93	0.40	18.95	27.70	101.00
noBM-noUni	1.64	0.03	0.37	0.54	0.97	0.37	17.68	26.48	125.00
noBM-Uni	1.65	0.03	0.36	0.53	0.97	0.37	17.86	26.88	125.00
BM-noUni	1.83	0.05	0.33	0.50	0.95	0.34	15.20	23.72	109.00
BM-Uni	1.40	0.05	**0.40**	**0.57**	0.95	0.41	**13.74**	21.38	96.00
M_{PET}-M_C	0.47	0.38	0.42	0.60	0.62	0.57	13.77	17.97	78.00

Table 6.2: Results of volume and surface comparisons for the segmented lungs in the CT and in the registered PET computed with the registration method including the breathing model.

then comparing the result of the registration with the CT lungs. This furnished less realistic results because the uncertainty of the segmentation in the PET is propagated by means of the transformation and errors are cumulated along the whole process. One improvement for this problem could be to use a fuzzy segmentation of the PET lungs, which would represent better the challenge of this task. Then this fuzzy segmentation could be deformed with the registration transformation. A gain in robustness can be expected.

- In some of the registered cases, the heart of the PET image has been deformed in an unrealistic way. This is due to the fact that our method constrains the surfaces of the lungs and the tumor, but the deformation in the rest of the images is not precisely constrained. This problem is clearly present in the example in Figure 6.3. A solution for this would be to take into account the heart as a rigid structure as we can consider that its shape does not vary much during breathing. The cardiac cycle cannot be taken into account here because the heart in the PET image can be considered as an average image during acquisition time. The method for heart segmentation proposed in Chapter 3 can be extended to PET images and then the inclusion of this organ in the registration method will be straightforward since the method proposed in Chapter 4 can deal with several objects on which particular transformations are imposed. The addition of rigidity constraints avoids the unrealistic deformation of the heart and it furnishes satisfactory results, as it can be observed on the first example in Figure 6.4.

- A detailed study should be carried out in order to identify all sources of imprecision. For instance, the conversion from volume to mesh and from mesh to volume implies some error in the total volume of the objects. The inaccuracy of the segmentation, due to the partial volume effect in particular, as well as the interpolation of the deformed images also introduce some imprecision that should be quantified.

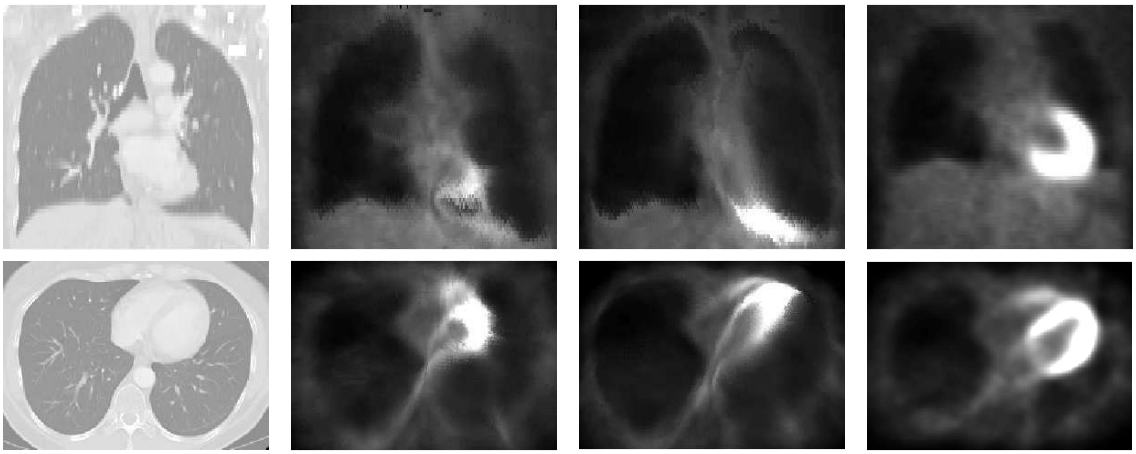

(a) (b) (c) (d)

Figure 6.3: Coronal (top row) and axial (bottom row) views of a CT image (a), the corresponding PET (d) and the registration results without (b) and with (c) a breathing model. In both cases, the heart has been unrealistically deformed.

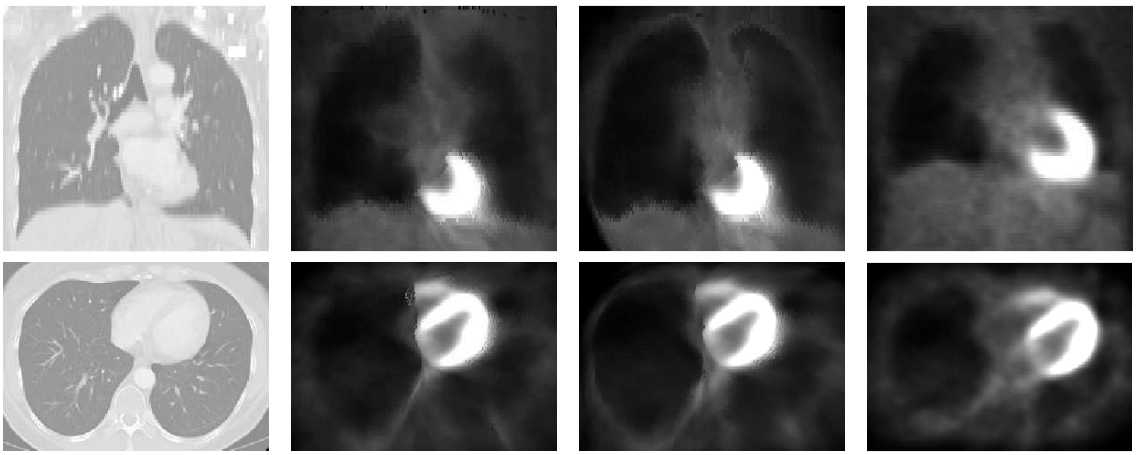

(a) (b) (c) (d)

Figure 6.4: Coronal (top row) and axial (bottom row) views of a CT image (a), the corresponding PET (d) and the registration results without (b) and with (c) a breathing model. For the same case as in Figure 6.3, rigidity constraints have been added to the registration and, therefore, the results are visually much better.

With respect to the evaluation stage, different points have to be commented:

- Evaluation of registration results is not easy. Even with the defined metrics it is not obvious to know which measure is more adapted to the comparison. For this reason, a specific combination of the proposed criteria could be defined in order to decide quantitatively which result is the best. For example, the approach proposed by [Chambon, 2005] could be used. She establishes a classification based on the average of the ranks associated to each criterion.
- The evaluation stage have to be improved with more datasets and more tests in order to

compare in detail some steps of the method. For example, we have compared here two different distributions of landmarks but there are other possible manners of selecting features: randomly, homogeneously, using points with high displacement during the breathing cycle, etc. The influence of the number of landmarks should also be studied.

- The evaluation protocol designed for the evaluation of registered images has not been conceived to take into account pathological cases. The web interface can be improved in collaboration with radiologists so that it fits better their requirements and their expertise to evaluate specifically tumor registration.

- In addition, the evaluation should be performed by a group of medical experts and radiologist in order to validate the proposed approach.

CHAPTER 7

Conclusions and future work

7.1 Overview and contributions

In this work we deal with medical data consisting of 3D CT and PET images of pathological cases, exhibiting tumors in the lungs. We have developed a registration algorithm adapted to the presence of these pathologies in the thoracic region. We proposed a method that benefits from *anatomical knowledge* in order to improve the robustness and accuracy of the different steps of the algorithm. This integration of anatomical knowledge is the common link of this work. This knowledge is used in order to guide the segmentation and registration of CT and PET images. The combination of the perceptual level and the semantic level simplifies the algorithms, improves the effectiveness, increases the automaticity, makes them more robust and closer to reality. In the next paragraphs the main contributions of this work are summarized and the possible or necessary improvements are commented.

Structures segmentation
The first step consists of an automatic segmentation of structures clearly identifiable in CT and PET: lungs, liver, kidneys, heart and tumor. The addition of anatomical knowledge and *consistency tests*, in order to detect potential errors and repair them, improves the robustness of the algorithm for images coming from different patients and different medical centers. Thus, the segmentation of the contours of the body and the lungs in CT and in PET, as well as the segmentation of the skeleton in CT, clearly benefit from the integration of anatomical knowledge even if some parameters could be better tuned to cope with the variability.

The most challenging task is the segmentation of the lungs in PET when the transmission PET image is not available and the exam has not been acquired with a combined CT/PET device. In particular for this case, the proposed approach does not allow to obtain very precise results for all the cases. Thus, a further evaluation of the segmentation results is necessary in order to validate our method. One possible improvement is to compute a fuzzy segmentation of the lungs in PET. This approach is better adapted to the type of information furnished by this modality due to the inherent spatial imprecision. Moreover, for the evaluation of the registration with the segmented lungs, a fuzzy approach would avoid the propagation of erroneous segmentations.

The processing chains for the kidneys and the liver still have to be adapted in order to furnish an automatic and robust algorithm by adding consistency tests as for the other structures.

Heart segmentation
The method proposed for heart segmentation uses fuzzy structural knowledge coming from *spatial relations* in order to segment the heart in non-contrast CT images in a robust way. This type of approach was not used in this context before. First, spatial relations are used to define the region of interest of the heart and then, from the fuzzy sets representing the spatial relations, a new external force is derived and is introduced in the evolution scheme of a deformable model.

The most sensitive step of our method is the initialization of the deformable model. If the small sphere is not centered inside the heart, the results of the segmentation may be unsatisfactory. This step can be improved by adding an interactive interface at this stage in order to let the user correct the initialization if necessary. This kind of interaction is easily accepted and even often desired by clinicians. The subsequent steps of the proposed approach have proved to be robust enough for the targeted applications.

Tumor segmentation
The method we propose for tumor segmentation benefits from medical and expert knowledge and furnishes correct results. The *semi-interactive* stage is not a disadvantage because physicians prefer to control this crucial step.

However, for the cases where the tumors are in contact with the walls of the lungs or if they have an important size or contain a necrosis, the proposed algorithm is not accurate enough in some cases. The algorithm should thus be improved in order to furnish robust results for all the situations.

Registration with rigidity constraints
Our registration method consists in computing a deformation of the PET image guided by a group of landmarks and with *tumor-based constraints*. The proposed algorithm avoids undesired tumor misregistrations and preserves tumor geometry and intensity. One of the originalities of our method is that the positions of the landmarks are *adapted to anatomical shapes*. They are *automatically* and uniformly detected by combining mean and Gaussian curvatures and matched with ICP algorithm. These landmarks guide the deformation of the PET image towards the CT image. Thus, the proposed approach has two main advantages:

1. the registration remains consistent and robust even if the tumor segmentation is not perfect;

2. the registration preserves the local differences, which can be very useful because we could discover a part of the anatomy that is touched by the pathology and could not be seen in the CT image.

The originality of the proposed approach is again to strongly rely on anatomical structures to guide a feature-based registration algorithm, to integrate constraints specific to these structures on the one hand, and to the pathologies on the other hand.

Still some aspects have to be improved. Regarding landmarks selection, other curvature operators can be used. For example, the multiplication with the gradient magnitude improves the results as concluded by [Hartkens et al., 2002b]. The interpolation of the resulting image does not furnish visually optimal results in all cases. To avoid this problem, the inverse transformation should be computed by interpolating directly in the source PET image.

Breathing model
In order to improve the registration by introducing physiologically plausible deformations, we have also introduced a *breathing model*. This is another originality of the proposed approach. This guarantees that the deformations are more realistic compared to a geometrical approach. Although this part is still at an early stage of development, very promising results have been obtained.

A study of the different criteria for the selection of the appropriate "closest CT" has to be performed, as the RMS distance is a global criterion which does not take into account local differences or similarities between the surfaces. Another improvement would be the selection of landmarks including points undergoing important displacements during the respiration, and making these points guide the registration procedure.

7.2 Future work

Deeper evaluation
The results obtained in the different parts of this work are very promising. However, the segmentation methods proposed for the different structures of the thorax (lungs, heart) and for tumors should be applied to larger databases, with manual segmentations obtained from a common agreement of a group of experts to go further in the evaluation.

The registration method, in particular combined with the breathing model, has to be validated too. More datasets should be used and more tests have to be performed in order to compare in detail some steps of the method.

The evaluation protocol designed for the evaluation of registered images has not been conceived to take into account pathological cases. It must therefore be adapted, taking into account specific requirements of this particular application as well as expertise and reviewing tools from radiotherapists. The web interface can be improved in collaboration with radiologists so that it fits better their requirements. Other methods, as those mentioned in Chapter 6, can also be used in order to improve the evaluation of the results. Indeed, as explained in the general introduction, the ultimate goal of this research is to provide a good definition of the position and motion of the tumors, while preserving PET information, in order to precisely control the radiation dose which should be applied in radiotherapy.

Inclusion of the heart in registration
Future work aims at applying our heart segmentation algorithm to other imaging modalities such as positron emission tomography (PET) images. Our method can also be used for diagnosis of other cardiovascular diseases. In particular, the new combined devices PET/CT and SPECT/CT, widely used in cardiology and oncology, often furnish non-contrast and low-resolution CT images. Our approach is adapted to this type of data.

Further applications include the use of the segmentation of the heart in registration algorithms, necessary even in PET/CT and SPECT/CT combined devices, and subsequently, in radiotherapy planning procedures. In particular, in our registration method, the inclusion of the heart in the registration procedure can eliminate the unrealistic deformations produced in the region between the lungs due to the lack of constraints. Our method constraint the surfaces of the lungs and the tumor, but the deformation in the rest of the images is not precisely constrained. Therefore, a solution for this would be to take into account the heart as a rigid structure as we can consider that its shape does not vary much during breathing,

it is just slightly translated in the thorax. The inclusion of this organ in the registration method is thus straightforward.

Breathing model more adapted to tumoral cases
In this work, we consider the impact of the physiology on lung surface deformation, based on reference data of normal human subjects for the computation of the breathing model. The methodology presented in this work will further benefit from the inclusion of patho-physiology specific data once established. The use of normal lung physiology serves to demonstrate improvements in CT and PET registration using a physics-based 3D breathing lung model. Future investigations are expected based on refining the deformation model using patho-physiological conditions and including a more precise characterization of the tumor movement and its influence on the breathing. Ultimately, validation of the breathing model in pathological cases should be task-based performance on a clinical problem.

Comparison with other methods
Our registration method can be compared with other methods (cf. Chapter 1). This will provide some conclusions on the limits of each method and their application fields.

Another issue is the combination of the proposed approach with the one by [Camara et al., 2007] in order to develop a hybrid algorithm which will account for features and intensity information at the same time.

The breathing model described in this work can be used for CT-CT mono-modality registration and compared with other existing methods as the one by [Sarrut et al., 2006].

Clinical applications
It is necessary to carry out a detailed study of the rigidity properties of the tissues surrounding a pathology. As a first approach, we have assumed that the rigidity of the tissues decreases with the distance to the tumor. Replacing the distance by another function would then be straightforward using our formulation.

Our approach can be integrated as a powerful software tool for clinical applications. It could be used in order to "make breath" the PET image so that any instant of a 4D CT (or a simulated 4D CT) has its corresponding PET. This would notably ease the tracking of the really pathological tissues during treatment. This would be very useful in radiotherapy planning in order to define with a better precision the areas to be irradiated and reduce security margins, which is the main goal of the work presented here.

APPENDIX A

Segmentation algorithms for the kidneys and the liver in CT and PET

In this appendix, the algorithms for the segmentation of the kidneys and the liver, both in CT and in PET, are summarized.

As a hierarchical approach is used, we rely on the previously segmented structures (the lungs) as described in Chapter 3. Thus, the region of interest of the kidneys and the liver is defined as the region below the lungs, and this knowledge is integrated in the segmentation algorithms (Figures A.1 to A.3). Then, the kidneys are detected because they are easier to segment by using the anatomical knowledge that they are symmetrical structures. A similar algorithm is used to segment the kidneys in CT and in PET (Figure A.1).

The segmentation of the liver takes into account the segmented kidneys. The algorithm is slightly different for CT and PET. In CT, we repeat three times a k-means classification followed by a largest component selection (Figure A.2). This "k-means filtering" is necessary in CT because there are more structures with the same grey level as the liver than in PET (Figure A.3). Therefore, it is necessary to use the algorithm adapted to each modality for the segmentation of these organs.

The proposed algorithms have been applied on 5 data sets coming from different medical centers. Each dataset is composed of one PET image and one CT image. The sizes of the CT images are typically of $256 \times 256 \times Z$ voxels with Z varying from 154 to 256 and their resolutions are $dx \times dy \times dx$ mm^3 for the three directions of the space, with dx and dy varying from 2.0 to 2.3 mm and dz varying from 3.7 to 5 mm. The sizes of the PET images are typically of $144 \times 144 \times Z$ or $256 \times 256 \times Z$ voxels with Z varying from 192 to 287 voxels. Their resolutions are typically of $4 \times 4 \times 4$ mm^3.

Some examples of intermediate and final results for kidneys and liver segmentation are illustrated in Figure A.4 for a CT image and in Figure A.5 for a PET image. It can be observed that the final results are very accurate in CT. However, in PET, due mainly to the low resolution of the images, the results do not include all the regions belonging to the targeted organs. This also depends on the tracer used for the acquisition of the PET images and how it fixes these organs.

The inclusion of consistency tests would improve the robustness of the proposed algorithms. For the moment, these algorithms sometimes have to be adapted to the different cases.

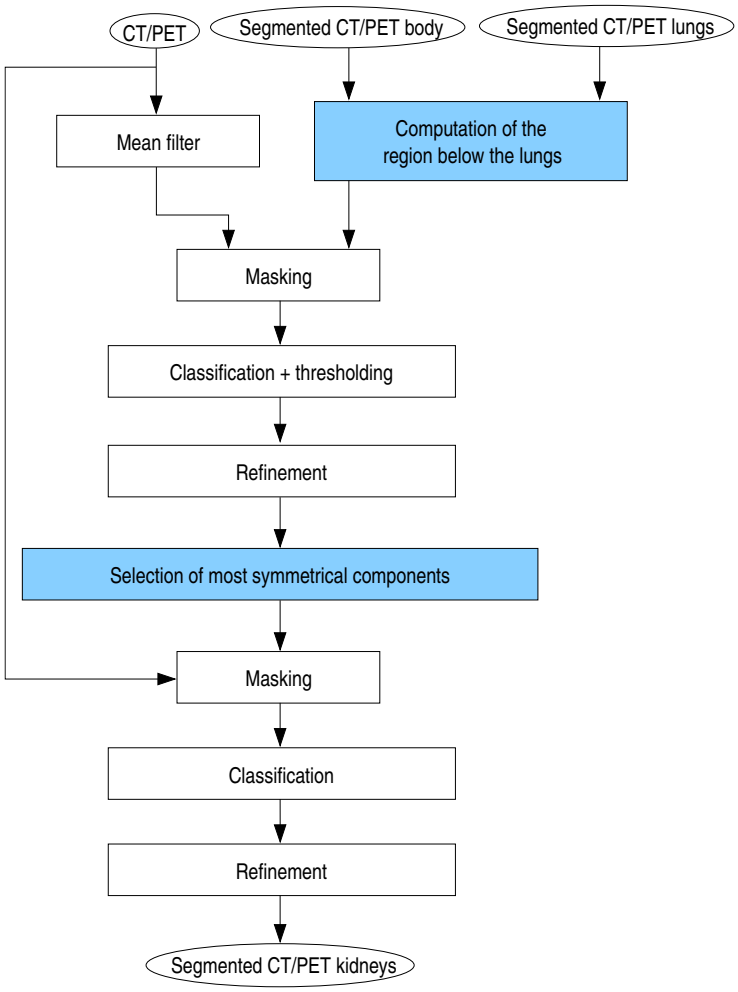

Figure A.1: Diagram of the segmentation of the kidneys in CT and in PET. Boxes in light blue indicate the integration of anatomical knowledge *directly in the method*.

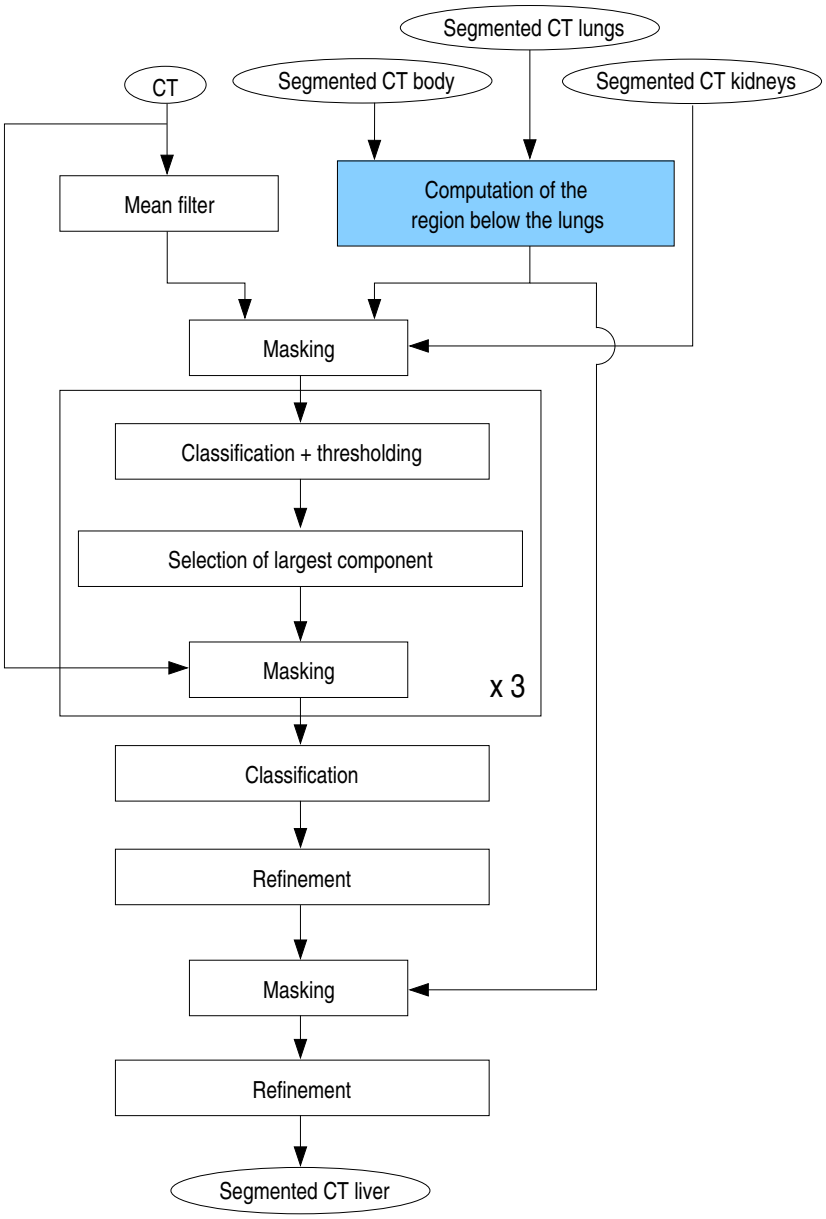

Figure A.2: Diagram of the segmentation of the liver in CT.

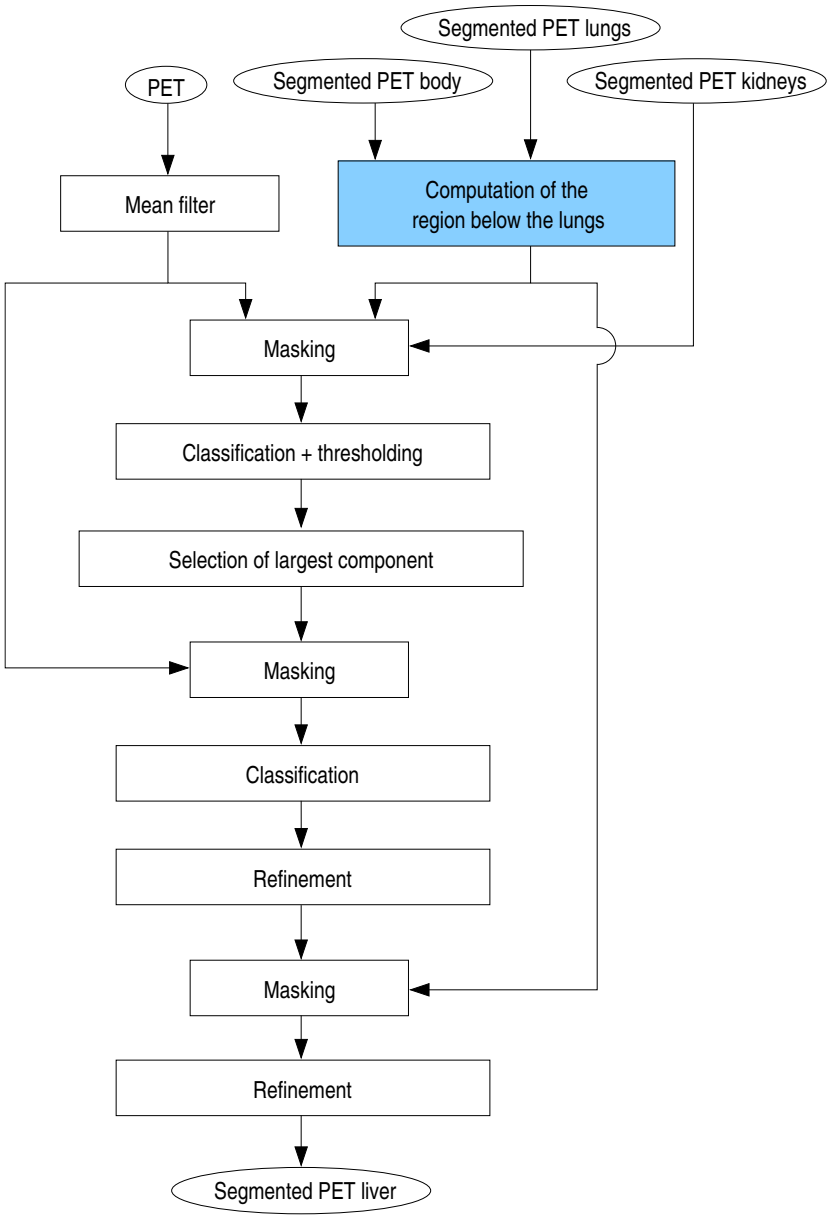

Figure A.3: Diagram of the segmentation of the liver in PET.

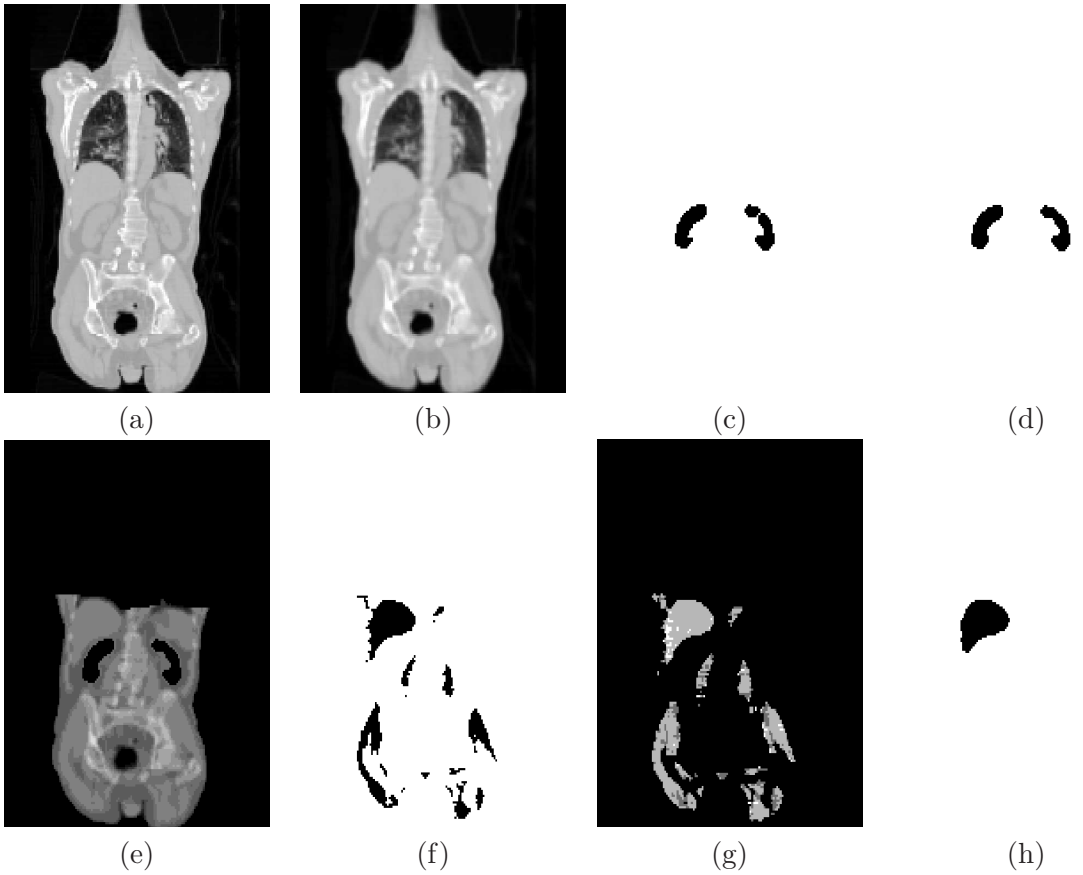

Figure A.4: Coronal views of some results of kidneys and liver segmentation on a CT image: (a) original CT image, (b) result after the mean filter, (c) most symmetrical components after the k-means classification, (d) final segmented kidneys, (e) result of the k-means classification after masking the CT image with the region below the lungs and the segmented kidneys, (f) result of class selection in the first iteration of the "k-means filtering", (g) result of applying the k-means algorithm at the second iteration, (h) final segmented liver.

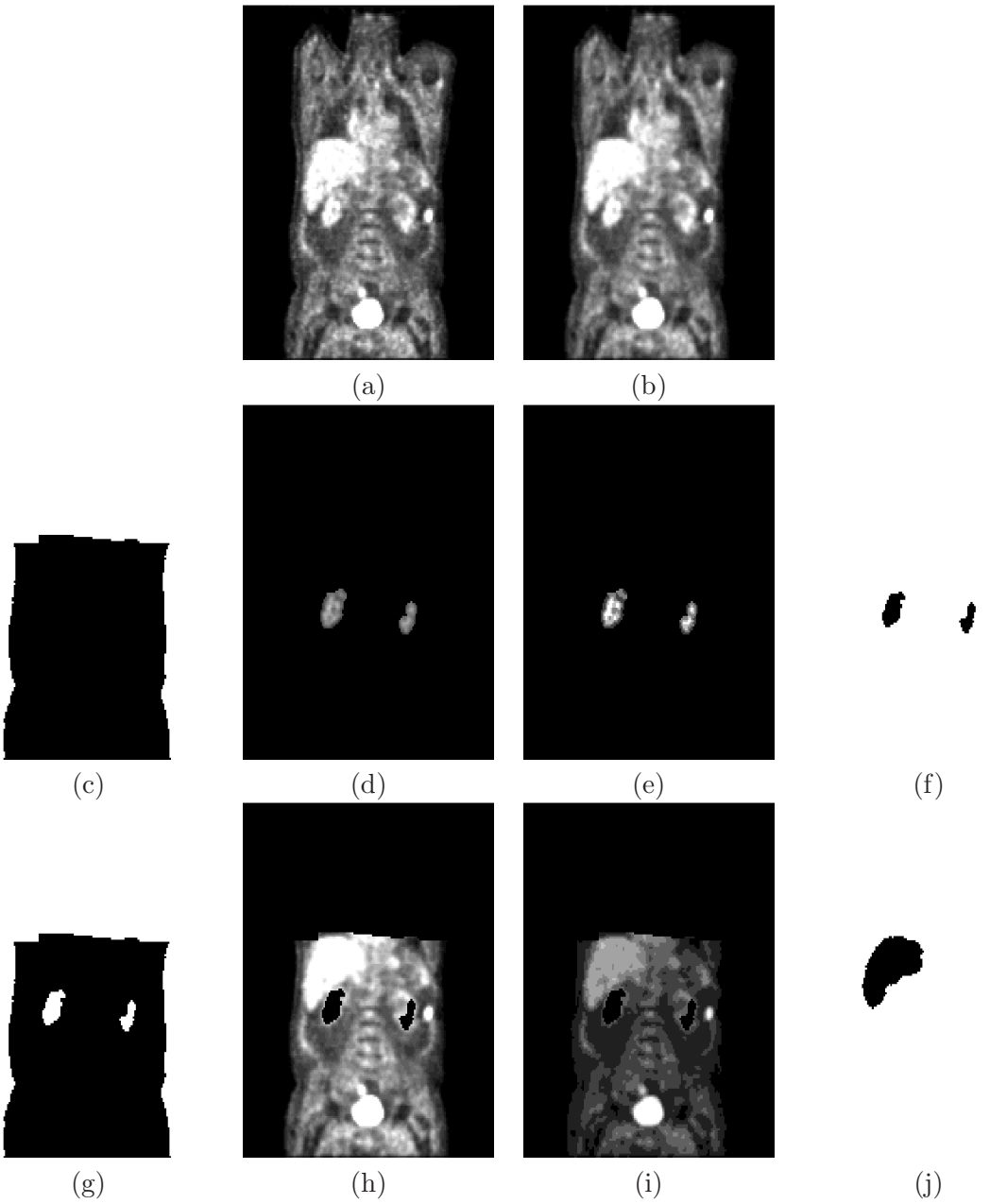

Figure A.5: Coronal views of some results of kidneys and liver segmentation on a PET image: (a) original PET image, (b) result after the mean filter, (c) mask of the region below the lungs, (d) PET image masked with the most symmetrical components, (e) last k-means classification, (f) final segmented kidneys, (g) mask of the region below the lungs excluding the kidneys, (h) result of masking the filtered PET with the previous mask, (i) result of k-means classification on the selected region for the liver, (j) final segmented liver.

APPENDIX B

Different definitions of the fuzzy spatial relation "between"

Usual anatomical descriptions of the heart include a common statement: "the heart is between the lungs". Our method relies on modeling this statement.

A complete study of the spatial relation "between" has been made by [Bloch et al., 2006]: different definitions of this spatial relation were proposed, compared and discussed according to different types of situations. The main ones are discussed here in light of the specificities of the addressed problem (heart segmentation). We restrict ourselves to definitions designed for objects having similar spatial extensions. This work has also been published in [Moreno et al., 2008b].

B.1 Crisp definitions

The most intuitive crisp definition is based on the convex hull of the union of the objects. However this approach is not appropriate to find the ROI of the heart because some parts of the heart are not included in this convex hull as shown in Figure B.1. A more flexible definition is therefore required. This is a strong argument in favor of one of the following fuzzy definitions.

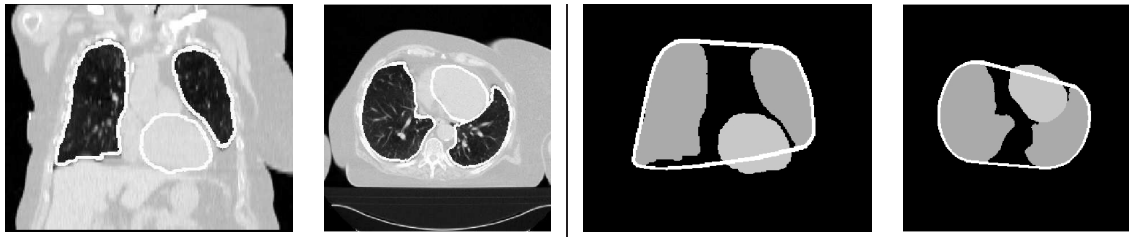

(a) (b) (c) (d)

Figure B.1: Coronal (a,c) and axial (b,d) views of an example of the segmentation of the lungs and the heart. The contours of these organs are superimposed on the original image (on the left) and the convex hull is superimposed on the segmented lungs and heart (on the right): some parts of the heart are not contained in this region.

B.2 Fuzzy dilations

The region between A_1 and A_2 is defined as a fuzzy set in the image domain. Our problem involves non-convex shapes (the lungs) which have important concavities facing each other (the cavity of the heart). For this reason, the fuzzy directional dilation definitions of the relation "between" are adapted to this case. The simplest definition is:

$$\beta_{FDil1}(A_1, A_2) = D_{\nu_2}(A_1) \cap D_{\nu_1}(A_2) \cap A_1^C \cap A_2^C, \tag{B.1}$$

where A_1 and A_2 represent the objects (the lungs in our case), A^C represents the (fuzzy) complementation of A and $D_{\nu_i}(A_j)$, $i, j \in \{1, 2\}$, is the fuzzy dilation of A_j with the fuzzy structuring element ν_i: $D_\nu(\mu)(x) = \sup_y t[\mu(y), \nu(x - y)]$ where μ denotes the (fuzzy) set to be dilated, ν the structuring element, t a t-norm and x and y points of space [Bloch and Maître, 1995].

The structuring elements are derived from the angle histogram between the objects [Miyajima and Ralescu, 1994]. For instance, if object A_2 is mainly to the right of object A_1, then Equation B.1 defines the region which is both to the right of A_1 and to the left of A_2 (excluding A_1 and A_2). This definition is illustrated in Figure B.2(a).

Another definition of "between", which removes the concavities of the objects which are not facing each other, is:

$$\begin{aligned}\beta_{FDil2}(A_1, A_2) = {} & D_{\nu_2}(A_1) \cap D_{\nu_1}(A_2) \cap A_1^C \cap A_2^C \\ & \cap [D_{\nu_1}(A_1) \cap D_{\nu_1}(A_2)]^C \cap [D_{\nu_2}(A_1) \cap D_{\nu_2}(A_2)]^C.\end{aligned} \tag{B.2}$$

In this case, if object A_2 is mainly to the right of object A_1, then Equation B.2 defines the region which is both to the right of A_1 and to the left of A_2 (excluding A_1 and A_2), but which is not to the left of both A_1 and A_2 nor to the right of both. Figure B.2(b) shows the region between the lungs obtained with this definition.

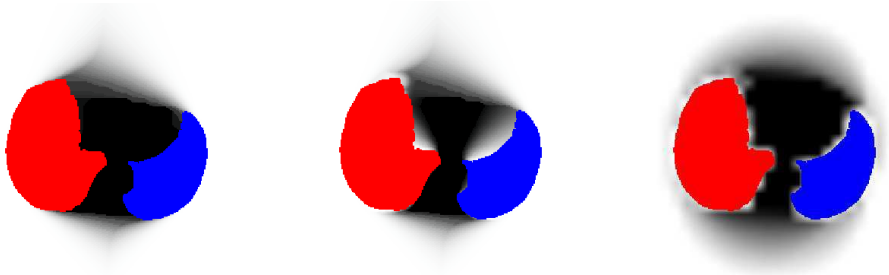

(a) (b) (c)

Figure B.2: Fuzzy regions between the lungs, superimposed on an axial slice of the segmented lungs (in red and blue): (a) β_{FDil1}, (b) β_{FDil2} and (c) β_{FVisib}. Their membership values vary from 0 (white) to 1 (black). It can be observed that β_{FDil1} does not remove the concavities of the objects which are not facing each other.

B.3 Admissible segments

The notion of visibility plays an important role in the definition of "between" as illustrated by Bloch et al. [Bloch et al., 2006]. The visible points are those which belong to admissible

segments[1] and the region $\beta_{Adm}(A_1, A_2)$ between A_1 and A_2 can then be defined as the union of admissible segments. However, the definition of admissible segments may be too strict in some cases, in a similar manner as the convex hull definition (see Figure B.1). For this reason, the notion of approximate (or fuzzy) visibility has been introduced. Thus, a segment $]a_1, P]$ with $a_1 \in A_1$ (respectively $[P, a_2[$ with $a_2 \in A_2$) is said semi-admissible if it is included in $A_1^C \cap A_2^C$. At each point P of space, we compute the angle the closest to π between two semi-admissible segments from P to A_1 and A_2 respectively. This is formally defined as:

$$\begin{aligned}\theta_{min}(P) = \min\{|\pi - \theta|, \theta = \\ \angle([a_1, P], [P, a_2]),]a_1, P] \text{ and } [P, a_2[\text{ semi-admissible}\}.\end{aligned} \tag{B.3}$$

The region between A_1 and A_2 is then defined as the fuzzy region of space with membership function:

$$\beta_{FVisib}(A_1, A_2)(P) = f(\theta_{min}(P)) \tag{B.4}$$

where f is a function from $[0, \pi]$ to $[0, 1]$ such that $f(0) = 1$, f is decreasing, and becomes 0 at the largest acceptable distance to π (this value can be tuned according to the context). The result obtained with this definition is illustrated in Figure B.2(c).

B.4 Selected definition

In order to decide which definitions better match our problem, we have compared them with respect to two criteria:

1. *Concavities.* The fuzzy dilation definition β_{FDil1} does not remove the concavities of the objects which are not facing each other (see Figure B.2). However, β_{FDil2} and β_{FVisib} do. Therefore, we prefer to use β_{FDil2} or β_{FVisib}, in order not to include the small concavities of the lungs which do not correspond to the heart but to vessels and bronchi.

2. *Complexity.* For the methods based on fuzzy dilations, the complexity is $O(NN_\nu)$ where N denotes the cardinality of the bounded space in which the computation is performed (the image) and N_ν is the cardinality of the support of the structuring element used in the fuzzy dilations. The morphological approach additionally requires the computation of the angle histogram which has a complexity of $O(N_1 N_2)$, where N_i denotes the cardinality of A_i. The computation of $\beta_{Adm}(A_1, A_2)$ for the admissible segments method is of the order of $N_1 N_2 \sqrt{N}$. Finally, the fuzzy visibility approach has a complexity of $O(NN_1N_2)$.

As β_{FDil2} and β_{FVisib} furnish comparable results with respect to concavities, we prefer β_{FDil2} due to its lower complexity. In order to reduce computing time, images can be under-sampled to obtain the region between the lungs, since a very precise result is not necessary at this stage. In this case, the small concavities may be removed by the under-sampling and therefore the differences between β_{FDil1} and β_{FDil2} are notably reduced.

Finally, we define: $\beta_{btw}(A_1, A_2) = \beta_{FDil2}(A_1, A_2)$. The interest of the selected fuzzy definitions is that the between region extends smoothly outside the convex hull of the union of both objects which is a required feature for our application (see Figure B.1).

[1] A segment $]x_1, x_2[$, with x_1 in A_1 and x_2 in A_2, is said to be admissible if it is included in $A_1^C \cap A_2^C$.

B.5 Results using different definitions

Figure B.3 shows some results (using parameters detailed in Section 3.3) of the segmentation of the heart with different definitions of the spatial relation "the heart is between the lungs". The results obtained using any of the fuzzy definitions β_{FDil1}, β_{FDil2} or β_{FVisib} are very satisfactory and very similar in all cases.

(a) (b) (c)

Figure B.3: Coronal views of some results of heart segmentation with different definitions of the spatial relation "between": (a) using β_{FDil1} and (b) using β_{FDil2}. A similar result is obtained with β_{FVisib}. (c) Result of heart segmentation using β_{FVisib}, when the acceptable distance to π is not tuned correctly.

For the use of β_{FVisib}, however, the acceptable distance to π (i.e. the shape of the function f in Equation B.4) has to be tuned appropriately in order to obtain a correct result. Otherwise, incorrect results of heart segmentation can be obtained as illustrated in Figure B.3(c). This value could vary for different anatomies. The definitions of "between" that use fuzzy dilations do not have this limitation as the shape of the structuring element is computed from the angle histogram, which is adapted automatically to each particular case.

B.6 Conclusion

In this appendix, several definitions of the spatial relation "between" are presented. The discussion of the results shows that a fuzzy dilation definition which removes concavities is best adapted to our problem.

APPENDIX C

Metrics: criteria to compare volumes and surfaces

Comparison of objects is always attached to subjective criteria. However, in order to quantify the quality of results, there exist several measures which are typically used to compare an object A (automatically segmented) and an object M (manually segmented). Some of these criteria and some examples are described in this Appendix.

C.1 Volume comparison

Here A and M represent the filled volumes of the segmented objects. In the following $|A|$ and $|M|$ represent the cardinalities of the sets of voxels A and M respectively.

- False positive:

$$FP(M,A) = \frac{|A| - |M \cap A|}{|M|}$$

  and false negative:

$$FN(M,A) = \frac{|M| - |M \cap A|}{|M|}$$

  It is important to notice that the normalization is calculated with respect to M, which is the reference volume, the manual segmentation (the ground truth). Thus, FP represents the voxels of the automatic segmentation that are detected as being in the object but that, in fact, do not belong to it. FN represents the voxels that are in the object but are not detected by the automatic segmentation. Depending on the application, the relevance of FP or FN varies. For example, if the goal is to detect the extension of a tumor for treatment, FN should be very close to 0.

  FP and FN can also be normalized with respect to A. In that case, for example, a small FP_A indicates a good accuracy of the segmentation:

$$FP_A(M,A) = \frac{|A| - |M \cap A|}{|A|}$$

- Percentage error with respect to M:

$$PE_M(M,A) = \frac{|M \cup A| - |M \cap A|}{|M|} \times 100, \quad \text{or}$$

$$PE_M(M,A) = [FP(M,A) + FN(M,A)] \times 100$$

and with respect to A:

$$PE_A(M,A) = \frac{|M \cup A| - |M \cap A|}{|A|} \times 100$$

- Intersection-union ratio between both volumes:

$$IUR(M,A) = \frac{|M \cap A|}{|M \cup A|}$$

- Similarity index between both volumes:

$$S(M,A) = \frac{2|M \cap A|}{|M| + |A|}$$

As explained in [Zijdenbos et al., 1994] the similarity index S is sensitive to variations in shape, size and position (as illustrated in Section C.3) and a value of $S > 0.7$ indicates a strong agreement. The value of S is equal to 1 when A and M totally overlap.

- Sensitivity between both volumes:

$$SENS(M,A) = \frac{|M \cap A|}{|M|}$$

- Specificity between both volumes:

$$SPEC(M,A) = \frac{|M \cap A|}{|A|}$$

The sensitivity ($SENS$) and specificity ($SPEC$) measures give additional information about how the overlap of both structures is achieved (see Section C.3). Both criteria are also equal to 1 if total overlap is achieved.

C.2 Surface comparison

Here A and M represent the surfaces of the segmented objects.

- Mean distance between the surfaces:

$$D_{mean}(M,A) = \frac{1}{2}[d_{mean}(M,A) + d_{mean}(A,M)]$$

with

$$d_{mean}(M,A) = \frac{1}{|M|} \sum_{m \in M} D(m,A)$$

where $D(m,A) = [\min_{a \in A} d(m,a)]$ and d is the Euclidean distance.

- RMS (root mean square) distance between the surfaces:

$$D_{RMS}(M,A) = \sqrt{\frac{1}{2}[d_{RMS}(M,A)^2 + d_{RMS}(A,M)^2]}$$

with

$$d_{RMS}(M,A) = \sqrt{\frac{1}{|M|}\sum_{m\in M} D(m,A)^2}.$$

- Hausdorff distance between the surfaces:

$$D_H(M,A) = \max(d_H(M,A), d_H(A,M))$$

with

$$d_H(M,A) = \max_{m\in M} D(m,A).$$

As this measure is a maximum distance, it is a particularly severe evaluation which is sensitive to "peaks" in the segmentation (see Section C.3 for some examples).

C.3 Illustrative examples

Figure C.1 illustrates several examples of comparison between objects (in 2D for the sake of readability). The detailed descriptions of these objects are in Table C.1.

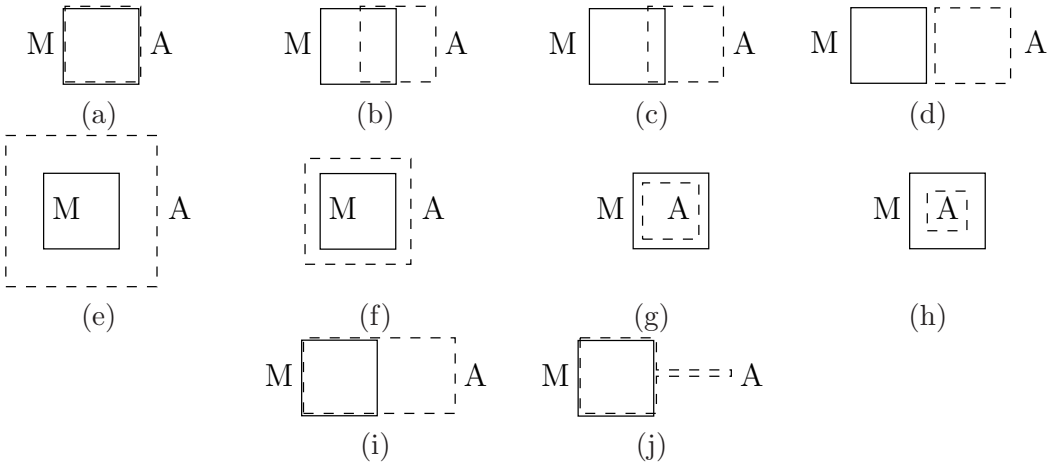

Figure C.1: Illustrative examples for volume/surface comparison. M (continuous line) represents the manually segmented object and A (dashed line) represents the automatically segmented object.

Tables C.2 and C.3 show the results of the comparisons of objects A and M using the different criteria defined in Sections C.1 and C.2 respectively. Here we present a brief interpretation of the criteria and these results:

- The ideal case with a perfect segmentation is illustrated in (a). Here, all values are 0 except IUR, S, $SENS$ and $SPEC$ which are equal to 1. In general, the lower (closer to 0) values for FP, FN, PE_M, PE_A and the distances D_{mean}, D_{RMS} and D_H, the better. And the higher (closer to 1) values for IUR, S, $SENS$ and $SPEC$, the better.

	Minimum x	Maximum x	Minimum y	Maximum y
Object M	50	100	75	125
Object A in example (a)	50	100	75	125
Object A in example (b)	75	125	75	125
Object A in example (c)	87	137	75	125
Object A in example (d)	105	155	75	125
Object A in example (e)	25	125	50	150
Object A in example (f)	40	110	65	135
Object A in example (g)	57	93	82	118
Object A in example (h)	63	88	88	113
Object A in example (i)	50	150	75	125
Object A in example (j) (two rectangles)	50 100	100 150	75 98	125 102

Table C.1: Description of the examples in Figure C.1. Units are mm.

- When the automatic segmentation A contains the manual segmentation M, FN takes value 0 and $SENS$ is equal to 1 (examples (e), (f), (i) and (j)). When M contains A, FP is 0 and $SPEC$ is 1 (examples (g) and (h)).

- The difference between FP and S is that S is more sensitive to variations in shape, size and position. For example, if object A completely overlaps object M which is approximatively one half of A (case (i)), FP is almost 1, which means "incorrect detection", whereas S value is 0.67, which means "not so bad detection" (as the value is close to 0.7).

- IUR and S behave slightly differently. IUR takes lower values than S and it decreases faster than S when the differences between A and M increase (see examples (a) to (d)). Therefore, IUR is more severe than S.

- When both segmentations have the same sizes ($|A| = |M|$), S, $SENS$ and $SPEC$ have the same values (see examples (a) to (d)).

- $SENS$ and $SPEC$ give additional information about how the overlap of both structures is achieved. For instance, if the comparison of A and M yields a low sensitivity value but a high specificity one (example (h)), it means that the automatic segmentation is too small. Therefore, a correct result will provide high (close to 1) and similar

values of $SENS$ and $SPEC$ (example (j)).

- One very bad result is illustrated in (d). Here the automatic segmentation A is not at all superimposed on the manual segmentation M. Thus, FP and FN are equal to 1, and PE_M and PE_A have maximum values. IUR, S, $SENS$ and $SPEC$ are 0. However, the values of the distances (mean, RMS or Hausdorff) are comparable with the results for other cases (for example, cases (e), (i) or (j)). We can conclude that the quality of a segmentation cannot be only evaluated by taking into account the distances criteria D_{mean}, D_{RMS} and D_H.

- In particular, Hausdorff distance D_H is a very severe criterion. It measures the maximum distance between one point in M and one point in A. Thus the values of D_H for cases (i) and (j) are the same. The value of D_H in case (d) is very similar to the previous ones, however the segmentation in (d) is clearly worse than in (i) or (j). The conclusion is that the information furnished by D_H is sensitive to "peaks" in the segmentation and it has to be completed with other criteria.

Which is the best segmentation among the examples illustrated in Figure C.1?

Obviously, the best segmentation is illustrated in (a). But, among the other results, which can be considered as the closest to this ideal case?

With respect to the volume measures it is clear that the best case is (j). FP and FN have very small values or 0, error percentages PE_M and PE_A are very small, and IUR, S, $SENS$ and $SPEC$ are very close to 1. The mean distance D_{mean} is very small too. However D_{RMS} and D_H are not the best. The best distance measures are those of case (g), but the volume criteria are not specially good. In particular, the value of FN could be too high for some applications (for example, if M is a tumor and the automatic segmentation does not detect it completely). This can also be deduced from the value of $SENS$.

Example	FP	FN	PE_M (%)	PE_A (%)	IUR	S	$SENS$	$SPEC$
(a)	0.000	0.000	0.0	0.0	1.00	1.00	1.00	1.00
(b)	0.490	0.490	98.0	98.0	0.34	0.51	0.51	0.51
(c)	0.725	0.725	145.1	145.1	0.16	0.27	0.27	0.27
(d)	1.000	1.000	200.0	200.0	0.00	0.00	0.00	0.00
(e)	2.922	0.000	292.2	74.5	0.25	0.41	1.00	0.25
(f)	0.938	0.000	93.8	48.4	0.52	0.68	1.00	0.52
(g)	0.000	0.474	47.4	90.0	0.53	0.69	0.53	1.00
(h)	0.000	0.740	74.0	284.8	0.26	0.41	0.26	1.00
(i)	0.980	0.000	98.0	49.5	0.50	0.67	1.00	0.50
(j)	0.096	0.000	9.6	8.8	0.91	0.95	1.00	0.91

Table C.2: Results of volume comparisons for the examples in Figure C.1.

As a general conclusion, we can state that surface criteria have to be completed with volume criteria. However, the selection of a criterion (or a group of criteria) in order to

Example	D_{mean}	D_{RMS}	D_H
(a)	0.0	0.0	0
(b)	12.5	16.1	25
(c)	18.5	23.2	37
(d)	30.0	36.3	55
(e)	26.2	26.3	35
(f)	10.2	10.3	14
(g)	7.1	7.2	9
(h)	13.0	13.1	18
(i)	9.9	19.3	50
(j)	4.5	12.5	50

Table C.3: Results of surface comparisons for the examples in Figure C.1. Values are in mm.

compare two objects depends on the particular application and on the type of differences to be highlighted by the user. Thus, in some measure, comparison still remains subjective.

APPENDIX D

Explicit Incorporation of Prior Anatomical Information into a Nonrigid Registration of Thoracic and Abdominal CT and 18-FDG Whole-Body Emission PET Images

Journal article [Camara et al., 2007]:

- O. Camara, G. Delso, O. Colliot, A. Moreno-Ingelmo and I. Bloch, *Explicit Incorporation of Prior Anatomical Information into a Nonrigid Registration of Thoracic and Abdominal CT and 18-FDG Whole-Body Emision PET Images*, IEEE Transactions on Medical Imaging, vol. 26, number 2, pages 164-178, February, 2007.

See at the end of the manuscript.

Bibliography

Adams, R. and Bischof, L. (1994). Seeded Region Growing. *IEEE Transactions on Pattern Analysis and Machine Intelligence*, 16:641–647.

Ali, R., Schottlander, D., Reilhac, A., Yaghoubi, S., and Brady, M. (2006). Development and Validation of a Simulated Human Torso Dynamic FHBG-PET Dataset. Poster at American Molecular Imaging Conference, Orlando, Florida, USA.

Almhdie, A., Léger, C., Deriche, M., and Lédée, R. (2006). A New Implementation of the ICP Algorithm for 3D Surface Registration Using a Comprehensive Look Up Matrix. In *European Signal Processing Conference (EUSIPCO)*, Florence, Italy.

Ansari, N. and Delp, E. (1991). On Detecting Dominant Points. *Pattern Recognition*, 24(5):441–451.

Armato III, S. and Sensakovic, W. (2004). Automated Lung Segmentation for Thoracic CT: Impact on Computed-Aided Diagnosis. *Academy of Radiology*, 11(9):1011–1021.

Arsigny, V., Pennec, X., and Ayache, N. (2005). Polyrigid and Polyaffine Transformations: A Novel Geometrical Tool to Deal with Non-Rigid Deformations – Application to the Registration of Histological Slices. *Medical Image Analysis*, 9:507–523.

Ashburner, J. and Friston, K. (2005). Unified Segmentation. *NeuroImage*, 26(3):839–851.

Assen, H., Danilouchkine, M., Frangi, A., Ordás, S., Westenberg, J., Reiber, J., and Lelieveldt, B. (2006). SPASM: A 3D-ASM for Segmentation of Sparse and Arbitrarily Oriented Cardiac MRI Data. *Medical Image Analysis*, 10(2):286–303.

Atif, J., Hudelot, C., Fouquier, G., Bloch, I., and Angelini, E. (2007). From Generic Knowledge to Specific Reasoning for Medical Image Interpretation Using Graph-Based Representations. In *International Joint Conference on Artificial Intelligence (IJCAI)*, pages 224–229, Hyderabad, India.

Atif, J., Ripoche, X., and Osorio, A. (2004). Combined Quadratic Mutual Information to a New Adaptive Kernel Density Estimator for Non Rigid Image Registration. In *SPIE Medical Imaging*, volume 5370, San Diego, California, USA.

Atoui, H., Sarrut, D., and Miguet, S. (2004). Usefulness of Image Morphing Techniques in Cancer Treatment by Conformal Radiotherapy. In *SPIE Medical Imaging: Visualization, Image-Guided Procedures, and Display*, volume 5367, pages 332–340.

Azar, A., Xu, C., Pennec, X., and Ayache, N. (2006). An Interactive Hybrid Non-Rigid Registration Framework for 3D Medical Images. In *IEEE International Symposium on Biomedical Imaging (ISBI)*, pages 824–827, Arlington, Virginia, USA.

Bahlmann, C., Li, X., and Okada, K. (2006). Local Pulmonary Structure Classification for Computer-Aided Nodule Detection. In *SPIE Medical Imaging*, volume 6144, San Diego, California, USA.

Bajcsy, R. and Kovačič, S. (1989). Multiresolution Elastic Matching. *Computer Vision, Graphics, and Image Processing (CVGIP)*, 46(l):1–21.

Beil, W., Rohr, K., and Stiehl, H. (1997). Investigation of Approaches for the Localization of Anatomical Landmarks in 3D Medical Images. In *Computer Assisted Radiology and Surgery (CARS)*, pages 265–270, Berlin, Germany.

Besl, P. and McKay, N. (1992). A Method for Registration of 3-D Shapes. *IEEE Transactions on Pattern Analysis and Machine Intelligence*, 14(2):239–256.

Betke, M., Hong, H., Thomas, D., Prince, C., and Ko, J. (2003). Landmark Detection in the Chest and Registration of Lung Surfaces with an Application to Nodule Registration. *Medical Image Analysis*, 7(3):265–281.

Blaffert, T. and Wiemker, R. (2004). Comparison of Different Follow-Up Lung Registration Methods with and without Segmentation. In *SPIE Medical Imaging*, volume 5370, pages 1701–1708, San Diego, California, USA.

Bloch, I. (1999). Fuzzy Relative Position between Objects in Image Processing: a Morphological Approach. *IEEE Transactions on Pattern Analysis and Machine Intelligence*, 21(7):657–664.

Bloch, I., Colliot, O., and Cesar, R. (2006). On the Ternary Spatial Relation "Between". *IEEE Transactions on Systems, Man, and Cybernetics SMC-B*, 36(2):312–327.

Bloch, I. and Maître, H. (1995). Fuzzy Mathematical Morphologies: A Comparative Study. *Pattern Recognition*, 28(9):1341–1387.

Bloch, I. and Ralescu, A. (2003). Directional Relative Position between Objects in Image Processing: A Comparison between Fuzzy Approaches. *Pattern Recognition*, 36:1563–1582.

Boldea, V. (2006). *Intégration de la respiration en radiothérapie : apport du recalage déformable d'images*. PhD thesis, Université Lyon.

Bookstein, F. (1989). Principal Warps: Thin-Plate Splines and the Decomposition of Deformations. *IEEE Transactions on Pattern Analysis and Machine Intelligence*, 11(6):567–585.

Borgefors, G. (1986). Distance Transformations in Digital Images. *Computer Vision, Graphics, and Image Processing (CVGIP)*, 34(3):344–371.

Boykov, Y. and Funka-Lea, G. (2006). Graph Cuts and Efficient N-D Image Segmentation. *International Journal of Computer Vision*, 70(2):109–131.

Brinkley, J., Bradley, S., Sundsten, J., and Rosse, C. (1997). The Digital Anatomist Information System and its Use in the Generation and Delivery of Web-Based Anatomy Atlases. *Computers and Biomedical Research*, 30:472–503.

Bro-Nielsen, M. and Gramkow, C. (1996). Fast Fluid Registration of Medical Images. In *4th International Conference Visualization in Biomedical Computing (VBC'96)*, volume 1131 of *Lecture Notes in Computer Science (LNCS)*, pages 267–276, Hamburg, Germany.

Busayarat, S. and Zrimec, T. (2006). Ray-Tracing Based Registration for HRCT Images of the Lungs. In *International Conference on Medical Image Computing and Computer-Assisted Intervention (MICCAI), Part II*, volume 4191 of *Lecture Notes in Computer Science (LNCS)*, pages 670–677, Copenhagen, Denmark.

Buvat, I., Castiglioni, I., Feuardent, J., and Gilardi, M. (2003). Unified Description and Validation of Monte Carlo Simulators in PET. *IEEE Nuclear Science Symposium Conference Record*, 4:2554–2558.

Cachier, P., Mangin, J., Pennec, X., Rivière, D., Papadopoulos-Orfanos, D., Régis, J., and Ayache, N. (2001). Multisubject Non-Rigid Registration of Brain MRI Using Intensity and Geometric Features. In Niessen, W. and Viergever, M., editors, *4th International Conference on Medical Image Computing and Computer-Assisted Intervention (MICCAI)*, volume 2208 of *Lecture Notes in Computer Science (LNCS)*, pages 734–742, Utrecht, The Netherlands. Springer-Verlag Berlin / Heidelberg.

Camara, O., Colliot, O., and Bloch, I. (2004). Computational Modeling of Thoracic and Abdominal Anatomy Using Spatial Relationships for Image Segmentation. *Real-Time Imaging*, 10(4):263–273.

Camara, O., Delso, G., Colliot, O., Moreno-Ingelmo, A., and Bloch, I. (2007). Explicit Incorporation of Prior Anatomical Information into a Nonrigid Registration of Thoracic and Abdominal CT and 18-FDG Whole-Body Emision PET Images. *IEEE Transactions on Medical Imaging*, 26(2):164–178.

Camara-Rey, O. (2003). *Non-Linear Registration of Thoracic and Abdominal CT and PET Images: Methodology Study and Application in Clinical Routine / Recalage non-linéaire d'images TDM et TEP dans les régions thoraciques et abdominales : étude méthodologique et application en routine clinique*. PhD thesis, ENST 2003 E 043, Ecole Nationale Supérieure des Télécommunications (ENST), Paris, France.

Castellanos, N. P., Angel, P. L. D., and Medina, V. (2004). Nonrigid Medical Image Registration Technique as a Composition of Local Warpings. *Pattern Recognition*, 37:2141–2154.

Castro-Pareja, C. R. and Shekhar, R. (2004). Physically Correct Mesh Manipulation in Multi-Level Free-Form Deformation-Based Nonrigid Registration. In *26th Annual International Conference of the IEEE Engineering in Medicine and Biology Society (EMBS)*, pages 1687–1690, San Francisco, CA, USA.

Chambon, S. (2005). *Mise en correspondance stéréoscopique d'images couleur en présence d'occultations*. PhD thesis, Université Paul Sabatier – Toulouse III, Toulouse, France.

Chambon, S., Moreno, A., Santhanam, A., Brocardo, R., Rolland, J., Angelini, E., and Bloch, I. (2008). Introduction d'un modèle de respiration dans une méthode de recalage à partir de points d'intérêt d'images TEP et TDM du poumon – Using a 3D breathing model for landmark-based CT-PET lung registration. In *16^e Congrès Francophone AFRIF-AFIA Reconnaissance des Formes et Intelligence Artificielle (RFIA)*, Amiens, France.

Chambon, S., Moreno, A., Santhanam, A., Rolland, J., Angelini, E., and Bloch, I. (2007). CT-PET Landmark-based Registration using a Dynamic Lung Model. In *International Conference on Image Analysis and Processing (ICIAP)*, pages 691–696, Modena, Italy.

Chang, Y. and Li, X. (1994). Adaptive Image Region Growing. *IEEE Transactions on Image Processing*, 3:868–872.

Christensen, G. E., Rabbit, R. D., and Miller, M. I. (1996). Deformable Templates Using Large Deformation Kinematics. *IEEE Transactions on Image Processing*, 5(10):1435–1447.

Clarysse, P., Frouin, F., Garreau, M., Lalande, A., Rousseau, J., Sarrut, D., and Vasseur, C. (2004). Intégration de Connaissances et Modélisation en Imagerie Médicale. *ITBM-RBM Innovation et technologie en biologie et médecine*, 25(3):139–149.

Cohen, L. (1991). On Active Contour Models and Balloons. *Computer Vision, Graphics, and Image Processing: Image Understanding (CVGIP:IU)*, 53(2):211–218.

Collins, D., Le Goualher, G., and Evans, A. (1998a). Non-Linear Cerebral Registration with Sulcal Constraints. In *First International Conference on Medical Image Computing and Computer-Assisted Intervention (MICCAI)*, volume 1496 of *Lecture Notes in Computer Science (LNCS)*, pages 974–984, Cambridge, USA.

Collins, D., Zijdenbos, A., Kollokian, V., Sled, J., Kabani, N., Holmes, C., and Evans, A. (1998b). Design and Construction of a Realistic Digital Brain Phantom. *IEEE Transactions on Medical Imaging*, 17(3):463–468. Web site: http://www.bic.mni.mcgill.ca/brainweb/.

Colliot, O., Camara, O., and Bloch, I. (2004a). Integration of Fuzzy Structural Information in Deformable Models. In *Information Processing and Management of Uncertainty in Knowledge-Based Systems (IPMU)*, volume 2, pages 1533–1540, Perugia, Italy.

Colliot, O., Camara, O., and Bloch, I. (2006). Integration of Fuzzy Spatial Relations in Deformable Models - Application to Brain MRI Segmentation. *Pattern Recognition*, 39(8):1401–1414.

Colliot, O., Camara, O., Dewynter, R., and Bloch, I. (2004b). Description of Brain Internal Structures by Means of Spatial Relations for MR Image Segmentation. In *SPIE Medical Imaging*, volume 5370, pages 444–455, San Diego, California, USA.

Connolly, J. L., Schnitt, S. J., Wang, H. H., Dvorak, A. M., and Dvorak, H. F. (2000). *Cancer Medicine*, chapter Principles of Cancer Pathology. B.C. Decker Inc., fifth edition. Web sites: www.bcdecker.com and http://www.ncbi.nlm.nih.gov/books/bv.fcgi?rid=cmed.chapter.6534.

Cotes, J. (1993). *Lung Function Assessment and Application in Medicine*. Blackwell Scientific Publications.

Crawford, C., King, K., Ritchie, C., and Godwin, J. (1996). Respiratory Compensation in Projection Imaging Using a Magnification and Displacement Model. *IEEE Transactions on Medical Imaging*, 15(3):327–332.

D'Agostino, E., Maes, F., Vandermeulen, D., and Suetens, P. (2003). A Viscous Fluid Model for Multimodal Non-Rigid Image Registration Using Mutual Information. *Medical Image Analysis*, 7(4):565–575.

DAIA (2004). *Digital Anatomist Interactive Atlases*. Web site: http://www9.biostr.washington.edu/da.html.

Dameron, O. (2003). *Modeling, Representing and Sharing Anatomical Knowledge on Brain Cortex*. PhD thesis, Laboratoire IDM (Unité/Projet VisAGeS U746), Université de Rennes 1, Rennes, France.

Dawson, S. (2002). A Critical Approach to Medical Simulation. *Bulletin of the American College of Surgeons*, 87(11):12–18.

DeCarlo, D., Kaye, J., Metaxas, D., Clarke, J., Webber, B., and Badler, N. (1995). Integrating Anatomy and Physiology for Behavior Modeling. In Satava, R., Morgan, K., and Sieburg, H., editors, *Medicine Meets Virtual Reality III: Interactive Technology and the New Paradigm for Healthcare*, pages 81–87, Amsterdam, The Netherlands. IOS Press.

Delso, G. (2003). *Registro Elástico de Imágenes Médicas Multimodales. Aplicación en Oncología*. PhD thesis, Centre de Recerca en Enginyeria Biomèdica, Universitat Politècnica de Catalunya, Barcelona, Spain.

Ding, H., Jiang, Y., Furmancyzk, M., Prkewas, A., and Reinhardt, J. (2005). Simulation of Human Lung Respiration Using 3-D CFD with Macro Air Sac System. In *Western Simulation Conference Society for Modeling and Simulation International*, New Orleans, USA.

Duay, V., D'Haese, P., Li, R., and Dawant, B. (2004). Non-Rigid Registration Algorithm with Spatially Varying Stiffness Properties. In *IEEE International Symposium on Biomedical Imaging (ISBI)*, pages 408–411.

eAnatomy (2006). *e-Anatomy*. Web site: http://www.e-anatomy.org/.

Ecabert, O., Peters, J., Lorenz, C., von Berg, J., Vembar, M., Subramanyan, K., Lavi, G., and Weese, J. (2005). Towards Automatic Full Heart Segmentation in Computed-Tomography Images. In *Computers in Cardiology*, volume 32, pages 223–226, Lyon, France.

Ecabert, O., Peters, J., Walker, M., Berg, J., Lorenz, C., Vembar, M., Olszewski, M., and Weese, J. (2007). Automatic Whole Heart Segmentation in CT Images: Method and Validation. In Pluim, J. and Reinhardt, J., editors, *SPIE Medical Imaging*, volume 6512, San Diego, California, USA.

Edwards, P. J., Hill, D. L. G., Little, J. A., and Hawkes, D. J. (1998). A Three-Component Deformation Model for Image-Guided Surgery. *Medical Image Analysis*, 2(4):355–367.

Exchange3D (2006). *Exchange3D.com*. Web site: http://www.exchange3d.com/.

Fatemizadeh, E., Lucas, C., and Soltanian-Zadeh, H. (2003). Automatic Landmark Extraction from Image Data Using Modified Growing Neural Gas Network. *IEEE Transactions on Information Technology in Biomedicine*, 7(2):77–85.

Fetita, C. I. and Prêteux, F. (2004). Modélisation et Segmentation 3D des Nodules Pulmonaires en Imagerie TDM Volumique. In *14^e Congrès Francophone AFRIF-AFIA Reconnaissance des Formes et Intelligence Artificielle (RFIA)*, pages 573–581, Toulouse, France.

Feuardent, J., Soret, M., de Dreuille, O., Foehrenbach, H., and Buvat, I. (2003). Reliability of SUV Estimates in FDG PET as a Function of Acquisition and Processing Protocols. In *IEEE Nuclear Science Symposium Conference Record*, volume 4, pages 2877–2881.

Fischer, B. and Modersitzki, J. (2003). Combination of Automatic Non-Rigid and Landmark Based Registration: the Best of Both Worlds. In *SPIE Medical Imaging: Image Processing*, volume 5032, pages 1037–1048.

FMA (2005). *Foundational Model of Anatomy*. Web site: http://sig.biostr.washington.edu/projects/fm/.

FME (2005). *Foundational Model Explorer*. Web site: http://fme.biostr.washington.edu:8089/FME/index.html.

Frantz, S., Rohr, K., and Stiehl, H. (1998). Multi-Step Differential Approaches for the Localization of 3D Point Landmarks in Medical Images. *Journal of Computing and Information Technology*, 6(4):435–447.

Funka-Lea, G., Boykov, Y., Florin, C., Jolly, M.-P., Moreau-Gobard, R., Ramaraj, R., and Rinck, D. (2006). Automatic Heart Isolation for CT Coronary Visualization Using Graph-Cuts. In *IEEE International Symposium on Biomedical Imaging (ISBI)*, pages 614–617, Arlington, Virginia, USA.

Gee, J., Sundaram, T., Hasegawa, I., Uenatsu, H., and Hatabu, H. (2002). Characterization of Regional Pulmonary Mechanics from Serial MRI Data. In *5th International Conference on Medical Image Computing and Computer-Assisted Intervention (MICCAI), Part I*, volume 2489 of *Lecture Notes in Computer Science (LNCS)*, pages 762–769, Tokyo, Japan. Springer-Verlag Berlin / Heidelberg.

Giraud, P. (2000). *La radiothérapie conformationnelle du cancer du poumon : du volume tumoral macroscopique au volume traité*. PhD thesis, Université Paul Sabatier, Toulouse, France.

Goerres, G., Kamel, E., Seifert, B., Burger, C., Buck, A., Hany, T., and von Schulthess, G. (2002). Accuracy of Image Coregistration of Pulmonary Lesions in Patients with Non-Small Cell Lung Cancer Using an Integrated PET/CT System. *The Journal of Nuclear Medicine*, 43(11):1469–1475.

Graham, M., Purdy, J., Emami, B., Harms, W., Bosch, W., Lockett, M., and Perez, C. (1999). Clinical Dose-Volume Histogram Analysis for Pneumonitis after 3D Treatment for Non-Small Cell Lung Cancer (NSCLC). *International Journal of Radiation Oncology Biology Physics*, 45(2):323–329.

Gray's Anatomy (2005). *The Anatomical Basis of Clinical Practice*. Elsevier, Churchill Livingston, thirty-ninth edition. Web sites "Gray's Anatomy of the Human Body" (2000): http://education.yahoo.com/reference/gray/subjects/ or http://www.bartleby.com/107/.

Gregson, P. H. (1994). Automatic Segmentation of the Heart in 3D MR Images. In *Canadian Conference on Electrical and Computer Engineering*, volume 2, pages 584–587.

Guerrero, R., Rounds, D., and Booher, J. (1977). An Improved Organ Culture Method for Adult Mammalian Lung. *InVitro*, 13(8):517–524.

Guerrero, T., Zhang, G., Segars, W., Huang, T., Bilton, S., Ibbott, G., Dong, L., Forster, K., and Lin, K. (2005). Elastic Image Mapping for 4-D Dose Estimation in Thoracic Radiotherapy. *Radiation Protection Dosimetry*, 115(1-4):497–502.

Guimond, A., Roche, A., Ayache, N., and Meunier, J. (2001). Multimodal Brain Warping Using the Demons Algorithm and Adaptative Intensity Corrections. *IEEE Transactions on Medical Imaging*, 20(1):58–69.

Haber, E. and Modersitzki, J. (2004). Numerical Methods for Volume Preserving Image Registration. *Inverse Problems*, 20:1621–1638.

Haber, E. and Modersitzki, J. (2005). A Scale Space Method for Volume Preserving Image Registration. In *Scale-Space and PDE Methods in Computer Vision, 5th International Conference, Scale-Space 2005*, volume 3459 of *Lecture Notes in Computer Science (LNCS)*, pages 561–572, Hofgeismar, Germany.

Hachama, M., Desolneux, A., and Richard, F. (2006a). Combining Registration and Abnormality Detection in Mammography. In *International Workshop on Biomedical Image Registration (WBIR)*, volume 4057 of *Lecture Notes in Computer Science (LNCS)*, pages 178–185, Utrecht, The Netherlands. Springer-Verlag Berlin / Heidelberg.

Hachama, M., Richard, F., and Desolneux, A. (2006b). A Mammogram Registration Technique Dealing With Outliers. In *IEEE International Symposium on Biomedical Imaging (ISBI): Macro to Nano*, pages 458–461, Arlington, Virginia, USA.

Hachama, M., Richard, F., and Desolneux, A. (2006c). Combiner le Recalage des Images et la Détection des Lésions en Mammographie. In *Journée d'Études Algéro-Françaises en Imagerie Médicale (JETIMM)*, pages 39–44, Algiers, Algeria.

Harrison, R., Vannoy, S., Haynor, D., Gillispie, S., Kaplan, M., and Lewellen, T. (1993). Preliminary Experience with the Photon History Generator Module of a Public-Domain Simulation System for Emission Tomography. *IEEE Nuclear Science Symposium Conference Record*, pages 1154–1158. Web site: http://depts.washington.edu/simset/html/simset_main.html.

Hartkens, T., Hill, D. L. G., Castellano-Smith, A. D., Hawkes, D. J., Maurer Jr., C. R., Martin, A. J., Hall, W. A., Liu, H., and Truwit, C. L. (2002a). Using Points and Surfaces to Improve Voxel-Based Non-Rigid Registration. In *5th International Conference on Medical Image Computing and Computer-Assisted Intervention (MICCAI), Part II*, volume 2489 of *Lecture Notes in Computer Science (LNCS)*, pages 565–572, Tokyo, Japan. Springer-Verlag Berlin / Heidelberg.

Hartkens, T., Rohr, K., and Stiehl, H. (2002b). Evaluation of 3D Operators for the Detection of Anatomical Point Landmarks in MR and CT Images. *Computer Vision and Image Understanding*, 86(2):118–136.

Hellier, P. (2000). *Recalage non rigide en imagerie cérébrale : méthodes et validation*. PhD thesis, Université de Rennes 1, France.

Hellier, P. and Barillot, C. (2000). Coupling Dense and Landmark-Based Approaches for Non Rigid Registration. Research report 4076, Institut National de Recherche en Informatique et en Automatique (INRIA).

Hellier, P. and Barillot, C. (2003). Coupling Dense and Landmark-Based Approaches for Non Rigid Registration. *IEEE Transactions on Medical Imaging*, 22(2):217–227.

Hoffman, E., Clough, A., Christensen, G., Lin, C., McLennan, G., Reinhardt, J., Simon, B., Sonka, M., Tawhai, M., Van Beek, E., and Wing, G. (2004). The Comprehensive Imaging-Based Analysis of the Lung. *Academy of Radiology*, 11:1370–1380.

Horn, B. K. P. and Schunck, B. G. (1981). Determining Optical Flow. *Artificial Intelligence*, 17:185–203.

Hu, S., Hoffman, E., and Reinhardt, J. (2001). Automatic Lung Segmentation for Accurate Quantitation of Volumetric X-ray CT Images. *IEEE Transactions on Medical Imaging*, 20(6):490–498.

Huang, S. and Ingber, D. (2005). Cell Tension, Matrix Mechanics, and Cancer Development. *Cancer Cell*, 8(3):175–176.

Huesman, R., Klein, G., Kimdon, J., Kuo, C., and Majumdar, S. (2003). Deformable Registration of Multimodal Data Including Rigid Structures. *IEEE Transactions on Nuclear Science*, 50(3):4S–14S.

Jan, S., Santin, G., Strul, D., Staelens, S., Assie, K., Autret, D., Avner, S., Barbier, R., Bardies, M., Bloomfield, P., Brasse, D., Breton, V., Bruyndonckx, P., Buvat, I., Chatziioannou, A., Choi, Y., Chung, Y., Comtat, C., Donnarieix, D., Ferrer, L., Glick, S., Groiselle, C., Guez, D., Honore, P., Kerhoas-Cavata, S., Kirov, A., Kohli, V., Koole, M., Krieguer, M., Laan, D., Lamare, F., Largeron, G., Lartizien, C., Lazaro, D., Maas, M., Maigne, L., Mayet, F., Melot, F., Merheb, C., Pennacchio, E., Perez, J., Pietrzyk, U., Rannou, F., Rey, M., Schaart, D., Schmidtlein, C., Simon, L., Song, T., Vieira, J., Visvikis, D., Van de Walle, R., Wieers, E., and Morel, C. (2004). GATE: A Simulation Toolkit for PET and SPECT. *Physics in Medecine and Biology*, 49:4543–4561.

Johnson, H. and Christensen, G. (2002). Consistent Landmark and Intensity-Based Image Registration. *IEEE Transactions on Medical Imaging*, 21(5):450–461.

Jolly, M. (2006). Automatic Segmentation of the Left Ventricle in Cardiac MR and CT Images. *International Journal of Computer Vision*, 70(2):151–163.

Joshi, S. and Miller, M. (2000). Landmark Matching via Large Deformation Diffeomorphisms. *IEEE Transactions on Image Processing*, 9(8):1357–1370.

Juan, O. and Boykov, Y. (2006). Active Graph Cuts. In *IEEE Computer Society Conference on Computer Vision and Pattern Recognition*, volume 1, pages 1023–1029, Los Alamitos, California, USA.

Kass, M., Witkin, A., and Terzopoulos, D. (1987). Snakes: Active Contour Models. *International Journal of Computer Vision*, 1(4):321–331.

Kaus, M., von Berg, J., Niessen, W., and Pekar, V. (2003). Automated Segmentation of the Left Ventricle in Cardiac MRI. In *International Conference on Medical Image Computing and Computer-Assisted Intervention (MICCAI)*, volume 2878 of *Lecture Notes in Computer Science (LNCS)*, pages 432–439. Springer-Verlag.

Kaye, J., Primiano, F., and Metaxas, D. (1998). A Three-Dimensional Virtual Environment for Modeling Mechanical Cardiopulmonary Interactions. *Medical Image Analysis*, 2(2):169–195.

Khotanlou, H., Atif, J., Angelini, E., Duffau, H., and Bloch, I. (2007). Adaptive Segmentation of Internal Brain Structures in Pathological MR Images Depending on Tumor Types. In *IEEE International Symposium on Biomedical Imaging (ISBI)*, Washington DC, USA. To appear.

KidsHealth (2006). *KidsHealth - For Kids*. Web site: http://kidshealth.org/kid/body/.

Kim, J., Lee, J., Kim, J., Choe, B., Oh, C., Nam, S., Kwon, J., and Kim, S. (2003). Non-Linear Registration for Brain Images by Maximising Feature and Intensity Similarities with a Bayesian Framework. *Journal Medical and Biological Engineering and Computing*, 41(4):473–480.

Klette, R. and Rosenfeld, A. (2004). *Digital Geometry: Geometric Methods for Digital Picture Analysis*. Morgan Kaufmann.

Koivistoinen, H., Tohka, J., and Ruotsalainen, U. (2004). Comparison of Pattern Classification Methods in Segmentation of Dynamic PET Brain Images. In *6th Nordic Signal Processing Symposium (NORSIG)*, pages 73–76.

Krishnan, S., Beck, K., Reinhardt, J., Carlson, K., Simon, B., Albert, R., and Hoffman, E. (2004). Regional Lung Ventilation from Volumetric CT Scans Using Image Warping Functions. In *IEEE International Symposium on Biomedical Imaging (ISBI): Macro to Nano*, volume 1, pages 792–795.

Kwa, S. L. S., Lebesque, J. V., Theuws, J. C. M., Marks, L. B., Munley, M. T., Bentel, G., Oetzel, D., Spahn, U., Graham, M. V., Drzymala, R. E., Purdy, J. A., Lichter, A. S., Martel, M. K., and Ten Haken, R. K. (1998). Radiation Pneumonitis as a Function of Mean Lung Dose: An Analysis of Pooled Data of 540 Patients. *International Journal of Radiation Oncology Biology Physics*, 42(1):1–9.

Kybic, J. and Unser, M. (2003). Fast Parametric Elastic Image Registration. *IEEE Transactions on Image Processing*, 12(11):1427–1442.

Lartizien, C., Goertzen, A., Reilhac, A., Siegel, S., Costes, N., Magnin, I., Gimenez, G., and Evans, A. (2005). Validation of SORTEO Monte Carlo Simulations for the Geometry of the Concorde MicroPET R4 System. *IEEE Nuclear Science Symposium Conference Record*, 5:3036–3039.

Lavely, W., Scarfone, C., Cevikalp, H., Li, R., Byrne, D., Cmelak, A., Dawant, B., Price, R., Hallahan, D., and Fitzpatrick, J. (2004). Phantom Validation of Coregistration of PET and CT for Image-Guided Radiotheraphy. *Medical Physics*, 31(5):1083–1092.

Lee, Y.-B., Song, S.-M., Lee, J.-S., and Kim, M.-H. (2005). Tumor Segmentation from Small Animal PET Using Region Growing Based on Gradient Magnitude. In *7th International Workshop on Enterprise Networking and Computing in Healthcare Industry (HEALTHCOM 2005)*, pages 243–247, Busan, Korea.

Lelieveldt, B. P. F., van der Geest, R. J., Rezaee, M. R., Bosch, J. G., and Reiber, J. H. C. (1999). Anatomical Model Matching with Fuzzy Implicit Surfaces for Segmentation of Thoracic Volume Scans. *IEEE Transactions on Medical Imaging*, 18(3):218–230.

Li, B., Christensen, G. E., Hoffman, E. A., McLennan, G., and Reinhardt, J. M. (2003). Establishing a Normative Atlas of the Human Lung: Intersubject Warping and Registration of Volumetric CT Images. *Academy of Radiology*, 10:255–265.

Liang, J., McInerney, T., and Terzopoulos, D. (2006). United Snakes. *Medical Image Analysis*, 10(2):215–233.

Little, J. A., Hill, D. L. G., and Hawkes, D. J. (1997). Deformations Incorporating Rigid Structures. *Computer Vision and Image Understanding*, 66(2):223–232.

Loeckx, D., Maes, F., Vandermeulen, D., and Suetens, P. (2004). Nonrigid Image Registration Using Free-Form Deformations with Local Rigidity Constraint. In Barillot, C., Haynor, D., and Hellier, P., editors, *7th International Conference on Medical Image Computing and Computer-Assisted Intervention (MICCAI), Part I*, volume 3216 of *Lecture Notes in Computer Science (LNCS)*, pages 639–646, Rennes - St-Malo, France. Springer-Verlag Berlin / Heidelberg.

Lynch, M., Ghita, O., and Whelan, P. (2006). Automatic Segmentation of the Left Ventricle Cavity and Myocardium in MRI Data. *Computers in Biology and Medicine*, 36(4):389–407.

Maintz, J. and Viergever, M. (1998). A Survey of Medical Image Registration. *Medical Image Analysis*, 2(1):1–36.

Mäkelä, T., Pollari, M., Lötjönen, J., Pauna, N., Reilhac, A., Clarysse, P., Magnin, I., and Katila, T. (2003). Evaluation and Comparison of Surface and Intensity Based Rigid Registration Methods for Thorax and Cardiac MR and PET Images. In *Functional Imaging and Modeling of the Heart (FIMH), Second International Workshop*, volume 2674 of *Lecture Notes in Computer Science (LNCS)*, pages 224–233, Lyon, France.

Malandain, G. (2006). Les Mesures de Similarité pour le Recalage des Images Médicales. Technical report, Université Nice Sophia-Antipolis, Sophia Antipolis, France.

Martel, M. K., Ten Haken, R. K., Hazuka, M. B., Kessler, M. L., Strawderman, M., Turrisi, A. T., Lawrence, T. S., Fraass, B. A., and Lichter, A. S. (1999). Estimation of Tumor Control Probability Model Parameters from 3-D Dose Distributions of Non-Small Cell Lung Cancer Patients. *Lung Cancer*, 24(1):31–37.

Matsopoulos, G. K., Mouravliansky, N. A., Asvestas, P. A., Delibasis, K. K., and Kouloulias, V. (2005). Thoracic Non-Rigid Registration Combining Self-Organizing Maps and Radial Basis Functions. *Medical Image Analysis*, 9(3):237–254.

McClelland, J., Blackall, J., Tarte, S., Chandler, A., Hughes, S., Ahmad, S., Landau, D., and Hawkes, D. (2006). A Continuous 4D Motion Mmodel from Multiple Respiratory Cycles for Use in Lung Radiotherapy. *Medical Physics*, 33(9):3348–3358.

McInerney, T. and Terzopoulos, D. (1995). A Dynamic Finite Element Surface Model for Segmentation and Tracking in Multidimensional Medical Images with Application to Cardiac 4D Image Analysis. *Computerized Medical Imaging and Graphics*, 19(1):69–83.

McInerney, T. and Terzopoulos, D. (1996). Deformable Models in Medical Image Analysis: A Survey. *Medical Image Analysis*, 1(2):91–108.

Mead, J. (1956). Measurement of Inertia of the Lungs at Increased Ambient Pressure. *Journal of Applied Physiology*, 2(1):208–212.

Meier, U., López, O., Monserrat, C., Juan, M., and Alcañiz, M. (2005). Real-Time Deformable Models for Surgery Simulation: A Survey. *Computer Methods and Programs in Biomedicine*, 77(3):183–197.

Mellor, M. and Brady, M. (2005). Fluid Registration of Ultrasound Using Multi-Scale Phase Estimates. In Clocksin, W., Fitzgibbon, A., and Torr, P., editors, *Information Processing in Medical Imaging, British Machine Vision Conference (BMVC 2005)*, Oxford, UK.

Merck Manuals (2003). *The Merck Manuals Online Medical Library. Tissues and Organs.* Web site: http://www.merck.com/mmhe/sec01/ch001/ch001c.html.

Miyajima, K. and Ralescu, A. (1994). Spatial Organization in 2D Segmented Images: Representation and Recognition of Primitive Spatial Relations. *Fuzzy Sets and Systems*, 65(2/3):225–236.

Montagnat, J., Delingette, H., Scapel, N., and Ayache, N. (2000). Representation, Shape, Topology and Evolution of Deformable Surfaces. Application to 3D Medical Image Segmentation. Technical report, Institut National de Recherche en Informatique et en Automatique (INRIA), Sophia Antipolis, France. ISRN INRIA/RR–3954–FR+ENG.

Moreno, A., Chambon, S., Santhanam, A., Brocardo, R., Kupelian, P., Rolland, J., Angelini, E., and Bloch, I. (2007). Thoracic CT-PET Registration Using a 3D Breathing Model. In *10th International Conference on Medical Image Computing and Computer-Assisted Intervention (MICCAI), Part I*, volume 4791 of *Lecture Notes in Computer Science (LNCS)*, pages 626–633, Brisbane, Australia.

Moreno, A., Delso, G., Camara, O., and Bloch, I. (2005). CT and PET Registration Using Deformations Incorporating Tumor-Based Constraints. In *10th Iberoamerican Congress on Pattern Recognition (CIARP)*, volume 3773 of *Lecture Notes in Computer Science (LNCS)*, pages 1–12, La Habana, Cuba.

Moreno, A., Delso, G., Camara, O., and Bloch, I. (2006a). Non-linear Registration Between 3D Images Including Rigid Objects: Application to CT and PET Lung Images With Tumors. In *Workshop on Image Registration in Deformable Environments (DEFORM)*, pages 31–40, Edinburgh, UK.

Moreno, A., Takemura, C., Colliot, O., Camara, O., and Bloch, I. (2006b). Heart Segmentation in Medical Images Using the Fuzzy Spatial Relation "Between". In *Information Processing and Management of Uncertainty in Knowledge-Based Systems (IPMU)*, pages 2052–2059, Paris, France.

Moreno, A., Takemura, C., Colliot, O., Camara, O., and Bloch, I. (2008a). Using Anatomical Knowledge Expressed as Fuzzy Constraints to Segment the Heart in CT Images. *Pattern Recognition*. To appear.

Moreno, A., Takemura, C., Colliot, O., Camara, O., and Bloch, I. (2008b). Using the Fuzzy Spatial Relation "Between" to Segment the Heart in Computerized Tomography Images. In Bouchon-Meunier, B., Yager, R., Marsala, C., and Rifqi, M., editors, *Uncertainty and Intelligent Information Systems*, number ISBN 978-981-279-234-1, chapter 26. World Scientific. To appear.

Murphy, M. (2004). Tracking Moving Organs in Real Time. *Seminars in radiation oncology*, 14(1):91–100.

Narusawa, U. (2001). General Characteristics of the Sigmoidal Model Equation Representing Quasi-Static Pulmonary P-V Curves. *Journal of Applied Physiology*, 92(1):201–210.

Nehmeh, S., Erdi, Y., Pan, T., Pevsner, A., Rosenzweig, K., Yorke, E., Mageras, G., Schoder, H., Vernon, P., Squire, O., Mostafavi, H., Larson, S., and Humm, J. (2004). Four-Dimensional (4D) PET/CT Imaging of the Thorax. *Physics in Medecine and Biology*, 31(12):3179–3186.

Neicu, T., Shirato, H., Seppenwoolde, Y., and Jiang, S. (2003). Synchronized Moving Aperture Radiation Therapy (SMART): Average Tumour Trajectory for Lung Patients. *Physics in Medecine and Biology*, 48(2003):587–598.

Noble, N., Hill, D., Breeuwer, M., Schnabel, J., Hawkes, D., Gerritsen, F., and Razavi, R. (2002). Myocardial Delineation Via Registration in a Polar Coordinate System. In *5th International Conference on Medical Image Computing and Computer-Assisted Intervention (MICCAI), Part I*, volume 2488 of *Lecture Notes in Computer Science (LNCS)*, pages 651–658, Tokyo, Japan. Springer-Verlag Berlin / Heidelberg.

Noyola-Martinez, J., Guerrero, T., Borghero, Y., Sanders, K., Stevens, C., Guerrero, M., and Guerra, R. (2005). Mapping Gross Tumor Volumes from Exhale to Inhale Breath-Hold Computed Tomography Images. In Villanueva, J., editor, *Visualization, Imaging, and Image Processing*, Benidorm, Spain. 480-276.

Numerical Recipes (2007). *Numerical Recipes Library*. Web sites: http://nr.com/ or http://www.numerical-recipes.com/.

Okada, K., Comaniciu, D., and Krishnan, A. (2005). Robust Anisotropic Gaussian Fitting for Volumetric Characterization of Pulmonary Nodules in Multislice CT. *IEEE Transactions on Medical Imaging*, 24(3):409–423.

OpenGALEN (2005). *OpenGALEN Foundation*. Web site: http://www.opengalen.org/.

Papademetris, X., Jackowski, A., Schultz, R., Staib, L., and Duncan, J. (2004). Integrated Intensity and Point-Feature Nonrigid Registration. In Barillot, C., Haynor, D., and Hellier, P., editors, *7th International Conference on Medical Image Computing and Computer-Assisted Intervention (MICCAI), Part I*, volume 3216 of *Lecture Notes in Computer Science (LNCS)*, pages 763–770, Rennes - St-Malo, France. Springer-Verlag Berlin / Heidelberg.

Paszek, M., Zahir, N., Johnson, K., Lakins, J., Rozenberg, G., Gefen, A., Reinhart-King, C., Margulies, S., Dembo, M., Boettiger, D., Hammer, D., and Weaver, V. (2005). Tensional Homeostasis and the Malignant Phenotype. *Cancer Cell*, 8(3):241–254.

Pei, S. and Lin, C. (1992). The Detection of Dominant Points on Digital Curves by Scale-Space Filtering. *Pattern Recognition*, 25(11):1307–1314.

Pfeifer, B., Hanser, F., Trieb, T., Hintermüller, C., Seger, M., Fischer, G., Modre, R., and Tilg, B. (2005). Combining Active Appearance Models and Morphological Operators Using a Pipeline for Automatic Myocardium Extraction. In *Functional Imaging and Modeling of the Heart (FIMH), Third International Workshop*, volume 3504 of *Lecture Notes in Computer Science (LNCS)*, pages 44–53, Barcelona, Spain.

Plathow, C., Ley, S., Fink, C., Puderbach, M., Hosch, W., Schmähl, A., Debus, J., and Kauczor, H.-U. (2004). Analysis of Intrathoracic Tumor Mobility during Whole Breathing Cycle by Dynamic MRI. *International Journal of Radiation Oncology Biology Physics*, 59(4):952–959.

Pluempitiwiriyawej, C., Moura, J., Wu, Y., and Ho, C. (2005). STACS: New Active Contour Scheme for Cardiac MR Image Segmentation. *IEEE Transactions on Medical Imaging*, 24(5):593–603.

Pluim, J. and Fitzpatrick, J. (2003). Image Registration. *IEEE Transactions on Medical Imaging*, 22(11):1341–1343.

Pollari, M., Lotjonen, J., Makela, T., Pauna, N., Reilhac, A., and Clarysse, P. (2004). Evaluation of Cardiac PET-MRI Registration Methods Using a Numerical Breathing Phantom. In *IEEE International Symposium on Biomedical Imaging (ISBI): Macro to Nano*, volume 2, pages 1447–1450.

Precision Radiotherapy (2007). *Precision Radiotherapy – Learn – Conventional Radiotherapy*. Web site: http://www.mayfieldclinic.com/Precision/learn.htm.

Prêteux, F. (1993). *On a Distance Function Approach for Gray-Level Mathematical Morphology*, chapter 10, pages 323–349. E.R. Dougherty, Ed. M. Dekker, New York, USA.

Promayon, E., Baconnier, P., and Puech, C. (1997). Physically-Based Model for Simulating the Human Trunk Respiration Movements. In *Joint Conference Computer Vision, Virtual Reality and Robotics in Medicine and Medical Robotics and Computer-Assisted Surgery (CVRMed-MRCAS)*, volume 1205 of *Lecture Notes in Computer Science (LNCS)*, pages 379–388, Grenoble, France. Springer Verlag.

Raffy, P., Fetita, C., Beigelman, C., coise Prêteux, F., Wood, S., and Grenier, P. (2004). Evaluation of Computer-Aided Detection Performance Using Mathematically Simulated Lung Nodules. *International Congress Series*, 1268:935–940.

Reilhac, A., Batan, G., Michel, C., Grova, C., Tohka, J., Collins, D., Costes, N., and Evans, A. (2005). PET-SORTEO: Validation and Development of Database of Simulated PET Volumes. *IEEE Transactions on Nuclear Science*, 52(5):1321–1328. Part 1.

Reinhardt, J., Uppaluri, R., Higgins, W., and Hoffman, E. (2000). *Handbook of Medical Imaging*, chapter Pulmonary Imaging and Analysis, pages 1005–1060. Ed. M. Sonka and J. M. Fitzpatrick.

Reyes-Aguirre, M., Malandain, G., and Darcourt, J. (2004). Respiratory Movement Correction in Emission Tomography. Research report 5279, Institut National de Recherche en Informatique et en Automatique (INRIA), Sophia Antipolis, France. ISRN INRIA/RR–5279–FR+ENG.

Reyes-Aguirre, M., Malandain, G., Darcourt, J., and Malick Koulibaly, P. (2005a). Respiratory Motion Correction in Emission Tomography Imaging. In *Fully Three-Dimensional Image Reconstruction Meeting in Radiology and Nuclear Medicine*, Salt Lake City, Utah, USA.

Reyes-Aguirre, M., Malandain, G., Malick Koulibaly, P., González-Ballester, M., and Darcourt, J. (2005b). Respiratory Motion Correction in Emission Tomography Image Reconstruction. In Duncan, J. S. and Gerig, G., editors, *International Conference on Medical Image Computing and Computer-Assisted Intervention (MICCAI), Part II*, volume 3750 of *Lecture Notes in Computer Science (LNCS)*, pages 369–376, Palm Springs, California, USA. Springer Verlag Berlin / Heidelberg.

Ripoche, X., Atif, J., and Osorio, A. (2004). A 3D Discrete Deformable Model Guided by Mutual Information for Medical Image Segmentation. In *SPIE Medical Imaging*, volume 5370, San Diego, California, USA.

Rit, S., Sarrut, D., Boldea, V., and Ginestet, C. (2006). Extraction du Signal Respiratoire à partir de Projections Cone-Beam pour l'Imagerie TDM 4D. *Traitement du signal*, 23(3-4):307–319.

Rit, S., Sarrut, D., and Ginestet, C. (2005). Respiratory Signal Extraction for 4D CT Imaging of the Thorax from Cone-Beam CT Projections. In Duncan, J. S. and Gerig, G., editors, *International Conference on Medical Image Computing and Computer-Assisted Intervention (MICCAI)*, volume 3749 of *Lecture Notes in Computer Science (LNCS)*, pages 556–563, Palm Springs, California, USA. Springer-Verlag Berlin / Heidelberg.

Rizzo, G., Castiglioni, I., Arienti, R., Cattaneo, G., Landoni, C., Artioli, D., Gilardi, M., Messa, C., Reni, M., Ceresoli, G., and Fazio, F. (2005). Automatic Registration of PET and CT Studies for Clinical Use in Thoracic and Abdominal Conformal Radiotherapy. *Physics in Medecine and Biology*, 49(3):267–279.

Roche, A. (2001). *Recalage d'images médicales par inférence statistique*. PhD thesis, Université de Nice Sophia-Antipolis, France.

Rogers, J. and Rector, A. (2000). GALEN's Model of Parts and Wholes: Experience and Comparisons. In *Annual Fall Symposium of American Medical Informatics Association*, pages 714–718, Los Angeles, California, USA.

Rohlfing, T. and Maurer, C. (2001). Intensity-Based Non-Rigid Registration Using Adaptive Multilevel Free-Form Deformation with an Incompressibility Constraint. In Niessen, W. and Viergever, M., editors, *4th International Conference on Medical Image Computing and Computer-Assisted Intervention (MICCAI)*, volume 2208 of *Lecture Notes in Computer Science (LNCS)*, pages 111–119, Utrecht, The Netherlands. Springer-Verlag Berlin / Heidelberg.

Rohlfing, T., Maurer, C., Bluemke, D., and Jacobs, M. (2003). Volume-Preserving Nonrigid Registration of MR Breast Images Using Free-Form Deformation with an Incompressibility Constraint. *IEEE Transactions on Medical Imaging*, 22(6):730–741.

Rohr, K., Cathier, P., and Wörz, S. (2004). Elastic Registration of Electrophoresis Images Using Intensity Information and Point Landmarks. *Pattern Recognition*, 37(5):1035–1048.

Rohr, K., Stiehl, H., Sprengel, R., Beil, W., Buzug, T., Weese, J., and Kuhn, M. (1996). Nonrigid Registration of Medical Images Based on Anatomical Point Landmarks and Approximating Thin-Plate Splines. In *Bildverarbeitung für die Medizin*.

Rohr, K., Stiehl, H., Sprengel, R., Buzug, T., Weese, J., and Kuhn, M. (2001). Landmark-Based Elastic Registration Using Approximating Thin-Plate Splines. *IEEE Transactions on Medical Imaging*, 20(6):526–534.

Rosse, C. and Mejino, J. (2003). A Reference Ontology for Bioinformatics: The Foundational Model of Anatomy. *Journal of Biomedical Informatics*, 36:478–500.

Ruan, D., Fessler, J. A., Roberson, M., Balter, J., and Kessler, M. (2006). Nonrigid Registration Using Regularization that Accomodates Local Tissue Rigidity. In Reinhardt, J. M. and Pluim, J. P., editors, *SPIE Medical Imaging: Image Processing*, volume 6144, pages 346–354, San Diego, California, USA.

Rueckert, D., Aljabar, P., Heckemann, R., Hajnal, J., and Hammers, A. (2006). Diffeomorphic Registration Using B-Splines. In *International Conference on Medical Image Computing and Computer-Assisted Intervention (MICCAI), Part II*, volume 4191 of *Lecture Notes in Computer Science (LNCS)*, pages 702–709, Copenhagen, Denmark.

Rueckert, D., Sonoda, L. I., Hayes, C., Hill, D. L. G., Leach, M. O., and Hawkes, D. J. (1999). Non-Rigid Registration Using Free-Form Deformations: Application to Breast MR Images. *IEEE Transactions on Medical Imaging*, 18(8):712–721.

Santhanam, A. (2006). *Modeling, Simulation, and Visualization of 3D Lung Dynamics*. PhD thesis. (Co-advising with Dr. Pattanaik, CS), `http://odalab.ucf.edu/Publications/Dissertations/Santhanam_Anand_200608_PhD.pdf`.

Santhanam, A., Fidopiastis, C., Davenport, P., Langen, K., Meeks, S., and Rolland, J. (2006a). Real-Time Simulation and Visualization of Subject-Specific 3D Lung Dynamics. In *IEEE Computer-based Medical Systems (CBMS)*, pages 629–634, Salt Lake City, USA.

Santhanam, A., Fidopiastis, C., Hamza-Lup, F., Rolland, J., and Imielinska, C. (2004a). Physically-Based Deformation of High-Resolution 3D Models for Augmented Reality Based Medical Visualization. In *Augmented Environments for Medical Imaging (AMI-ARCS) & International Conference on Medical Image Computing and Computer-Assisted Intervention (MICCAI)*, volume 3216 of *Lecture Notes in Computer Science (LNCS)*, pages 21–31, Rennes - St-Malo, France.

Santhanam, A., Fidopiastis, C., Hoffman-Ruddy, B., and Rolland, J. (2004b). PRASAD: An Augmented Reality based Non-invasive Pre-operative Visualization Framework for Lungs. In *IEEE Virtual Reality*, pages 253–254, Chicago, USA.

Santhanam, A., Fidopiastis, C., Langen, K., Kupelian, P., Meeks, S., Davis, L., and Rolland, J. (2006b). Visualization of Tumor-Influenced 3D Lung Dynamics. In *SPIE Medical Imaging: Visualization, Image-Guided Procedures, and Display*, volume 6141, pages 86–97, San Diego, California, USA.

Santhanam, A., Fidopiastis, C., and Rolland, J. (2007a). 3D Lung Dynamics Using a Programmable Graphics Hardware. *IEEE Transactions on Information Technology in Biomedicine*. In press.

Santhanam, A., Fidopiastis, C., Rolland, J., and Davenport, P. (2007b). A Second Order Relation for Modeling the Pressure-Volume Relationship of Lungs. *Journal of Simulation in Healthcare*. Submitted.

Santhanam, A., Fidopiastis, C., Tal, A., Hoffman-Ruddy, B., and Rolland, J. (2004c). An Adaptive Driver and Real-Time Deformation Algorithm for Visualization of High-Density Lung Models. In *Medicine Meets Virtual Reality 12*, pages 333–339, Newport, California, USA. IOS Press.

Santhanam, A., Imielinska, C., Davenport, P., Kupelian, P., and Rolland, J. (2007c). Modeling Simulation and Visualization of Real-Time 3D Lung Dynamics. *IEEE Transactions on Information Technology in Biomedicine*. In press.

Santhanam, A., Pandurang, M., and Rolland, J. (2006c). An Inverse 3D Lung Deformation Analysis for Medical Visualization. In *Computer Animation and Social Agents*, Geneva, Switzerland. Computer Graphics Society.

Santhanam, A., Pattanaik, S., Rolland, J., Imielinska, C., and Norfleet, J. (2003). Physiologically-Based Modeling and Visualization of Deformable Lungs. In *IEEE Pacific Conference on Computer Graphics and Applications*, volume 11, pages 507–511, Canmore, Canada.

Sarrut, D. (2006). Deformable Registration for Image-Guided Radiation Therapy. *Zeitschrift für Medizinische Physik*, 16(4):285–297.

Sarrut, D., Boldea, V., Ayadi, M., Badel, J., Ginestet, C., Clippe, S., and Carrie, C. (2005). Non-Rigid Registration Method to Assess Reproducibility of Breath-holding with ABC in Lung Cancer. *International Journal of Radiation Oncology Biology Physics*, 61(2):594–607.

Sarrut, D., Boldea, V., Miguet, S., and Ginestet, C. (2006). Simulation of Four-Dimensional CT Images from Deformable Registration between Inhale and Exhale Breath-Hold CT Scans. *Medical Physics*, 33(3):605–617.

Schnabel, J. A., Tanner, C., Castellano-Smith, A. D., Degenhard, A., Leach, M. O., Hose, D. R., Hill, D. L. G., and Hawkes, D. J. (2003). Validation of Nonrigid Image Registration Using Finite-Element Methods: Application to Breast MR Images. *IEEE Transactions on Medical Imaging*, 22(2):238–247.

Schottlander, D., Guimond, A., Pan, X., Brady, M., Declerck, J., Collins, L., Evans, A., and Reilhac, A. (2006). Development and Use of a Kinetic FDG-PET Dataset Simulated from the MNI Standard Brain. In *SPIE Medical Imaging*, volume 6143, pages 548–556, San Diego, California, USA.

Schweikard, A., Glosser, G., Bodduluri, M., Murphy, M., and Adler, J. (2000). Robotic Motion Compensation for Respiratory Movement During Radiosurgery. *Computer Aided Surgery*, 5(4):263–277.

Segars, W., Lalush, D., and Tsui, B. (2001). Modeling Respiratory Mechanics in the MCAT and Spline-Based MCAT Phantoms. *IEEE Transactions on Nuclear Science*, 48(1):89–97.

Segars, W., Lalush, D., and Tsui, B. (2002a). Study of the Efficacy of Respiratory Gating in Myocardial SPECT Using the New 4-D NCAT Phantom. *IEEE Transactions on Nuclear Science*, 49(3):675–679.

Segars, W., Tsui, B., Da Silva, A., and Shao, L. (2002b). CT-PET Image Fusion Using the 4D NCAT Phantom with the Purpose of Attenuation Correction. In *IEEE Nuclear Science Symposium Conference Record*, volume 3, pages 1775–1779.

Segars, W., Tsui, B., Frey, E., Johnson, G., and Berr, S. (2004). Development of a 4D Digital Mouse Phantom for Molecular Imaging Research. *Molecular Imaging & Biology*, 6(3):149–159.

Seppenwoolde, Y., Shirato, H., Kitamura, K., Shimizu, S., van Herk, M., Lebesque, J. V., and Miyasaka, K. (2002). Precise and Real-Time Measurement of 3D Tumor Motion in Lung due to Breathing and Heartbeat, Measured during Radiotherapy. *International Journal of Radiation Oncology Biology Physics*, 53(4):822–834.

Sharp, G. C., Jiang, S. B., Shimizu, S., and Shirato, H. (2004). Prediction of Respiratory Tumour Motion for Real-Time Image-Guided Radiotherapy. *Physics in Medecine and Biology*, 49(3):425–440.

Shekhar, R., Walimbe, V., Raja, S., Zagrodsky, V., Kanvinde, M., Wu, G., and Bybel, B. (2005). Automated 3-Dimensional Elastic Registration of Whole-Body PET and CT from Separate or Combined Scanners. *The Journal of Nuclear Medicine*, 46(9):1488–1496.

Shen, J.-K., Matuszewski, B. J., and Shark, L.-K. (2005). Deformable Image Registration. In *IEEE International Conference on Image Processing (ICIP)*, volume 3, pages 1112–1115, Genova, Italy.

Shih, H. A., Jiang, S. B., Aljarrah, K. M., Doppke, K. P., and Choi, N. C. (2002). Planning Target Volume Determined with Fused CT Images of Fast, Breath-Hold, and Four Second Simulation CT Scans to Account for Respiratory Movement in 3D-CRT in Lung Cancer. In *Annual Meeting of The American Society for Therapeutic Radiology and Oncology*, New Orleans, LA, USA.

Shih, H. A., Jiang, S. B., Aljarrah, K. M., Doppke, K. P., and Choi, N. C. (2004). Internal Target Volume Determined with Expansion Margins beyond Composite Gross Tumor Volume in Three-Dimensional Conformal Radiotherapy for Lung Cancer. *International Journal of Radiation Oncology Biology Physics*, 60(2):613–622. Presented at the Annual Meeting of the American Society for Therapeutic Radiology and Oncology, October 5-8, 2002, New Orleans, LA, USA.

Shimizu, S., Shirato, H., Ogura, S., Akita-Dosaka, H., Kitamura, K., Nishioka, T., Kagei, K., Nishimura, M., and Miyasaka, K. (2001). Detection of Lung Tumor Movement in Real-Time Tumor-Tracking Radiotherapy. *International Journal of Radiation Oncology Biology Physics*, 51(2):304–310. Presented at the 42nd Annual Meeting of the American Society for Therapeutic Radiology and Oncology, October 22-26, 2000, Boston, USA.

Sibley, G. S., Jamieson, T. A., Marks, L. B., Anscher, M. S., and Prosnitz, L. R. (1998). Radiotherapy Alone for Medically Inoperable Stage I Non-Small Cell Lung Cancer: The Duke Experience. *International Journal of Radiation Oncology Biology Physics*, 40(1):149–154.

Sluimer, I., Prokop, M., and van Ginneken, B. (2005). Toward Automated Segmentation of the Pathological Lung in CT. *IEEE Transactions on Medical Imaging*, 24(8):1025–1038.

Sluimer, I., Schilham, A., Prokop, M., and van Ginneken, B. (2006). Computer Analysis of Computed Tomography Scans of the Lung: a Survey. *IEEE Transactions on Medical Imaging*, 25(4):385–405.

Smith, B., Mejino Jr., J., Schulz, S., Kumar, A., and Rosse, C. (2005). Anatomical Information Science. In Cohn, A. and Mark, D., editors, *7th International Conference on Spatial Information Theory (COSIT)*, volume 3693 of *Lecture Notes in Computer Science (LNCS)*, pages 149–164, Ellicottville, New York, USA.

Smyczynski, M., Segars, W., Narayanan, M., Pretorius, P., Gifford, H., Farncombe, T., Hoffman, E., Tsui, B., and King, M. (2001). Modeling the Respiratory Motion of Solitary Pulmonary Nodules for Investigating SPECT Tumor Imaging. In *IEEE Nuclear Science Symposium Conference Record*, volume 3, pages 1371–1375.

Staring, M., Klein, S., and Pluim, J. (2006). Evaluation of a Rigidity Penalty Term for Nonrigid Registration. In *Workshop on Image Registration in Deformable Environments (DEFORM)*, pages 41–50, Edinburgh, UK.

Sundaram, T., Avants, B., and Gee, J. (2005). Towards a Dynamic Model of Pulmonary Parenchymal Deformation: Evaluation of Methods for Temporal Re-parameterization of Lung Data. *International Conference on Medical Image Computing and Computer-Assisted Intervention (MICCAI)*, 3750:328–335.

Sundaram, T. and Gee, J. (2005). Towards a Model of Lung Biomechanics: Pulmonary Kinematics Via Registration of Serial Lung Images. *Medical Image Analysis*, 9(6):524–537.

Suri, J. S. (2000). Computer Vision, Pattern Recognition and Image Processing in Left Ventricle Segmentation: The Last 50 Years. *Pattern Analysis & Applications*, 3(3):209–242.

Takeuchi, M., Sedeek, K., Schettino, G., Suchodolski, K., and Kacmarek, R. (2001). Peak Pressure During Volume History and Pressure-Volume Curve Measurement Affects Analysis. *American Journal of Respiratory and Critical Care Medecine*, 164(7):1225–1230.

Tamir, E. (2002). *The Human Body Made Simple*. Churchill Livingston, second edition.

Tanner, C., Schnabel, J. A., Chung, D., Clarkson, M. J., Rueckert, D., Hill, D. L. G., and Hawkes, D. J. (2000). Volume and Shape Preservation of Enhancing Lesions When Applying Non-rigid Registration to a Time Series of Contrast Enhancing MR Breast Images. In *International Conference on Medical Image Computing and Computer-Assisted Intervention (MICCAI)*, volume 1935 of *Lecture Notes in Computer Science (LNCS)*, pages 327–337, Pittsburgh, USA.

Tanner, C., Schnabel, J. A., Degenhard, A., Castellano-Smith, A. D., Hayes, C., Leach, M. O., Hill, D. L. G., and Hawkes, D. J. (2002). Validation of Volume-Preserving Non-Rigid Registration. In *5th International Conference on Medical Image Computing and Computer-Assisted Intervention (MICCAI), Part I*, volume 2488 of *Lecture Notes in Computer Science (LNCS)*, pages 307–314, Tokyo, Japan. Springer-Verlag Berlin / Heidelberg.

Tauber, C., Batatia, H., and Ayache, A. (2006). Contours Actifs Basés sur Trois Energies : Détection des Cavités Cardiaques. In *15^e Congrès Francophone AFRIF-AFIA Reconnaissance des Formes et Intelligence Artificielle (RFIA)*, Tours, France.

Tawhai, M. and Burrowes, K. (2003). Developing Integrative Computational Models. *Anatomical Record*, 275B:207–218.

Teh, C. and Chin, R. (1989). On the Detection of Dominant Points on Digital Curves. *IEEE Transactions on Pattern Analysis and Machine Intelligence*, 11(8):859–872.

Thirion, J. (1996). Non-Rigid Matching Using Demons. In *IEEE Computer Society Conference on Computer Vision and Pattern Recognition*, pages 245–251, San Francisco, California, USA.

Thirion, J. (1998). Image Matching as a Diffusion Process: an Analogy with Maxwell's Demons. *Medical Image Analysis*, 2(3):243–260.

Thompson, C., Moreno-Cantu, J., and Picard, Y. (1992). PETSIM: Monte Carlo Simulation of all Sensitivity and Resolution Parameters of Positron Imaging Systems. *Physics in Medecine and Biology*, 37(3):731–749.

Tohka, J., Kivimaki, A., Reilhac, A., Mykkanen, J., and Ruotsalainen, U. (2004). Assessment of Brain Surface Extraction from PET Images Using Monte Carlo Simulations. *IEEE Transactions on Nuclear Science*, 51(5):2641–2648. Part 2.

Townsend, D., Carney, J., Yap, J., and Hall, N. (2004). PET/CT Today and Tomorrow. *The Journal of Nuclear Medicine*, 45(1 (Suppl.)):4S–14S.

Truong, M., Pan, T., and Erasmus, J. (2006). Pitfalls in Integrated CT-PET of the Thorax: Implications in Oncologic Imaging. *Journal of Thoracic Imaging*, 21(2):111–122.

Vaillant, M. and Davatzikos, C. (1999). Hierarchical Matching of Cortical Features for Deformable Brain Image Registration. In Kuba, A., Sámal, M., and Todd-Pokropek, A., editors, *16th International Conference on Information Processing in Medical Imaging (IPMI)*, volume 1613 of *Lecture Notes in Computer Science (LNCS)*, pages 182–195, Visegrád, Hungary.

Venegas, J., Harris, R., and Simon, B. (1998). A Comprehensive Equation for the Pulmonary Pressure-Volume Curve. *Journal of Applied Physiology*, 84(1):389–395.

Vik, T. (2004). *Modèles statistiques d'apparences non gaussiens. Application à la création d'un atlas probabiliste de perfusion cérébrale en imagerie médicale*. PhD thesis, Université Louis Pasteur, Strasbourg I, Strasbourg, France.

Vik, T., Heitz, F., Namer, I., and Armspach, J. (2005). On the Modeling, Construction and Evaluation of a Probabilistic Atlas of Brain Perfusion. *NeuroImage*, 24(4):1088–1098.

Villard, P. and Baudet, V. (2003). Modélisation Comportementale du Poumon pour l'Amélioration des Traitements Oncologiques. In *Journées des Jeunes Chercheurs, Société Française de Génie Biologique et Médical*, pages 182–183, Nantes, France.

Vincent, L. and Soille, P. (1991). Watersheds in Digital Spaces: an Efficient Algorithm Based on Immersion Simulations. *IEEE Transactions on Pattern Analysis and Machine Intelligence*, 13(6):583–598.

Vogel, W., van Dalen, J., Schinagl, D., Kaanders, J., Huisman, H., Corstens, F., and Oyen, W. (2006). Correction of an Image Size Difference between Positron Emission Tomography (PET) and Computed Tomography (CT) Improves Image Fusion of Dedicated PET and CT. *Physics in Medecine and Biology*, 27(6):515–519.

Voorhees, A., An, J., Berger, K., Goldring, R., and Chen, Q. (2005). Magnetic Resonance Imaging-Based Spirometry for Regional Assessment of Pulmonary Function. *Magnetic Resonance in Medicine*, 54:1146–1154.

Wagers, S., Bouder, T., Kaminsky, D., and Irvin, C. (2000). The Invaluable Pressure-Volume Curve. *Chest*, 117(2):578–583.

Wagner Jr., H. (2003). PET and PET/CT: Progress, Rewards, and Challenges. *The Journal of Nuclear Medicine*, 44(7):10N–14N.

Wagner Jr., H. (2004). Creating Lifetime Images of Health and Disease. *SNM Highlights Lecture*, pages 11N–41N.

Wang, K., He, Y., and Qin, H. (2005). Incorporating Rigid Structures in Non-Rigid Registration Using Triangular B-Splines. In *Variational, Geometric, and Level Set Methods in Computer Vision (VLSM'05)*, volume 3752 of *Lecture Notes in Computer Science (LNCS)*, pages 235–246.

Web Gallery (2006). *Web Gallery of Art. Drawings of the human body by Leonardo da Vinci*. Web site: http://keptar.demasz.hu/arthp/html/l/leonardo/drawings/body/.

West, J., Maurer, C., and Dooley, J. (2005). Hybrid Point-and-Intensity-Based Deformable Registration for Abdominal CT Images. In *SPIE Medical Imaging: Image Processing*, volume 5747, pages 204–211, San Diego, California, USA.

Wiemker, R., Rohr, K., Binder, L., Sprengel, R., and Stiehl, H. (1996). Application of Elastic Registration to Imagery from Airborne Scanners. In *XVIII Congress of the International Society for Photogrammetry and Remote Sensing (ISPRS'96)*, volume XXXI-B4, pages 949–954, Vienna, Austria.

Wolthaus, J., van Herk, M., Muller, S., Belderbos, J., Lebesque, J., de Bois, J., Rossi, M., and Damen, E. (2005). Fusion of Respiration-Correlated PET and CT Scans: Correlated Lung Tumour Motion in Anatomical and Functional Scans. *Physics in Medecine and Biology*, 50(7):1569–1583.

Wörz, S. and Rohr, K. (2006). Localization of Anatomical Point Landmarks in 3D Medical Images by Fitting 3D Parametric Intensity Models. *Medical Image Analysis*, 10(1):41–58.

Xiaohua, C., Brady, M., Lok-Chuen Lo, J., and Moore, N. (2005). Simultaneous Segmentation and Registration of Contrast-Enhanced Breast MRI. In Christensen, G. E. and Sonka, M., editors, *19th International Conference on Information Processing in Medical Imaging (IPMI)*, volume 3565 of *Lecture Notes in Computer Science (LNCS)*, pages 126–137, Glenwood Springs, CO, USA.

Xiaohua, C., Brady, M., and Rueckert, D. (2004). Simultaneous Segmentation and Registration for Medical Image. In Barillot, C., Haynor, D., and Hellier, P., editors, *7th International Conference on Medical Image Computing and Computer-Assisted Intervention (MICCAI), Part I*, volume 3216 of *Lecture Notes in Computer Science (LNCS)*, pages 663–670, Rennes - St-Malo, France. Springer-Verlag Berlin / Heidelberg.

Xu, C. and Prince, J. (1997). Gradient Vector Flow: A New External Force for Snakes. In *IEEE Computer Society Conference on Computer Vision and Pattern Recognition*, pages 66–71, Los Alamitos, San Juan, Puerto Rico.

Xu, C. and Prince, J. (1998). Snakes, Shapes, and Gradient Vector Flow. *IEEE Transactions on Medical Imaging*, 7(3):359–369.

Xu, C. and Prince, J. (2000). *Handbook of Medical Imaging*, chapter Gradient Vector Flow Deformable Models, pages 159–169. Ed. Isaac Bankman, Academic Press.

Xu, S., Taylor, R., Fichtinger, G., and Cleary, K. (2005). Lung Deformation Estimation and Four-Dimensional CT Lung Reconstruction. In Duncan, J. S. and Gerig, G., editors, *8th International Conference on Medical Image Computing and Computer-Assisted Intervention (MICCAI)*, volume 3750 of *Lecture Notes in Computer Science (LNCS)*, pages 312–319, Palm Springs, CA, USA. Springer-Verlag Berlin / Heidelberg.

Yang, J., Staib, L., and Duncan, J. (2004). Neighbor-Constrained Segmentation with Level Set Based 3-D Deformable Models. *IEEE Transactions on Medical Imaging*, 23(8):940–948.

Zhang, T., Keller, H., Jeraj, R., Manon, R., Welsh, J., Patel, R., Fenwick, J., Mehta, M., Mackie, T., and Paliwal, B. (2003). Breathing Synchronized Delivery - A New Technique for Radiation Treatment of the Targets with Respiratory Motion. *International Journal of Radiation Oncology Biology Physics*, 57(2):S185–S186.

Zhang, Z., Jiang, Y., and Tsui, H. (2006). Consistent Multi-Modal Non-Rigid Registration Based on a Variational Approach. *Pattern Recognition Letters*, 27:715–725.

Zhao, B., Gamsu, G., Ginsberg, M., Jiang, L., and Schwartz, L. (2003). Automatic Detection of Small Lung Nodules on CT Utilizing a Local Density Maximum Algorithm. *Journal of Applied Clinical Medical Physics*, 4(3):248–260.

Zhukov, L., Bao, Z., Guskov, I., Wood, J., and Breen, D. (2002). Dynamic Deformable Models for 3D MRI Heart Segmentation. In *SPIE Medical Imaging*, volume 4684, pages 1398–1405, San Diego, California, USA.

Zijdenbos, A., Dawant, B., Margolin, R., and Palmer, A. (1994). Morphometric Analysis of White Matter Lesions in MR Images: Method and Validation. *IEEE Transactions on Medical Imaging*, 13(4):716–724.

Zitovà, B. and Flusser, J. (2003). Image Registration Methods: A Survey. *Image and Vision Computing*, 21:977–1000.

Zordan, V., Celly, B., Chiu, B., and DiLorenzo, P. (2006). Breathe Easy: Model and Control of Human Respiration for Computer Animation. *Graphical Models*, 68(2):113–132.

Zubal, I., Harrell, C., Smith, E., Rattner, Z., Gindi, G., and Hoffer, P. (1994). Computerized 3-Dimensional Segmented Human Anatomy. *Medical Physics*, 21(2):299–302.

Explicit Incorporation of Prior Anatomical Information Into a Nonrigid Registration of Thoracic and Abdominal CT and 18-FDG Whole-Body Emission PET Images

Oscar Camara*, Gaspar Delso, *Member, IEEE*, Olivier Colliot, Antonio Moreno-Ingelmo, and Isabelle Bloch, *Member, IEEE*

***Abstract*—The aim of this paper is to develop a registration methodology in order to combine anatomical and functional information provided by thoracic/abdominal computed tomography (CT) and whole-body positron emission tomography (PET) images. The proposed procedure is based on the incorporation of prior anatomical information in an intensity-based nonrigid registration algorithm. This incorporation is achieved in an explicit way, initializing the intensity-based registration stage with the solution obtained by a nonrigid registration of corresponding anatomical structures. A segmentation algorithm based on a hierarchically ordered set of anatomy-specific rules is used to obtain anatomical structures in CT and emission PET scans. Nonrigid deformations are modeled in both registration stages by means of free-form deformations, the optimization of the control points being achieved by means of an original vector field-based approach instead of the classical gradient-based techniques, considerably reducing the computational time of the structure registration stage. We have applied the proposed methodology to 38 sets of images (33 provided by standalone machines and five by hybrid systems) and an assessment protocol has been developed to furnish a qualitative evaluation of the algorithm performance.**

***Index Terms*—Anatomical constraints, free-form deformations (FFD), nonrigid registration, oncology, thoracic and abdominal computed tomography (CT), whole-body positron emission tomography (PET.**

I. Introduction

THE combination of anatomical and functional information provided by computed tomography (CT) and positron emission tomography (PET) imaging modalities can have a significant impact [1] on improving medical decisions for diagnosis, staging, planning, radiotherapy, or monitoring. On the one hand, PET scans provide valuable knowledge about metabolic abnormalities, but give limited information on the anatomy around the increased uptake, making precise lesion localization quite difficult. On the other hand, CT is not as sensitive as PET but offers accurate anatomic detail, pinpointing the exact size, shape, and location of diseased tissue. The benefit of the combination of these complementary imaging modalities has been proven in a large number of clinical studies. An extensive review of these works can be found in [2].

Nevertheless, integrating data from these imaging modalities is a challenging task, in particular in thoracic and abdominal images. One needs to compensate for the elastic nature of the organs located in these regions, the large intrasubject variability in terms of motion, anatomy and metabolic activity and the different physical nature underlying both acquisition techniques, in order to achieve the combination of both types of information. All these factors add up to cause displacements of up to 10 cm between corresponding structures. For instance, Goerres *et al.* [3] found a maximum of displacement of 8.29 cm in the diaphragm between a PET scan and a CT image acquired at maximum inspiration. Until few years ago, physicians visually integrated information provided by CT and PET scans acquired in separated devices, using their anatomical knowledge and expertise to identify homologous points between the images. Unsurprisingly, this procedure was very rough and time-consuming, and uncertainty in the mapping from one image to another could lead to uncertainty in clinical decisions.

The development of combined PET-CT systems, introduced by scanner constructors in the late 1990s [4] represented a huge step towards an automatic solution of this problem. These machines allow the acquisition of anatomical and functional information in the same session and device, thus furnishing a hardware (or mechanical) integration. Nevertheless, these systems cannot deal with physiological motions between CT and PET acquisitions due to breathing, cardiac cycle or insufficient patient cooperation [3]. Several studies [5]–[8] have proven the presence of artifacts in images acquired with combined PET-CT machines in the lungs and the liver, mostly due to respiration.

Before the introduction of PET-CT combined machines, software-based registration techniques were the only way to compensate for differences between images acquired with

Manuscript received June 16, 2006; revised October 27, 2006. This work was supported by the French Ministry for Research under Grant 01B0267. *Asterisk indicates corresponding author.*

*O. Camara was with the TSI Department, Ecole Nationale Supérieure des Télécommunications, CNRS UMR 5141, Paris, France. He is now with Centre for Medical Image Computing, Department of Medical Physics, University College London, London WC1E 6BT, U.K (e-mail: o.camara-rey@ucl.ac.uk).

G. Delso was with the TSI Department, Ecole Nationale Supérieure des Télécommunications, CNRS UMR 5141, Paris, France. He is now with Medical Imaging Systems Group, Philips Medical Systems, 92156 Suresnes Cedex, France (e-mail: gaspar.delso@philips.com).

O. Colliot was with the TSI Department, Ecole Nationale Supérieure des Télécommunications, CNRS UMR 5141, Paris, France. He is now with CNRS, UPR 640 LENA, Cognitive Neuroscience and Brain Imaging Laboratory, Université Pierre et Marie Curie–Paris 6, Hôpital de la Pitié-Salpêtrière, Paris, France (e-mail: olivier.colliot@chups.jussieu.fr).

A. Moreno-Ingelmo and I. Bloch are with the TSI Department, Ecole Nationale Supérieure des Télécommunications, CNRS UMR 5141, Paris, France (e-mail: antonio.moreno@enst.fr; isabelle.bloch@enst.fr).

Color versions of one or more of the figures in this paper are available online at http://ieeexplore.ieee.org.

Digital Object Identifier 10.1109/TMI.2006.889712

standalone devices. Nowadays, such algorithms can also be used to cope with physiological-induced deformations between images acquired with hybrid systems. Some complete reviews on registration methods can be found in [9]–[13]. Several works have been published in the context of thoracic and abdominal CT-PET registration. A study of the role of image registration in nuclear medicine was published by Hutton *et al.* [14]. Some of these registration techniques [15]–[19] employed linear (rigid or affine) transformations in these regions. However, linear transformations being unable to compensate deformations due to normal metabolic activity, some authors have moved forward to nonrigid registration algorithms. Sato *et al.* [20] proposed a point-to-point matching methodology based on a Cauchy–Navier spline transformation. The main drawback of this method is the high computational cost associated to the optimization of the cost function. Meyer *et al.* [21] applied a mutual information-based algorithm in thoracic CT-PET and abdominal computed tomography single photon emission computed tomography (CT-SPECT) registration applications, using a full affine mapping and a five-point thin-plate spline (TPS) warped registration technique. The major drawback of this method is the manual selection of the control points required for the TPS model. A similar method was proposed by Slomka *et al.* [22], which is based on the extraction of corresponding control points from the lungs and the application of a TPS interpolation algorithm from the corresponding control points that furnishes a dense nonrigid transformation. The main drawback of this approach concerns the selection of the control points. For instance, when working with images having tumors within the lungs, the ray-tracing technique will find control points in the tumor rather than in the lung contours. Furthermore, there is a lack of information in the regions far away from lungs and body contours (even information within the structures is not taken into account). Tai *et al.* [23] have developed and evaluated a nonrigid CT and whole-body PET registration method using transmission PET scans. Erdi *et al.* [24] also employed the transmission PET image to guide the registration with the CT image in a thoracic application.

One elegant solution to the registration of chest CT and transmission PET images was proposed by Mattes *et al.* [25], in which deformations were modelled with a B-spline FFD transformation and using mutual information (MI) as the similarity measure. The authors pointed out that obtained results were not completely satisfactory on more deformable regions such as the diaphragm or the abdomen. Based on Mattes' work, Delzescaux *et al.* [26] studied the influence of the CT respiration phase and the free-form deformation (FFD) model ability to cope with nonlinear deformations due to respiration movements. They proposed to transform the CT image instead of the PET one in order to preserve the metabolic information provided by functional images, this approach being well-suited for radiotherapy applications. Carlsen and Wischmann [27] also proposed a FFD-based procedure using a CT-derived pseudo-transmission image to compute a nonrigid transformation based on tricubic B-splines. Recently, Shekhar *et al.* [28] proposed a MI-guided elastic registration technique based on multiple rigid-body registrations. They have applied their methodology to a set of images acquired with both standalone and combined machines, obtaining a registration accuracy comparable to interexpert difference in landmark identification.

All previous nonrigid techniques (except those ones proposed by Sato [20] and Shekhar [28]) assumed a linear relation, or even no deformations, between emission and transmission PET scans. This assumption is not always satisfied because emission and transmission images are not acquired in a simultaneous way. Apart from little differences that can appear in cardiac regions, the main danger of this assumption concerns pathologies or tumors that are only visible in emission PET images. If only the transmission PET scan is used to guide the registration process, tumors will not be taken into account. Furthermore, the liver may not be distinguishable from the surrounding structures in transmission PET scans, therefore, these methods cannot be used in abdominal registration applications. With respect to previous FFD-based registration techniques, none of them directly work on emission PET scans due to their low-SNR quality and the lack of constraints on the FFD transformation model. When working with emission PET images, these approaches tend to get trapped in local minima of the chosen similarity criterion if they are not initialized within a relatively narrow range near to the final solution.

In order to avoid these problems, one can introduce in the registration procedure prior information about the anatomical structures involved in the application. The incorporation of prior anatomical information in registration processes is at the core of current state-of-the-art research in nonrigid registration.

In the majority of cases, prior anatomical information is introduced in an *implicit* way. This approach forces the registration procedure to furnish plausible deformations that have been found by modeling the expected structure variability and the spatial relationships between these structures. Biomechanical finite element models (FEMs) such as the NURBS-based cardiac-torso (NCAT) phantom [29], [30] and statistical model methods such as the active appearance modeling (AAM) [31], the statistical deformation modeling (SDM) [32], or the statistical shape models proposed by Wang and Staib [33] can be used to obtain this prior knowledge. Two major drawbacks are associated to this approach in the context of our application. First, relying on anatomical atlases or expected structure morphology and movements seems too risky when working with pathological images due to the large interpatient variability. Tumors may appear anywhere in the image, considerably modifying the shape and volume of structures, as well as the spatial relationships between them. Secondly, implicit approaches ask for additional registration processes in order to align prior anatomical models to the image data. The main consequence is an increase of the computational overhead of the whole procedure, which is a critical point in our application.

Therefore, we propose a faster approach based on an *explicit* incorporation of anatomical prior information into the registration procedure. Some authors [34]–[37] have presented different ways of merging this anatomical prior information provided by some recognized features in the image with information provided by the whole set of grey-level intensities. Our approach consists in obtaining anatomical knowledge directly from the images to register, making use of a novel hierarchical segmentation technique, and computing a nonrigid transformation be-

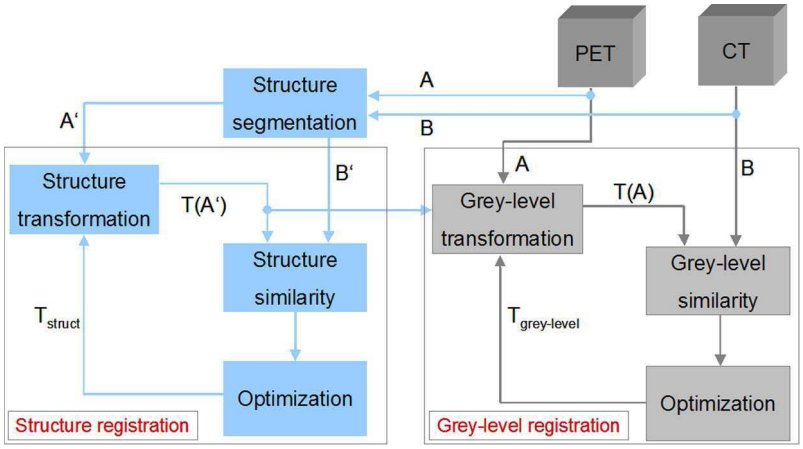

Fig. 1. General scheme of the proposed approach. Left part corresponds to the structure registration stage and the right part to the grey-level registration stage. Transformation obtained between the segmented structures initializes the registration phase that works with the whole set of intensities.

tween the corresponding segmented structures. This information is used to initialize deformations as close as possible to the final solution before applying whole-content registration techniques. With this initialization, the search of the global solution will be constrained and the algorithm will converge in a more robust and faster way. This approach does not make any assumption on the structures themselves or on their deformations, relying only on available information in the images and on a set of robust spatial relationships between the structures, permitting to work with almost any kind of unexpected situations. Moreover, the extraction of anatomical knowledge from the images is in general less expensive in terms of computational cost than registration procedures. The segmentation of corresponding structures in CT and emission PET images is achieved by means of a hierarchical segmentation method based on the mathematical modeling of robust spatial relationships between the targeted structures. Nonrigid deformations are modeled in both registration stages by means of FFD, but the optimization of the control points is achieved by an original vector field-based approach, called gradient vector flow-free-form deformations (GVF-FFD), instead of the classical gradient-based technique, considerably reducing (13 times faster) the computational time of the structure registration stage. We have applied the proposed methodology to 38 sets of images, 33 provided by standalone machines and 5 by hybrid systems. A visual assessment protocol has been developed to furnish a qualitative evaluation of the algorithm performance.

The paper is organized as follows. A general scheme of the proposed methodology is presented in Section II. Section III is devoted to the structure segmentation stage and the subsequent nonrigid registration stage applied on the segmented anatomical features is detailed in Section IV. The whole-content registration phase is presented in Section V. In Section VI, we describe the evaluation protocol developed to assess in a qualitative way the accuracy of the registration results. Finally, results are shown in Section VII and conclusions are given in Section VIII.

II. General Scheme

A general scheme of the proposed registration methodology is shown in Fig. 1. It is divided into two stages: a structure registration phase (left part of Fig. 1) in which homologous structures (A' and B') are extracted from both CT and PET images (A and B) and nonrigidly registered; and a grey-level registration phase (right part of Fig. 1) in which a nonrigid registration based on their full intensity content is applied to the original images (A and B). The second stage, initialized with the transformation (T_{struct}) provided by the structure registration stage, furnishes the final nonrigid transformation ($T_{\text{grey-level}}$).

In fact, the structure registration phase can be seen as the first step in an anatomical multiresolution procedure, first extracting from the data and processing the main anatomical structures, then transferring the result as an initial estimate to a higher level where finer anatomical detail is considered. Therefore, the grey-level registration phase can be considered as a refinement step of the structure registration results, capable of correcting errors the segmentation might have induced and improving the registration in those regions distant from the segmented structures.

The use of this strategy also implies a less expensive registration procedure in terms of computational cost, the reasons being the robustness improvement of the registration algorithm in the presence of local minima, and the reduction of the number of iterations required for the grey-level registration phase, due to the proximity of the initial transformation to the final solution.

III. Structure Segmentation

Our registration methodology requires a set of homologous structures that can be robustly located in both thoracic/abdominal emission PET and CT images. Based on discussions with medical experts, we finally chose to segment the following structures: skin, skeleton[1] , lungs, kidneys, and liver. Obtaining an accurate, fully automatic segmentation of the mentioned anatomical structures would be on itself a formidable task, in particular for functional images. Fortunately, segmentation accuracy is not a priority in this application since, in the proposed registration procedure, segmentation errors will not be propagated to the final registration result. The point is that if more

[1]The skeleton is only segmented in CT since its extraction with enough robustness in emission PET scans is difficult. Therefore, the skeleton is only used at the CT image segmentation stage as a support structure, but it does not play any role in the registration procedure.

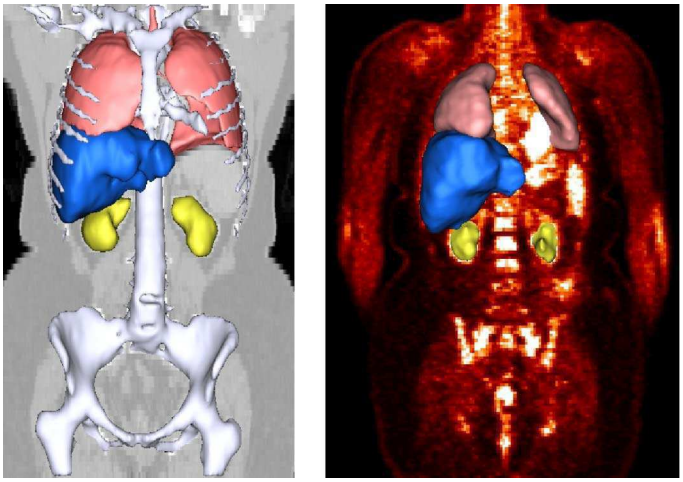

Fig. 2. Meshes of final segmented structures, including skeleton (white), lungs (red), kidneys (yellow), and liver (blue). Left: Rendering of CT segmented structures superimposed on a 2-D coronal grey-level slice. Right: 3-D rendering of PET segmented structures superimposed on a 2-D coronal grey-level slice.

organs are detected, then results are better because we have more constraints over the whole volume. But the segmentation of these organs does not need to be very accurate. Typically, segmentation errors of a few millimeters are not critical in our method. Indeed the second intensity-based, registration stage will be able to correct them. In summary, the quantity of information is important, but its accuracy is not. Therefore, the segmentation procedure will focus on speed and reliability rather than accuracy.

For the segmentation of the targeted structures, relying only on their grey-level intensities proved to be an insufficiently robust strategy, as they depend too much on the acquisition characteristics and suffer from a high inter-patient variability. Consequently, we decided to introduce higher-level information by exploiting the spatial relationships between organs, less sensitive to the deformations than shape and less acquisition-dependent than grey-level values. A hierarchical segmentation procedure has been proposed [38], based on the mathematical modeling of robust spatial relationships between the targeted structures to provide *prior* constraints that will be combined with information from the images. Detailing this method is outside the scope of this paper and the reader can refer to [38] for a complete description of the segmentation procedure. A similar strategy has been successfully used for the segmentation of internal brain structures [39]. An example of structure segmentation results in both CT and emission PET images is shown in Fig. 2, where meshes of final segmented structures, including skeleton, lungs, kidneys and liver, are superimposed on two-dimensional (2-D) coronal slices of CT and emission PET grey-level scans.

The proposed method has been positively evaluated by medical experts, in all CT and PET structures. Lung segmentation results are very accurate in CT images, obtaining subvoxel segmentation accuracy, while some errors (small enough for not inducing final misregistrations due to the grey-level registration stage of the proposed methodology) appear in emission PET scans due to the low SNR of these images. The liver is the most difficult structure to segment in both CT and PET images due to the presence of neighboring structures with similar grey-level values, such as the heart and aorta artery. Nevertheless, a reasonable approximation of the liver is obtained, notably separating it from the kidneys and the heart. On the other hand, we have often found (around 50% of the cases) small structures close to the liver that our segmentation procedure classifies as false positive liver voxels.

Finally, a retrospective segmentation evaluation based on the assessment of final registration results has also been performed. This has been used to verify that inaccuracies in the segmentation procedure stay within the capture range of the final grey-level registration, and can thus be corrected.

IV. Structure Registration

The main goal of this stage is to find a transformation between homologous CT and PET anatomical structures (lungs, kidneys, liver) that have been recognized in the previous segmentation phase. The registration method in this phase works with labeled images (a different label is affected to each three-dimensional (3-D) surface) and it must estimate the deformation between corresponding 3-D structures representing segmented thoracic and abdominal regions.

In our application, the registration procedure must be able to deal with structures having different characteristics in terms of geometry, local regularity and even topology (even if they have in general spherical topology). For instance, the algorithm must deal with the concavities caused by the bronchia in the CT lungs, which are seldom visible in PET; or the kidneys, fairly large, and smooth structures in CT but very crude in PET. Thus, the registration cannot impose severe regularity constraints.

First, an affine registration technique (see Section IV-A) is applied to the extracted homologous structures. Afterwards, a FFD-based registration technique (see Section IV-B), provides a nonrigid transformation between the CT and emission PET anatomical features.

Note that, when registering segmented images with nonrigid techniques such as the ones proposed in this paper, structures could locally slide along their interfaces without this being reflected in the registration similarity measure. Such effect, limited only by the regularity constraints imposed on the transformation, could lead to erroneous registration results. However, this is not a concern in the proposed implementation since the refined registration stage uses the whole content information and does not rely on interfaces anymore. This introduces additional constraints on the registration, which is then able to cope with all possible movements of structures.

A. *Affine Registration*

In general, nonrigid registration methods compute an initial rigid or affine transformation in order to cope with global deformations between the images to register. In the developed procedure, the segmented structures can be easily used to automatically establish a first approximation of the alignment. This includes translation and scaling in the three axes and cropping out the parts of the volumes without a correspondence or that have no interest for our application. This is achieved using a computed bounding box surrounding the structures to register

in both modalities. Trivial as it may seem, this simple step allows the whole system to be independent of the actual field-of-view (FOV) of the original images, unlike classical registration methods which need a prior manual adjustment (mainly in the z direction, as in [40]). Thus, once bounding boxes are built, translation and scale are already roughly recovered just by annotating the appropriate change in image origin position and voxel size. Then, we apply a classical affine registration technique [41] between CT and PET bounding boxes, using Powell's multidimensional direction set method [42] in order to refine the parameters of the affine transformation.

B. GVF-FFD

Nowadays, there is a large number of different nonrigid registration methods available in the literature, mainly differing in the transformation models used to compensate the deformations between the features to register. In our opinion, three of these models are particularly interesting for our application: those based on radial basis functions (RBFs), fluid methods, and FFD.

Radial basis functions [43], [44], formulate the transformation as a linear combination of kernel functions such as Thin-Plate [45] or Clamped-Plate [46] Splines. In general, registration methods based on RBF use anatomical features detected in both images as homologous control points. Then, after mapping each control point in the source image to its homologous in the target, the RBF are used to interpolate the control point displacements to create a dense mapping between both images. An interesting characteristic of these techniques is that there are no geometry restrictions to the control point distribution, i.e., it can be sparse and irregular. On the other hand, numerous and well-distributed control points in the image are required in order to assure acceptable registration results when the deformations are very local or do not respond to the inherent physical model. However, the selection of these control points in a simple and robust way remains a difficult problem, especially in emission PET images, and we would not be able to provide a large enough set of corresponding references adequately distributed all over the data volumes. Furthermore, as the range of each control point is not necessarily local, if the number of control points is elevated this technique is very expensive in computational terms.

Fluid-based techniques [47]–[49] are based on physical laws that provide an unconstrained model in which the source image is modeled as a viscous fluid which gradually deforms over time to match the target image. Such techniques have too many degrees of freedom for our purposes, being computationally expensive and inadequate to be applied in applications involving noisy imaging modalities such as PET.

FFD based techniques, introduced by Sederberg *et al.* [50], are a particular case of FEMs (which have been firstly used by Gee *et al.* [51] for medical image registration purposes) based on radial basis functions that has known an important success in the field of computer graphics. First used by Rueckert *et al.* [52] for medical image registration purposes, they model the transformation as a linear combination of spline basis functions. In this technique, deformations of the object volume are achieved by tuning an underlying mesh of control points but, unlike other RBF, FFD make use of a regularly distributed grid of control points, the position of these being independent of the underlying image (grid points no longer need to be homologous anatomical references), thus avoiding the control point selection phase. Some authors [53], [54] have compared the performance of fluid and FFD registration algorithms, concluding that FFD furnish slightly better or equivalent results to the fluid ones. The use of cubic B-splines to interpolate the displacements of the control point grid guarantees that moving any control point will only have a local effect on the image, significantly reducing the computational cost associated to its optimization.

Therefore, a nonrigid transformation based on B-spline FFD has been chosen to compensate the deformations involved in our application.

1) Gradient-Based Optimization: In this technique, deformations of the source volume (the PET scan in our application) are achieved by tuning a regular mesh of control points (ϕ being an uniformly spaced grid of $n_x \times n_y \times n_z$ control points $\phi_{i,j,k}$ with a spacing of δ and i, j, k being the indices within the grid). The spacing δ between the control points of the FFD grid has been chosen according to the magnitude of the local deformations and the resolution and the size of the images to register. We have empirically set the distance between control points to 20 mm, which has proven to provide accurate enough results.

In general, the optimization of the transformation parameters (i.e., control point displacements, $\phi_{i,j,k}$) is achieved by applying iteratively a gradient descent technique to all control points simultaneously [52], advancing along the gradient direction until no further improvement of the similarity measure is found. This gradient estimation is performed by computing local differences over the control point grid. This procedure is embedded in a multistep framework (the initial optimization step μ is divided by 2 at each level), in order to cope first with severe deformations and progressively take finer ones into account.

In addition, a local spring force regularization term has been included, pulling each node towards the centroid of its neighboring nodes, in order to avoid overfitting and to prevent the control point grid from autointersecting, which could lead to unwanted alterations of the structure topology. This force has been defined heuristically and, despite not strictly forbidding intersections, it has been observed to perform well, provided the optimization step is small with respect to node separation.

An advantage of working with labelled images is that a simple and robust criterion such as the root mean square (rms) can be used as the similarity measure that will guide the registration (rms-FFD) of the segmented structures. Some tests have been conducted using more sophisticated measures such as the label consistency, proposed by Rueckert *et al.* [55], but without substantial improvements in the results.

2) Vector Field-Based Optimization: An important drawback of the classical optimization method described above is its high computational burden. This is due to the nature of the optimization procedure, in which a local gradient estimation is needed at each iteration to update the control point displacements of the whole grid. For instance, in a grid of 10 nodes per dimension, the algorithm must compute at each iteration the gradient for 3000 parameters. Multiresolution and multigrid approaches accelerate the convergence of the algorithm, but the gradient estimation remains a problem in terms of computation time.

We have proposed [56] a novel approach to speedup the optimization of the control point displacements, using a 3-D vector field v computed using the contours of segmented target structures (in our case, CT structures) instead of the gradient-based procedure employed in the rms-FFD algorithm. This vector field provides at each image voxel a displacement vector tangent to a smooth path towards the nearest structure. Making the image evolve along these paths will generally assure a good matching.

Therefore, at each iteration m, we update the displacement of every control point in the FFD grid according to the information provided by the displacement vectors located in its neighborhood

$$\phi_{i,j,k}^{m+1} = \phi_{i,j,k}^{m} + \mu \frac{1}{R} \sum_{r=0}^{R} p_{r,i,j,k} v_r \tag{1}$$

where R denotes the number of source structure contour points under the influence of a given control point and $p_{r,i,j,k}$ is a weight based on the distance between the contour and the control points. The mean of the resulting vectors is taken as the optimal control point displacement direction. The magnitude of the displacement also depends on the step (μ) of the optimization procedure. At the end of each iteration, a local spring regularization term is applied to prevent the control point grid from autointersecting.

The convergence of the algorithm depends on the quality of the computed vector field v. In order to avoid undesirable oscillations around the target contour, a precomputed distance map is checked at the end of each iteration and used as a stop criterion. The multistep framework also helps reducing this problem by dealing with large deformations in the first iterations and with more local ones at the end.

The main advantage of this approach is that the vector field v is computed only once at the beginning of the procedure, unlike the gradient estimation that must be updated at each iteration. Moreover, as only the voxels belonging to the structure contours are scanned, the computational burden of the algorithm is substantially reduced. Algorithm 1 summarizes the proposed control point optimization procedure.

Algorithm 1 Optimization of control point displacements with a 3-D dense vector field

for all segmented structures to register **do**
  contour detection of the structures to match {already affinely registered}
  computation of v over target structure contours
  While $\mu \neq \mu_{\text{end}}$ **do**
    While distance(n) $\leq$ distance(n $-$ 1) **do**
      for all control points **do**
        computation of r
        store v values of r (i.e., v_r) and weight them with the distance with respect to the control point $(p_{r,i,j,k})$
        update control point displacement with (1)
      end for
      application of local spring regularization term
      apply FFD grid to source structure contours
      computation of the distance between target and source contours
    end while
    divide μ by 2
  end while
end for

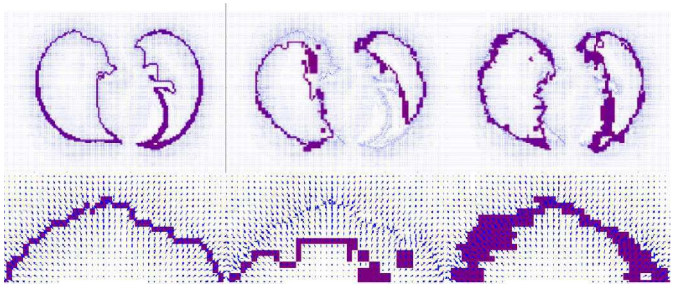

Fig. 3. Evolution of PET lung contours towards their corresponding CT ones using the GVF-FFD method. A 2-D axial slice of the GVF field derived from the CT contours is superimposed on them (left), on the PET contours before (center), and after (right) evolution. Top: 2-D axial slice. Bottom: detail.

The simplest way to obtain v would be to make use of a vector distance transform technique computed on CT structure contours. An alternative can be the use of the gradient vector flow (GVF) technique [57], that is usually employed to guide deformable models in segmentation applications. The advantage of the GVF with respect to the vector distance transform approach is the presence of a regularization term controlling the trade-off between the smoothness of the vector field and the fidelity to the contour gradients of the image. A smooth vector field is better suited for optimizing FFD control points in order to avoid local minima, at the expense of slightly increasing the computational cost of the algorithm due to the regularization term.

The left part of Fig. 3 shows a 2-D axial slice of the superimposition of CT lung contours on the GVF field computed over them. It can be observed that despite the regularization term, the local irregularities of the lungs are well coped with. An example of the evolution of PET lung contours towards their corresponding CT contours is also shown in Fig. 3. We can appreciate the remarkable improvement of the contour match after applying the GVF-FFD registration method (right in Fig. 3) with respect to results obtained by a rigid registration procedure (center in Fig. 3).

It must be pointed out that in our registration context, in which we need to register several thoracic and abdominal structures at the same time, some problems could arise if noncorresponding structures overlap since the labels are not taken into account in the contour evolution. We deal with this situation by computing the GVF field and making the source contours for each structure evolve independently. Therefore, at the end of the structure

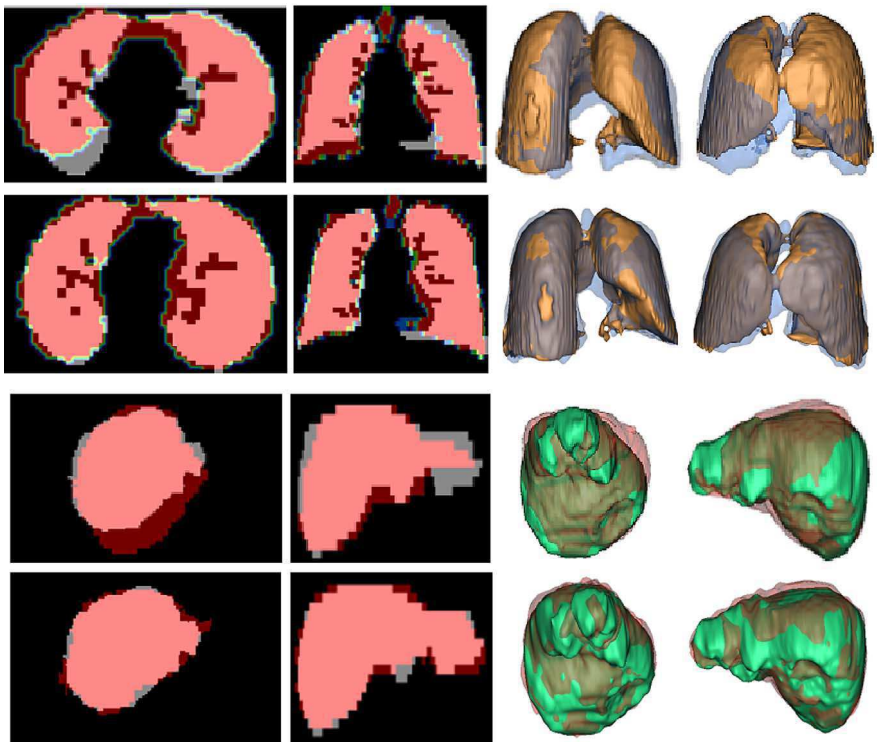

Fig. 4. Structure registration results obtained with the GVF-FFD method. Left part of the figure: 2-D coronal and axial slices of CT (grey) segmented lungs (top rows) and liver (bottow rows) are superimposed on their homologous PET structures (red), registered with a rigid transformation (first and third row) and with the GVF-FFD method (second and fourth row). Right part of the figure: a 3-D representation of the same structures is shown (CT lungs in blue, registered PET lungs in brown, CT liver in green, and registered PET liver in red).

registration procedure, an average of the displacements is taken for those control points affected by more than one structure.

C. *Evaluation of Structure Registration Methods*

Examples of results obtained by registering PET segmented structures (lungs and liver) with their homologous in CT images using the GVF-FFD and affine registration methods are displayed in Fig. 4. On the left part of the figure, 2-D axial and coronal slices of superimposed CT (grey) and registered PET (red) structures are shown. In a similar way, two different views of the superimposition of the 3-D CT (blue for CT lungs and green for CT liver) and registered PET (brown for registered PET lungs and red for registered PET liver) rendered structures are also shown.

We have computed three different registration measures between target and registered structures, aiming at comparing the performance of the affine, rms-FFD and GVF-FFD structure registration techniques. Let T and F be the set of voxels corresponding to the target and the registered source structures, respectively, and let the operator $|A|$ be the cardinality of the set of voxels A. The three criteria [58] used for estimating structure registration accuracy are the following:

$$\begin{aligned} \mathrm{OM} &= \frac{|T \cap F|}{|T \cup F|} \\ \mathrm{SENS} &= \frac{|T \cap F|}{|T|} \\ \mathrm{SPEC} &= \frac{|T \cap F|}{|F|} \end{aligned} \tag{2}$$

where OM is the Jaccard overlap measure, SENS the sensitivity, and SPEC the specificity.

The overlap measure (OM) is a classical criterion to evaluate the matching between two structures and consists of the quotient between intersection and union of structures to evaluate, which is equal to 1 if total overlap (best registration) is achieved. The sensitivity (SENS) and specificity (SPEC) measures give us additional information about how the overlap of both structures is achieved. For instance, if the registration of two structures yields a low sensitivity value but a high specificity one, it means that the registered source structure is too small. Both criteria are also equal to 1 if total overlap is achieved. It must be pointed out that the registered source must be thresholded at 50% of the nonzero label value of the structures in order to avoid an overestimation of the computed measures. In order to avoid this thresholding phase, the set of fuzzy overlap measures recently proposed by Crum *et al.* [59] could be used.

Both nonrigid structure registration methods have been applied to a database composed of 20 pairs of deformable structures (13 lungs and seven livers). These structures have been obtained applying the segmentation procedure described in [38] to CT and PET images of the same patient (eight cases) and using the NCAT phantom [29], [30] to generate structures at different stages of the respiratory and cardiac cycles (12 pairs of structures).

Table I summarizes the results (mean value $\pm$ standard deviation) furnished by the quantitative assessment measures computed on the whole set of registered structure pairs. Whereas rms-FFD technique provides the most accurate registration results, the GVF-FFD method still clearly surpasses the affine reg-

TABLE I
EVALUATION OF STRUCTURE REGISTRATION METHODS. OM: OVERLAP MEASURE. SENS: SENSITIVITY. SPEC: SPECIFICITY. VALUES CORRESPONDING TO THESE MEASURES REPRESENT THE MEAN AND THE STANDARD DEVIATION OF THESE MEASURES

	Lungs			Liver		
	OM	SENS	SPEC	OM	SENS	SPEC
Affine	0.731 ± 0.129	0.831 ± 0.171	0.869 ± 0.039	0.820 ± 0.034	0.893 ± 0.026	0.909 ± 0.033
RMS-FFD	0.857 ± 0.037	0.996 ± 0.003	0.860 ± 0.035	0.902 ± 0.006	0.998 ± 0.001	0.904 ± 0.006
GVF-FFD	0.821 ± 0.065	0.956 ± 0.048	0.852 ± 0.038	0.876 ± 0.016	0.987 ± 0.014	0.886 ± 0.006

istration technique. The three evaluated methods provide more accurate results in the liver than the lungs, and in a similar way, they perform slightly better with data coming from the NCAT phantom than from CT and PET derived structures. It is worth mentioning that differences between segmented structures coming from real CT and PET data are usually larger than those from the NCAT phantom, and that lung registration is more challenging than liver due to the presence of large surface irregularities to deal with. Sensitivity and specificity measures are close to 1 for both FFD-based methods, with specificity values slightly lower, proving that, in general, the registered source structure remains smaller than the target one. On the contrary, the affine method produces objects overpassing target structure sizes. Furthermore, we observe that differences of registration accuracy between results provided by the rms-FFD and GVF-FFD are larger in structures undergoing more local deformations such as the lungs. These effects are due to the tradeoff in the computation of the GVF vector field between the rejection of outliers and the capacity to cope with local deformations.

In addition to the registration accuracy measures, the convergence times of each structure registration method have been analyzed due to its major significance in our application. All values have been normalized by the dimensions of the images, so performances can be compared independently of image size. As expected, the GVF-FFD method shows much better performances (52.610 μs/voxel) than the rms-FFD technique (699.365 μs/voxel), i.e., around 13 times faster.

In consequence, the choice between the rms-FFD and GVF-FFD techniques will depend on the priorities for a given application, concerning registration accuracy or low computational costs. It has already been mentioned that, in the proposed method, the posterior grey-level registration phase will complement the structure registration stage, thus at this point only an approximation of the transformation between the structures to register is needed. Therefore, we prefer to use the GVF-FFD technique due to the good trade-off between its convergence times and the registration accuracy it provides. Nevertheless, if better registration accuracy were needed for a given application, the GVF-FFD technique could be used as a starting point, switching to rms-FFD to refine the results.

V. GREY-LEVEL REGISTRATION

The grey-level based registration phase is the last stage of the proposed registration methodology. This stage aims at refining registration results provided by the initial structure registration phase computed on segmented thoracic and abdominal structures. Furthermore, it must furnish a displacement field for regions far away from the segmented structures and even within them because at this point, reliable registration information based on their own characteristics (mostly grey-level values) has not yet been taken into account. For instance, this stage must provide and complete registration information corresponding to the ventricles of the heart, since the only information available up to this point came from the registration of the mediastinal wall, as the heart ventricles were not taken into account in the structure registration stage. Finally, another objective of this stage is the correction of misregistrations that may have been introduced by structure segmentation errors, taking advantage of the entire image grey-level information we are now working with.

This grey-level registration stage is essentially the method proposed by Rueckert *et al.* [52] in a nonrigid registration of contrast-enhanced breast magnetic resonance imaging (MRI) application. The nonrigid transformation is modeled by a FFD based on B-splines using normalized mutual information (NMI) as a similarity measure. This approach has been successfully used in several registration applications involving different imaging modalities [25], [32], [60], [61]. Nevertheless, the lack of constraints on the FFD model, the lack of uptake of several structures and the low SNR quality in the emission PET scans impede the straight use of this methodology in our application. In fact, this technique tends to converge towards local minima of the similarity criterion unless a very accurate initialization is provided. Fig. 5 shows a registration result obtained when applying a FFD-based registration technique without constraints between a pair of CT and emission PET scans of the same patient acquired with standalone machines.

We can observe in the nonrigidly registered emission PET image (bottom right in Fig. 5) that the FFD-based registration technique fails to provide acceptable results. For instance, we can observe that several critical structures are fully misregistered such as the liver or the kidneys and that the lung registration is not accurate enough. The set of intensities in emission PET scans corresponding to the boundaries of these structures are not well distinguished and, depending on the incremental step in the parameter optimization stage and the number of multigrid and multiresolution levels, some incorrect transformations can provide good similarity measure values. These parameters must be large enough to cope with severe deformations involved in these nonrigid regions, but the lack of constraints in the FFD model allowing any possible correspondence between the images produces these misregistrations. The tuning of the registration parameters could improve these results as well as the use of multigrid techniques, but we consider that, even if

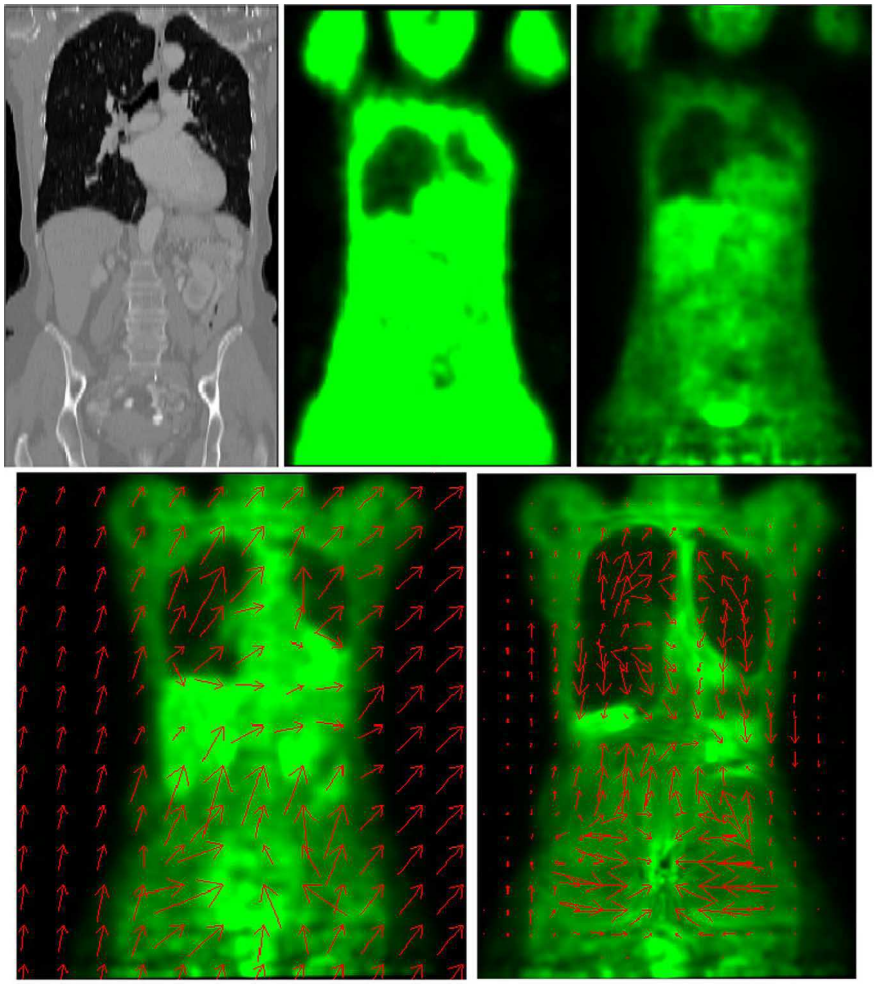

Fig. 5. Results obtained by computing an affine + FFD transformation without constraints between CT and emission PET images. Top: CT (left), transmission (center), and emission PET (right) original images. Bottom: registered emission PET images obtained by applying affine (left) and affine + FFD (right) transformations. Displacement field (red arrows) associated to each one of these transformations (affine on the left and FFD on the right) is superimposed on the images.

this NMI-FFD registration technique has been proven to be successful in some applications, it must be modified in order to deal with CT and emission PET images. For these reasons, in the proposed registration methodology, an accurate initialization is provided by the structure registration stage, furnishing to the NMI-FFD approach an initial transformation very close to the final solution, at least in the neighborhood of the segmented structures.

Furthermore, the inclusion of the previous initial structure registration phase allows us to skip some of the lower multiresolution steps of the time-consuming fine registration, thus substantially speeding up the overall process. The average computational time was around 2 h (the range goes from 50 min to 3 h), around 20 min corresponding to the segmentation and structure registration stages, in a Linux condor cluster (one CPU per registration) when applying the proposed registration methodology, thus reducing by an order of three the time needed for the FFD registration technique without constraints. It is difficult to compare these computational costs with other published in the literature in other medical imaging applications due to the influence of the image sizes and resolutions, the image quality, the nature of the deformations to cope with, the number of degrees of freedom in the transformation model or the available computational power. Nevertheless, just for giving a reference, Crum *et al.* [53] stated that fluid and B-spline FFD techniques took between 2 h and 10 h per registration in an intersubject brain registration application working with MR images. Considering that in our application processed images are larger, the fact that the poor image quality of PET images could easily make the algorithm converge towards local minima and the larger deformations we need to cope with, we think that results obtained by the proposed methodology in terms of computational cost are meritorious.

VI. Evaluation

Evaluating the result accuracy of a nonrigid registration method is a complex problem both conceptually and in practice. Indeed, nonrigid motions are difficult to perceive in three dimensions, and it must be checked that the registration algorithm corrects deformations in mobile structures while not introducing new errors in the more stable ones. This problem is aggravated in our application due to the lack of gold standard since manual segmentations in emission PET images will not be reliable enough to assess either a segmentation or a registration

procedure. Furthermore, even combined PET-CT scanners are unable to furnish a perfectly registered image that could be used as a reference for assessing nonrigid registration methods.

A. Visual Assessment Protocol

Even if it is a semi-objective validation technique, visual inspection by medical experts allows in our application to judge and classify, into a scoring scale of error values, registration results for the most important anatomical structures. Mattes *et al.* [25] have employed this approach to evaluate the registration accuracy of a nonrigid approach applied on chest CT and transmission PET images. We present a similar visual assessment protocol[2] that allows physicians and registration specialists to rapidly generate a semiobjective and qualitative measure of the registration accuracy, being repetitive enough to allow statistical interpretation of the results.

For this purpose, several anatomically significant 2-D slices of both the original CT and registered emission PET volumes, are presented. Slices have been evenly spaced through the volume in order to display the most significant thoracic and abdominal structures. For example, for a $256 \times 256 \times 97$ volume, six coronal and six axial slices are employed. This is performed by means of an automatic procedure that uses CT segmented structures in order to decide which 2-D slices must be chosen for evaluation purposes. However, the user has also access to all 2-D axial slices of the CT and the registered emission PET volume if they must be checked in order to confirm any evaluation score. Furthermore, the user has the possibility of changing the display intensity range settings of the 2-D slices.

Each pair of 2-D slices has been marked with a ruler that defines some reference or landmark points as it crosses significant anatomical structures, such as the chest wall (ribcage), the mediastinal wall (heart), the diaphragmatic wall (liver), or the stomach and kidneys walls. These references allow the user to estimate differences in the position of the mentioned structures in both 2-D slices and then score the registration accuracy of the method. For instance, in the case of the lungs, the user must evaluate the registration result accuracy in the anterior, posterior, inferior, and superior part of both, left and right lungs. Fig. 6 shows one pair of these 2-D slices, corresponding to axial (top) and coronal (bottom) slices.

This procedure is certainly limited in the sense that the evaluation only measures local translation errors at the reference points that are placed on the surface of some structures, and no assessment about registration result accuracy in other regions or even within the evaluated structures is provided. In general, an expert user needs about 20–30 min to complete the validation process, thus considerably faster than Mattes' evaluation interface [25].

The scoring (or dissatisfaction) scale has been defined by medical specialists keeping in mind that the goal of the registration method was to attain errors below the resolution of PET images (in general, voxel dimensions of PET images are around $4.0 \times 4.0 \times 4.0$ mm^3 in our database). Table II shows the scale and its correspondences in millimeters and in pixels.

[2]It has been developed under the supervision of Dr. H. Foehrenbach, from the H. I. A. Val de Grâce, Paris, France.

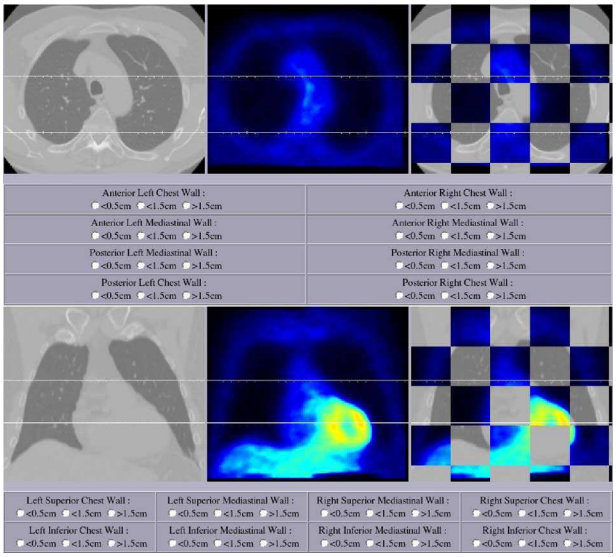

Fig. 6. Example of 2-D axial (top) and coronal (bottom) slices of the CT (left), registered PET (center) volumes, and the chessboard display (left) used in the visual assessment protocol. They are marked with the rulers (white) that define landmark points where registrations must be evaluated.

TABLE II
EVALUATION SCORING SCALE

Score	mm	Pixels	Quality
0	0-5	0-1	Good
1	5-15	1-3	Acceptable
2	15-	3-	Unacceptable

We have estimated the interobserver consistency of the developed visual assessment protocol in order to verify if it is repetitive and objective enough to be used for the evaluation of registration algorithms. A group of three clinicians of three different clinical centres, all of them with a strong experience in oncology, have used the developed evaluation protocol in order to assess registration result accuracy furnished by the proposed methodology.

The evaluation procedure has been used by these physicians in an independent way and assessment results have been sent back by means of the developed online *html* web form. They have assessed five registration thoracic and/or abdominal cases selected from the available database, each one with different degrees of registration accuracy, for the estimation of the interobserver consistency. The number of landmark points in which the registration has been assessed was: 208 for the lungs; 20 for the kidneys; 36 for the liver; 22 for the heart; and 10 for the stomach.

In order to have an estimation of the interobserver consistency for each targeted region, we have computed the percentage of landmark points in which the three evaluators have scored the registration accuracy with the same score; only two of the evaluators have agreed with the same score; or when the three evaluators do not agree at all. Obtained results are summarized in Fig. 7. We can appreciate a good performance of the proposed visual assessment protocol in all the targeted structures in terms

TABLE III
VISUAL ASSESSMENT PROTOCOL RESULTS. STRUCT: STRUCTURE REGISTRATION. FINAL: GREY-LEVEL REGISTRATION. RMS: RMS-FFD INITIALIZATION METHOD. GVF: GVF-FFD INITIALIZATION METHOD

	Score = 0 (%)				Score = 1 (%)				Score = 2 (%)			
	Struct		Final		Struct		Final		Struct		Final	
	RMS	GVF	RMS	GVF	RMS	GVF	RMS	GVF	RMS	GVF	RMS	GVF
Lungs	60.63	54.25	72.04	71.15	28.70	34.32	19.48	20.43	10.67	11.43	8.48	8.42
Heart	62.90	58.36	70.63	70.93	31.08	35.27	24.62	23.55	6.02	6.37	4.75	5.52
Liver	55.83	51.88	65.41	66.54	35.03	37.58	27.05	26.19	9.14	10.54	7.54	7.27
Kidneys	77.50	78.22	77.50	77.71	20.83	20.11	20.83	20.62	1.67	1.67	1.67	1.67
Stomach	33.19	31.12	41.09	39.15	18.79	20.37	21.30	22.17	48.02	48.51	37.61	38.68

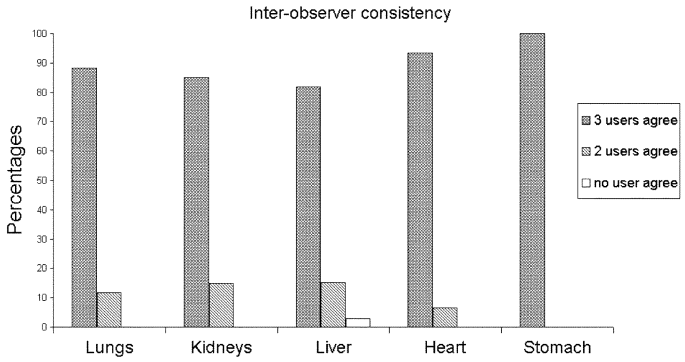

Fig. 7. Interobserver consistency measure.

of inter-observer consistency. All cases in which one evaluator disagrees with the others involve scores differing only in one step of the scoring scale, i.e., from good to acceptable or from acceptable to unacceptable, but never from good to unacceptable. We also observe that there exists more discrepancies for the liver and kidneys than for the lungs. This is due to the presence of several structures in abdominal CT images having similar intensity values. On the other hand, discrepancies in the lungs are mostly due to the lack of strong contours in emission PET images, in particular after applying the nonrigid transformation. An interesting conclusion from Fig. 7 is that the protocol can correctly assess the registration accuracy when it is not satisfactory, such as in the stomach. Finally, it must be pointed out that only in one reference point, the three evaluators have completely disagreed, also proving the appropriateness of the visual assessment protocol.

VII. RESULTS

A. Database and Study Description

During this work, 33 data sets composed of CT, emission and transmission PET scans acquired with standalone machines of thoracic and/or abdominal regions provided by LifeScan Louisville, KY, Centre Hospitalier Universitaire (C.H.U.), Liège, Belgium, Percy Hospital, France, and Hôpital d'Instruction des Armées (H.I.A.) du Val de Grâce, France, have been used. Furthermore, five additional data sets were available from Centre Hospitalier Princesse Grace (C.H.P.G.) of Monaco and C.H.U. of Liège, acquired with a combined CT-PET machine.

A common problem when using images from different sites is the lack of homogeneity in terms of image quality, due to the use of different scanners and clinical protocols employed to acquire the images. We have designed our registration procedure in order to be as much independent as possible of image acquisition characteristics in order to avoid reformatting our image database to a common standard. Therefore, CT images have a size of 256×256 or 512×512 pixels in the xy plane (axial plane) and between 60 and 125 slices (depending on their FOV, corresponding to a thoracic and/or an abdominal case), with voxel dimensions approximately $1.0 \times 1.0 \times 5.0\ \text{mm}^3$. PET images have a size of 144×144 pixels in the xy plane (axial plane) with 160 to 230 slices, with voxel dimensions around $4.0 \times 4.0 \times 4.0\ \text{mm}^3$.

We have employed the visual assessment protocol on the registration results furnished by the proposed methodology, without comparing them with the ones provided, for instance, by the FFD registration approach without constraints. We consider that, by means of a visual inspection of Fig. 5, one can clearly observe that the absence of anatomical constraints on the FFD registration procedure involves inaccurate results. On the other hand, we have used the evaluation protocol with the images obtained after the structure registration stage, both using the rms-FFD and the GVF-FFD strategies to compare them with the final results and thus to have an estimation of the performance of the grey-level registration stage.

Therefore, the visual assessment protocol has been used by five expert evaluators to assess the 33 different CT and emission PET image registrations coming from standalone machines[3], including thoracic and abdominal cases. Results obtained from the visual assessment protocol are summarized in Table III. It shows, for each significant thoracic and abdominal structure, the percentage of landmark points in which the registration error is scored as good, acceptable or unacceptable, according to the scoring scale of Table II.

[3]We consider that the reduced number of cases acquired with combined machines does not allow to obtain reliable statistics when applying the visual assessment protocol, thus they are just visually evaluated.

B. RMS-FFD Versus GVF-FFD Initialization Methods

Results shown in Table III are similar to those ones obtained in Section IV-C with respect to the performance of the two initialization methods presented in this paper: the GVF-FFD strategy provides less accurate results than the rms-FFD technique. Nevertheless, the grey-level registration stage compensates for these differences, at the expense of a minor addition in computational cost (around 100 min for the rms-FFD and 108 min for the GVF-FFD).

C. Structure Versus Grey-Level Registration

Concerning the comparison between results after the structure and the grey-level registration stages, we can observe a substantial improvement at the end of the procedure for all structures, except the kidneys. This enhancement involves the correction of possible segmentation errors (the lungs and the liver) as well as the fact of taking into account the grey-level information of not-segmented structures (the heart and the stomach). The lack of improvement in the kidneys is due to the good quality of their segmentation (very spherical structures) and the lack of strong deformations on these structures.

D. Stand-Alone Machines

Inspection of Table III illustrates the good performance of the proposed nonrigid registration methodology for the majority of the evaluated regions including lungs, kidneys, liver, and heart. On the other hand, some misregistrations appear near the stomach. These results are slightly better (registration errors under PET voxel size of 4 mm against 5 mm errors) to those ones recently presented by Shekhar *et al.* [28], but this could be due to the different image databases or the evaluation protocols used in both studies. A proper comparison of both registration methodology performances would be very useful to elucidate which one is better suited for this particular application or to combine their respective strengths into a more robust algorithm.

In particular, results obtained in the thoracic wall are very satisfactory, even in the diaphragmatic region where the transformation computation was very critical due to the large deformations suffered in this region. The upper part of both lungs have in all cases small registration errors, while some landmark points corresponding to the lower part of the lungs have a score of 1. The unacceptable errors found in the lungs correspond to the posterior mediastinal wall, due to the large differences in this region between CT and emission PET images.

The proposed registration methodology takes advantage of the proximity of the heart to the lungs and the strong constraints imposed on them to furnish good and acceptable registration errors of the heart.

We can observe that the kidneys produce the lowest registration errors, and this is due to the lack of strong deformations on these structures and their good initialization furnished by the segmentation-based registration stage. Landmark points corresponding to the kidneys that have a score of 2 concern those ones of the right kidney close to the stomach, due to the influence of this structure on their registration. On the other hand, most of the landmark points corresponding to the left kidney have a score of 0 (even if there are some scores of 1 in zones close to the liver).

The proposed registration methodology provides good and acceptable registration errors in the liver, despite the difficulties of this structure. Its landmark points scored as 0 correspond in general to the upper part and the left wall of the liver, while the ones in which the registration has been scored as 1 are located on the lower part of the liver. Some unacceptable registration errors are found on the right wall of the liver since, sometimes, there are small abdominal structures close and having similar intensity values to the liver that can produce good similarity measure values, even if the registration is not well done.

Most important registration errors have been found in the stomach (it is the only targeted structure having a mean of scores close to 1), due to the severity of its deformations and the lack of strong constraints imposed on this structure. Nevertheless, some good and acceptable scores have been assigned to the landmark points corresponding to the stomach that are relatively close to the kidneys and the lungs because they take advantage of the initialization registration stage applied to these structures.

One final registration result example is shown in Fig. 8. This case is very interesting due to the presence of a malignant tumor located in the left lung. The challenge of the transformation computation between these images is illustrated in the top row of coronal slices in Fig. 8, where it can be easily seen that the tumor is found in distant coronal slices after applying an affine registration transformation to the emission PET image (Fig. 8, top row, center). The application of the proposed nonrigid registration methodology has allowed to obtain a transformation capable of placing the tumor in the correct coronal slice (Fig. 8, top row, right).

Nevertheless, it must be pointed out that the performance of the proposed methodology is not optimal in all pathological cases, strongly depending on the location of the tumor. The majority of problems arise when the tumor is located within a structure suffering strong deformations such as the lungs, since the structure registration applies a transformation to the tumor that does not necessarily correspond to its own movement. On the other hand, as shown in Fig. 8, this situation is no more a problem when the pathology is located close to the edge of a segmented structure. The inclusion of tumors as an additional structure in the segmentation and first registration stages, as detailed in [62], would reduce these problems.

E. Combined Machines

The proposed registration methodology has been also applied to five images acquired with a combined CT-PET system. Minor or no improvement has been visually observed on all but one of the sets of images acquired by a hybrid system when applying the proposed registration methodology. Fig. 9 demonstrates the special case in which there is a substantial improvement on the superimposition of the CT and PET images, located in the cardiac region, after applying our procedure. Nevertheless, it must be pointed out that only five of these pairs of images were available and most of them did not present either substantial visible artifacts or visible tumors, i.e., cases in which a retrospective nonrigid registration algorithm could give additional information to the mechanical registration furnished by these machines.

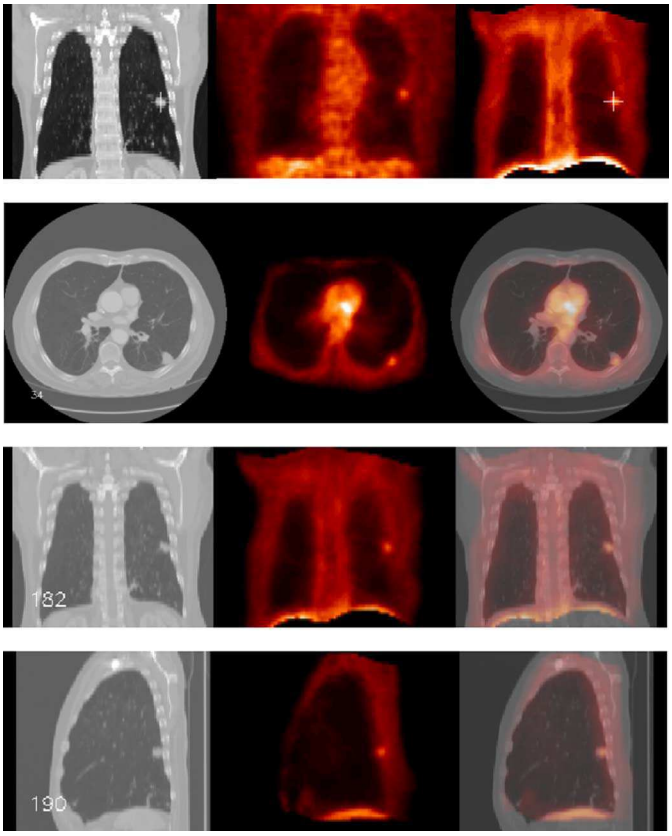

Fig. 8. Final registration result. 2-D coronal slices (top row) of the CT image (left), the emission PET image registered with an affine transformation (center), and the emission PET image registered with the proposed nonrigid registration methodology (right). Mark on the top row points out where the tumor is located. It can be seen that the tumor is found in different coronal slices after applying an affine transformation (center) and that this problem is solved using the proposed nonrigid registration methodology (right). An axial (second row), a coronal (third row), and a sagittal (bottom row) 2-D slices of the CT (left) and the registered emission PET (center) images, and their superimposition (right) are shown.

Therefore, we cannot draw any conclusions about the application of the proposed methodology on these images until a more exhaustive database is available.

VIII. Conclusion

We have presented a registration methodology adapted to cope with deformations between CT and emission PET images in order to combine anatomical and functional information provided by these imaging modalities. It is mostly based on the explicit incorporation of prior anatomical information into the registration procedure.

We have visually shown (see Fig. 5) that a FFD registration technique without constraints fails to provide accurate enough results when it is directly applied on the grey-level images. Nevertheless, this model has proved to be a flexible technique allowing us to construct an original registration methodology and providing us a simple way of interaction between the feature-based and intensity-based registration phases. This interaction between these two theorically confronted methods, derived from the chosen strategy, has allowed us to combine their associated advantages while canceling their drawbacks.

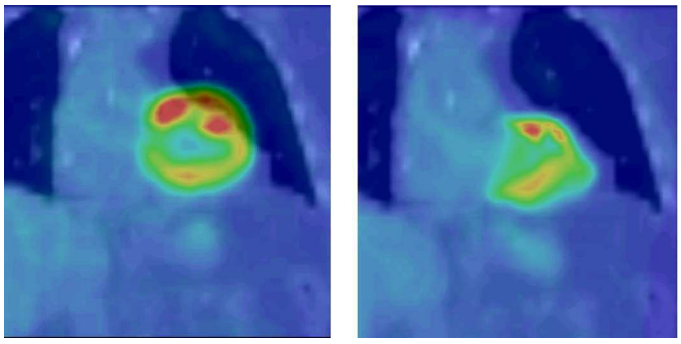

Fig. 9. Case from a combined CT-PET machine in which the proposed methodology corrects a large misalignment in the cardiac region. Two-dimensional coronal slices of the superimposition of the original CT image and the original emission PET image before (left) and after (right) registration.

Segmentation results have proven to be accurate enough for a structure registration procedure to initialize the final grey-level registration stage close to the optimal solution in the region around the available structures.

Results provided by the application of a visual assessment protocol to the pairs of images registered by the proposed methodology prove that we obtain acceptable registration errors for the majority of the targeted thoracic and abdominal structures, except for the stomach. This is due to the absence of this structure in the initialization phase, the strong deformations the stomach undergoes and the presence of close small structures with similar values misleading the intensity-based registration stage.

These promising registration results illustrate the fact that better registration is achieved around structures that have been recognized with the segmentation procedure. Furthermore, the inclusion of the structure registration stage involves a considerable reduction (three times) of the computational cost of the procedure. This allows us to think that the introduction of the proposed methodology in a clinical environment as an additional step in the routine is feasible. Then, a more exhaustive clinical validation of our approach in a larger population could be done. This would confirm the promising results obtained in this work in a relatively limited database or identify cases that the method could potentially fail on. However, a better code optimization and the use of parallelization methods as proposed by Rohlfing *et al.* [63] are still needed to make it possible.

The proposed registration methodology has been also applied to five pairs of images acquired with a PET-CT hybrid system. A substantial improvement has been obtained in one of these sets of images, but we cannot draw any conclusions about it due to the reduced number of processed images.

Current work is focused on the development of a gold standard, using the NCAT phantom [29], [30] and the SIMSET (http://depts.washington.edu/~simset/html/simset_main.html) open-source software, that will allow us to assess in a quantitative way the proposed registration methodology. Furthermore, future work includes a more principled incorporation of tumor-based constraints into the registration procedure aiming at preserving functional information after applying the nonrigid transformation.

ACKNOWLEDGMENT

The authors would like to thank J.-F. Stévenet, P. Briandet, Dr. H. Foehrenbach, Dr. P. Rigo, Dr. Marchandise, Y. Martelli, S. Hammer, the research team of S.H.F.J. in Orsay and the members of Segami Corporation for their contribution to this project. This work has been performed at the TSI Department at the Ecole Nationale Supérieure des Télécommunications, CNRS UMR 5141, Paris, France, in collaboration with SEGAMI.

REFERENCES

[1] H. Wagner, "Fused image tomography: An integrating force," *Nucl. Med.*, vol. 40, no. 8, pp. 13N–32N, 1999.

[2] O. Camara, "Non-linear registration of thoracic and abdominal CT and 18-FDG whole-body emission PET images: Methodological study and application in clinical routine," Ph.D. dissertation, Ecole Nationale Supérieure des Télécommunications (ENST), Paris, France, 2003.

[3] G. Goerres, E. Kamel, T. Heidelberg, M. Schwitter, C. Burger, and G. von Schulthess, "PET-CT image co-registration in the thorax: Influence of respiration," *Eur. J. Nucl. Med.*, vol. 29, no. 3, pp. 1337–1343, 2002.

[4] T. Beyer, D. Townsend, T. Brun, P. Kinahan, M. Charron, R. Roddy, J. Jerin, J. Young, L. Byars, and R. Nutt, "A combined PET/CT scanner for clinical oncology," *J. Nucl. Med.*, vol. 41, no. 3, pp. 1369–1379, 2000.

[5] T. Blodgett, T. Beyer, G. Antoch, S. Mueller, L. Freudenberg, and T. Akhurst, "The effect of respiration motion on PET/CT image quality," in *Proc. Conf. Soc. Nucl. Med. (SNM'02)*, 2002, p. 58.

[6] M. Osman, C. Cohade, and R. Wahl, "Respiratory motion artifacts on PET emission images obtained using CT attenuation correction on PET-CT," in *Proc. Conf. Soc. Nucl. Med. (SNM'02)*, 2002, p. 305.

[7] M. Osman, C. Cohade, Y. Nakamoto, L. Marshall, J. Leal, and R. Wahl, "Clinically significant inaccurate localization of lesions with PET/CT: Frequency in 300 patients," *J. Nucl. Med.*, vol. 44, pp. 240–243, 2003.

[8] D. Townsend, J. Carney, J. Yap, and N. Hall, "PET/CT today and tomorrow," *J. Nucl. Med.*, vol. 45, no. 1, pp. 4S–14S, 2003, (Suppl).

[9] L. Brown, "A survey of image registration techniques," *ACM Comput. Surveys*, vol. 24, no. 4, pp. 325–376, Dec. 1992.

[10] J. Maintz and M. Viergever, "A survey of medical image registration," *Med. Image Anal.*, vol. 2, no. 1, pp. 1–36, 1998.

[11] D. Hill, P. Batchelor, M. Holden, and D. Hawkes, "Medical image registration," *Phys. Med. Biol.*, vol. 46, pp. R1–R45, 2001.

[12] H. Lester and S. Arridge, "A survey of hierarchical non-linear medical image registration," *Pattern Recognit.*, vol. 32, pp. 129–149, 1999.

[13] B. Zitova and J. Flusser, "Image registration methods: A survey," *Image Vision Comput.*, vol. 21, pp. 977–1000, 2003.

[14] B. Button, M. Braun, L. Thurfjell, and D. Lau, "Image registration: An essential tool for nuclear medicine," *Eur. J. Nucl. Med.*, vol. 29, pp. 559–577, 2002.

[15] R. Wahl, L. Quint, R. Cieslak, A. Aisen, R. Koeppe, and C. Meyer, "Anatometabolic tumor imaging: Fusion of FDG PET with CT or MRI to localize foci of increased activity," *J. Nucl. Med.*, vol. 34, pp. 1190–1197, 1993.

[16] J. Yu, F. Fahey, H. Gage, C. Eades, B. Harkness, C. Pelizzari, and J. Keyes Jr., "Intermodality, retrospective image registration in the thorax," *J. Nucl. Med.*, vol. 36, no. 12, pp. 2333–2338, 1995.

[17] J. Cai, J. Chu, D. Recine, M. Sharma, C. Nguyen, R. Rodebaugh, V. Saxena, and A. All, "CT and PET lung image registration and fusion in radiotherapy treatment planning using the Chamfer-matching method," *Int. J. Radiation Oncol., Biol., Phys.*, vol. 43, no. 4, pp. 883–891, 1989.

[18] E. Parsai, K. Ayyangar, R. Dobelbower, and J. Siegel, "Clinical fusion of three-dimensional images using Bremsstrahlung SPECT and CT," *J. Nucl. Med.*, vol. 38, no. 2, pp. 319–324, 1997.

[19] F. Maes, D. Vandermeulen, G. Marchal, and P. Suetens, "Clinical relevance of fully automated multimodality image registration by maximization of mutual information," in *Proc. Image Registration Workshop*, 1997, pp. 323–330.

[20] M. Sato, A. E. Hassanien, and M. Nakajima, "Non-linear registration of medical images using Cauchy-Navier splines transformation," in *SPIE Conf. Image Process.*, 1999, pp. 3661–3677.

[21] C. Meyer, J. Boes, B. Kim, P. Bland, K. Zasadny, P. Kison, K. Koral, K. Frey, and R. Wahl, "Demonstration of accuracy and clinical versatility of mutual information for automatic multimodality image fusion using affine and thin-plate spline warped geometric deformations," *Med. Image Anal.*, vol. 1, pp. 195–206, 1996.

[22] P. Slomka, D. Dey, C. Przetak, U. Aladl, and R. Baum, "Automated 3-dimensional registration of stand-alone 18F-FDG whole-body PET with CT," *J. Nucl. Med.*, vol. 44, no. 7, pp. 1156–1167, 2003.

[23] Y. Tai, K. Lin, C. Hoh, S. Huang, and E. Hoffman, "Utilization of 3-D elastic transformation in the registration of chest X-ray CT and whole-body PET," *IEEE Trans. Nucl. Sci.*, vol. 44, no. 4, pp. 1606–1612, Aug. 1997.

[24] Y. Erdi, K. Rosenzweig, A. Erdi, H. Macapinlac, Y. Hu, L. Braban, J. Humm, O. Squire, C. Chui, S. Larson, and E. Yorke, "Radiotherapy treatment planning for patients with non-small cell lung cancer using positron emission tomography (PET)," *Radiotherapy Oncol.*, vol. 62, no. 1, pp. 51–60, 2002.

[25] D. Mattes, D. Haynor, H. Vesselle, T. Lewellen, and W. Eubank, "PET-CT image registration in the chest using free-form deformations," *IEEE Trans. Med. Imag.*, vol. 22, no. 1, pp. 120–128, Jan. 2003.

[26] T. Delzescaux, H. Foehrenbach, and V. Frouin, "A performance study for whole-body helicoidal CT/PET-FDG a posteriori registration using rigid and non-rigid FFD-based methods," *J. Nucl. Med.* vol. 44, 2003.

[27] I. Carlsen and H. Wischmann, "Multi-resolution elastic registration of PET-CT images," *Proc. Conf. Soc. Nucl. Med. (SNM'03)*, vol. 44, 2003.

[28] R. Shekhar, V. Walimbe, S. Raja, V. Zagrodsky, M. Kanvinde, G. Wu, and B. Bydel, "Automated 3-dimensional elastic registration of whole-body PET and CT from separate or combined scanners," *J. Nucl. Med.*, vol. 46, no. 9, pp. 1488–1496, 2005.

[29] W. Segars, "Development and application of the new dynamic NURBS-based cardiac-torso (NCAT) phantom," Ph.D. dissertation, Dept. Biomed. Eng., Univ. North Carolina, Chapel Hill, 2001.

[30] W. Segars and B. Tsui, "Study of the efficacy of respiratory gating in myocardial SPECT using the new 4D NCAT phantom," *IEEE Trans. Nucl. Sci.*, vol. 49, no. 3, pp. 675–679, Jun. 2002.

[31] T. Cootes, G. Edwards, and C. Taylor, "Active appearance models," *IEEE Trans. Pattern Anal. Mach. Intell.*, vol. 23, no. 6, pp. 681–685, 2001.

[32] D. Rueckert, A. Frangi, and V. T. O. O. A. J. A. Schnabel, "Automatic construction of 3-D statistical deformation models of the brain using nonrigid registration," *IEEE Trans. Med. Imag.*, vol. 22, no. 8, pp. 1014–1025, Aug. 2003.

[33] Y. Wang and L. Staib, "Physical model-based non-rigid registration incorporating statistical shape information," *Med. Image Anal.*, vol. 4, pp. 7–20, 2000.

[34] P. Cachier, E. Bardinet, D. Dormont, X. Pennec, and N. Ayache, "Iconic feature based nonrigid registration: The PASHA algorithm," *Computer Vision Image Understand.*, vol. 89, no. 2–3, pp. 272–298, 2003.

[35] P. Hellier and C. Barillot, "Coupling dense and landmark-based approaches for nonrigid registration," *IEEE Trans. Med. Imag.*, vol. 22, no. 2, pp. 217–227, Feb. 2003.

[36] J. Kim, J. Lee, Y. Lee, J. Kim, I. Kim, and S. Kim, "Intensity based affine registration including feature similarity for spatial normalization," *Comput. Biol. Med.*, vol. 32, no. 5, pp. 389–402, 2002.

[37] T. Liu, D. Shen, and C. Davatzikos, "Deformable registration of cortical structures via hybrid volumetric and surface warping," *NeuroImage*, vol. 22, no. 4, pp. 1790–1801, 2004.

[38] O. Camara, O. Colliot, and I. Bloch, "Computational modelling of thoracic and abdominal regions by means of spatial relationships," *Real-Time Imag.*, vol. 10, no. 4, pp. 263–273, 2004.

[39] O. Colliot, O. Camara, R. Dewynter, and I. Bloch, "Description of brain internal structures by means of spatial relations for MR image segmentation," in *Proc. SPIE Conf. Med. Imag.: Image Process.*, 2004, vol. 5370, pp. 444–455.

[40] F. Maes, "Segmentation and registration of multimodal medical images: From theory, implementation and validation to a useful tool in clinical practice," Ph.D. Dissertation, Katholieke Univ. Leuven, Leuven, Belgium, 1998.

[41] F. Maes, A. Collignon, D. Vandermeulen, G. Marchal, and P. Suetens, "Multimodality image registration by maximization of mutual information," *IEEE Trans. Med. Imag.*, vol. 16, no. 2, pp. 187–198, Apr. 1997.

[42] M. Powell, "An efficient method for finding the minimum of a function of several variables without calculating derivatives," *Comput. J.*, vol. 7, pp. 155–162, 1964.

[43] N. Arad, N. Dyn, D. Riesfeld, and Y. Yeshwin, "Image warping by radial basis functions: Application to facial expressions," *Comput. Vision, Graphics Image Process.: Graphical Models Image Process.*, vol. 56, no. 2, pp. 161–172, 1994.

[44] D. Ruprecht and H. Muller, "Image warping with scattered data interpolation," *IEEE Computer Graphics Appl.*, vol. 15, no. 2, pp. 37–43, Mar. 1995.

[45] K. Rohr, *Landmark-Based Image Analysis: Using Geometric and Intensity Models*, ser. Computational Imaging and Vision. Norwell, MA: Kluwer, 2001, vol. 21.

[46] S. Marsland and C. Twining, "Clamped-plate splines and the optimal flow of bounded diffeomorphisms," in *Proc. Leeds Annu. Statist. Res. Workshop*, 2002, pp. 91–95.

[47] M. Bro-Nielsen and C. Gramkow, "Fast fluid registration of medical images," *Visualization Biomed. Comput. (VBC'96)*, pp. 267–276, 1996.

[48] G. Christensen, M. Miller, U. Grenander, and M. Vannier, "Individualizing neuroanatomical atlases using a massively parallel computer," *IEEE Computer*, vol. 29, no. 1, pp. 32–38, 1996.

[49] E. D'Agostino, F. Maes, D. Vandermeulen, and P. Suetens, "A viscous fluid model for multimcdal non-rigid image registration using mutual information," in *Proc. Int. Conf. Med. Image Comput. Computer-Assisted Intervention (MICCAI'02)*, 2002, pp. 23–26.

[50] T. Sederberg and S. Parry, "Free form deformation of solid geometric models," in *Proc. Int. Conf. Comput. Graphics Interactive Techniques (SIGGRAPH'86)*, 1986, vol. 20, pp. 151–160.

[51] J. Gee, D. Haynor, M. Reivich, and R. Bajcsy, "Finite element approach to warping of brain images," in *Proc. SPIE Conf. Med. Imag.: Image process.*, 1994, vol. 2434, pp. 327–337.

[52] D. Rueckert, I. Somoda, C. Hayes, D. Hill, M. Leach, and D. Hawkes, "Nonrigid registration using free-form deformations: Applications to breast MR images," *IEEE Trans. Med. Imag.*, vol. 18, no. 8, pp. 712–721, Aug. 1999.

[53] W. Crum, D. Rueckert, M. Jenkinson, D. Kennedy, and S. Smith, "A framework for detailed objective comparison of non-rigid registration algorithms in neuroimaging," in *Proc. Int. Conf. Med. Image Comput. Computer-Assisted Intervention (MICCAI'04)*, 2004, pp. 679–686.

[54] O. Camara, W. Crum, J. Schnabel, E. Lewis, M. Schweiger, D. Hill, and N. Fox, "Assessing the quality of Mesh-Warping in normal and abnormal neuroanatomy," in *Med. Image Understand. Anal. (MIUA'05)*, 2005, vol. 1, pp. 79–82.

[55] A. Frangi, D. Rueckert, J. Schnabel, and W. Niessen, "Automatic construction of multiple-object three-dimensional statistical shape models: Application to cardiac modeling," *IEEE Trans. Med. Imag.*, vol. 21, no. 9, pp. 1151–1166, Sep. 2002.

[56] O. Camara, G. Delso, and I. Bloch, "Free form deformations guided by gradient vector flow: A surface registration method in thoracic and abdominal PET-CT applications," in *Proc. Workshop Biomed. Image Registration (WBIR'03)*, 2003, pp. 224–233.

[57] C. Xu and J. Prince, "Generalized gradient vector flow external forces for active contours," *Signal Process., Int. J.*, vol. 71, no. 2, pp. 131–139, Dec. 1998.

[58] J. Montagnat, "Modèles déformables pour la segmentation et la modélisation d'images médicales 3D et 4D," Ph.D. dissertation, INRIA, Sophia-Antipolis, France, 1999.

[59] W. Crum, O. Camara, and D. Hill, "Generalised overlap measures for evaluation and validation in medical image analysis," *IEEE Trans. Med. Imag.*, to be published.

[60] J. Schnabel, C. Tanner, A. Castellano-Smith, A. Degenhard, M. Leach, D. Hose, D. Hill, and D. Hawkes, "Validation of nonrigid image registration using finite-element methods: Application to breast MR images," *IEEE Trans. Med. Imag.*, vol. 22, no. 2, pp. 238–247, Feb. 2003.

[61] D. Perperidis, M. Lorenzo-Valdes, R. Chandrashekara, A. Rao, R. Modiaddin, G. Sanchez-Ortiz, and D. Rueckert, "Building a 4D atlas of the cardiac anatomy and motion using MR imaging," in *Proc. Int. Conf. Med. Image Computing Computer-Assisted Intervention (MICCAI'04)*, 2004, pp. 263–273.

[62] A. Moreno, G. Delso, O. Camara, and I. Bloch, "Non-linear registration between 3-D images including rigid objects: Application to CT and PET lung images with tumors," in *Proc. Workshop Image Registration Deformable Environments (DEFORM'06)*, 2006, pp. 31–40.

[63] T. Rohlfing and C. Maurer Jr., "Nonrigid image registration in shared-memory multiprocessor environments with application to brains, breasts and bees," *IEEE Trans. Inf. Technol. Biomed.*, vol. 7, no. 1, pp. 16–25, 2003.